Thompson, Jake A. (2024) *Using theoretical chemistry to model the redox properties of polyoxometalates and their potential as ammonia synthesis catalysts.* PhD thesis.

https://theses.gla.ac.uk/84572/

Using Theoretical Chemistry to Model the Redox Properties of Polyoxometalates and their potential as Ammonia Synthesis Catalysts

Jake A. Thompson

Supervisors:
Dr. Laia Vilà-Nadal
Dr. Rebeca González-Cabaleiro
Prof. Justin Hargreaves
Prof. Cindy Smith

School of Chemistry
University of Glasgow

Acknowledgements

All work contained within this thesis was carried out between Oct. 2020 and Nov. 2023 in the School of Chemistry, University of Glasgow. Many people have contributed over this period, I would first like to acknowledge the EPSRC Doctoral Training Partnership (DTP) for funding this Ph.D project. I would like to thank my primary supervisors: **Dr. Laia Vilà-Nadal** and **Dr. Rebeca González-Cabaleiro** for giving me the opportunity to work with you and allowing me to explore my passion in chemistry. **Prof. Justin Hargreaves** for allowing me to explore my interests in ammonia synthesis. **Dr. Angela Daisley**, **Rachel Young** & **Mohamed Hosny Elsayed Mostafa Mahmoud** for helping with running ammonia synthesis reactions in the Hargreaves lab. **Prof. Mark Symes** and **Fiona Todman** for our collaboration on electrochemical properties of metal-substituted POMs. **Dr. John Errington** and all members of his group, in particular **Dr. Pascual-Borras** and **Dom Sheils** for giving me the opportunity to explore POM synthesis in organic solution. **Daniel Malcolm, Jake Jacobs,** and **Michael Nicolaou** for all your support. Technical staff: **Euan Stobbs** & **Marcox Pun** for training and troubleshooting of teaching lab equipment. **Claire Wilson**, **Alec Mungall**, and **Gangi Ubbara** for providing on XRD, NMR, and ESI-MS training. And finally, a huge thank you to **Mum**, **Dad**, and my brother, **Ben**. And last but not least, I would like to thank my partner **Kennedy** and our dog, **Kamala**.

Abstract

Polyoxometalates (POMs) have attracted significant interest owing to their structural diversity, redox stability, and functionality at the nanoscale. These structures have attracted significant interest as catalysts in fields including but not limited to: (i) water oxidation; (ii) carbon dioxide reduction; (iii) and nitrogen activation. In this thesis, we provide an in-depth investigation into modelling the structural and electronic behaviours in Keggin-based POMs by means of Density Functional Theory (DFT) calculations, validating with experimental testing. This PhD systematically studies the influence of Hartree-Fock (HF) exchange and the explicitly located counterions on reproducing experimental redox potentials and chemical shifts. Additionally, the present work explores the potential of mono-substituted Keggin POMs as ammonia synthesis catalysts and rationalising their catalytic behaviour using their structural stability and electronic characteristics.

Chapter 1 provides a general introduction to POMs, before focusing on lacunary derivatives which comprise the bulk of our research. In Chapter 2, we provide an overview of quantum mechanics by first introducing the time-independent Schrödinger equation before outlining the fundamentals of DFT, briefly discussing the importance of exchange-correlation functionals and basis sets. This chapter concludes by discussing modern quantum chemical calculations used to model redox and spectroscopic properties in POMs. Chapter 3 details all experimental work carried out during this Ph.D.

In Chapter 4, DFT calculations have been employed to systematically explore the influence of the exchange-correlation functional for Mn(III/II), Fe(III/II), and Co(III/II), and Ru(III/II) redox couples present in $K_5[PW_{11}M(H_2O)O_{39}]$. Early work employed reduction energies (REs) using fully anionic systems coupled with implicit solvent models to reproduce experimental potentials. This assumption has proven useful for Keggin and Wells-Dawson anions, as the reduction process involves adding a single electron to non-bonding orbitals, hence, the entropic and vibrational contributions to ΔG are negligible. In this work, $[PW_{11}M(H_2O)O_{39}]^{q-}$ systems have been modelled using an COSMO solvation model coupled with explicitly located counterions to render the system charge neutral. The incorporation of K^+ counterions induced a positive shifting in potentials of > 500 mV which proved beneficial where M = Mn(III/II)/Co(III/II). By contrast, locating counterions were to the detriment for M = Fe(III/II)/Ru(III/II) due to over-stabilisation of the ion-pairs. Generally, exceeding 25 % Hartree–Fock (HF) exchange is not recommended for $K_5[PW_{11}M(H_2O)O_{39}]$ systems due to their tendency to over exaggerate the proximity of the ion-pairing. Further work exploring the nature of the cation-POM pairing is crucial in obtaining a reasonable agreement between theoretical and experimental results.

In Chapter 5, we have systematically studied the accuracy of exchange-correlation functionals and applied basis sets for replicating experimental chemical shifts in Keggin, $Na_3[PW_{12}O_{40}]$ and their lacunary clusters: $Na_7[PW_{11}O_{39}]$, $Na_8H[A{-}PW_9O_{34}]$, and $Na_8H[B{-}PW_9O_{34}]$. In this work, we have provided an analysis of the geometric and electronic factors controlling experimental chemical shifts across several computational methods. Early work attempted to model chemical shifts

using fully anionic systems with implicit solvent models. Anionic systems modelling using implicit solvation models were highly sensitive to P-O distance in which HF exchange from 15 % (B3LYP*) to 50 % (BH&H), caused chemical shifts to alter by up to ca. 8 ppm for $[PW_{12}O_{40}]^{3-}$, despite only a minor change to P-O of ca. 0.03 Å. These approach typically benefited from hybrid exchange-correlation functionals as opposed to GGA-based methods. Later, the work explicitly located counterions ($X = Li^+$, Na^+, K^+) to render the system charge neutral, approximating the solvent environment by means of an COSMO solvation model. Herein, explicitly located counterions generally induced deshielding of resonance signals with respect to their anionic systems. Such signals were progressively shifted upfield as a function of HF exchange, for example, -10.27 (15 % B3LYP*) to -18.55 ppm (50 % BH&H) in $Li3[PW_{12}O_{40}]^{3-}$ salts and -10.80 (15 % B3LYP*) to -19.04 ppm (50 % BH&H) in $Na_3[PW_{12}O_{40}]$. Unfortunately, obtaining reliable chemical shifts for $[B-PW_9O_{34}]^{9-}$ proved challenging and relies on linear scaling to correct for errors attributed to direct electrostatic interactions between the located counterions and central tetrahedron. Optimal results were accomplished using the PBE/TZP//PBE0/TZP level of theory achieving a MAE and MSE of 4.0 ppm.

In Chapter 6, DFT calculations have been employed to systematically assess the accuracy of various *x-c* functionals in reproducing experimental redox properties in $X_5[PW_{11}M(H_2O)O_{39}]$ salts; where X= Li, Na or K and M = Mn(III/II), Fe(III/II) or Co(III/II). Herein, increasing contributions to HF-exchange coincided with positive shifting of computed potentials, $U^0{}_{Calc}$, attributed to the overstabilisation of the ion-pairing. In some instances, strong sensitivity towards HF exchange was observed, for example, $Li_5[PW_{11}Co(H_2O)O_{39}]$ salts ranged by > 1000 mV shifting from 0 to 50 % exchange. The effect of the applied basis set, restricted to the GGA-PBE functional was explored. By increasing the size of the basis set (TZP $\rightarrow$ TZ2P $\rightarrow$ QZ4P) negative shifting by 200 mV was induced. The challenge in attaining accurate potentials is effectively controlling the proximity of the ion-pairing. Herein, we propose an economical route by explicitly specifying the heteroatom – counterion, d_{P-X} distances at discrete intervals (6 - 10 Å) as opposed to necessitating CPU-expensive optimisations with hybrid *x-c* functionals. Expansion of the solvation shell (from the optimised state to 8 Å) reduced closed-contact electrostatic interactions in the ion-pairing, resulting in a systematic (negative) shifting of computed potentials. Furthermore, we employed polynomial relations to precisely determine explicitly located heteroatom – counterion distances enabling the minimization of computed error ($U^0{}_{Error} \rightarrow 0$ V).

Chapter 7 provides a pioneering study exploring the efficacy of mono-transition-metal-substituted polyoxotungstates, $K_5[PW_{11}M(H_2O)O_{39}]$ (M = M = Mn(II), Fe(II), Co(II), Ni(II), Cu(II), Zn(II)) as heterogeneous ammonia catalysts. The significance of the metal composition was shown to be significant given the range in synthesis rates of 12.37 μmol h^{-1} g^{-1}. The most active catalyst was $K_5[PW_{11}Mn(H_2O)O_{39}]$ reporting a rate of 20.09 μmol h^{-1} g^{-1}, whilst $K_5[PW_{11}Zn(H_2O)O_{39}]$ only produced 7.72 μmol h^{-1} g^{-1}. Structural studies on the post-reaction catalysts revealed the disappearance of the two bands attributed to the asymmetric stretching of the P–O bond upon heating. The breakdown of υ(P–O) vibrations for $K_5[PW_{11}M(H_2O)O_{39}]$; M = Ni, Cu, and Zn suggests comparatively poorer thermal stability, closely correlating with the temperatures of decomposition shown previous work. XRD patterns for $K_5[PW_{11}M(H_2O)O_{39}]$; M = Ni, Cu, and Zn suggest the crystal structure has decomposed forming phosphotungstate bronze $(PO_2)_2(WO_3)_{24}$ crystals.

Publications

The following articles were published as a result of the work undertaken over the course of this programme.

1. R. González-Cabaleiro, **J. A. Thompson** and L. Vilà-Nadal, *Front. Chem.*, **9**, 2021, 1-11. L.V-N conceived the idea, designed the project and together with R.G.-C coordinated the efforts of the research team. L.V.-N and R.G.-C co-wrote the paper with input from J.A.T.

2. **J. A. Thompson**, R. González-Cabaleiro, and L. Vilà-Nadal, *Chem. Rxiv*, 2022, 1–17. L.V.-N. and R.B.-C. conceived the idea together with J.A.T. who designed the modelling approach, performed all the theoretical calculations, and analyzed all the data. J.A.T. wrote the paper and made all the figures in the manuscript with input from L.V. -N and R.B.-C.

3. **J. A. Thompson**, R. González-Cabaleiro, and L. Vilà-Nadal, *Inorg. Chem.*, 2023, **31**, 12260–12271. L.V.-N. and R.B.-C. conceived the idea together with J.A.T. who designed the modelling approach, performed all the theoretical calculations, and analyzed all the data. J.A.T. wrote the paper and made all the figures in the manuscript with input from L.V. -N and R.B.-C.

4. **J. A. Thompson** and L. Vilà-Nadal, *Dalton Trans*, 2024, **53**, 564-571. L.V.-N. conceived the idea together with J. A. T. who designed the modelling approach, performed all calculations, synthesised, and fully characterised all the compounds and analysed all the data. J. A. T. wrote the paper and made all tables and figures in the manuscript with input from L.V.-N.

5. **J. A. Thompson**, F. Todman, M. D. Symes and L. Vilà-Nadal, 2024. Manuscript in progress. J. A. T. designed the modelling approach, performed all the theoretical calculations, and analysed all the data. J.A.T performed all compound characterisations, including electrochemical experiments with training and input from F. T. J.A.T wrote the paper and made all figures and tables in the manuscript with input from F.T, L.V.–N and M.D.S.

Conferences

1. **J. A. Thompson**, R. González-Cabaleiro, and L. Vilà-Nadal. ”Reducing Systematic Uncertainty in Computed Redox Potentials for Aqueous Transition-Metal-Substituted Polyoxotungstates”. University of Glasgow, 19 -20th August 2023. Selected for presentation at Computational Chemistry Symposia, Glasgow.

2. **J. A. Thompson**, R. González-Cabaleiro, and L. Vilà-Nadal. ”Structural and electronic properties of metal-substituted polyoxometalates”. University of Edinburgh, 29 -30th August 2022. Selected for poster. presentation at Computational Chemistry Symposia, Edinburgh.

3. **J. A. Thompson**, R. González-Cabaleiro, and L. Vilà-Nadal. ”Heterogeneous Ammonia Catalysis using metal-substituted polyoxometalates”. Poster in ‘Sustainable nitrogen activation Faraday Discussion’ 27 - 29th March 2023, London, United Kingdom, Royal Society of Chemistry, Faraday discussions

4. **J. A. Thompson**, R. González-Cabaleiro, and L. Vilà-Nadal. ”Structural and electronic properties of metal-substituted polyoxometalates”. La Rochelle, 21 -23rd June 2022. Selected for spotlight presentation at international Conference on ”Polyoxometalate chemistry for fundamentals and applications at POM Basics 2022".

5. **J. A. Thompson**, R. Gonzalez-Cabaleiro, and L. Vila-Nadal. ”Sustainable Nitrogen Fixation using metal-substituted poloxometalates”. University of Newcastle, 9 - 10th Dec 2021. Selected for presentation at International Network on Polyoxometalate (INPOMs) science conference on ”Polyoxometalate chemistry for fundamentals and applications.

6. **J. A. Thompson**, R. González-Cabaleiro, and L. Vilà-Nadal. Poster presentation titled: ”Sustainable Nitrogen. RSC global Twitter poster conference, 3 - 4th Feb 2021.

Contents

List of Figures

List of Tables

Chapter 1

Introduction

In this chapter, we provide an introduction to polyoxometalates (POMs) beginning with their synthetic procedure, followed by an overview of their self-assembly mechanisms. Thereafter, we focus attention onto several classes of POMs including but not limited to: Lindqvist, Keggin, Wells-Dawson and their corresponding lacunary derivatives. Later, we present examples of how synthetic parameters can affect the equilibrium between monomeric and sandwich architectures.

1.1 Introduction to Polyoxometalates

Polyoxometalates (POMs) are a versatile class of molecular metal-oxo clusters which present unique structural and electronic properties.[1–5] They are constructed from early transition metals (also known as addenda atoms) in their highest oxidation states (W(VI), Mo(VI), V(V)) employing $\mathrm{MO_x}$ units as the principal building block.[1–4] The polyhedral building blocks, MO_x, are connected through corner, edge or face sharing.[6] POMs have attracted significant interest attributed to their structural diversity, capable of adopting several moieties ranging from two coordinated metal species e.g. $\{\mathrm{Mo_2}\}$ to $\{\mathrm{Mo_{154}}\}$ rings up to 3.6 nm in diameter.[7] These diverse features have attracted significant interest in fields including: (i) medicine[8] (ii) magnetism[9,10]; (iii) protein hydrolysis[11]; (iv) and redox catalysis[12].

The synthesis of high nuclearity structures consists of acidifying aqueous alkaline salts containing the relevant metal oxide anions.[4] Equation 1.1 follows a simple condensation-type reaction and leads to the formation of charge dense polyoxoanion clusters, in solution. Generally, these reactions are performed as one-pot syntheses, thereby avoiding complex and time consuming separation steps.[4] Their self assembly process can be modified through multiple synthetic variables.[4] Common variables include: pH, concentration of reagents, metal oxide precursors, heteroatom, and the temperature.[4] Syntheses are commonly performed in water, although polar organic solvents (e.g. acetonitrile) can produce different clusters relative to the equivalent aqueous setup.[13,14]

$$x\,\mathrm{Mo_4}^{q-} + z\,\mathrm{H}^+ \longrightarrow [\mathrm{M}_x\mathrm{O}_y]^{m-} + \mathrm{z/_2H_2O} \tag{1.1}$$

Isolation from solution is achieved using simple counterions including but not limited to: $\mathrm{Na^+}$, $\mathrm{K^+}$, $\mathrm{NH_4}^+$ or organic alkylammonium cations. Aqueous solubility can fine-tuned by incorporating small alkali metal cations ($\mathrm{Li^+}$ and $\mathrm{Na^+}$). By contrast, larger alkali metal cations (e.g. $\mathrm{Cs^+}$) show poor solubility in aqueous solution.[15,16] Organic solubility can be achieved by employing large alkylammonium or alkylphosphonium cations.[13–15] In select cases, counterions have been employed to direct POM self-assembly.[17] Yan and co-workers reported that employment of triethanolammonium ($\mathrm{TEAH^+}$) or dimethylammonium ($\mathrm{DMAH^+}$) can direct assembly of the "peanut-like" structural motif $(TEAH)_6[H_2W_{18}O_{57}(SO_3)]$ or the "Trojan Horse" $(DMAH)_8[W_{18}O_{56}(SO_3)_2(H_2O)_2]$ clusters.[17]

1.1.1 History of Polyoxometalates

In 1826, J. J. Berzelius reported that acidification, using excess phosphoric acid on ammonium molybdate, $(NH_4)_2MoO_4$ produced a light yellow crystalline solid, later deduced to be $(NH_4)_3$-$[PMo_{12}O_{40}]$.[18] However, the analytical composition of heteroypoly acids was not precisely determined until the discovery of tungstosilicic acids and their salts, discovered by Marignac in 1862.[19,20] Thereafter, the field developed significantly, so that several hundred had been discovered by the first decade of the 20^{th} century. Before the emergence of X-ray diffraction methods, exact composition and morphology of the crystal was unknown. Hence, only theoretical insights into the structural composition were presented. An early example of this was Miolati-Rosenheim (MR) theory, which suggested heteropoly acids were comprised of six-coordinate heteroatoms with $MO_4{}^{2-}$ or $M_2O_7{}^{2-}$ units as ligands or bridging groups, e.g. $H_8[Si(W_2O_7)_6]$.[1] In the following years, Pauling challenged the Rosenheim structures by noting Mo^{6+} and W^{6+} had crystal radii appropriate for an octahedral coordination environment with oxygen.[1] Pauling had proposed an alternative theory postulating the central tetrahedral, XO_4, heteroatom was encapsulated by twelve corner-sharing $\{MO_6\}$ octahedra with the resulting formula: $H_4[SiO_4W_{12}O_{18}(OH)_{36}]$.[21] In 1933, J. F. Keggin using X-ray powder diffraction data solved the structure of phosphotungstic acid, $H_3PW_{12}O_{40}$, which showed $\{MO_6\}$ octahedra were connected through edge and corner-sharing.[22,23] In 1937, the discovery of $[Te(VI)Mo_6O_{24}]$ was reported by Anderson and then subsequently crystallographically determined by Evans in 1948.[24,25] Wells-Dawson heteropolyanions were initially proposed by Wells and later confirmed by Dawson in 1945 and 1953, respectively.[26] In 1953, the $[Nb_6O_{19}]^{8-}$ was the first of the Lindqvist family to be characterised.[27]. More recently, Müller and co-workers isolated single crystals of the molybdate wheel from blue Mo solutions with a general formula: $[Mo_{154}(NO)_{14}O_{448}H_{14}(H_2O)_{70}]^{28-}$, $[Mo(VI)_{126}Mo(V)_{28}]$ or $\{Mo_{154}\}$ - see Figure 1.1.[28]

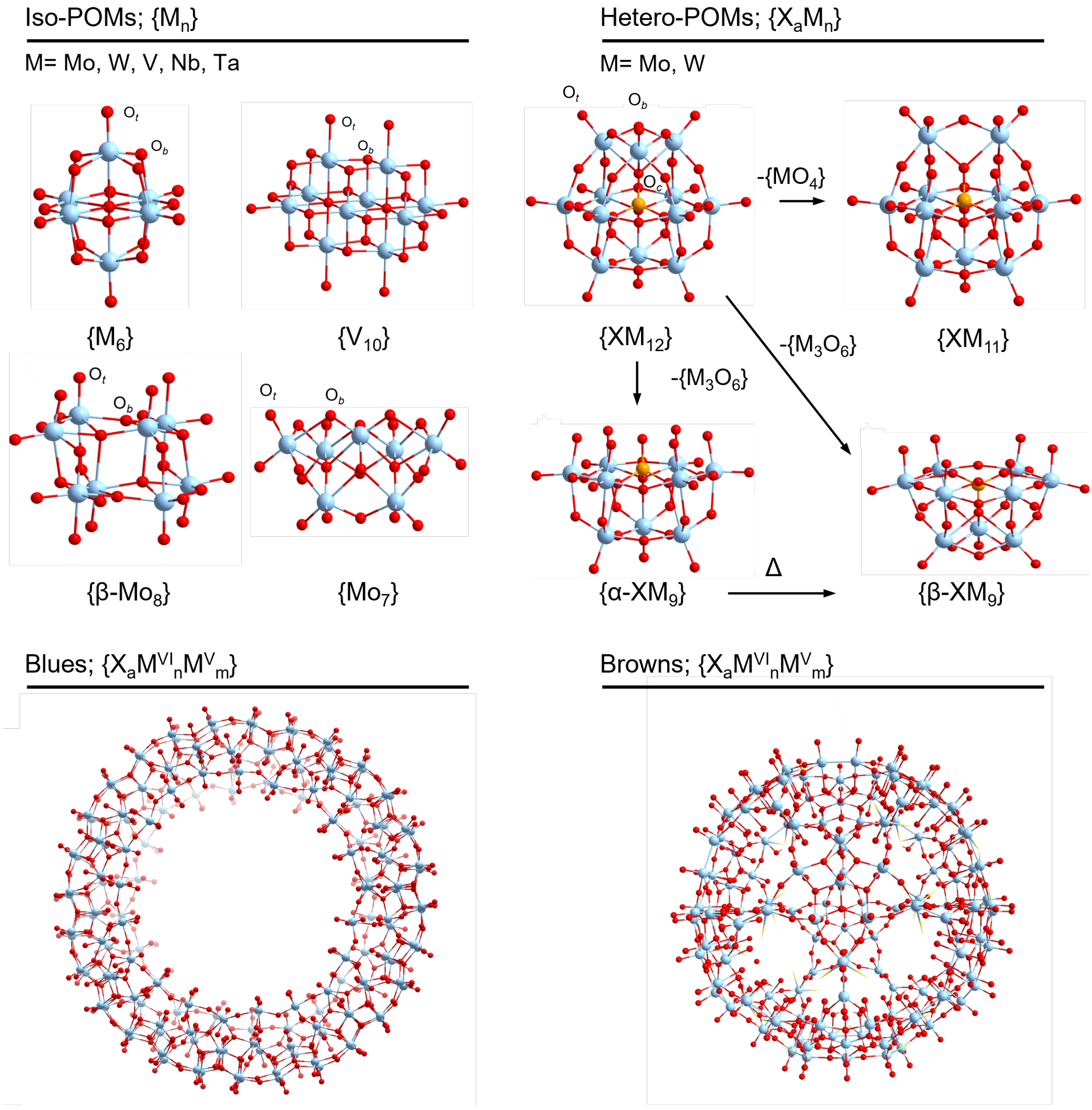

Figure 1.1: Schematic depictions showcasing products of the self-assembly mechanism of POM clusters. Iso-polyanions (top-left) shown are Lindvist, $\{W_6\}$ Decavanadate, $\{V_{10}\}$, Heptametalates, $\{M_7\}$, and β-octamolybdate, $\{Mo_8\}$. Hetero-polyanions (top-right) depicted are Keggin, $\{XM_{12}\}$ and their lacunary derivatives: $\{XM_{11}\}$ and $\{XM_9\}$. Polyhedral representations of the $\{Mo_{154}\}$ (bottom-left) and $\{Mo_{134}\}$ (bottom-right) are shown. Colours corresponding to M = Cyan; and O = red.

1.1.2 Structure and Bonding in Polyoxometalates

The self assembly mechanism for POMs can be described as a condensation-type reaction employing MO_x units as the principal building block. These building blocks can be bridged together through face, corner and edge sharing.[6] MO_6 octahedra are common building blocks in POMs, comprising Mo(V/VI), W (V/VI), V (IV/V)[29], Nb (V)[30], and Ta(V).[31] The transition metals are usually obtained in their two highest oxidation states, d^0 or d^1.[6] These empty metallic d-orbitals permit strong π-bonding with O^{2-} atoms.[6] π-bonding is formed between empty metallic d-orbitals (d_{xy}, d_{xz}, d_{yz}) and the occupied oxo-orbital (p_x, p_y) of appropriate symmetry. In turn, terminal oxygen atoms feature decreased basicity with respect to the bridging oxo-atoms, which impedes their growth leading to the formation of discrete clusters.[2] The polarisation of terminal oxygen groups results in weak binding to protons resulting in high Brønsted-acidity.[2]

1.1.3 Isopolyoxometalates

Isopolyoxometalates are given the general formula, $[M_yO_z]^{q-}$, whereby M consists of group 5 or 6 metal cations bridged by oxygen atoms. Iso-POMs are highly tunable in terms of structure, redox, and solution properties by modification of the addenda atom and cluster topology.

1.1.3.1 Lindqvist

Lindqvist clusters are bridged together through 4 μ_2-O atoms, and 1 terminal μ_1- O atoms - see Figure 1.2. The following structures: $[Mo_6O_{19}]^{2-}$, $[W_6O_{19}]^{2-}$, $[Nb_6O_{19}]^{8-}$,[32,33] and $[Ta_6O_{19}]^{8-}$[34] feature six edge-sharing octahedra with O_h symmetry. Lindqvist clusters feature shorter terminal bonding, for example Mo-O_t in$[Mo_6O_{19}]^{2-}$ is 0.2 Å shorter (≈ 1.7 Å) compared to the bridging Mo-O_b reporting at ≈ 1.9 Å.[35]

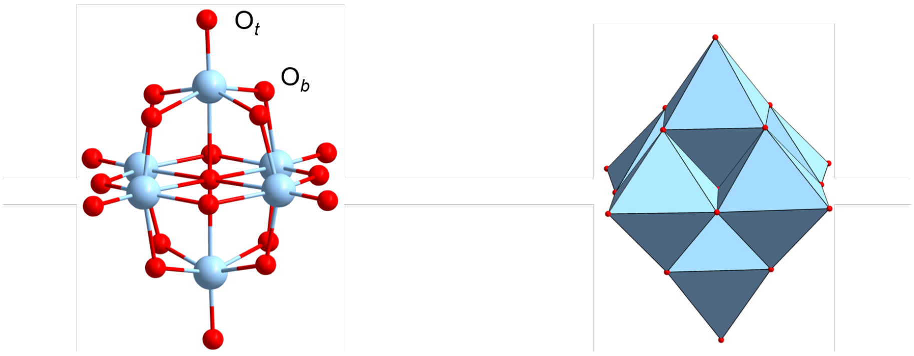

Figure 1.2: Schematic depictions for the Lindqvist anion, $[M_6O_{19}]^{2-}$, M = Mo(VI) or W(VI). The structure is constructed from terminal, O_t and bridging, O_b, oxygen atoms. Colours corresponding to M = Cyan; and O = red.

Lindqvist possess strongly electron withdrawing μ_1- O atoms which can interact with electrophilic transition metals (Co, Ni) to form complex counterions.[36] Cronin and co-workers have reported that treating $[Mo_6O_{19}]^{2-}$ with Ag(I) cations led to aggregation of (Ag{Mo_8}Ag) building blocks in coordinating solvent.[37]. Organoimido derivatives of $[M_6O_{19}]^{2-}$; M = W(VI) or Mo(VI) have been reported using phosphinimines[38,39], isocyanates[40,41], or aromatic amines[42,43]. Incorporating transition-metals to the metal-oxo framework has led to the discovery of heterometallic clusters. For example, Parac-Vogt and co-workers reported the hydrolysis of selected dipeptides in the presence of a Zr(IV)-substituted Lindqvist.[44] Further examples of Zr(IV)-substituted Lindqvist-based catalysis has been reported with epoxidation catalysis of C=C bonds in unfunctionalized alkenes.[45,46]

1.1.3.2 Decavanadates

Decavanadates, $[H_xV_{10}O_{28}]^{(6-x)-}$ are produced by acidification of metavanadate anions, $VO_3{}^-$, over a wide range of pH values.[47] Decavanadates feature a rectangular array of {VO_6} octahedra sandwiched between two {V_2O_8} dimers on either side of the plane - see Figure 1.3. Decavanadates can support several protonation states, ranging from x= 1 to 4, depending on solution pH.[47–51] A comparison with the V(V)-based hexavanadate which has only been isolated in the presence of alkoxides ligands, taking the form: $((C_4H_9)_4N)V^{V}{}_6O_{12}(OCH_3)_7]$ required to stabilise the high charge density of the $\{V_6O_{19}\}$ cluster.[52–54]

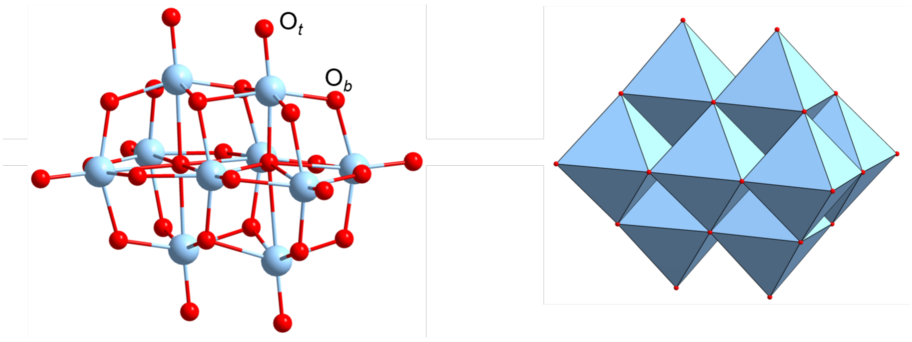

Figure 1.3: Schematic depictions for the decavanadate anion, $[V_{10}O_{28}]^{6-}$. The structure is constructed from terminal, O_t and bridging, O_b, oxygen atoms. Colours corresponding to V(V) = Cyan; and O = red.

1.1.3.3 Heptametalates

Heptametalates, $[M_7O_{24}]^{6-}$; M = Mo(VI) or W(VI) can be obtained at the pH range approximately 3 to 5.5 and 6.0 for the heptamolybdate (paramolybdate) and heptatungstate (paratungstate), respectively.[1] These structures are employed as precursors in the formation of larger clusters, for example, $[Mo_{36}O_{112}(H_2O)_{18}]^{8-}$, comprised of 2 MoO_6 octahedra units bonded directly to two Mo_{17} units - see Figure 1.4.[55]

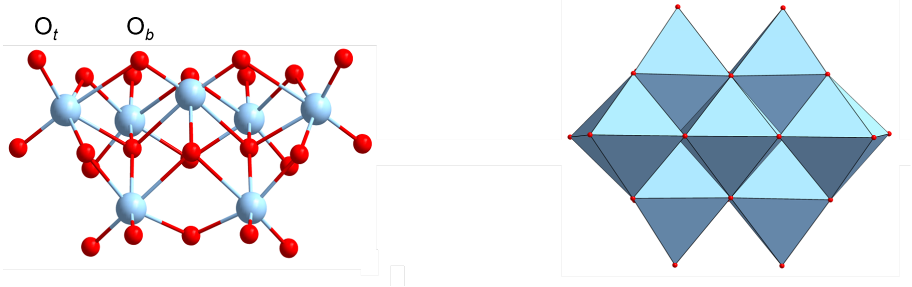

Figure 1.4: Schematic depictions for the heptametalate anion, $[M_7O_{24}]^{6-}$; M = Mo(VI) or W(VI). The structure is constructed from terminal, O_t and bridging, O_b, oxygen atoms. Colours corresponding to M = Cyan; and O = red.

Krebs and co-workers reported the crystal structure for the open-shell cluster unit, $[Mo_{36}O_{112}(H_2O)_{18}]^{8-}$, which can be isolated as the main species in highly acidic solution, $pH < 2$.[1,56] The cluster can be visualised as two $\{Mo_{17}\}$ fragments, bridged by two $\{Mo_1\}$ units, producing an open-shell ellipsoidal cluster.[56] Each $\{Mo_{17}\}$ fragment is comprised of the heptamolybdate, $[Mo_7O_{24}]^{6-}$ used as an essential building unit.[56]

1.1.3.4 Octamolybdates

Acidification of molybdate solutions to pH 3-4, in the presence of tetrabutylammonium cations (TBA^+) leads to precipitation of α-$[Mo_8O_{26}]^{4-}$.[57] Raman studies have established the β-$[Mo_8O_{26}]^{4-}$ isomer dominants at pH 2.0 whilst the α-$[Mo_8O_{26}]^{4-}$ structure dominants at pH 2.7.[58] Klemperer and Shum found the addition of counterions such as K^+ and $N(CH_3)_4{}^+$ to a solution of acidified aqueous sodium molybdate (pH 3.0- 4.0) induced facile isomerization to the β-$[Mo_8O_{26}]^{4-}$.[59]

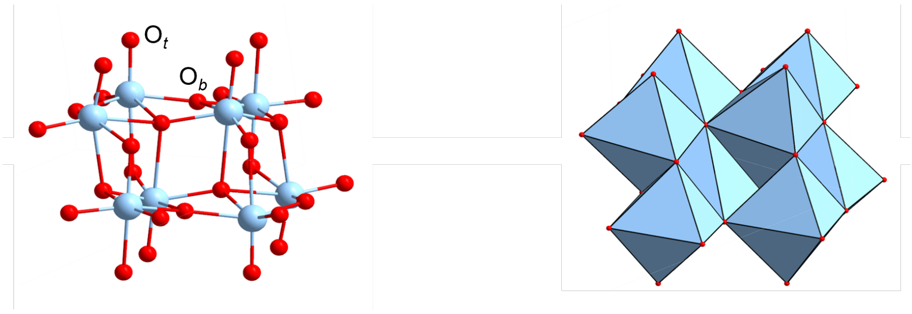

Figure 1.5: Schematic depictions for the octamolybdate anion, β-$[Mo_8O_{26}]^{4-}$. The structure is constructed from terminal, O_t and bridging, O_b, oxygen atoms. Colours corresponding to Mo = Cyan; and O = red.

Formation of the β-$[Mo_8O_{26}]^{4-}$ cluster can be achieved through acidification of molybdate solutions to pH 2-3.[60] The cluster is comprised of eight distorted corner and edge-sharing $\{MoO_6\}$ octahedra, shown in Figure 1.5.[60] β-$[Mo_8O_{26}]^{4-}$ clusters contains 16 $Mo{=}O_t$ groups by which each metal centre contains two short terminal bonds with *cis* geometry.[60] These terminal oxo-groups can behave as chelating ligands leading to the formation of several complexes featuring copper(II)[61], lanthanum(III)[62], and gadolinium(III)[63]. This strategy has been extended enabling controllable molecular growth of $\{Ag(Mo_8)Ag\}_n$-type polymers using β-$[Mo_8O_{26}]^{4-}$ and $\{Ag_2\}$ synthons.[64] The authors reported that employment of sterically bulky cations coupled with varying chain lengths and coordinating solvents can be used to produce clusters with different dimensionalities.[64]

1.1.3.5 Metatungstates

The formation of isopolytungstates are formed by acidification of an aqueous tungstate solutions to pH $\approx$ 4.[65] A prominent example, α-$[H_2W_{12}O_{40}]^{6-}$ cluster resembles the Keggin topology.[65] However, the central cavity is occupied by two protons, instead of tetrahedral heteroatoms, such as $PO_4{}^{3-}$.[65] Sécheresse and co-workers reported α-$[H_2W_{12}O_{40}]^{6-}$ cluster could be used as a fundamental building block for 3-D polyoxotungstate architectures, in the presence of copper(II).[66] The authors reported the nature of the clusters and their connectivity to copper(II) were controlled by initial pH and the presence or absence of heteroelement (P(V), Si(IV)).[66] In the absence of heteroatoms, the molecular compound $[Cu(en)_2(H_2O)]_2[\{Cu(en)_2\}H_2W_{12}O_{40}]$ was formed at pH 5, whilst at neutral pH, 3-D networks of $[\{Cu(en)_2\}_3\{Cu(en)_2\}H_2W_{12}O_{42}]$ were produced.[66]

Acidification of aqueous tungstate solutions to pH < 1, isolates the Ψ-metatungstate, $[H_4W_{11}O_{38}]^{6-}$ clusters.[65] The cluster is comprised of three building blocks: $[W_4O_{16}]$, $[W_3O_{13}]$, and $[W_2O_{10}]$. The $[W_4O_{16}]$ sub-unit formed the backbone of the cluster which are connected to the $[W_3O_{13}]$ triad bridged by two $[W_2O_{10}]$ units - see Figure 1.6. Cronin and co-workers reported the Ψ-metatungstate can be used to form the $\{W_{36}\}$ moiety - the largest isopolytungstate currently known.[67]

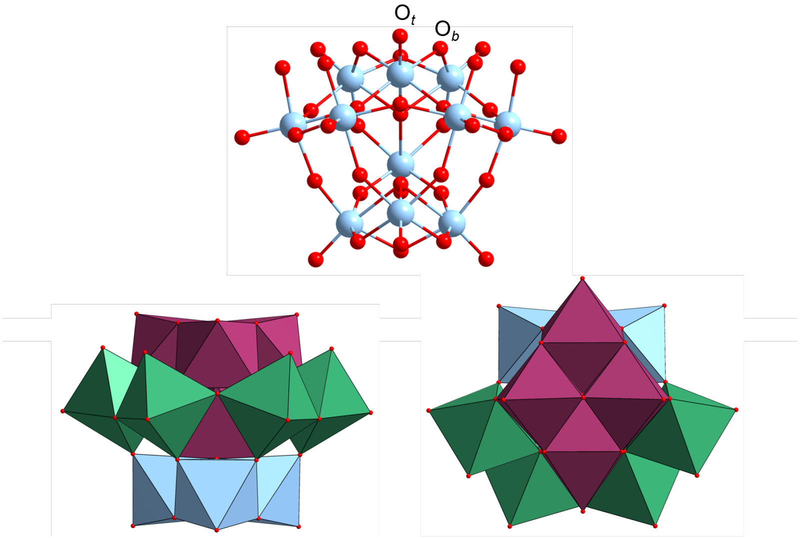

Figure 1.6: Schematic depiction of the Ψ-metatungstate $[H_4W_{11}O_{38}]^{6-}$. The formal sub-units $[W_4O_{16}]$ (purple); $[W_3O_{13}]$ (blue) $[W_2O_{10}]$ (green) used for the construction of the cluster. Herein, $\{W_4\}$ and $\{W_3\}$ building blocks are bridged by two dioctahedral $\{W_2\}$ linkers. Colours corresponding to W = Cyan; and O = red.

1.1.4 Heteropolyoxometalates

Heteropolyanions, $[X_xM_yO_z]^{q-}$, x ≤ y, contain p-, d- or f-block heteroatoms, denoted as X, e.g: P(V), Si(IV), and B(III).[1,2] Heteropolyanions are highly tuneable in terms of structure, stability, and electronic properties by by modification of the central heteroatom. Various topologies are available including: (i) Anderson-Evans $[XM_6O_{24}]^{q-}$, (ii) Keggin $[XM_{12}O_{40}]^{q-}$, and Wells-Dawson $[X_2M_{12}O_{62}]^{q-}$.[1,2]

1.1.4.1 Anderson-Evans

Anderson-Evans is assigned the general formula $[XM_6O_{24}]^{q-}$ where M = Mo(IV) or W(IV), X = p-, d- or f-block heteroatom, and q = 2 to 6 - see Figure 1.7.[2,68,69] Anderson-Evans clusters are usually isolated from their respective polyoxoanion solutions following acidification to approximately pH 3.0 - 4.0, although structures incorporating Cu(II) or Mn(II) heteroatoms have not been recrystallized due to issues with stability.[2,68,69] This structure is templated from a central, edge-sharing XO_6 unit encapsulated by six edge-sharing MO_6 octahedra in a planar manner with overall D_{3d}. In 1974, the first Anderson-Evans structure was identified as $[TeMo_6O_{24}]^{6-}$.[70] Thereafter, the discovery of Anderson-Evans structures incorporating heteroatoms with oxidation states in the range 2 - 7 have been isolated. Anderson-Evans structures can be classified into two subsets: A-type, which are deprotonated, highly charge dense species containing Te(VI) and I(VII) heteroatoms, and B-type, which are protonated, often observed in lower oxidation states.[71] For B-type clusters, protons bound to the μ_3-O atoms of the central XO_6 octahedron are non-acidic.[71]

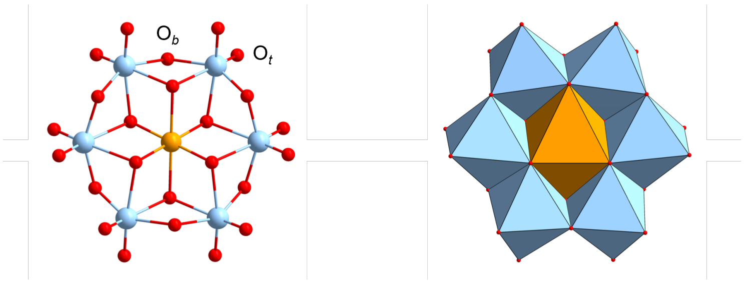

Figure 1.7: Schematic representation for the Anderson-Evans anion, $[XM_6O_{24}]^{q-}$ where M = Mo(IV) or W(IV), X = p-, d- or f-block heteroatom, and $q = 2$ - 6. The structure is constructed from terminal, O_t and bridging, O_b, oxygen atoms. Colours corresponding to M = Cyan, X = orange, and O = red. central heteroatom.

Functionalisation of B-type Anderson-Evans using tris(alkoxo) ligands, $-RC(CH_2OH)_3$ (R = alkyl, aryl, etc) can be used to formulate new organic-inorganic hybrids.[72–74] An indirect method involving of treating the α-$[Mo_8O_{26}]^{4-}$ cluster with tris(alkoxo) ligands and heteroatom acetate salts has been reported for the formation of the functionalised Anderson-Evans clusters.[72–74] The tris(alkoxo) ligands can adopt two separate binding arrangement.[72] The first arrangement involves coordination of each tris(alkoxo) ligand directly to the central heteroatom., whilst the seconded involves bonding of the ligand to two μ_3- O atoms and one μ_2- O atoms, located directly above the tetrahedral cavity adjacent to the XO_6 octahedron of the Anderson-Evans cluster.[72] There are examples of coordination compounds with these clusters, for example, $[IMo_6O_{18}]^{7-}$ clusters were treated with either Ce(III) or La(III) cations to form unique two-dimensional (2-D) networks comprising rare earth coordination polymer chains joint together by Anderson-Evans polyoxoanions.[75]

1.1.4.2 Keggin

Keggin anions can be assigned the general formula $[XM_{12}O_{40}]^{q-}$ M = Mo(VI) or W(VI), X = p-, d- or f-block heteroatoms - see Figure 1.8. The crystal structure was first reported by J. F. Keggin in 1933 for phosphotungstic acid using powder XRD.[22,23] The Keggin anion is comprised of four M_3O_{13} triads linked through corner sharing, possessing overall T_d symmetry. Each addenda atom contains a single terminal oxo-ligand. Generally, heteroatoms are p-block elements (e.g. B(III), Si(IV), Ge(IV), P(V), and S(VI)), although, some reports have incorporated transition metals, such as Zn(II).[76] Rotational isomerism of the M_3O_{13} triads introduces $\alpha-$, β-, γ-, δ-, and ϵ- isomers as reported by Baker and Figgis.[77,78] The $\alpha-$Keggin is the most stable isomer due to increasing coulombically-unfavourable edge-shared octahedron in the other isomers.[79]

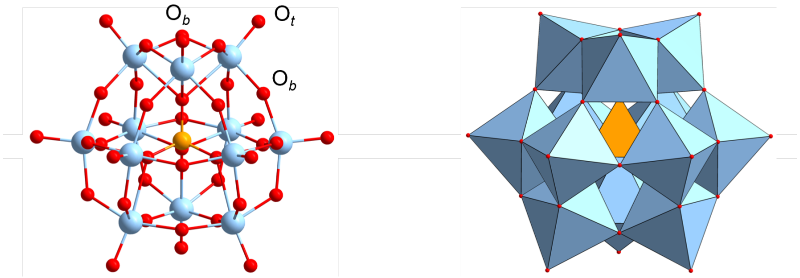

Figure 1.8: Schematic representation for the Keggin anion, α-$[XM_{12}O_{40}]^{q-}$. The structure is constructed from terminal, O_t and bridging, O_b, oxygen atoms. Colours corresponding to M = Cyan, X = orange, and O = red.

Base hydrolysis of the Keggin anion achieved through the addition of base produces lacunary polyanions; whereby {MO} units are removed. These complexes formally lose one M=O vertex and possess reactive cavities with high charge density around the defective region due to the negatively charged oxygen ligands.[80] The stability of the Keggin anion towards base hydrolysis is correlated with the charge of the central heteroatom as follows: $[PW_{12}O_{40}]^{3-}$ (pH 1.5); $[SiW_{12}O_{40}]^{4-}$ (pH 4.5); $[BW_{12}O_{40}]^{5-}$ (pH 7.0).[81] Base decomposition produces the following lacunary derivatives: $[XM_{11}O_{39}]^{q-12}$, $[XM_{10}O_{36}]^{q-12}$, and $[XM_9O_{34}]^{q-14}$, discussed in Section 1.2.1. Further isomerism is introduced from the emergence of A- and B-type lacunary isomers based orientation of XO_4 tetrahedron relative to the vacancy.[82] B-type isomers, the central tetrahedron, XO_4, possess an oxygen ligand accessible to coordination with other groups.[82] By contrast, A-type tri-lacunary species, XO_4 tetrahedron forms coordinate bonds with the tungsten-oxygen cage and cannot bond directly to any peripheral heteroatoms.[83] That said, A-type isomers are capable of interacting with peripheral heteroatoms by means of the terminal oxygen groups.[84]

1.1.4.3 Wells-Dawson

Wells-Dawson clusters can be assigned the general formula $[X_2M_{18}O_{62}]^{q-}$ M = Mo(VI) or W(VI), X = p-, d- or f-block heteroatoms - see Figure 1.9.[85] The structure is comprised of two $\{M_6O_{27}\}$ "belts" sandwiched between two $\{M_3O_{13}\}$ caps.[85] M_3O_{13} caps are composed of three edge-sharing MO_6 units which bond directly to the M_6O_{27} belts through corner sharing. Encapsulated within the framework are two XO_4 tetrahedrons, with one μ_4- O atom which bond directly to the M_3O_{13} caps. The remaining three O atoms have μ_3 bonding character and coordinate to the M_6O_{27} belt oxides. Each belt is composed of six corner-sharing MO_6 octahedra in a planar arrangement. Rotational isomerism of $[X_2M_{18}O_{62}]^{q-}$ can be introduced through 60° rotations of the belt and/or cap groups producing: α, α*, β, β*, γ, and γ* isomers.[86] Density Functional Theory (DFT) calculations have quantified the relative stability of these rotational isomers, following the order $\alpha > \beta > \gamma > \gamma^* > \beta^* > \alpha^*$.[87]

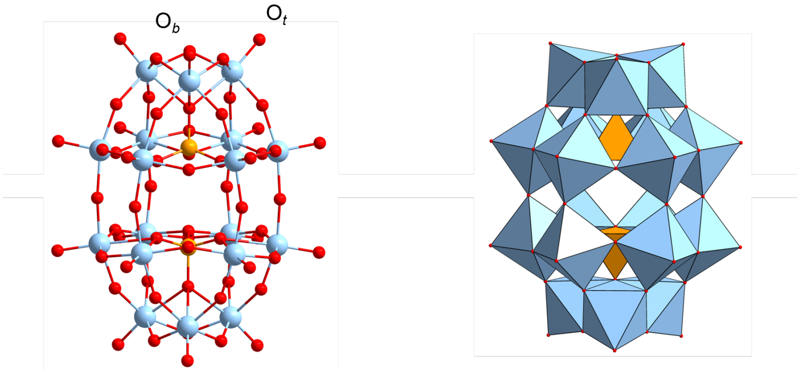

Figure 1.9: Schematic representation for the Wells-Dawson anion, α-$[X_2M_{18}O_{62}]^{q-}$. The structure is constructed from terminal, O_t and bridging, O_b, oxygen atoms. Colours corresponding to M = Cyan, X = orange, and O = red.

Base hydrolysis of Wells-Dawson clusters can be achieved by exceeding solution pH of ≈ 6.[88] α-$[X_2M_{18}O_{62}]^{q-}$ exhibit α_1 and α_2- isomerism formed by the removal of a tungsten-oxo unit from the $\{W_6O_{27}\}$ belt and $\{W_3O_{13}\}$ cap, respectively.[88] The entire removal of the $\{W_3O_{13}\}$ cap produces the tri-lacunary $[\alpha\text{-}X_2W_{15}O_{56}]^q$ derivative. Further degradation produces $[\alpha\text{-}H_2X_2W_{12}O_{48}]^q$ in which two tungsten-oxo units are removed from each belt and one from each cap.[88] Lacunary clusters can behave as inert, pentadentate ligands containing five $\mu_2$bridging oxoligands. Conventionally, hexa-coordinate heteroatoms are incorporated into polytungstates so the sixth coordination site are occupied by solvent ligands from the local environment.

1.2 Transition-Metal-Substituted Polyoxometalates

1.2.1 Monomeric Structures

Experimental reports on mono-substituted heteropolyanions, $[XW_{11}M(L)O_{39}]^{q-}$ and $[X_2W_{17}M(L)O_{61}]^{q-}$; L = H_2O or DMSO are extensive. This subclass of compounds represents the largest and most versatile class of lacunary compounds. These complexes have attracted significant interest in fields such as: (i) water splitting[12]; (ii) carbon dioxide reduction[89]; and Bronsted-acid catalysis[11], attributed to their diverse properties by incorporating several heteroatoms into their framework. The diversity of compounds and their corresponding ligands have been tabulated in Table 1.1. Monomeric compounds are prepared by direct combination of the lacunary ligand and an appropriate heteroatom complex, in aqueous or non-aqueous solution.[90–92] Solution behaviour of these compounds can be fine-tuned by modification of the counter-ions.[93] High aqueous solubility with charge dense alkali cations, e.g Li^+ and Na^+ can be achieved.[93] By contrast, poor aqueous solubility is seen with larger alkali cations, for example, Cs^+.[93] Whilst, solvation in non-polar solvent has been achieved by means of large alkylammonium[93,94] or alkylphosphonium[93,95] cations.

Table 1.1: Reported examples for the mono-substituted Keggin, $[XW_{11}M(H_2O)O_{39}]^{q-}$, and Wells-Dawson, $[X_2W_{17}M(H_2O)O_{61}]^{q-}$, anions taken from the literature.

$[XW_{11}M(L)O_{39}]^{q-}$	XO_4, $q = 4$	XO_4, $q = 5$	XO_4, $q = 6$
Sc	[a]PO_4^{3-}[96]		
Cr	[a]PO_4^{3-}[97]	[a]SiO_4^{4-}[98]	
Ti	[e]PO_4^{3-}[99]		
Mn	[a]PO_4^{3-}[90]	[a]PO_4^{3-}[90] , [a]GeO_4^{4-}[90] , [a]SiO_4^{4-}[90],	[a]GeO_4^{4-}[90], [a]SiO_4^{4-}[90], [a]BO_4^{5-}[90]
Fe	[a]AsO_4^{3-}[100], [a]PO_4^{3-}[100]	[a]SiO_4^{4-}[100], [a]GeO_4^{4-}[100]	[a]BO_4^{5-}[100]
Co		[a]PO_4^{3-}[91,98]	[a]SiO_4^{4-}[101]
Ru	[a,b]PO_4^{3-}[91,102]	[a,b]PO_4^{3-}[91,102], [a,f]SiO_4^{4-}[92], [a,b]GeO_4^{4-}[103]	
Rh	[a,c,d]PO_4^{3-}[104]		
Ir	[a]PO_4^{3-}[105]		
Ni		[a]PO_4^{3-}[98]	[a]GeO_4^{4-}[89], [a]SiO_4^{4-}[106]
Cu		[a]PO_4^{3-}[107]	[a]SiO_4^{4-}[90], [a]GeO_4^{4-}[90]
Zn		PO_4^{3-}[98]	
$[X_2W_{17}M(L)O_{61}]^{q-}$	XO_4, $q = 6$	XO_4, $q = 7$	XO_4, $q = 8$
Cr		[a]PO_4^{3-}[97]	
Mn		[a]AsO_4^{3-}[90], [a]PO_4^{3-}[90,108]	[a]AsO_4^{3-}[90], [a,d]PO_4^{3-}[109]
Fe		[a]PO_4^{3-}[108]	[a,d]PO_4^{3-}[109]
Co			[a,d]PO_4^{3-}[109]
Ru		[a,b]PO_4^{3-}[110]	[a,b]PO_4^{3-}[110]
Ir	[a]PO_4^{3-}[111]		
Ni			[a,d]PO_4^{3-}[109]
Cu			AsO_4^{3-}, [a,d]PO_4^{3-}[90,109]
Zn			PO_4^{3-}

Due to the extensive number of ligands reported to occupy the sixth coordination site, only the most common examples have been included: [a]H_2O, [b]C_2H_6OS, [c]Cl^-, [d]Br^-, [e]OH, [f]C_5H_5N

An early example of Ru-substituted Keggin synthesis involved the treatment of $[SiW_{11}O_{39}]^{8-}$ with ruthenium(III) chloride, $RuCl_3{\cdot}xH_2O$ to yield a substance formulated as $K_5[SiW_{11}Ru(H_2O)O_{39}]$, which was shown to be active for alkene oxidation.[112–114] Later, cyclic voltammetric studies on the product suggested the material was a mixture of undefined products because commercially available hydrated ruthenium(III) chloride contains an assortment of Ru-based species.[114,115] Despite the product not being fully characterised, the product demonstrated catalytic activity towards alkene oxidation.[112–114] Since then, more labile precursors i.e. [Ru(dmso)$_4$Cl$_2$][116] and [Ru(acac)$_3$][117] under hydrothermal conditions. Besson and co-workers extended for the preparation of Ru(III) aqua derivatives by treating $[PW_{11}O_{39}]^{7-}$ with [Ru(dmf)$_6$] under microwave irradiation (1:1 molar ratio).[118]

Mono-substituted Keggin clusters have been reported with an extensive number of ligands. For example, introduction of dimethyl sulfoxide ligands has been achieved by treating the lacunary anions, e.g. $[PW_{11}O_{39}]^{7-}$, with [Ru(dmso)$_4$Cl$_2$] precursors.[116] The binding mode through the S-atom was confirmed through by ^{31}P NMR[91], EPR (X = P(V))[119], single-crystal X-ray diffraction (X= Si(IV))[120] and DFT calculations.[121] Ueda and co-workers reported prolonged (ca. 5 days) hydrothermal reaction between $[SiW_{11}O_{39}]^{8-}$ and [Ru(acac)$_3$] produces the carbonyl-ruthenium, Cs$_6$[SiW$_{11}$Ru(CO)O$_{39}$] salt.[122] The Ru(CO) moiety was redox active and was reversibly oxidized to the ruthenium(III) derivative which demonstrated impressive solution stability.[122] The authors reported oxidised ruthenium(III) slowly released CO, reforming the aqua species followed by the dimeric complex via condensation.[122] High-yield syntheses of Rh(III)-based derivatives containing halide (X = Cl, Br) ligands has been accomplished using hydrothermal methods. Controlled electrolytic reduction of $[PW_{11}Rh(Cl)O_{39}]^{5-}$ produced the dimeric $[(PW_{11}RhO_{39})_2]^{10-}$ anion providing a route for the formation of $[PW_{11}Rh(L)O_{39}]^{q-}$ (L = I, CN, H$_2$O, DMSO) derivatives.[104] In 2006, osmium(VI) and rhenium(VI)-nitrido derivatives were synthesised by treating the lacunary complex with $[ReCl_4N]^-$ or $[OsCl_4N]^-$ precursors and isolated as tetrabutylammonium salts. This work has been extended to incorporate manganese(V)[123], chromium(V)[124], and ruthenium(V)[125] heteroatoms and have been extensively studied via DFT calculations.[126] Proust and co-workers reported treating triphenylphosphine with the ruthenium(V)-nitrido, $[PW_{11}O_{39}\{Ru(VI)N\}]^{4-}$ complex produced the bis(triphenylphosphane)iminium cation by means of N-atom transfer.[125]

Preparation of the α_2-Ru(III)-substituted Wells-Dawson was reported by Pope and co-workers by reaction of $[\alpha_2\text{-}P_2W_{17}O_{61}]^{10-}$ with [Ru(H$_2$O)$_6$](C$_7$H$_7$SO$_3$)$_2$.[91] Later, Nomiya and co-workers reported the synthesis of $[\alpha_2\text{-}P_2W_{17}Ru(H_2O)O_{61}]^{7-}$ by treating the lacunary with Ru(DMSO)$_4$Cl$_2$ followed by oxidation with liquid bromine. However, both reaction mixtures were not pure, containing $[P_2W_{18}O_{62}]^{6-}$.[127] In 2014, Sadakane and co-workers reported the synthesis of [α_1-P$_2$W$_{17}$Ru (DMSO)O$_{61}$]8- and $[\alpha_2\text{-}P_2W_{17}Ru(DMSO)O_{61})]^{8-}$ prepared from the mono-lacunary derivative.[110] Treating $[\alpha_2\text{-}P_2W_{17}O_{61}]^{10-}$ with Ru(DMSO)$_4$Cl$_2$ under hydrothermal conditions, produced $[\alpha_2\text{-}P_2W_{17}Ru(DMSO)O_{61})]^{8-}$ as a major product. By contrast, treating $[\alpha_2\text{-}P_2W_{17}O_{61}]^{10-}$ with Ru(C$_6$H$_6$)$_4$Cl$_2$ under hydrothermal conditions produces $[P_2W_{17}Ru(H_2O)O_{61}]^{7-}$ with an 8:1 isomeric mixture of α_1 :α_2.[110] In 2016, isomerically pure samples of α_2-$[P_2W_{17}Ru(H_2O)O_{61}]^{7-}$ were prepared by cleavage of the Ru-S bond of the corresponding DMSO derivatives α_2-$[P_2W_{17}Ru\text{-}(DMSO)O_{61}]^{8-}$, respectively.[128]

1.2.2 Sandwich Structures

Lacunary clusters containing group IV centres such as: Zr(IV), Hf(IV) and Ce(IV) derive clusters with 1:2, 2:2, and/or 1:1 metal: 'ligand' stoichiometries. By contrast to six-coordinate centres, group(IV) heteroatoms can support higher coordination numbers (> 6) due to their greater ionic radii. In 2006, Zr(IV) and Hf(IV) 1:2 complexes: (Et$_2$NH$_2$)$_{10}$[Zr(α-PW$_{11}$O$_{39}$)$_2$]·$_7$H$_2$O and (Et$_2$NH$_2$)$_{10}$[Hf(α-PW$_{11}$O$_{39}$)$_2$]·$_2$H$_2$O were obtained by treating saturated $[PW_{11}O_{39}]^{7-}$ (*in situ*) with Na$_2$CO$_3$, with MCl$_2$O·8H$_2$O (M = Zr(IV), Hf(IV).[129] The crystal structure revealed the bridging heteroatom was supported in a square antiprismatic symmetry with four oxygen ligands, supplied from each lacunary ligand of C$_2$ symmetry.[129] The crystal structure of 2:2-type complexes were obtained by treating the $[PW_{11}O_{39}]^{7-}$ ligand and $MCl_2O \cdot 8H_2O$ in a 1:1 molar reaction - see Figure 1.10. The central $[M_2(\mu\text{-OH})_2(H_2O)_2]^{6+}$ cluster was composed of two edge-sharing units linked by two μ-OH groups.[130] The lacunary clusters behave as tetradentate oxygen donor ligands, yielding seven coordinate M(IV) centres. Inter-conversion between the 1:2 and 2:2 stoichiometries can be achieved under appropriate conditions.[130] Yoshitaka and co-workers using ^{31}P NMR spectroscopy demonstrated the conversion of 1:2-Keggin $[\{PW_{11}O_{39}M(IV)(\mu\text{-OH})(H_2O)\}_2]^{8-}$ (M(IV) = Hf, Zr) to the 2:2-Keggin $(Et_2NH_2)_{10}[M(IV)(\alpha\text{-}PW_{11}O_{39})_2]$; complex by addition of monolacunary $K_7[PW_{11}O_{39}]$ salts in solution, through detection of -9.23 and -13.84 ppm resonance signals.[130] The reverse reaction was achieved by treating the 2:2-Keggin $(Et_2NH_2)_{10}[M(\alpha\text{-}PW_{11}O_{39})_2]$ (M(IV) = Hf, Zr) complex with excess MCl_2O to regenerate the 1:2-Keggin complex.[130]

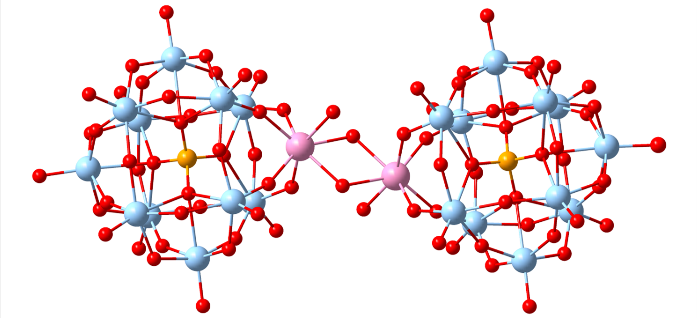

Figure 1.10: Schematic representation for the 2:2 sandwich complex, $[\{\alpha\text{-}PW_{11}O_{39}Hf(IV)(\mu\text{-}OH)(H_2O)\}_2] \cdot 7H_2O$. Colours corresponding to W = Cyan; Si = orange, Hf = pink, and O = red.

The formation of 3:2 metal: 'ligand' stoichiometries comprising units $[M_3(\mu\text{-OH})_3]^{9+}$; M = Zr(IV) or Hf(IV) sandwiched between two $[A\text{-}PW_9O_{34}]^{9-}$ fragments were first reported in 2009.[131] Nomiya and co-workers obtained 3:2 sandwich $[M_3(\mu\text{-OH})_3(A\text{-}PW_9O_{34})_2]^{9-}$; M = Zr(IV) or Hf(IV) clusters by treating tri-lacunary fragments with $M(SO_4)_2nH_2O$ precursor.[131] The authors reported a 7:3 mixture of clusters containing $\alpha,\alpha\text{-}[M_3(\mu\text{-OH})_3(\alpha\text{-A-}PW_9O_{34})_2]^{9-}$ and $\alpha,\beta\text{-}[M_3(\mu\text{-OH})_3(\alpha\text{-A-}PW_9O_{34})(\beta\text{-A-}PW_9O_{34})]^{9-}$; where M = Zr(IV) or Hf(IV), confirmed through ^{31}P-NMR spectroscopy.[131] These crude products could be purified by 1h reflux in aqueous HCl solution to isolate the α,α-junction complex.[131]

Sandwich structures derived from divacant lacunary precursors are extensive, for example: $[Ru(IV)_4(\mu\text{-O})_4(\mu\text{-OH})_2(H_2O)_4(\gamma\text{-}SiW_{10}O_{36})_2]^{10-}$ [132] and $[Ru(IV)_4(\mu\text{-O})_4(\mu\text{-OH})_4Cl_4(\gamma\text{-}SiW_{10}O_{36})_2]^{12-}$ [133] comprising a tetraruthenium, $\{Ru_4O_4\}$ core stabilized by two $[\gamma\text{-}SiW_{10}O_{36})_2]$ clusters. Electrochemical studies have revealed the tetraruthenium(IV) core species can undergo several stepwise, reversible redox process to tetraruthenium(V) and tetraruthenium(III) states.[134] Hence, these structures have attracted significant interest in the oxidative conversion of water to dioxygen, proceeding via the tetraruthenium(IV) intermediate state.[134] Recently, Sadakane and coworkers have reported examples of pyridine coordination to the tetraruthenium core forming $[(\gamma\text{-}SiW_{10}O_{36})_2(\{Ru(IV)(py)\}_4O_4\text{- }(OH)_2]^{10-}$ clusters.[134] The authors reported the aqua ligands are exchangeable with pyridine, presenting a new complex with multi-electron transfer processes over a wide pH range (1-12).[134]

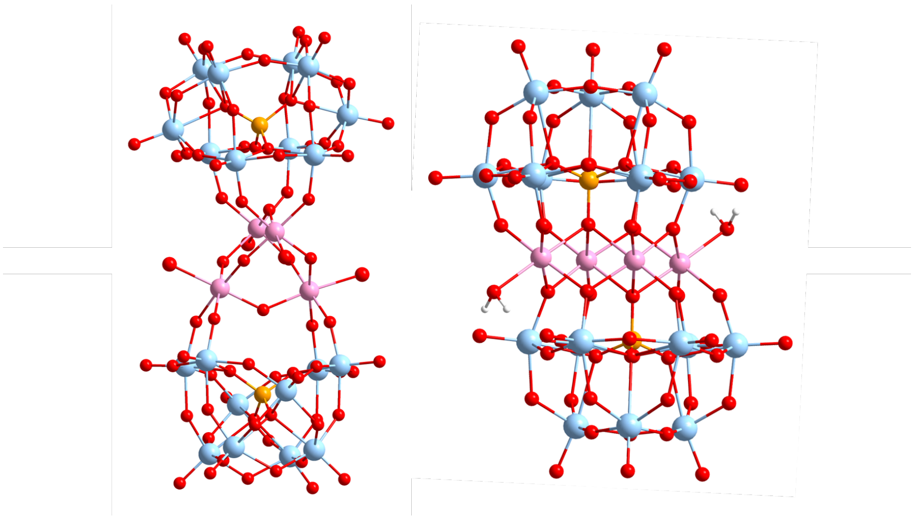

Figure 1.11: Schematic representation for the ruthenium-containing silicotungstate, [(γ-SiW$_{10}$O$_{36}$)$_2$Ru$_4$Cl$_4$O$_2$(OH)$_4$]$\cdot$23H$_2$O comprising of two [γ-SiW$_{10}$O$_{36}$]$^{8-}$ sub-units sandwiching a tetra-nuclear ruthenium-oxygen core, [Ru$_4$O$_2$(OH)$_4$]$_4$ (left). Sandwich structures based on B-type tri-lacunary fragments (right), [Ru$_4$(H$_2$O)$_2$(PW$_9$O$_{34}$)$_2$]$^{10-}$. Colours corresponding to W = Cyan; Si = orange, Ru= pink, and O = red.

In 2001, Kortz and Matta synthesised the trimeric mangansese(II)-substituted, [(β_2-SiW$_{11}$MnO$_{38}$-(OH)$_3$]$^{15-}$ cluster by treating by K$_8$[γ-SiW$_{10}$O$_{36}$] with MnCl$_2$$\cdot$2H$_2$O at pH 3.9 - see Figure 1.12.[135] This cluster comprises a trimeric assembly linked through Mn-O-W bridges possessing overall c_3 symmetry.[135] This work has been extended to di-lacunary Keggin clusters, in which Wang and co-workers reported the incorporation of ligands i..e CO$_3$$^{2-}$ into the trimeric assembly.[136] Single-crystal X-ray structural analysis reveals the cluster reveals the ligand resides inside the three Keggin {SiW$_{10}$Mn(II)Mn(III)O$_{38}$} units bridged by three μ^2-O atoms.[136] Kortz and co-workers isolated the potassium salt of K$_{10}$[Mn(H$_2$O)$_2$(γ-SiW$_{10}$O$_{35}$)$_2$] by treating K$_8$[γ-SiW$_{10}$O$_{36}$] with MnCl$_2$$\cdot$2H$_2$O at pH 4.5.[137] The structure was crystallised with a triclinic phase with C$_{2v}$ symmetry in which the two γ-SiW$_{10}$O$_{36}$ fragments are connected through one hexa-coordinate MnO$_4$(OH$_2$)$_2$ and two W-O-W bridges.[137] The authors reported cyclic volumetric experiments demonstrating prominent Mn(II)/Mn(IV) peaks.[137]

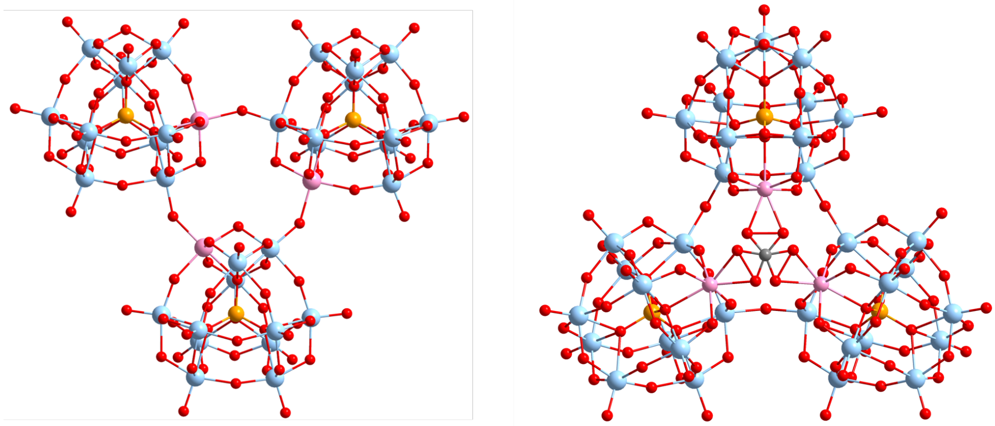

Figure 1.12: Schematic representation of the trimeric mangansese(II)-substituted, $[(\beta_2\text{-SiW}_{11}\text{MnO}_{38}(\text{OH})_3]^{15-}$ cluster (left), reported by Kortz and co-workers[135] and the $\text{CO}_3{}^{2-}$ containing, dimanganese-substituted silicotungstate trimer $\text{K}_9[\text{H}_{14}\{\text{SiW}_{10}\text{Mn(II)Mn(III)O}_{38}\}_3(\text{CO}_3)]\cdot 39\text{H}_2\text{O}$. Colours corresponding to W = Cyan, X = orange, Mn = pink, and O = red.

Sandwich structures based on Pd(II) producing bimetallic clusters rather than lacunary-based complexes. For example, Angus-Dunne and co-workers reported the Lindqvist sandwich complex, $[\text{Pd(II)}_2(\text{W}_5\text{O}_{18})_2]^{8-}$, featuring two distinct O-Pd(II)-O bridges bridging the two clusters.[138] The reaction between the lacunary $[\text{PW}_{11}\text{O}_{39}]^{7-}$ and α_2-$[\text{P}_2\text{W}_{17}\text{O}_{61}]^{10-}$ complexes and Palladium(II) precursors produce bimetallic sandwich structures rather than lacunary-based complexes, which would result in an unusual octahedral or square-pyramidal coordination sphere.[139] Kortz and co-workers reported the preparation of three bimetallic $[\text{Pd}_2([\text{PW}_{11}\text{O}_{39})_2]^{10-}$ and $[\text{Pd}_2(\alpha_2\text{-P}_2\text{W}_{17}\text{O}_{61})_2]$ clusters.[139] The authors reported both the *anti* and *syn* isomers, with respect to the orientation of the polytungstate ligand are able to co-exist, in solution.[139]

1.3 Electronic Properties of Polyoxometalates

The classical structure of polyoxometalates has often been described by means of the Clathrate model. This model describes the above systems as being comprised of neutral metal cages, M_xO_y, which encapsulate anions. Hence, the aforementioned structures can be reformulated as A@E, where E is the metal oxide framework that surrounds A, which carries the molecular charge. Indeed, this concept has been employed in work rationalising the relative stability of α/β isomers, much as described by Weinstock *et al.*[80] By artificially separating the molecular cage and the charged fragment(s), the individual effects by the cage and the anion can be analysed. In 2006, Lopez *et al.* using theoretical DFT calculations quantified the effect of the metal oxide framework and anionic fragment on the redox properties of Keggin- type heteropolyanions.[140] The authors reported no correlation between the energy of the HOMO, and the size of the metal oxide framework, M_xO_{3x}.[140] However, the energy of the LUMO, is stabilised when the cage expands i.e: -5.6 and 6.4 eV for W_6O_{18} and $\text{W}_{30}\text{O}_{90}$, respectively.[140] The stabilisation in the LUMO increases the electron affinity for the enlarged anions. The effects of the heteroatom on the frontier molecular orbitals in $[\text{XW}_{12}\text{O}_{40}]^{q-}$ where X = Al(III), Si(IV), P(V), and q = 3 to 5 were not constant as previously observed for the molecular cage.[140] The energies of the LUMO were shown to be linearly dependant on q/m of the anion i.e: -4.32 and -4.12 eV for $[\text{PW}_{12}\text{O}_{40}]^{3-}$ and $[\text{SiW}_{12}\text{O}_{40}]^{4-}$.[140] The lowest unoc-

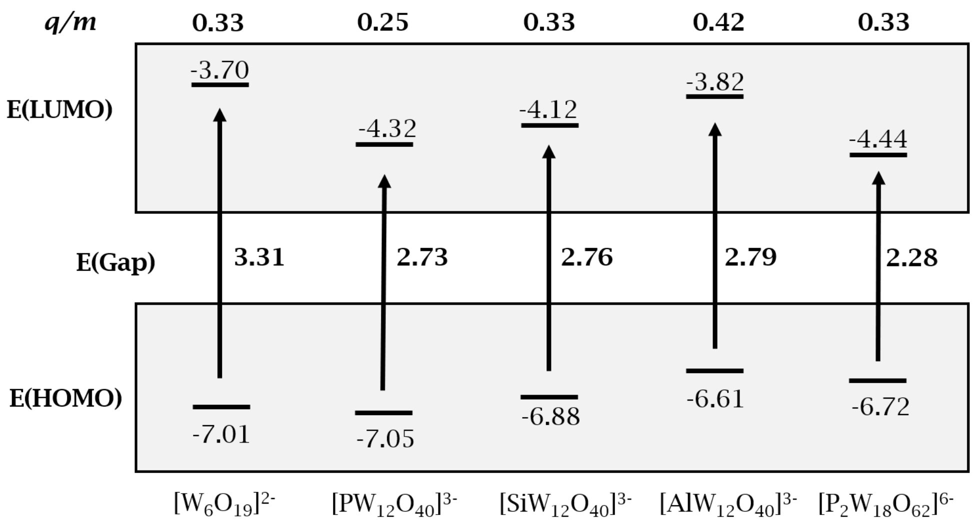

Figure 1.13: Schematic depiction of the frontier orbital energies (eV) for various polyoxoanions. The LUMO energy deprecates with reduction in the q/m ratio for Keggin-type orbitals. Energy data taken from Lopez *et al.*[140]

cupied orbital in fully oxidised heteropolyanions are comprised of symmetry adapted non-bonding orbitals at the metal ions. Hence, the cluster does not change geometry upon reduction because of the non-bonding character of the LUMO, making them suitable candidates for electrocatalysis.[141] The electrons are accepted by the addenda ions which are delocalised across the metal oxide framework through intramolecular electron transfers, known as 'electron hopping'.[141,142] The reduction potentials of heteropolyanions are controlled by the following parameters: (i) the rotation of the M_3O_{13} triads; (ii) and the valence of the central heteroatom.[142,143] The first study rationalising the reduction potentials on a series of isostructural Keggin polytungstates (α-$[PW_{12}O_{40}]^{3-}$, α-$[SiW_{12}O_{40}]^{4-}$, α-$[FeW_{12}O_{40}]^{5-}$, α-$[CoW_{12}O_{40}]^{6-}$, $[H_2W_{12}O_{40}]^{6-}$) was conducted by Pope *et al.* using polarographic and potentiometric methods.[143] In acidic media (1 M H_2SO_4), heteropolyanions may be reduced without protonation until an overall charge of -6 is achieved.[143] In neutral solutions, a charge of -8 is allowed without subsequent protonation.[143] Furthermore, no Co(I) or Fe(II) species were observed suggesting the reduction takes place exclusively on the tungsten ions.[143] In aqueous media, the two-electron reduction potentials and the charge on the Keggin heteropolyanion were shown to be inversely proportional with a gradient of —0.18 V/Q.[143] Furthermore, the isomeric dependence on reduction potential was investigated in silicotungstic acid ($[SiW_{12}O_{40}]^{4-}$) using cyclic voltammetry.[86] It has been confirmed the reduction potentials follow the trend: γ-$[SiW_{12}O_{40}]^{4-}$ > β-$[SiW_{12}O_{40}]^{4-}$ > α-$[SiW_{12}O_{40}]^{4-}$, with potential differences of approximately 100 mV in aqueous media.[86]

1.4 Redox Chemistry with Polyoxometalates

Electrochemical properties of POMs have been extensively studied using electrochemical techniques, i.e., cyclic voltammetry, in various solutions containing different electrolytes and electrodes. Early work by Pope and co-workers measured the redox potentials for W-based Keggin: $[XW_{12}O_{40}]^{q-}$; X = P(V), Ge(IV), Si(IV), B(III) revealing an inverse relation between pH independent redox potentials and anion charge of -0.18 V/Q.[143] The redox potentials for Keggin: $[XW_{12}O_{40}]^{q-}$ followed the trend: P(V) > Ge(IV) > Si(IV) > B(III). Later, Nadjo and co-workers using Density Functional Theory (DFT) calculations demonstrated clusters supporting the same formal charge display different capacities for accepting electrons is attributed to ionic radii associated with the central heteroatom. For example, $[GeW_{12}O_{40}]^{4-}$ shows more negative (more difficult to reduce) redox potential of -0.19 V vs -0.23 V (vs SCE) in $[SiW_{12}O_{40}]^{4-}$ attributed to the larger ionic radii associated with the Ge(IV) heteroatom.[144] Comparison between the P(V)-based Keggin and Wells-Dawson clusters reveals the latter are more reducible attributed to lower lying HOMO orbitals, confirmed through Density Functional Theory (DFT) calculations.[144]

Rotational isomerism is achieved by $\pi/3$ rotation of the M_3O_{13} caps and/or M_6O_{27} belts for Keggin and Wells-Dawson clusters.[77,86] Redox potentials occur at more positive potentials for the β-form than the corresponding α-isomer, e.g., β-$[PM_{12}O_{40}]^{3-}$ > α-$[PM_{12}O_{40}]^{3-}$ (M = Mo(VI), W(VI)).[145] The electronic structure of W-based Keggin and Wells-Dawson clusters comprises of two sets of identifiable bands: (i) an oxo-band comprised of occupied oxo-ligands; (ii) and the addenda band encompassing unoccupied metallic orbitals. Herein, electrons are accepted by addenda atoms and are delocalised across framework through intra-molecular electron transfers, known as 'electron hopping'. The Clathrate model has previously been applied to rationalise the electronic structure of POMs, which describes systems as being comprised of neutral metal cages, M_xO_y, encapsulating XO_4 tetrahedron.[146] These structures can be reformulated as A@E, where E is the metal oxide framework that surrounds A, which carries the molecular charge. Poblet and co-workers applied this model to rationalise differences in stability between the α-, and β W-based Keggin clusters. The authors reported β-$PW_{12}O_{40}{}^{3-}$ are more reducible that α-Keggin anions because of lower-lying d_{xy} metal orbital.[145,146]

Redox measurements on singular metal-substituted, $[XW_{11}M(H_2O)O_{39}]^{q-}$ and $[X_2W_{17}M(H_2O)O_{61}]^{q-}$; are extensive. The electrochemical behaviour of Mn(II) and Co(II)-substituted Keggin clusters can be oxidised to Mn(III), Mn(IV) or Mn(V), and Co(III), respectively. Electrochemical oxidation of Mn(III) to Mn(IV) or Mn(V) causes deprotonation of the terminal water ligand to hydroxyl and oxo-groups, respectively.[147,148] Electrochemical reduction of Fe(III/II) redox couples occur at more positive potentials relative to W(VI).[148] However, oxidative Fe(II/III) couples are not routinely observed.[148] Electrochemical reduction for Ni(II)-based Keggin clusters occurs at W(VI) which is shifted to more negative potentials with respect to the corresponding lacunary anion.[148,149] Cyclic voltammograms for $[XW_{11}Ni(H_2O)O_{39}]^{q-}$; X = P(V) or Si(IV), observed no redox waves attributed to the peripheral heteroatom. Weakley and co-workers explored the heteroatom on Mn(III)/Mn(II) redox potentials in $[XW_{11}Mn(III/II)(H_2O)O_{39}]^{q-}$; X = P(V), Ge(IV), Si(IV), B(III) anions, reporting a range in potential of 0.45 V.[90] Cavaleiro and co-workers reported consecutive reduction of Cu(II) to Cu(0) (via Cu(I) intermediate) induced with the consequent adsorption of the ejected heteroatom to the glassy carbon electrode surface.[107] In the anodic scan, Cu(0) was re-oxidised regenerating the original Cu(II) complex, via a Cu(I) intermediate. The electrochemistry of Ru(II)-substituted clusters have been extensively reported supporting numerous oxidation states.[107] Detailed electrochemical experiments on $[XW_{11}Ru(H_2O)O_{39}]^{q-}$ (X = P(V) or Si(IV) have shown II, III, IV, and V oxidation states of the Ru can be accessed reversibly.[150] The terminal aqua ligand is deprotonated to terminal hydroxo- and oxo- ligands at IV and V oxidation states, respectively.[150] The terminal ligand, water, can be substituted with other organic molecules for example: dimethyl sulfoxide (DMSO), pyridine, and CO. The redox waves attributed to Ru(III/II) are shifts to more positive potentials than the corresponding aqua, $[XW_{11}Ru(H_2O)O_{39}]^{q-}$, complex.[150,151]

1.5 Applications of Polyoxometalates

1.5.1 Water Oxidation

Early examples of polyoxometalte-based water oxidation catalysts (WOC) were reported by Bonchio[132] and Hill[152] using $[Ru_4(\mu\text{-}O)_4(\mu\text{-}OH)_2(H_2O)_4(\gamma\text{-}SiW_{10}O_{36})_2]^{10-}$ clusters, comprised of a tetra- ruthenium oxide core, $\{Ru_4O_4\}$ inserted between $SiW_{10}O_{36}$ clusters. The lacunary fragments behave as tetradentate oxygen donor ligands which stabilise the tetraruthenium oxide core. The $\{Ru_4O_4\}$ core comprises four redox-active Ru(IV) sites, by which each metal centre exhibits a terminal water ligand. Hill and co-workers reported no catalytic current was observed at pH 1 and 4.7, however at pH 7, redox waves attributed to water oxidation was observed $E^0 > 0.9$ V vs Ag/AgCl.[152] DFT calculations focusing on $[Ru_4(\mu\text{-}O)_4(\mu\text{-}OH)_2(H_2O)_4(\gamma\text{-}SiW_{10}O_{36})_2]^{10-}$ have reported the oxidative mechanism is initiated following the generation of the activated (S_6) intermediate; featuring two Ru–oxo groups.[153] The proposed cycle begins with the S_2 $\{Ru(IV)_2Ru(V)_2\}$ state, undergoing series of proton coupled electron transfer to the S_6 $\{Ru(V)_2Ru(VI)_2\}$ intermediate. Hereafter, the lowest energy pathway for O–O bond formation can proceed via an intermolecular mechanism.[153] This consists in the nucleophilic attack at the Ru–O moiety by a solvent water molecule, evolving oxygen and returning to the S_2 state, in solution.

Earlier work has employed Earth abundant elements as reaction sites for water oxidation. In 2010, Hill and co-workers using $[Co_4(H_2O)_2(PW_9O_{34})_2]^{10-}$ clusters which featured a tetracobalt oxide core, $\{Co_4O_4\}$ sandwiched between two B-type tri-lacunary polytungstate ligands, discussed earlier.[154] Subsequent DFT calculations were employed to deduce the water oxidation mechanism by the $[Co_4(H_2O)_2(PW_9O_{34})_2]^{10-}$ and $[Co_4(H_2O)_2(VW_9O_{34})_2]^{10-}$ analogues.[155] The generation of the S_2 state proceeds by an an electron-then-proton transfer, followed by a subsequent PCET step.[155] The authors reported formation of the dioxygen bond is the rate determining step which proceeds via the nucleophilic attack at the Co(III)-O· active species.[155] The higher catalytic activity of $[Co_4(H_2O)_2(VW_9O_{34})_2]^{10-}$ was attributed to coupling of the d-orbitals of Co and V orbitals increasing the electrophilicity of the Co(III)-O moiety.[155] DFT calculations have been employed with iron-based, $[Fe_4(H_2O)_2(PW_9O_{34})_2]^{6-}$, clusters, however higher applied voltages are required with respect to the $Co_4O_4\}$ analogues.[156]

1.5.2 Carbon Dioxide Reduction

Electrocatalytic reduction of CO_2 can generate several products including: (i) COOH ($2e^-/2H^+$ reduction), (ii) CO ($2e^-/2H^+$ reduction) (iii) CH_3OH ($6e^-/6H^+$ reduction), (iv) and CH_4 ($8e^-/8H^+$ reduction). In 1998, Kozik and co-workers reported the first example CO_2 reduction using α-$[SiW_{11}O_{39}Co]^{6-}$ in toluene chosen because of its non-polar and non-coordinating properties.[157] The authors reported that copper(II)- and manganese(III)-substituted heteropolyanions do not react with the substrate, whilst germano- and silicotungstates containing Co(II), Ni(II), and Mn(II) were capable of forming complexes with CO_2. By contrast phospho- and borotungstates are not reactive.[157] Transition-metal-substituted heteropolyanions can be transferred from water to nonpolar solvent by using tetraheptylammonium bromide as a phase-transfer agent.[157] The authors reported that such polyanions possess a vacant site, usually occupied by coordinated solvent, i.e water. For complexes containing Co(II), a colour change from pink (hydrated) to green ("anhydrous") was detected spectroscopically.[157] In 2010, Chen and co-workers reported transition-metal-substituted Keggin-based germanotungstates were active in conversion of CO_2 to cyclic carbonates in the gas-phase.[89] The activity of Keggin-based germanotungstates were significantly influenced by (i) transition metal, (ii) counterion, (iii) reaction temperature, (iv) and CO_2 pressure.[89] For example, employment of the $[(n\text{-}C_7H_{15})_4N]_6GeW_{11}MnO_{39}]$ unit procured yields of 95 % whilst $[(n\text{-}C_7H_{15})_4N]_6GeW_{11}CuO_{39}]$ demonstrated yields of 2 %.[89] Recently. Zha and co-workers reported an efficient reductive process of CO_2 using POMs as co-catalysts to overcome the inherent poor selectivity of indium.[158] The reaction system consisting of $[SiW_9V_3O_{40}]^{7-}$ and In demonstrated 96% faradaic efficiency towards the acetate CH3COO over HCOOH.[89]

1.5.3 Hydrogen Evolution

Electrocatatytic reduction of water to liberate hydrogen and oxygen is an attractive proposition to reforming fossil fuels because the electrical energy can be provided by renewable technology and the starting material (water) can be recovered following the consumption of the hydrogen fuel.[159,160] Symes and Cronin reported decoupling of hydrogen and oxygen evolution using $H_3PMo_{12}O_{40}$ and a electron-coupled-proton buffer (ECPB) such that these gases can be produced in separate spaces preventing their mixing.[159] Later, Chen and co-workers reported the mechanism of multi-electron redox processes occurring at the Wells–Dawson structure $X_6[P_2W_{18}O_{62}]$ wherein the cluster, comprising of 18 metal centres, can uptake up to 18 electrons reversibly per cluster.[160] The authors demonstrated using DFT, molecular dynamics, UV–vis, electron paramagnetic resonance spectroscopy, and small-angle X-ray scattering spectra showing that cluster protonation and aggregation allow the formation of highly electron-rich meta-stable systems which can produce hydrogen in dilute conditions.[160]

1.6 Project Aims

The objective of this PhD is to advance the understanding of the the structural and electronic properties of Keggin-based polyoxometalates in different physical environments using Density Functional Theory (DFT) calculations and validating these models with experimental data. The specific aims of this work are as follows:

- Develop a universal computational method for predicting experimental redox potentials and NMR chemical shifts in mono-substituted polyoxotungstates, $X_5[PW_{11}M(H_2O)O_{39}]$ systems; where Mn(III/II), Fe(III/II), Co(III/II) and X = Li, Na and K.

- Systematically investigate the influence of Hartree-Fock (HF) exchange in reproducing literature reported potentials and NMR chemical shifts whilst exploring the effect of explicitly locate counterions to neutralize the charge in the clusters.

- Investigate the potential of mono-substituted polyoxotungstates, $K_5[PW_{11}M(H_2O)O_{39}]$; where M = Mn(II), Fe(II), Co(II), Ni(II), Cu(II), Zn(II) as ammonia synthesis catalysts. Correlating the structural stability and electronic characteristics of these complexes with their catalytic performance.

Bibliography

[1] M. T. Pope, *Heteropoly and Isopoly Oxometalates*, Springer-Verlag, Berlin, 1983.

[2] M. T. Pope and A. Müller, *Angew. Chem. Int. Ed.*, 1991, **30**, 34–48.

[3] A. Müller, F. Peters, M. T. Pope and D. Gatteschi, *Chem. Rev.*, 1998, **98**, 239–272.

[4] D.-L. Long, R. Tsunashima and L. Cronin, *Angew. Chem. Int. Ed.*, 2010, **49**, 1736–1758.

[5] L. Vilà-Nadal and L. Cronin, *Nat. Rev. Mater.*, 2017, **2**, 1–15.

[6] H. N. Miras, L. Vilà-Nadal and L. Cronin, *Chem. Soc. Rev.*, 2014, **43**, 5679–5699.

[7] A. Oleinikova, H. Weingärtner, M. Chaplin, E. Diemann, H. Bögge and A. Müller, *ChemPhysChem*, 2007, **8**, 646–649.

[8] T. Yamase, *J. Mater. Chem.*, 2005, **15**, 4773–4782.

[9] J. J. Baldoví, J. J. Borrás-Almenar, J. M. Clemente-Juan, E. Coronado and A. Gaita-Ariño, *Dalton Trans.*, 2012, **41**, 13705–13710.

[10] J. M. Clemente-Juan, E. Coronado and A. Gaita-Ariño, *Chem. Soc. Rev.*, 2012, **41**, 7464–7478.

[11] F. d. Azambuja, J. Moons and T. N. Parac-Vogt, *Acc. Chem. Res.*, 2021, **54**, 1673–1684.

[12] D. Gao, I. Trentin, L. Schwiedrzik, L. González and C. Streb, *Molecules*, 2019, **25**, 157.

[13] D. E. Katsoulis and M. T. Pope, *J. Chem. Soc., Chem. Commun.*, 1986, 1186–1188.

[14] D. Gabb, C. P. Pradeep, T. Boyd, S. G. Mitchell, H. N. Miras, D.-L. Long and L. Cronin, *Polyhedron*, 2013, **52**, 159–164.

[15] L. B. Fullmer, P. I. Molina, M. R. Antonio and M. Nyman, *Dalton Trans.*, 2014, **43**, 15295–15299.

[16] M. Blasco-Ahicart, J. Soriano-Lopez, J. J. Carbó, J. M. Poblet and J.-R. Galan-Mascaros, *Nat. Chem.*, 2018, **10**, 24–30.

[17] J. Yan, D.-L. Long, H. N. Miras and L. Cronin, *Inorg. Chem.*, 2010, **49**, 1819–1825.

[18] J. J. Berzelius, *Pogg. Ann. Phys. Chem.*, 1826, **6**, 369.

[19] C. Marignac, *C. R. Acad. Sci.*, 1862, **55**, 888.

[20] C. Marignac, *Ann. Chim.*, 1862, **25**, 262.

[21] L. Pauling, *J. Am. Chem. Soc.*, 1929, **51**, 2868–2880.

[22] J. F. Keggin, *Nature*, 1933, **131**, 908–909.

[23] J. Keggin, *Proc. Roy. Soc. A*, 1934, **144**, 75.

[24] J. S. Anderson, *Nature*, 1937, **140**, 850–850.

[25] H. T. Evans Jr, *J. Am. Chem. Soc.*, 1948, **70**, 1291–1292.

[26] B. Dawson, *Acta. Crystallogr.*, 1953, **6**, 113–126.

[27] I. Lindqvist, *Ark. Kemi*, 1953, **5**, 247–250.

[28] *Angew. Chem. Int. Ed.*, 1995, **34**, 2122–2124.

[29] W. Klemperer, T. Marquart and O. Yaghi, *Mater. Chem. Phys.*, 1991, **29**, 97–104.

[30] Y. Hou, L. N. Zakharov and M. Nyman, *J. Am. Chem. Soc.*, 2013, **135**, 16651–16657.

[31] W. H. Nelson and R. S. Tobias, *Inorg. Chem.*, 1963, **2**, 985–992.

[32] M. Nyman, T. M. Alam, F. Bonhomme, M. A. Rodriguez, C. S. Frazer and M. E. Welk, *J. Clust. Sci.*, 2006, **17**, 197–219.

[33] D. Shiels, M. Pascual-Borràs, P. G. Waddell, C. Wills, J.-M. Poblet and R. J. Errington, *Chem. Comm.*, 2023, **59**, 7919–7922.

[34] E. Balogh, T. M. Anderson, J. R. Rustad, M. Nyman and W. H. Casey, *Inorg. Chem.*, 2007, **46**, 7032–7039.

[35] A. J. Bridgeman and G. Cavigliasso, *Chem. Phys.*, 2002, **279**, 143–159.

[36] Y. Guo, X. Wang, Y. Li, E. Wang, L. Xu and C. Hu, *J. Coord. Chem.*, 2004, **57**, 445–451.

[37] E. F. Wilson, H. Abbas, B. J. Duncombe, C. Streb, D.-L. Long and L. Cronin, *J. Am. Chem. Soc.*, 2008, **130**, 13876–13884.

[38] Y. Du, A. L. Rheingold and E. A. Maatta, *J. Am. Chem. Soc.*, 1992, **114**, 345–346.

[39] A. Proust, R. Thouvenot, M. Chaussade, F. Robert and P. Gouzerh, *Inorganica Chim. Acta*, 1994, **224**, 81–95.

[40] J. B. Strong, R. Ostrander, A. L. Rheingold and E. A. Maatta, *J. Am. Chem. Soc.*, 1994, **116**, 3601–3602.

[41] T. R. Mohs, G. P. Yap, A. L. Rheingold and E. A. Maatta, *Inorg. Chem.*, 1995, **34**, 9–10.

[42] Y. Wei, B. Xu, C. L. Barnes and Z. Peng, *J. Am. Chem. Soc.*, 2001, **123**, 4083–4084.

[43] Y. Wei, M. Lu, C. F.-c. Cheung, C. L. Barnes and Z. Peng, *Inorg. Chem.*, 2001, **40**, 5489–5490.

[44] H. G. T. Ly, G. Absillis, S. R. Bajpe, J. A. Martens and T. N. Parac-Vogt, *Eur. J. Inorg. Chem.*, 2013, **2013**, 4601–4611.

[45] N. V. Maksimchuk, I. D. Ivanchikova, G. M. Maksimov, I. V. Eltsov, V. Y. Evtushok, O. A. Kholdeeva, D. Lebbie, R. J. Errington, A. Solé-Daura, J. M. Poblet and J. J. Carbo, *ACS Catal.*, 2019, **9**, 6262–6275.

[46] N. V. Maksimchuk, V. Y. Evtushok, O. V. Zalomaeva, G. M. Maksimov, I. D. Ivanchikova, Y. A. Chesalov, I. V. Eltsov, P. A. Abramov, T. S. Glazneva, V. V. Yanshole, O. A. Kholdeeva, R. J. Errington, A. Solé-Daura, J. M. Poblet and J. J. Carbó, *ACS Catal.*, 2021, **11**, 10589–10603.

[47] H. T. Evans Jr, *Inorg. Chem.*, 1966, **5**, 967–977.

[48] b. V. Day, W. Klemperer and D. Maltbie, *J. Am. Chem. Soc*, 1987, **109**, 2991–3002.

[49] J. Y. Kempf, M. M. Rohmer, J. M. Poblet, C. Bo and M. Benard, *J. Am. Chem. Soc*, 1992, **114**, 1136–1146.

[50] J. Arrieta, *Polyhedron*, 1992, **11**, 3045–3068.

[51] S. Nakamura and T. Ozeki, *J. Chem. Soc., Dalton Trans.*, 2001, 472–480.

[52] M. I. Khan, Q. Chen, J. Zubieta and D. P. Goshorn, *Inorg. Chem.*, 1992, **31**, 1556–1558.

[53] Q. Chen and J. Zubieta, *Coord. Chem. Rev.*, 1992, **114**, 107–167.

[54] M. I. Khan, Q. Chen, H. Hope, S. Parkin, C. J. O'Connor and J. Zubieta, *Inorg. Chem.*, 1993, **32**, 2929–2937.

[55] K.-H. Tytko, B. Schönfeld, B. Buss and O. Glemser, *Angew. Chem., Int. Ed. Engl.*, 1973, **12**, 330–332.

[56] B. Krebs and I. Paulat-Böschen, *Acta Crystallogr. B.*, 1982, **38**, 1710–1718.

[57] J. Fuchs and H. Hartl, *Angew. Chem., Int. Ed. Engl.*, 1976, **15**, 375–376.

[58] S. Himeno, H. Niiya and T. Ueda, *Bull. Chem. Soc. Jpn.*, 1997, **70**, 631–637.

[59] W. Klemperer and W. Shum, *J. Am. Chem. Soc*, 1976, **98**, 8291–8293.

[60] T. J. Weakley, *Polyhedron*, 1982, **1**, 17–19.

[61] A. Kitamura, T. Ozeki and A. Yagasaki, *Inorg. Chem.*, 1997, **36**, 4275–4279.

[62] K. Pavani, S. E. Lofland, K. V. Ramanujachary and A. Ramanan, *Eur. J. Inorg. Chem.*, 2007, 568–578.

[63] C.-D. Wu, C.-Z. Lu, X. Lin, H.-H. Zhuang and J.-S. Huang, *Inorg. Chem. Commun.*, 2002, **5**, 664–666.

[64] H. Abbas, A. L. Pickering, D.-L. Long, P. Kögerler and L. Cronin, *Chem. Eur. J.*, 2005, **11**, 1071–1078.

[65] J. J. Hastings and O. W. Howarth, *J. Am. Chem. Soc., Dalton Trans.*, 1992, 209–215.

[66] L. Lisnard, A. Dolbecq, P. Mialane, J. Marrot and F. Sécheresse, *Inorganica Chim. Acta*, 2004, **357**, 845–852.

[67] D.-L. Long, H. Abbas, P. Kögerler and L. Cronin, *J. Am. Chem. Soc*, 2004, **126**, 13880–13881.

[68] K. Nomiya, T. Takahashi, T. Shirai and M. Miwa, *Polyhedron*, 1987, **6**, 213–218.

[69] P. A. Lorenzo-Luis, P. Gili, A. Sánchez, E. Rodriguez-Castellón, J. Jiménez-Jiménez, C. Ruiz-Pérez and X. Solans, *Transit. Met. Chem.*, 1999, **24**, 686–692.

[70] H. T. Evans, *Acta Crystallogr. B.*, 1974, **30**, 2095–2100.

[71] A. Perloff, *Inorg. Chem.*, 1970, **9**, 2228–2239.

[72] B. Hasenknopf, R. Delmont, P. Herson and P. Gouzerh, *Eur. J. Inorg. Chem.*, 2002, **2002**, 1081–1087.

[73] P. R. Marcoux, B. Hasenknopf, J. Vaissermann and P. Gouzerh, *Eur. J. Inorg. Chem.*, 2003, **2003**, 2406–2412.

[74] Y.-F. Song, D.-L. Long and L. Cronin, *Angew. Chem.*, 2007, **46**, 3900–3904.

[75] H. An, Y. Li, D. Xiao, E. Wang and C. Sun, *Cryst. Growth Des.*, 2006, **6**, 1107–1112.

[76] K. Nakajima, K. Eda and S. Himeno, *Inorg. Chem.*, 2010, **49**, 5212–5215.

[77] L. C. Baker and J. S. Figgis, *J. Am. Chem. Soc.*, 1970, **92**, 3794–3797.

[78] K. Yamamura and Y. Sasaki, *J. Chem. Soc., Chem. Commun.*, 1973, 648–649.

[79] M. T. Pope, *Inorganic Chemistry*, 1976, **15**, 2008–2010.

[80] I. A. Weinstock, J. J. Cowan, E. M. Barbuzzi, H. Zeng and C. L. Hill, *J. Am. Chem. Soc*, 1999, **121**, 4608–4617.

[81] N. I. Gumerova and A. Rompel, *Chem. Soc. Rev.*, 2020, **49**, 7568–7601.

[82] G. Herve and A. Teze, *Inorg. Chem.*, 1977, **16**, 2115–2117.

[83] S.-T. Zheng, D.-Q. Yuan, H.-P. Jia, J. Zhang and G.-Y. Yang, *Chem Comm.*, 2007, 1858–1860.

[84] L. Lisnard, P. Mialane, A. Dolbecq, J. Marrot, J. M. Clemente-Juan, E. Coronado, B. Keita, P. de Oliveira, L. Nadjo and F. Sécheresse, *Chem. Eur. J.*, 2007, **13**, 3525–3536.

[85] B. Dawson, *Acta Crystallogr.*, 1953, **6**, 113–126.

[86] J. Zhang, A. M. Bond, P. J. Richardt and A. G. Wedd, *Inorg. Chem.*, 2004, **43**, 8263–8271.

[87] L. Vila-Nadal, S. G. Mitchell, D.-L. Long, A. Rodríguez-Fortea, X. López, J. M. Poblet and L. Cronin, *Dalton Trans.*, 2012, **41**, 2264–2271.

[88] N. Vila, P. A. Aparicio, F. Secheresse, J. M. Poblet, X. Lopez and I. M. Mbomekalle, *Inorg. Chem.*, 2012, **51**, 6129–6138.

[89] F. Chen, T. Dong, Y. Chi, Y. Xu and C. Hu, *Catal. Letters*, 2010, **139**, 38–41.

[90] C. M. Tourné, G. F. Tourné, S. Malik and T. Weakley, *J. Inorg. Nucl. Chem.*, 1970, **32**, 3875–3890.

[91] C. Rong and M. T. Pope, *J. Am. Chem. Soc*, 1992, **114**, 2932–2938.

[92] M. Sadakane, S. Moroi, Y. Iimuro, N. Izarova, U. Kortz, S. Hayakawa, K. Kato, S. Ogo, Y. Ide, W. Ueda *et al.*, *Chem. Asian J.*, 2012, **7**, 1331–1339.

[93] R. Liu and C. Streb, *Advanced Energy Materials*, 2021, **11**, 2101120.

[94] J. A. Gamelas, F. A. Couto, M. C. N. Trovão, A. M. Cavaleiro, J. A. Cavaleiro and J. D. P. de Jesus, *Thermochim. Acta*, 1999, **326**, 165–173.

[95] S. Herrmann, M. Kostrzewa, A. Wierschem and C. Streb, *Angew. Chem., Int. Ed.*, 2014, **53**, 13596–13599.

[96] D. Zhang, W. Zhang, Z. Lin, J. Dong, N. Zhen, Y. Chi and C. Hu, *Inorg. Chem.*, 2020, **59**, 9756–9764.

[97] C. Rong and F. C. Anson, *Inorg. Chem.*, 1994, **33**, 1064–1070.

[98] E. Coronado, J. R. Galán-Mascarós, C. Giménez-Saiz, C. J. Gómez-García and S. Triki, *J. Am. Chem. Soc*, 1998, **120**, 4671–4681.

[99] O. A. Kholdeeva, T. A. Trubitsina, G. M. Maksimov, A. V. Golovin and R. I. Maksimovskaya, *Inorg. Chem.*, 2005, **44**, 1635–1642.

[100] J. E. Toth and F. C. Anson, *J. Electroanal. Chem. Interf. Electrochem.*, 1988, **256**, 361–370.

[101] J. Gamelas, A. Gaspar, D. Evtuguin and C. P. Neto, *Appl. Catal. A: Gen.*, 2005, **295**, 134–141.

[102] M. Sadakane, N. Rinn, S. Moroi, H. Kitatomi, T. Ozeki, M. Kurasawa, M. Itakura, S. Hayakawa, K. Kato, M. Miyamoto, S. Ogo, Y. Ide and T. Sano, *Z. Anorg. Allg. Chem.*, 2011, **637**, 1467–1474.

[103] S. Ogo, N. Shimizu, T. Ozeki, Y. Kobayashi, Y. Ide, T. Sano and M. Sadakane, *Dalton Trans.*, 2013, **42**, 2540–2545.

[104] X. Wei, R. E. Bachman and M. T. Pope, *J. Am. Chem. Soc*, 1998, **120**, 10248–10253.

[105] M. N. Sokolov, S. A. Adonin, D. A. Mainichev, C. Vicent, N. F. Zakharchuk, A. M. Danilenko and V. P. Fedin, *Chem Comm.*, 2011, **47**, 7833–7835.

[106] H. Liu, C. J. Gómez-García, J. Peng, J. Sha, Y. Li and Y. Yan, *Dalton Trans.*, 2008, 6211–6218.

[107] J. A. Gamelas, M. S. Balula, H. M. Carapuça and A. M. Cavaleiro, *Electrochem. Commun.*, 2003, **5**, 378–382.

[108] J. H. Choi, J. K. Kim, S. Park, J. H. Song and I. K. Song, *Appl. Catal. A: Gen.*, 2012, **427**, 79–84.

[109] D. K. Lyon, W. K. Miller, T. Novet, P. J. Domaille, E. Evitt, D. C. Johnson and R. G. Finke, *J. Am. Chem. Soc*, 1991, **113**, 7209–7221.

[110] S. Ogo, N. Shimizu, K. Nishiki, N. Yasuda, T. Mizuta, T. Sano and M. Sadakane, *Inorg. Chem.*, 2014, **53**, 3526–3539.

[111] H. Liu, B. Yue, W. Sun, Z. Chen, S. Jin, J. Deng, G. Xie, Q. Shao and T. Wu, *Transit. Met. Chem.*, 1997, **22**, 321–325.

[112] R. Neumann and C. Abu-Gnim, *J. Chem. Soc., Chem. Commun.*, 1989, 1324–1325.

[113] R. Neumann and C. Abu-Gnim, *J. Am. Chem. Soc*, 1990, **112**, 6025–6031.

[114] N. V. Izarova, M. T. Pope and U. Kortz, *Angew. Chem. Int. Ed.*, 2012, **51**, 9492–9510.

[115] W. J. Randall, T. J. Weakley and R. G. Finke, *Inorg. Chem.*, 1993, **32**, 1068–1071.

[116] K. Nomiya, H. Torii, K. Nomura and Y. Sato, *J. Chem. Soc., Dalton Trans.*, 2001, 1506–1512.

[117] M. Higashijima, *Chem. Lett.*, 1999, **28**, 1093–1094.

[118] C. Besson, S.-W. Chen, R. Villanneau, G. Izzet and A. Proust, *Inorg. Chem. Commun.*, 2009, **12**, 1042–1044.

[119] C. C. Rong, H. So and M. T. Pope, *Eur. J. Inorg. Chem.*, **2009**, 5211–5214.

[120] M. Sadakane, D. Tsukuma, M. H. Dickman, B. Bassil, U. Kortz, M. Higashijima and W. Ueda, *Dalton Trans.*, 2006, 4271–4276.

[121] A. Bagno, M. Bonchio, A. Sartorel and G. Scorrano, *ChemPhysChem*, **4**, 517–519.

[122] M. Sadakane, Y. Iimuro, D. Tsukuma, B. S. Bassil, M. H. Dickman, U. Kortz, Y. Zhang, S. Ye and W. Ueda, *Dalton Trans.*, 2008, 6692–6698.

[123] G. Izzet, E. Ishow, J. Delaire, C. Afonso, J.-C. Tabet and A. Proust, *Inorg. Chem.*, 2009, **48**, 11865–11870.

[124] V. Lahootun, J. Karcher, C. Courillon, F. Launay, K. Mijares, E. Maatta and A. Proust, *Eur. J. Inorg. Chem.*, **2008**, 4899–4905.

[125] V. Lahootun, C. Besson, R. Villanneau, F. Villain, L.-M. Chamoreau, K. Boubekeur, S. Blanchard, R. Thouvenot and A. Proust, *J. Am. Chem. Soc*, **129**, 7127–7135.

[126] S. Romo, N. S. Antonova, J. J. Carbó and J. M. Poblet, *Dalton Trans.*, 2008, 5166–5172.

[127] M. Sadakane, D. Tsukuma, M. H. Dickman, B. Bassil, U. Kortz, M. Higashijima and W. Ueda, *Dalton Trans.*, 2006, 4271–4276.

[128] K. Nishiki, N. Umehara, Y. Kadota, X. López, J. M. Poblet, C. A. Mezui, A.-L. Teillout, I. M. Mbomekalle, P. de Oliveira, M. Miyamoto *et al.*, *Dalton Trans.*, 2016, **45**, 3715–3726.

[129] C. N. Kato, A. Shinohara, K. Hayashi and K. Nomiya, *Inorg. Chem.*, 2006, **45**, 8108–8119.

[130] K. Nomiya, Y. Saku, S. Yamada, W. Takahashi, H. Sekiya, A. Shinohara, M. Ishimaru and Y. Sakai, *Dalton Trans.*, 2009, 5504–5511.

[131] Y. Saku, Y. Sakai, A. Shinohara, K. Hayashi, S. Yoshida, C. N. Kato, K. Yoza and K. Nomiya, *Dalton Trans.*, 2009, 805–813.

[132] A. Sartorel, M. Carraro, G. Scorrano, R. D. Zorzi, S. Geremia, N. D. McDaniel, S. Bernhard and M. Bonchio, *J. Am. Chem. Soc*, 2008, **130**, 5006–5007.

[133] S. Yamaguchi, K. Uehara, K. Kamata, K. Yamaguchi and N. Mizuno, *Chem. Lett.*, 2008, **37**, 328–329.

[134] K. Kokumai and M. Sadakane, *Z. Anorg. Allg. Chem.*, 2022, **648**, e202200029.

[135] U. Kortz and S. Matta, *Inorg. Chem.*, 2001, **40**, 815–817.

[136] L. Yang, Q. Liu, P. Ma, J. Niu and J. Wang, *Dalton Trans.*, 2015, **44**, 13469–13472.

[137] B. S. Bassil, M. H. Dickman, M. Reicke, U. Kortz, B. Keita and L. Nadjo, *Dalton Trans.*, 2006, 4253–4259.

[138] S. J. Angus-Dunne, R. C. Burns, D. C. Craig and G. A. Lawrance, *J. Chem. Soc., Chem. Commun.*, 1994, 523–524.

[139] N. V. Izarova, A. Banerjee and U. Kortz, *Inorg. Chem.*, 2011, **50**, 10379–10386.

[140] X. López, J. A. Fernández and J. M. Poblet, *Dalton Transactions*, 2006, 1162–1167.

[141] X. López, C. Bo and J. M. Poblet, *Journal of the American Chemical Society*, 2002, **124**, 12574–12582.

[142] J.-J. J. Chen and M. A. Barteau, *Ind. Eng. Chem. Res.*, 2016, **55**, 9857–9864.

[143] M. T. Pope and G. M. Varga Jr, *Inorg. Chem.*, 1966, **5**, 1249–1254.

[144] I.-M. Mbomekallé, X. López, J. M. Poblet, F. Sécheresse, B. Keita and L. Nadjo, *Inorg. Chem.*, 2010, **49**, 7001–7006.

[145] X. López and J. M. Poblet, *Inorg. Chem.*, 2004, **43**, 6863–6865.

[146] X. Lopez, J. M. Maestre, C. Bo and J.-M. Poblet, *J. Am. Chem. Soc*, 2001, **123**, 9571–9576.

[147] M. Sadakane and E. Steckhan, *J. Mol. Catal. A Chem.*, 1996, **114**, 221–228.

[148] M. S. Balula, J. A. Gamelas, H. M. Carapuça, A. M. Cavaleiro and W. Schlindwein, *Eur. J. Inorg. Chem.*, 2004, **2004**, 619–628.

[149] F. A. Couto, A. M. Cavaleiro, J. D. P. de Jesus and J. E. Simão, *Inorganica Chim. Acta*, 1998, **281**, 225–228.

[150] M. Sadakane and M. Higashijima, *Dalton Trans.*, 2003, 659–664.

[151] S. Ogo, M. Miyamoto, Y. Ide, T. Sano and M. Sadakane, *Dalton Trans.*, 2012, **41**, 9901–9907.

[152] Y. V. Geletii, B. Botar, P. Kogerler, D. A. Hillesheim, D. G. Musaev and C. L. Hill, *Angew. Chem., Int. Ed.*, 2008, **120**, 3960.

[153] S. Piccinin, A. Sartorel, G. Aquilanti, A. Goldoni, M. Bonchio and S. Fabris, *PNAS*, 2013, **110**, 4917–4922.

[154] Q. Yin, J. M. Tan, C. Besson, Y. V. Geletii, D. G. Musaev, A. E. Kuznetsov, Z. Luo, K. I. Hardcastle and C. L. Hill, *Science*, 2010, **328**, 342–345.

[155] J. Soriano-López, D. G. Musaev, C. L. Hill, J. R. Galán-Mascarós, J. J. Carbó and J. M. Poblet, *J. Catal.*, 2017, **350**, 56–63.

[156] K. Azmani, M. Besora, J. Soriano-Lopez, M. Landolsi, A.-L. Teillout, P. de Oliveira, I.-M. Mbomekallé, J. M. Poblet and J.-R. Galán-Mascarós, *Chem. Sci.*, 2021, **12**, 8755–8766.

[157] S. H. Szczepankiewicz, C. M. Ippolito, B. P. Santora, T. J. Van de Ven, G. A. Ippolito, L. Fronckowiak, F. Wiatrowski, T. Power and M. Kozik, *Inorg. Chem*, 1998, **37**, 4344–4352.

[158] B. Zha, C. Li and J. Li, *J. Catal.*, 2020, **382**, 69–76.

[159] M. D. Symes and L. Cronin, *Nat. Chem*, 2013, **5**, 403–409.

[160] J.-J. Chen, L. Vila-Nadal, A. Solé-Daura, G. Chisholm, T. Minato, C. Busche, T. Zhao, B. Kandasamy, A. Y. Ganin, R. M. Smith *et al.*, *J. Am. Chem. Soc.*, 2022, **144**, 8951–8960.

Chapter 2

Theory

In this chapter, we provide an overview of quantum mechanics by first introducing the time-independent Schrödinger equation, which is then separated into electronic and nuclear motion by means of the Born-Oppenheimer approximation. Thereafter, we outline the fundamentals of Density Functional Theory (DFT), briefly outlining the importance of exchange-correlation functionals and basis sets. The chapter concludes with outlining modern quantum chemical calculations employed on POMs, focusing on redox and spectroscopic modelling.

2.1 Electronic Structure

The fundamentals of quantum mechanics are derived from the time-independent Schrödinger equation, shown in Equation 2.1.

$$\hat{H}\Psi = \mathrm{E}\Psi \tag{2.1}$$

$\hat{H}$ is the Hamiltonian operator, Ψ corresponds to the wavefunction, and E relates to the total energy of the system. The Hamiltonian operator describes the kinetic and potential energies of the electrons and nuclei for a given chemical system, shown in Equation 2.2:

$$\hat{H} = \hat{T}_n + \hat{T}_e + \hat{V}_{ne} + \hat{V}_{ee} + \hat{V}_{nn} \tag{2.2}$$

Herein, the $\hat{T}_n$ and $\hat{T}_e$ operators correspond to the kinetic energy of the nuclei and electrons, respectively. The nucleus-nucleus repulsion is denoted as $_{nn}$, the electron-electron Coulomb interaction corresponds to $\hat{V}_{ee}$, and the nuclei and the electrons is represented by $\hat{V}_{ne}$. The Hamiltonian operator, $\hat{H}$, can be rewritten as follows:

$$\hat{H} = -\sum_{\mathrm{i=1}}^{N}\frac{\hbar^2}{2m_e}\nabla_i^2 - \sum_{\mathrm{A=1}}^{M}\frac{\hbar^2}{2M_A}\nabla_i^2 + \sum_{\mathrm{i=1}}^{N}\sum_{\mathrm{A=1}}^{M}\frac{e^2Z_A}{r_{iA}} + \sum_{\mathrm{i=1}}^{N}\sum_{\mathrm{i>j}}^{N}\frac{e^2}{r_{ij}} + \sum_{\mathrm{A=1}}^{M}\sum_{\mathrm{B>A}}^{m}\frac{Z_AZ_B}{r_{AB}} \tag{2.3}$$

The mass of the nucleus and electron is denoted as M$_A$ and m$_e$, respectively. The distance between two electrons, i and j, two nuclei, A and B, one electron and nuclei are represented by r$_{ij}$, R$_{AB}$ and r$_{iA}$ respectively. The fundamental constants featuring in the Hamiltonian serve as base units: By definition, $m_e = \mathrm{e}_0 = \hbar = 4\pi\epsilon_0 = 1$. The Laplace operator, ∇_i^2 is represented as:

$$\nabla_i^2 = \frac{\partial^2}{\partial x_i^2} + \frac{\partial^2}{\partial y_i^2} + \frac{\partial^2}{\partial z_i^2} \tag{2.4}$$

2.1.1 The Born-Oppenheimer Approximation

The Born-Oppenheimer approximation allows separation of the electronic and nuclear motion by treating at fixed nuclear positions ($\{R_i\}$). Protons are around 2000x heavier than the electron, therefore, the nuclei travel significantly slower in a molecule. Hence, the kinetic energy of the nuclei is considered to be zero ($\hat{T}_n \rightarrow 0$) and $\hat{V}_{nn}$ is a constant. Employment of the Born-Oppenheimer approximation yields the electronic Hamiltonian equation, described below:

$$\hat{H}_{elec} = \sum_{\mathrm{i=1}}^{N} \frac{\hbar^2}{2m_e}\nabla_i^2 - \sum_{\mathrm{i=1}}^{N}\sum_{\mathrm{A=1}}^{M} \frac{e^2 Z_A}{r_{iA}} + \sum_{\mathrm{i=1}}^{N}\sum_{\mathrm{i>j}}^{N} \frac{e^2}{r_{ij}} = +\hat{V}_{ne} + \hat{V}_{ee} \tag{2.5}$$

Solving for the electronic Schrödinger equation for a given $\{R_i\}$ will yield electronic energy, E_{elec} and the electronic wavefunction, Ψ_{elec} for the ground state. The total energy is the sum of the electronic and nuclear energy: $E_{\mathrm{tot}} = E_{\mathrm{elec}} + V_{nn}$.

$$\hat{H}_{\mathrm{elec}}\Psi_{\mathrm{elec}}(\mathrm{r}_1, \mathrm{r}_2, \ldots \mathrm{r}_\mathrm{N}) = \mathrm{E}_{\mathrm{elec}}\Psi_{\mathrm{elec}}(\mathrm{r}_1, \mathrm{r}_2, \ldots \mathrm{r}_\mathrm{N}) \tag{2.6}$$

$\Psi(\mathrm{r}_1,\ \mathrm{r}_2,\ \ldots\ \mathrm{r}_\mathrm{N})$ depends on 3N spatial and N spin coordinate per electron, represented by r. The exact solution of the time-independent Schrödinger equation is known only for the hydrogen atom. The Born interpretation states the square of the wavefunction gives rise to the probability ($|\Psi|^2$) of finding a particle at a given point. The wavefunction is constricted to certain boundary conditions which include being: (i) single-valued; (ii) finite, (iii) and continuous. The wavefunction is antisymmetric with respect to interchange of two electrons which leads to the change of sign, shown below:

$$\Psi(\mathrm{r}_1, \mathrm{r}_2, \ldots \mathrm{r}_\mathrm{N}) = -\Psi(\mathrm{r}_2, \mathrm{r}_1, \ldots \mathrm{r}_\mathrm{N}) \tag{2.7}$$

2.1.2 Slater Determinants

Slater determinants are antisymmetric many-electron functions employed to represent an antisymmetric N-electron wavefunction. Exact solutions for many-body chemical systems ($N > 1$) are not known. Given N orbitals, ψ_i, an antisymmetric N-electron wavefunction for the ground state, Ψ_0, can be constructed.

$$\Psi_0 = \Phi_{SD} = \text{-}\frac{1}{N!}\begin{vmatrix} \chi_1(1) & \chi_2(1) & \cdots & \chi_N(1) \\ \chi_1(2) & \chi_2(2) & \cdots & \chi_N(2) \\ \vdots & \vdots & \ddots & \vdots \\ \chi_1(N) & \chi_2(N) & \cdots & \chi_N(N) \end{vmatrix}$$

Slater determinants are arranged so that each column contains the same spin orbital and every row contains the same electron. The $\frac{1}{N!}$ parameter is the normalization constant. Each spin orbital functions, $\chi(\mathrm{X})$, are products of a spatial and the spin function. The spatial element of the function can take 3N coordinates and the spin function can adopt either spin up (α) or spin down (β).

$$\chi(\mathrm{x}) = \phi(\mathrm{r})\sigma(\mathrm{s}), \mathrm{s} = \alpha \,\mathrm{or}\, \beta \tag{2.8}$$

The Slater determinants represents the antisymmetric N-electron wavefunction which is minimised in accordance to the variation principle. It states the expectation value for the Hamiltonian with respect to any acceptable trial function, ϕ, will always be greater than the ground state energy, E_0, see equation 2.9.

$$\mathrm{E}[\Phi] = \langle\frac{\Phi|\,\hat{\mathrm{H}}\,|\,\Phi}{\Phi|\,\Phi}\rangle \tag{2.9}$$

Here, the E[Φ] functional is minimised with respect to all N-electron wave functions. If E[Φ] = E_0, Φ is equivalent to the exact ground state wavefunction, Ψ.

2.2 Hartree-Fock Method

Recalling Equation 2.5, $\hat{H}_{\text{elec}}$ can be separated into two parts: 1-electron (kinetic energy and electron-nuclei potential) and the 2-electron terms (electron-electron repulsion), shown below:

$$\hat{H}_{\text{elec}} = -\sum_{\text{i}=1}^{N}\frac{1}{2}\nabla_i^2 - \sum_{\text{i}=1}^{N}\sum_{\text{A}=1}^{M}\frac{Z_A}{r_{iA}} + \sum_{\text{i}=1}^{N}\sum_{\text{j}>\text{i}}^{N}\frac{1}{r_{\text{ij}}} = \sum_{\text{i}=1}^{N} h(x_i) \tag{2.10}$$

The core Hamiltonian, $\hat{h}(i)$, corresponds to the kinetic energy and electron-nuclei potential terms. However, electron-electron repulsion is not divisible into single electron components. In Hartree-Fock, electron-electron repulsion, for all pairs, is treated as the mean potential of one electron in an average field of remaining electrons.

$$-\sum_{\text{i}=1}^{N} f(x_i), \hat{f}_{\text{i}} = -\frac{1}{2}\nabla_i^2 - \sum_{\text{A}=1}^{M}\frac{Z_A}{r_{iA}} + V_{HF}(x_i) \tag{2.11}$$

$V_{HF}(i)$ describes the repulsive potential experienced by an electron by the N-1 remaining, denoted as the Hartree-Fock potential. Thereby, replacing $\frac{1}{r_{\text{ij}}}$ which can not easily solved. Although this equation is a one-electron problem, the Hartree-Fock potential,$V_{HF}(i)$, depends on the entire system's wave function.

$$\text{V}_{\text{HF}}(x_1) = \sum_{\text{j}} (\hat{J}_{\text{j}}(x_1) - \hat{K}_{\text{j}}(x_1)) \tag{2.12}$$

$$\hat{J}_{\text{j}}(x_1) = \int |\chi_j(x_2)|^2 \frac{1}{\text{r}_{12}} \text{d}x_2 \tag{2.13}$$

$$\hat{K}_{\text{j}}(x_1)\chi_i(x_1) = \chi \cdot_j (x_2)\frac{1}{\text{r}_{12}}\chi_i(x_2)\text{d}x_2\chi_i(x_1) \tag{2.14}$$

$V_{HF}(i)$ is composed of two terms: the classical Coulomb repulsion term, and the non classical exchange integral. Equation 2.12 must be solved iteratively using a self-consistent field (SCF) procedure.[1] Initially, the integrals of the Fock operator are obtained from the trial wavefunction. Thereafter, improved wavefunctions are obtained and improved Fock matrices are constructed. This process is repeated until convergence criteria is reached.

2.3 Density Functional Theory

2.3.1 Electron Density

Despite the initial success of wavefunction methods, i.e. Hartree-Fock, many-electron wavefunctions are not experimentally observable and only acquires meaning through the Born interpretation, described earlier. The alternate method for describing physical systems is through the electron density concept. For an N electron system, the probability of locating an electron within a given volume, *dr*, can be expressed as:

$$\rho(r) = \text{N}\int \ldots \int |\phi(\text{x}_1, \text{x}_2, \ldots, \text{x}_\text{N})|^2 \,\text{dr}_1\text{dr}_2 \cdot .. \,\text{d}_\text{N} \tag{2.15}$$

The spatial and spin variables are described by x = (r, σ(s)). Electron density is experimentally observable, for example, though x-ray experiments. $\rho(r)$ possess many properties which fully describe the properties of any physical system. Integration of $\rho(r)$ gives the total number of electrons in the system:

$$\int \rho(r)\mathrm{dr} = \mathrm{N} \tag{2.16}$$

2.3.2 Hohenberg and Kohn Theorems

Hohenberg and Kohn proposed that the ground state electron density ($\rho(r)$) determines $\hat{H}$ and thus all the properties of a given system, see Equation 2.17.

$$\rho(r) \longrightarrow \{N, Z_{\mathrm{A}}, R_{\mathrm{A}}\} \longrightarrow \hat{\mathrm{H}} \longrightarrow \Psi_0 \longrightarrow \mathrm{E}_0 \tag{2.17}$$

Energy is a functional of the ground state density:

$$\mathrm{E} = \mathrm{E}[\rho_0] = \mathrm{T}[\rho_0] + \mathrm{V}[\rho_0] = \mathrm{T}[\rho_0] + \mathrm{E_{ee}}[\rho_0] + \mathrm{E_{Ne}}[\rho_0] = \mathrm{F_{HK}}[\rho] + \mathrm{V_{Ne}}[\rho] \tag{2.18}$$

$\mathrm{F}_{HK}[\rho]$ corresponds to the Hohenberg and Kohn functional which describes the kinetic energy, $\mathrm{T}[\rho_0]$, and the electron-electron repulsion, $\mathrm{E_{ee}}[\rho_0]$. Equation 2.18 can be expressed as:

$$\mathrm{F_{HK}}[\rho] = \mathrm{T}[\rho_0] + \mathrm{J}[\rho] + \mathrm{E_{ncl}}[\rho] \tag{2.19}$$

In Equation 2.19, $\mathrm{J}[\rho]$ represents the classical coulomb interaction and $\mathrm{E_{ncl}}[\rho]$ corresponds to the non-classical interactions derived from electronic motion, i.e. self-interaction, exchange and coulomb correlation. $\mathrm{E_{ncl}}[\rho]$ is an unknown quantity and its determination remains a challenge in the development of DFT theories.

The second Hohenberg-Kohn theorem proposed that the energy of a trial density is always greater than the exact ground-state energy:

$$\mathrm{E}[\rho] \geq \mathrm{E}[\rho_0] \tag{2.20}$$

The best approximation to $[\rho_0]$ can thus be found by minimizing the energy with respect to changes in the density.

2.3.3 Kohn - Sham Approach

The practical approach for computing the ground state density from the Kohn-Sham proposal considers accounting for the kinetic energy, correlation and exchange effects using a system of non-interacting electrons[2], whose Hamiltonian can be expressed as:

$$\hat{H}_{\mathrm{s}} = \sum -\frac{1}{2}{\nabla_i}^2 + \sum \mathrm{V_{ne}}(\mathbf{r}) \tag{2.21}$$

The first term corresponds to the kinetic energy operator and the second denotes the external potential. The Hamiltonian, $\hat{H}_{\mathrm{s}}$, is marked with the subscript "s" which indicates a non-interacting system. For this reference system, the wavefunction can be approximated using a singular Slaters determinant, built from Kohn-Sham $\{{\varphi_i}^{KS}\}$ orbitals.

$$\rho_s = \sum |{\varphi_i}^{\mathrm{KS}}|^2 = \rho \tag{2.22}$$

$$\mathrm{T}_s = -\frac{1}{2}\sum {\nabla_i}^2 {\varphi_i}^{\mathrm{KS}} \tag{2.23}$$

Here, the square of the Kohn-Sham orbitals, $|\varphi_i{}^{KS}|^2$, equates to the sum of the electron density - see Equation 2.22. Additionally, the kinetic energy of the reference system, T_s, in terms of $\varphi_i{}^{KS}$ is shown by Equation 2.23. The Kohn-Sham total-energy functional is:

$$\mathrm{E}^{\mathrm{KS}}[\varrho] = \mathrm{T}_s[\{\varphi_i{}^{\mathrm{KS}}\}] + \mathrm{V}_{\mathrm{ne}}[\varrho] + \mathrm{J}[\varrho] + \mathrm{E}_{\mathrm{xc}}[\varrho] \tag{2.24}$$

$\mathrm{E}_{xc}[\varrho]$ corresponds to the non-classical contributions to both kinetic energy and electron-electron interactions.

$$\mathrm{E}_{\mathrm{xc}}[\varrho] = \mathrm{T}[\{\varrho\}] - \mathrm{T}_s[\{\varphi_i{}^{\mathrm{KS}}\}] + \mathrm{V}_{\mathrm{ee}}[\varrho] - \mathrm{J}[\varrho] \tag{2.25}$$

$\mathrm{E}^{KS}[\varrho]$ is minimised with respect to $[\varrho]$ to satisfy the KS equations:

$$\hat{h}^{\mathrm{KS}}\varphi_i{}^{\mathrm{KS}}(\mathbf{r}) = \epsilon_i{}^{\mathrm{KS}}\varphi_i{}^{\mathrm{KS}}(\mathbf{r}) \tag{2.26}$$

$$\hat{h}^{\mathrm{KS}} = -\frac{1}{2}\nabla_i{}^2 + \upsilon_{\mathrm{ext}}(\mathbf{r}) + \int \frac{\rho(\mathbf{r'})}{\mathbf{r\text{-}r'}}\mathrm{d}\mathbf{r'} + \upsilon_{\mathrm{xc}}(\mathbf{r}) \tag{2.27}$$

$$= -\frac{1}{2}\nabla_i{}^2 + \upsilon^{\mathrm{KS}}(\mathbf{r}) \tag{2.28}$$

Trial ρ(r) functions are guessed to determine for $\upsilon^{KS}(\mathbf{r})$ then Equation 2.28 is solved to generate a new density. The new density is employed to better approximate for $\upsilon^{KS}(\mathbf{r})$, and the process is repeated in a self-consistent manner until the density reaches convergence within a given threshold. It is important to recognise that the Kohn-Sham would determine the exact ground state energy if $\mathrm{E}_{xc}[\rho]$ was known. Modern computational methods are focused on building improved approximations of $\mathrm{E}_{xc}[\rho]$ to minimise error.

2.3.4 Exchange-Correlation Functionals

2.3.4.1 LDA: Local Density Approximation

The simplest exchange-correlation functional employed in modern calculations comes from the local-density approximation (LDA) approximation. This approximation treats density as a uniform electron gas and the exchange-correlation functional is written as:

$$\mathrm{E}_{\mathrm{xc}}^{\mathrm{LDA}} = \int \rho(\mathrm{r})\epsilon_{\mathrm{xc}}(\rho(\mathrm{r}))dr \tag{2.29}$$

$\epsilon_{xc}(\rho(\mathrm{r}))$ corresponds to the exchange-correlation energy per electron as a function of the density. For uniform electron gases, $\epsilon_{xc}(\rho(\mathrm{r}))$ is spatially uniform so is not reflective of the rapid variation of densities in a molecule.

2.3.4.2 GGA: Generalised Gradient Approximation

The emergence of generalised gradient approximations (GGA), which include an electron density gradient are shown in Equation 2.30:

$$\mathrm{E}_{\mathrm{xc}}^{\mathrm{GGA}} = \int \rho(\mathrm{r})\epsilon_{\mathrm{xc}}(\rho(\mathrm{r}))dr + \int \mathrm{b}_{\mathrm{xc}}(\rho)\frac{|\nabla\rho(\mathrm{r})|^2}{\rho^{\frac{4}{3}}}dr \tag{2.30}$$

Lopez and co-workers reported GGA functionals overdelocalize electron density in reduced substituted Wells-Dawson anions, delocalizing electron density across over the belt-tungstens rather than the peripheral heteroatom.[3–5] By contrast, Kremleva and co-workers reported accurate redox potential for the tri-Mn-substituted Keggin anion were best described by Perdew-Burke-Ernzerhof (PBE) compared to more expensive hybrid functionals.[6] The authors postulate this was due to a fortuitous error cancellation.[6] Therefore, it is advisable to screen across multiple functionals for more accurate calculation.

2.3.4.3 Hybrid Functionals

Energy contribution by correlation effects, E_c, is neglected in Hartree–Fock. However, Hartree–Fock methods provide an exact treatment for the exchange contribution, E_x. The exchange contribution to E_{xc}, is more significant than the corresponding correlation energy.[1]

$$\mathrm{E_{xc}} = \mathrm{E}_x^{\mathrm{HF}} + z\,(\mathrm{E}_{\mathrm{xc}}^{\mathrm{DFT}} + \mathrm{E}_x^{\mathrm{HF}}) \tag{2.31}$$

Employing E^{LDA} defines Beckes half-and-half (BH&H) functional derived in 1993.[7] In this approximation, $\alpha = 0.5$ which corresponds to:

$$\mathrm{E_{xc}}^{\mathrm{H\&H}} = {}_x^{\mathrm{HF}} + \alpha(\mathrm{E}_x^{\mathrm{LDA}} + \mathrm{E}_c^{\mathrm{LDA}}) \tag{2.32}$$

Models that incorporate exact exchange are denoted as hybrid methods, with significant popularity owing to the B3LYP functional ($\alpha = 0.2$).[8] Poblet and co-workers have reported hybrid functionals best describe electron localisation owing to exact HF exchange. However, correct ordering and relative reduction energies (REs) relative to electrochemical measurements was achieved with the hybrid-B3LYP functional for the Wells-Dawson anion.[5] Additionally, such functionals have also been employed for the computation of redox potentials achieving superior results over GGA-PBE functionals.[9]

$$\mathrm{E}_{\mathrm{xc}}^{\mathrm{B3LYP}} = (1-\alpha)\mathrm{E}_x^{\mathrm{LDSA}} + \alpha\mathrm{E}_x^{\mathrm{B88}} + b_x^{\mathrm{HF}} + c\,\mathrm{E}_c^{\mathrm{LYP}} + (1-\mathrm{c})\mathrm{E}_c^{\mathrm{LDSA}} \tag{2.33}$$

2.3.4.4 Long Range Hybrid Functionals

The non-Coulomb element in exchange functionals often decay too rapidly and become highly inaccurate at large distances. Long range hybrid functionals offer a solution by incorporating long-range correction terms:

$$\mathrm{E}_x^{\mathrm{B97X}} = \mathrm{E}_{\mathrm{x,sr}}^{\mathrm{B97}} + \mathrm{c_X}\mathrm{E}_{\mathrm{x,sr}}^{\mathrm{B97}} + \mathrm{E}_{\mathrm{x,lr}}^{\mathrm{B97}} \tag{2.34}$$

Herein, lr and sr correspond to long-range and range-range terms, respectively. In practice, computation with hybrid methodologies are often expensive. Benchmarking with different levels of theory are imperative for achieving an optimal balance between accuracy and expense. Therefore, we have employed several generalized gradient approximation (GGA), hybrid, and range-separated hybrid functional throughout this work.

2.3.5 Basis Sets

Basis sets are a collection of (basis) functions used to approximate the wavefunction for a given molecule. Slater Type Orbitals (STOs) or Gaussian Type Orbitals (GTOs) are commonly employed. STOs expressed in polar coordinates is given below:

$$\chi_{z,n,l,m}(\mathrm{r},\theta,\phi) = NY_{l,m}r^{n-1}\exp(-\zeta\mathrm{r}) \tag{2.35}$$

N corresponds to the normalization constant and $Y_{l,m}$ are the spherical harmonics (describes "shape" of orbital). STOs closely describe the behaviour of hydrogen atomic orbitals because they cusp at r=0 and demonstrate an ideal rate of decay as one moves from the nucleus. By the contrary, GTOs do not cusp at $r = 0$ and decay too rapidly far from the nucleus. Hence, these type-orbitals often poorly describe the close and long-range to the nucleus. The expression for

GTO is shown by Equation 2.36.

$$\chi_{z,n,l,m}(\mathrm{r},\theta,\phi) = NY_{l,m}r^{2n-2-1}\exp(-\zeta \mathrm{r}^2) \tag{2.36}$$

Furthermore, increasing the number of basis functions will improve the description of electron distribution in a chemical system. The smallest number of basis functions that can be applied is by employing a minimal basis set. For example, the hydrogen atom will be described using a singular s function. In practise, the minimal basis set is not sufficient. Further improvements are obtained by employing double- (DZ) and triple- Zeta basis sets. For example, employing a DZ basis set to hydrogen will incur two basis functions. Autschbach and co-workers have reported that employing larger basis sets induced minimal improvements with respect to the geometry of the Keggin in gas-phase.[10]

Additional improvements can be obtained by including polarising functions which are crucial for describing chemical bonding. For example, adding p -functions to describe bonding in hydrogen. Polarisation functions coupled to TZ basis set produces the Triple ζ plus Polarisation (TZP) type basis. Recently, computation of four redox waves attributed to the Wells-Dawson anion were accurately reproduced by means of the Slater-type TZP with polarisation.[11] Computational modelling of POMs is a delicate balance between accuracy and computational expense. Polarisation offers an inexpensive route to achieving accurate description to chemical bonding in POMs.[12]

2.4 Polyoxometalates in Computational Chemistry

Quantum chemical calculations have primarily focused on the classical structures: (i) Lindqvist $[M_6O_{19}]^{q-}$; (ii) Keggin, $[XM_{12}O_{40}]^{q-}$; and Wells-Dawson, $[X_2M_{18}O_{62}]^{q-}$, clusters. In 1986, the first example of modelling for the dodecamolybdophosphate $[PMo_{12}O_{40}]^{3-}$ was reported by Taketa and Katsuki using the Xα method to describe the properties of the frontier molecular orbitals (FMOs).[13] During the 1990s, Bernard and co-workers applied the *ab initio* Hartree-Fock Self-Consistent (HF-SCF) method to study the elecontric structure of the decavanadate anion, $[V_{10}O_{28}]^{6-}$.[14] The authors reported the basicity of different oxygen sites through molecular electrostatic potential distribution analysis. The distribution plot demonstrated the OV_3 and OV_3 bridging oxo ligands carry are the most nucleophilic and thus the more likely coordination sites for small cations.[14]

The emergence of Density Functional Theory (DFT) permitted the detailed analysis of these clusters without significant computational cost. Poblet and co-workers explored rotational isomerism of Keggin heteropolyanions, α/β-$[XM_{12}O_{40}]^{q-}$, by simulating the relative stability of these isomers; deducing the enhanced stability of α-$[XM_{12}O_{40}]^{q-}$ was attributed to the higher energy associated with lowest occupied molecular orbital (LUMO).[15] The calculations reported were performed using the LDA functional, with Vosko-Wilk-Nusair (VWN) parametrization, in the gas phase.[15] Later, Zhang *et al.* emphasised the importance of incorporating implicit solvation for reproducing experimental geometries.[12] Several GGA functionals were tested by the authors and deduced PBE / BP86 provided the closest description to the experimental geometries.[12] Implicit solvent effects are incorporated by means of continuum models (COSMO, PCM or SMD), which are crucial for reproducing electronic and redox properties, discussed later. In 2004, Lopez and co-workers reported clusters comprising low values of q/m e.g. ≤ 0.8, are adequately modelling in gas-phase.[16] The incorporation of implicit solvation was labelled as strictly necessary for clusters exceeding $q/m = 0.8$. Another example emphasising the importance of implicit solvation is illustrated by the protonated W-based Keggin ions. Gas-phase calculations suggested protonation would preferably bind to terminal oxo- groups instead of the bridging atoms. The incorporation of solvation inverts these findings, indicting the bridging oxygen atoms are more basic.[17,18] The employment of generalised gradient approximation (GGA) and hybrid functionals have been extensively employed to reproduce equilibrium geometries in Keggin, $[XM_{12}O_{40}]^{q-}$, often showing very subtle differences. The incorporation of double-zeta atomic basis sets have been reported to accurately reproduce experimental geometries of POMs.[19] However, the inclusion of triple-zeta atomic basis sets are recommended for computation of redox[20], thermochemistry[5,20], and spectroscopic properties i.e NMR[21,22].

Classical Molecular Dynamics (MD) have been employed to study the solution behaviour with an explicitly located solvent environment. Several authors have reported the distribution of solvent molecules and counter-ions surrounding POM clusters.[23–25] In addition, Car-Parrinello MD (CPMD) calculations been employed to simulate the first nucleation steps in the formation of Keggin polyoxometalates.[26] In a similar manner, QM/MM calculations have been employed to study redox potentials in W-based Keggin anions.[20] Falbo and co-workers treated aqueous solvent explicitly to permit the study of the structure dynamics and charge distribution of the Keggin, the solvent environment, and counter-ion interactions.[20]

2.4.1 Redox Calculations

The challenge with modern quantum chemical calculations is the selection of the optimal exchange-correlation functional. Computation of experimental redox properties are optimally performed using calculations incorporating Hartree-Fock exchange. However, there are no universal solutions to each problem because the exact form of the exchange-correlation functional is unknown. Hence, exploration and parametrization of different families of exchange-correlation functionals is a prerequisite for most theoretical reports. For instance, Poblet and co workers recognised pure GGA functionals often poorly describe electron delocalization in mono-substituted Wells-Dawson, $[P_2W_{17}MO_{62}]^{q-}$ (M = V, Mo) anions by incorrectly localising the additional electron at the belt region.[5] Further analysis revealed employment of the B3LYP functional (20 % HF exchange) reproduced the correct ordering and relative reduction energies (REs) with respect to experimental measurements. Early quantum chemical calculations on POMs have focused on charged systems under implicit solvation models. Early work employed reduction energies (REs); defined as the energy difference between the one-electron reduced and oxidized forms, in the presence of a implicit solvent model (COSMO) to reproduce experimental redox potentials.[5,27] This assumption has been shown to well reproduce redox potentials for plenary Keggin and Wells-Dawson anions because the reductive process involves the addition of one electron to an non-bonding orbitals rendering the entropic and vibrational contributions in ΔG as negligible contributions. However, Falbo and co-workers reported for the effect of zero-point energy (ZPE) and entropy corrections to redox calculations decreased $U^0{}_{red}$ by ca. 0.15 V for $[SiW_{12}O_{40}]^{4-}$.[20] Additionally, reduction of chemical systems without non-bonding orbitals will exacerbate entropic and vibrational contributions leading to large errors. Chemical systems supporting large charges will strongly exacerbate strong self-interaction errors (SIE) leading to large errors in redox calculation. Kremleva and co-workers reported that charge neutralisation with explicitly located Li^+ counterions significantly reduced redox error in tri-Mn-substituted Keggin anions.[6] However, the authors noted the understanding of electrolyte environment to adequately model the Li-POM ion pair is essential for achieving quantitative agreement between theoretical and experimental data.

In this section, we will provide an overview to compute the redox potentials of compounds with implicit solvation models. The general electrochemical concepts that allow for computation of reduction potentials are given by the half-reaction for the reduction of an oxidised species, Ox(aq).

$$\mathrm{Ox\,(aq) + n}e^{-}\mathrm{(g)} \longrightarrow \mathrm{Red\ (aq)} \tag{2.37}$$

The gas and solution phase are represented by (g) and (aq), respectively. The number of electrons is represent by the integer, n. The Gibbs free energy change for a given temperature, T, under non-standard conditions is calculated by:

$$\Delta_r \mathrm{G} = \Delta_r \mathrm{G}^{\circ} + \mathrm{RTln}\frac{\alpha_{\mathrm{Ox}}}{\alpha_{\mathrm{Red}}} \qquad \alpha_{\mathrm{x}} = \gamma_x \frac{\mathrm{c}_x}{\mathrm{c}^0} \tag{2.38}$$

In Equation 2.38, R corresponds to the ideal gas constant, $\Delta_r \mathrm{G}^{\circ}$ is the difference in Gibbs free energy under standard conditions, and α refers to the activity for a given substance. The activity of the oxidised species is represented by α_x, and depends on the bulk, c_x, standard concentration, c^0, and the activity coefficient denoted γ_x. The absolute redox potential is related to the Gibbs free energy change of the Nerst Equation, shown by:

$$\mathrm{E}_{abs} = -\frac{\Delta_r \mathrm{G}}{n\,\mathrm{F}} = \mathrm{E}_{abs} + \frac{\mathrm{RT}}{n\,\mathrm{F}} \cdot \ln\frac{\alpha_{\mathrm{Ox}}}{\alpha_{\mathrm{Red}}} \tag{2.39}$$

$$\Delta_r \mathrm{G} = -n\,\mathrm{FE}_{abs} \tag{2.40}$$

Equation 2.39 - 2.40 allows the computation of redox potentials for a given reaction. The terms: F and E_{abs} denote the Faraday constant and the standard redox potential, respectively. Conventionally, redox potentials are measured with respect to a reference half-reaction. A common example is the standard hydrogen electrode (SHE) which assumes hydrogen production occurring under standard conditions (1 atm at 298.15 K) under a Pt electrode. Equation 2.40 returns computed redox potentials which are referenced against the SHE using the formula below:

$$\mathrm{E}_{rel} = \mathrm{E}_{abs} - \mathrm{E}_{SHE} \tag{2.41}$$

Cramer et al. established a value for E_{SHE} at 4.28 eV corresponding to the free energy change for hydrogen electron half reaction.[28] Equation 2.41 permits the calculation of redox potential relative to the hydrogen electrode.

2.4.2 NMR Calculations

Nuclear magnetic resonance (NMR) of active nuclei ($\mathrm{I} \neq 0$) is employed for characterising molecular structures, in solution and solid state. This technique obtains information regarding the chemical environment of the active nuclei (^{17}O, ^{29}Si, ^{31}P, ^{183}W). Computation of NMR spectra has attracted significant interest for predicting chemical shifts of active nuclei, present in POM clusters. Early examples of ^{183}W chemical shifts were carried out for basic molecules such as: $\mathrm{W(CO)_6}$, $\mathrm{WF_6}$ and $\mathrm{WCl_6}$, which revealed linear correlations between the experimental and theoretical values.[29] However, early examples of computed chemical shifts for the W-based Keggin proved unsuccessfully because of large systematic error attributed to the use of basis sets with effective core potentials.[19,30] Early quantum chemical calculations on POMs focused on charged systems without account for relativistic corrections or implicit solvation. Quasi-relativistic corrections by means of zeroth-order relativistic approximation (ZORA) are crucial for reproducing accurate shielding and chemical shifts. Bagno and co-workers computed ^{183}W chemical shifts for $[\mathrm{PW_{11}O_{39}}]^{7-}$ reported the W1-W5 signals were deshielded relative to W6; such that W2 and W3 reproduced trends shown the experimental.[30] Later, incorporating spin-orbit (SO) corrections coupled with zeroth-order regular approximation (ZORA) formalism and implicit solvation into the calculations.[31] Bagno and co-workers reported ^{183}W chemical shifts reporting an average mean error of 35 ppm.[31] The importance of implicit solvation for calculating accurate chemical shifts has been widely reported. Bagno and co-workers reported computed ^{183}W chemical shifts were more accurate under implicit solvation, with respect to the gas-phase.[31] Poblet and co-workers emphasised the sensitivity of computed chemical shifts with structural distortion to W-based Keggin anions.[32] The author reported a linear correlation with between W-O$_{b,c}$ distance and computed chemical shifts, attributed to the larger interaction between the dorbitals of the metal and the corresponding orbitals of the oxo ligands.[32]

In practice, an external magnetic field, B$_0$, is applied to an atom, causing circulations in the electron cloud surrounding the nucleus, inducing a magnetic moment, μ, opposed to B$_0$, is produced. This effect corresponds to the magnetic shielding of the nucleus that reduces B$_0$ to σB$_0$; herein σ is denoted the shielding constant.

$$\mathrm{B}_{\mathrm{Local}} = \mathrm{B}_0(1\text{-}\sigma) \tag{2.42}$$

The magnetic shielding constant, σ corresponds to the sum of diamagnetic (σ^d) and paramagnetic, (σ^p) contributions of the induced electronic motion, shown in Equation 9.7

$$\sigma_{\mathrm{Local}} = \sigma^d + \sigma^p \tag{2.43}$$

Herein, the diamagnetic contribution opposes the external magnetic field and shields the nucleus in question. By contrast, the applied magnetic field is reinforced by the paramagnetic contribution, thereby deshielding the nucleus. The magnetic shielding constant is negative if the diamagnetic contribution dominates, and is positive otherwise. The interaction of the nuclear magnetic moment with an external magnetic field splits the degenerate ground state into discrete $2I+1$ nuclear energy levels. The adsorption of energy inducing transition between two of these states is detected and plotted as spectral lines, which is called a resonance signal. Convention expresses these resonance frequencies in terms of an empirical quantity called chemical shift, related to the difference between the resonance frequency, ν_s, of the nucleus and the reference sample, ν_{ref}:

$$\delta/\,\mathrm{ppm} = 10^{\,6}\,(\,\frac{\nu_s - \nu_{\mathrm{ref}}}{\nu_{\mathrm{ref}}}\,) \tag{2.44}$$

The fundamental quantity underpinning chemical shift is the magnetic shielding tensor, σ, which is written as the sum of the diamagnetic (σ^d), paramagnetic, (σ^p), and spin-orbit, (σ^{SO}), contributions. The paramagnetic contribution is determined by the magnetically perturbed molecular orbitals (MOs). This contribution depends on electronic structure and is thereby, exchange-correlation functional dependent. The majority contributor of the paramagnetic tensor is occupied-virtual coupling, initiated by the applied magnetic field. For the paramagnetic tensor, its principal contribution v_{ai} is expressed in Equation 9.9. The diamagnetic part depends on the ground-state wave function. The diamagnetic contributions are mostly constant for most chemical systems, such that the chemical shifts are dominated by the paramagnetic contribution, for a given nucleus.

$$v_{ai} \propto -\frac{\langle \psi_a \,|\, \hat{M} |\, \psi_i \,\rangle}{2\,(\epsilon_i{}^0 - \epsilon_a{}^0)} \tag{2.45}$$

The orbital energies for the occupied and unoccupied MOs, involve in electron transition are denoted: $\epsilon_i{}^0$ and $\epsilon_a{}^0$, respectively. The integral in the numerator is the first-order magnetic coupling between these orbitals.

Bibliography

[1] F. Jensen, *Introduction to Computational Chemistry*, Wiley & Sons, 2017.

[2] W. Kohn and L. J. Sham, *Phys. Rev.*, 1965, **140**, 1133–1138.

[3] I.-M. Mbomekallé, X. López, J. M. Poblet, F. Sécheresse, B. Keita and L. Nadjo, *Inorg. Chem.*, 2010, **49**, 7001–7006.

[4] P. A. Aparicio, J. M. Poblet and X. López, *Eur. J. Inorg. Chem.*, **2013**, 1910–1916.

[5] P. A. Aparicio, X. López and J. M. Poblet, *J. Mol. Eng. Mater.*, 2014, **2**, 1440004.

[6] A. Kremleva, P. A. Aparicio, A. Genest and N. Rösch, *Electrochim. Acta*, 2017, **231**, 659–669.

[7] A. D. Becke, *J. Chem. Phys.*, 1993, **98**, 1372–1377.

[8] W. Y. C. Lee and R. G. Parr, *Phys. Rev. B*, 1988, **37**, 785.

[9] A. Kremleva and N. Rosch, *J. Phys. Chem. C*, 2018, **122**, 18545–18553.

[10] A. Bagno, M. Bonchio and J. Autschbach, *Chem. Eur. J.*, 2006, **12**, 8460–8471.

[11] J.-J. Chen, L. Vila-Nadal, A. Solé-Daura, G. Chisholm, T. Minato, C. Busche, T. Zhao, B. Kandasamy, A. Y. Ganin, R. M. Smith *et al.*, *J. Am. Chem. Soc.*, 2022, **144**, 8951–8960.

[12] F.-Q. Zhang, H.-S. Wu, X.-F. Qin, Y.-W. Li and H. Jiao, *J. Mol. Struct.*, 2005, **755**, 113–117.

[13] H. Taketa, S. Katsuki, K. Eguchi, T. Seiyama and N. Yamazoe, *J. Phys. Chem.*, 1986, **90**, 2959–2962.

[14] J. Y. Kempf, M. M. Rohmer, J. M. Poblet, C. Bo and M. Benard, *J. Am. Chem. Soc.*, 1992, **114**, 1136–1146.

[15] X. Lopez, J. M. Maestre, C. Bo and J.-M. Poblet, *J. Am. Chem. Soc.*, 2001, **123**, 9571–9576.

[16] X. López, J. A. Fernández, S. Romo, J. F. Paul, L. Kazansky and J. M. Poblet, *J. Comput. Chem.*, **25**, 1542–1549.

[17] X. López, J. J. Carbó, C. Bo and J. M. Poblet, *Chem. Soc. Rev.*, 2012, **41**, 7537–7571.

[18] J. A. Fernández, X. López and J. M. Poblet, *J. Mol. Catal. A Chem.*, 2007, **262**, 236–242.

[19] A. Bagno and M. Bonchio, *Chem. Phys. Lett.*, 2000, **317**, 123–128.

[20] E. Falbo and T. J. Penfold, *J. Phys. Chem. C*, 2020, **124**, 15045–15056.

[21] M. Pascual-Borràs, X. López, A. Rodríguez-Fortea, R. J. Errington and J. M. Poblet, *Chem. Sci.*, 2014, **5**, 2031–2042.

[22] M. Pascual-Borràs, X. López and J. M. Poblet, *Phys. Chem. Chem. Phys.*, 2015, **17**, 8723–8731.

[23] X. López, C. Nieto-Draghi, C. Bo, J. B. Avalos and J. M. Poblet, *J. Phys. Chem. A*, 2005, **109**, 1216–1222.

[24] J. M. Cameron, L. Vilà-Nadal, R. S. Winter, F. Iijima, J. C. Murillo, A. Rodríguez-Fortea, H. Oshio, J. M. Poblet and L. Cronin, *J. Am. Chem. Soc.*, 2016, **138**, 8765–8773.

[25] A. Kremleva and N. Rösch, *J. Phys. Chem. C*, 2018, **122**, 18545–18553.

[26] L. Vilà-Nadal, S. G. Mitchell, A. Rodríguez-Fortea, H. N. Miras, L. Cronin and J. M. Poblet, *Phys. Chem. Chem. Phys.*, 2011, **13**, 20136–20145.

[27] X. López, J. A. Fernández and J. M. Poblet, *Dalton Trans.*, 2006, 1162–1167.

[28] D. G. Truhlar, C. J. Cramer, A. Lewis and J. A. Bumpus, *J. Chem. Educ.*, 2004, **81**, 596.

[29] A. Rodriguez-Fortea, P. Alemany and T. Ziegler, *J. Phys. Chem. A*, 1999, **103**, 8288–8294.

[30] A. Bagno, M. Bonchio, A. Sartorel and G. Scorrano, *ChemPhysChem*, **4**, 517–519.

[31] A. Bagno, M. Bonchio and J. Autschbach, *Chem. Eur. J.*, **12**, 8460–8471.

[32] L. Vilà-Nadal, J. P. Sarasa, A. Rodríguez-Fortea, J. Igual, L. P. Kazansky and J. M. Poblet, *Chem. Asian J.*, **5**, 97–104.

Chapter 3

Experimental

The present chapter outlines all experimental work carried out during this Ph.D. During this time, we have worked in close collaboration with experimentalists during the elaboration of this thesis, specifically with the groups of Prof. M. D. Symes (Chapter 6) and Prof. J. S. J. Hargreaves (Chapter 7).

3.1 Experimental

3.1.1 Materials

All reagents and solvents were supplied by Sigma Aldrich Chemical Company Ltd., Thermo Fisher Scientific, and Cambridge Isotope Laboratories. The stated otherwise, unless stated otherwise, were used without further purification.

3.1.2 Instrumentation

FT-IR spectra were recorded on a Nicolet 170SX-FT/IR spectrometer in the range of 400–4000 cm^{-1}.

UV-Vis spectra were measured in the region of 200–400 nm for 30 μM solutions in distilled water at 25 °C using a Shimadzu 1800 spectrophotometer matched quartz cell.

^{31}**P NMR** spectroscopy was performed using a Bruker DPX 400 spectrometer with 85 % phosphoric acid as an external standard. All spectra were recorded using 50 mg samples dissolved in D_2O. All tetrabutylammonium salts were recorded using 50 mg samples dissolved in CD_3CN.

Electrospray ionization mass spectrometry was obtained in negative-ion mode on the Agilent Q-TOF 6520 LC/MS mass spectrometer. The electrospray ionization source conditions: Vcap, 3500 V; skimmer, 65 V; nebulizer, 30 psi; drying and nebulizer gas, N_2; drying gas flow, 10 L min^{-1}; drying gas temperature, 300 °C; fragmentor, 80 V; scan range 100–2000 m/z. The sample solutions with the concentration of approximately 1000 ppm were made and analysed by direct injection using an automatic sampler with a flow rate of 0.2 mL min^{-1}.

Powder X-ray diffraction experiments were recorded using a Siemens D5000 X-ray diffractometer (40 kV, 40 mA) employing a CuKα X-ray source (1.5418 Å). A scanning range of 5-85 ° 2θ with a step size of 0.02° and counting time of 1 second per step. XRD patterns for $K_5[PW_{11}M(H_2O)O_{39}]$; M= Ni, Cu were performed by Mr Mohamed Hosny Elsayed Mostafa Mahmoud.

3.1.3 Electrochemical Procedure

All electrochemical experiments were controlled by a Gamry Instruments Interface1010E potentiostat and carried out under inert (N_2) atmosphere, ambient temperature and pressure.[1–3] Cyclic voltammetry experiments were conducted in a single-compartment cell using a three-electrode set-up comprised of a glassy carbon working electrode (3.0 mm diameter, 0.0707 cm^2 area, BASi), a platinum wire counter electrode (1.0 mm diameter, 50 mm length, Alfa Aesar) and an Ag/AgCl reference electrode (3.0 M NaCl, BASi). The glassy carbon electrode was cleaned with Alumina polishing compound (0.05 µm, BASi), followed by distilled water and acetone. All electrochemical experiments were conducted at scan rates of 10 mV s^{-1}. All potentials were reported with respect to the Standard Hydrogen Electrode (SHE), shown in Table 3.1. All scans were recorded using 10 mM heteropolyanion (HPA) and an appropriate 0.2 M acetate (pH 4.80) solution.

Table 3.1: Three run average redox potential of 10 mM aqueous solutions of $K_5[PW_{11}M(H_2O)O_{39}]$; M = Mn(III/II), Fe(III/II), and Co(III/II) referenced against the Standard Hydrogen Electrode (SHE).

System	$E_{1/2}$ or E_{pa} / V	Peak Separation / V
$Li_5[PW_{11}Mn(H_2O)O_{39}]$	0.924 ±0.021	0.253
$Li_5[PW_{11}Fe(H_2O)O_{39}]$	0.200 ±0.003	0.079
*$Li_5[PW_{11}Co(H_2O)O_{39}]$	1.528 ±0.012	N/A
$Na_5[PW_{11}Mn(H_2O)O_{39}]$	0.873 ±0.014	0.250
$Na_5[PW_{11}Fe(H_2O)O_{39}]$	0.204 ±0.005	0.072
*$Na_5[PW_{11}Co(H_2O)O_{39}]$	1.515 ±0.007	N/A
$K_5[PW_{11}Mn(H_2O)O_{39}]$	0.859 ±0.014	0.235
$K_5[PW_{11}Fe(H_2O)O_{39}]$	0.194 ±0.009	0.071
*$K_5[PW_{11}Co(H_2O)O_{39}]$	1.507 ±0.008	N/A

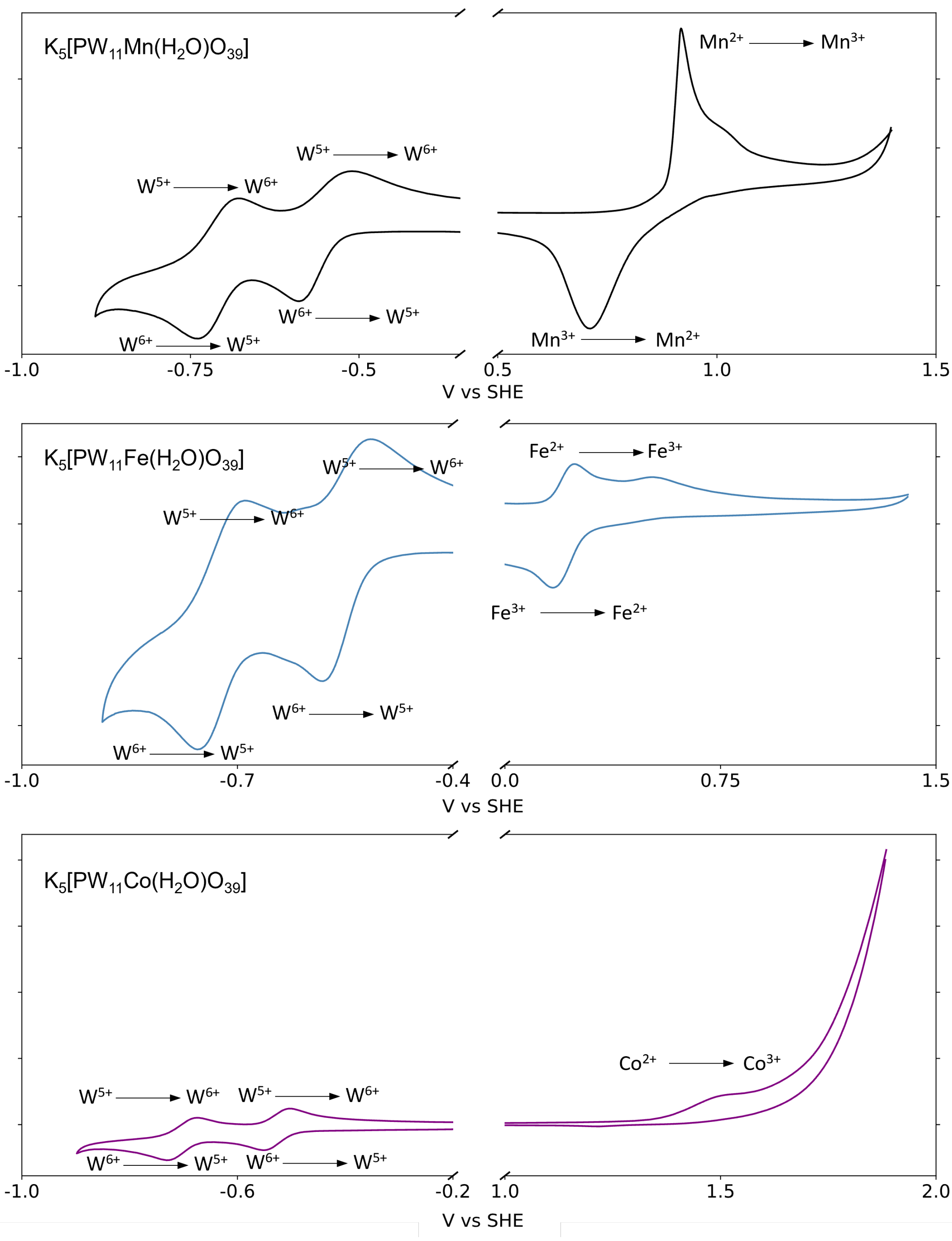

Figure 3.1: Cyclic voltammograms of 10 mM aqueous solutions of $K_5[PW_{11}M(H_2O)O_{39}]$; M = Mn(III/II), Fe(III/II), and Co(III/II) which were recorded in an appropriate 0.2 M acetate (pH 4.80) solution. All potentials are referenced against SHE.

3.1.4 Ammonia Synthesis Procedure

The following procedure was adapted in accordance to previous work under supervision of Dr. Angela Daisley.[4,5] 0.3 g of catalyst was placed in a silica reactor tube held together by quartz wool and held centrally within the heated zone of the furnace, similar to that used by Aika and Kojima.[6,7] Reactant feedstocks (H_2/N_2 (BOC, H_2 99.998 %, N_2 99.995 %), ratio of 3:1 respectively)) was passed at 60 mL min^{-1} and heated to reaction temperature, 400 °C. Upon reaching reaction temperature, vent gas was flowed through the sulphuric acid solution (1.08 x 10 $^{-3}$ mol L^{-1}, 200 mL at ambient temperature). Ammonia yield was determined by reading the reduction in conductivity, corresponding to the consumption of protons by NH_3, with respect to time. The activity data was taken after 30 mins, by which the catalyst was stabilised at reaction temperature. The reactor consisted of taps, pressure gauges and mass flow controllers (Brooks 5850TR). The temperature for all reactions were monitored using a K-type thermocouple. Stainless steel tubing (1/4 inch) was employed to deliver feedstock to the silica reactor (10.5 mm internal diameter) and the temperature was regulated by a Carbolite furnace. The vent gas was passed through the sulphuric acid bubbler and the decrease in conductivity was measured using a conductivity meter.

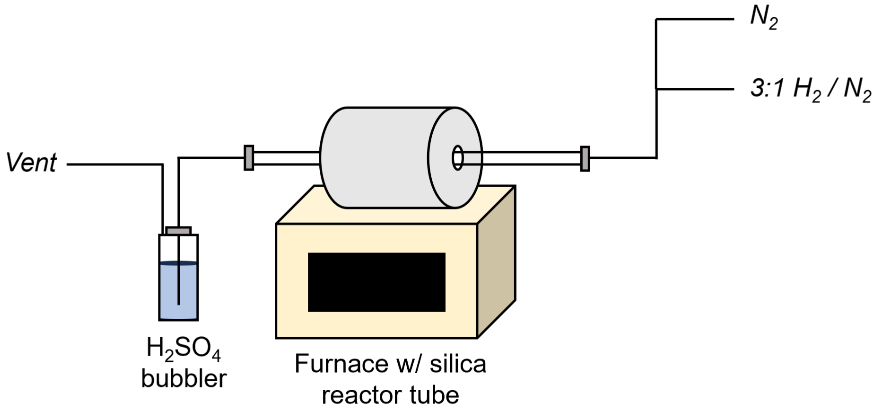

Figure 3.2: Ammonia Synthesis set-up featuring silica reactor tubing held centrally within the heated zone of the furnace.

3.1.5 Preparation

3.1.5.1 $Li_3[PW_{12}O_{40}]$

$Li_3[PW_{12}O_{40}]$ was prepared in accordance to the literature.[8]. Phosphotungstic acid (5.0 g, 1.74 mmol) was dissolved in water (20 mL). LiCl (0.22 g, 5.21 mmol) was dissolved in the phosphotungstic solution, under stirring for 1 hr. The solvent was evaporated off at 373 K producing a white crystalline powder (5.05 g, 98.6 %). ^{31}P-NMR (400 MHz, D_2O): δ -15.41, IR: 1080 (s), 980 (s), 890 (s) cm^{-1}, UV (H_2O): 256 nm, MS: m/z 958.82 (M^+, 100 %).

3.1.5.2 $Na_3[PW_{12}O_{40}]$

$Na_3[PW_{12}O_{40}]$ was prepared in accordance to the literature.[8] Phosphotungstic acid (5.0 g, 1.74 mmol) was dissolved in water (20 mL). NaCl (0.10 g, 5.21 mmol) was dissolved in the phosphotungstic solution, under stirring for 1 hr. The solvent was evaporated off at 373 K producing a white crystalline powder (4.97 g, 98.6 %). ^{31}P-NMR (400 MHz, D_2O): δ -15.41, IR: 1080 (s), 980 (s), 890 (s) cm^{-1}, UV (H_2O): 256 nm, MS: m/z 958.82 (M^+, 100 %).

3.1.5.3 $[(n\text{-}C_4H_9)_3][PW_{12}O_{40}]$

$[(n\text{-}C_4H_9)_3][PW_{12}O_{40}]$ was prepared in accordance to the literature.[8] Phosphotungstic acid hydrate (5.0 g, 1.74 mmol) was dissolved in water (20 mL). $(n\text{-}C_4H_9)_4NBr$ (TBABr) (1.67 g, 5.21 mmol) was dissolved in the phosphotungstic solution, under stirring for 1 h. The precipitate was collected, washed, and then dried with gentle heating producing a white crystalline powder (5.74 g, 85.9 %).

^{31}P-NMR (400 MHz, CD_3CN): δ -15.35, IR: 1080 (s), 980 (s), 890 (s) cm^{-1}, UV (CH_3CN): 265 nm, MS: m/z 958.82 (M$^+$, 100 %).

3.1.5.4 $Li_7[PW_{11}O_{39}]$

$Li_7[PW_{11}O_{39}]$ was prepared in accordance to the literature.[9] Phosphotungstic acid (5.0 g, 1.74 mmol) was dissolved in water (20 mL). Phosphotungstic acid (5.0 g, 1.74 mmol) was dissolved in water (20 mL). LiCl (0.22 g, 5.21 mmol) was dissolved in the phosphotungstic solution. Aqueous solution of 1 M lithium hydrogencarbonate (6.79 g, 100 mL) was added drop wise until pH of the suspension reached pH 4.80. The crystalline salt was isolated by solvent evaporation and recrystallised from hot water. The crystals were dried with gentle heating producing a white crystalline powder (4.13 g, 87.1 %). ^{31}P-NMR (400 MHz, D_2O): δ -11.65, IR: 1080 (s), 980 (s), 890 (s) cm^{-1}, UV (H_2O): 247 nm, MS: m/z 958.82 (M$^+$, 100 %).

3.1.5.5 $Na_7[PW_{11}O_{39}]$

$Na_7[PW_{11}O_{39}]$ was prepared in accordance to the literature.[9] Phosphotungstic acid (5.0 g, 1.74 mmol) was dissolved in water (20 mL). NaCl (0.10 g, 5.21 mmol) was dissolved in the phosphotungstic solution. Aqueous solution of 1 M sodium hydrogencarbonate (8.40 g, 100 mL) was added drop wise until pH of the suspension reached pH 4.80. The crystalline salt was isolated by solvent evaporation and recrystallised from hot water. The crystals were dried with gentle heating producing a white crystalline powder (4.02 g, 81.4 %). δ -11.13, IR: 1080, 980, 890 cm^{-1}, UV (H_2O): 247 nm. ^{31}P-NMR (400 MHz, D_2O): δ -10.82, IR:1080 (s), 980 (s), 890 (s) cm^{-1}, UV (H_2O): 247 nm, MS: m/z 958.82 (M$^+$, 100 %).

3.1.5.6 $K_7[PW_{11}O_{39}]$

$K_7[PW_{11}O_{39}]$ was prepared in accordance to the literature.[9] Phosphotungstic acid (25.0 g, 8.68 mmol) was dissolved in distilled water (100 mL). KCl (1.94 g, 26.04 mmol) was then added to the phosphotungstic solution. Aqueous solution of 1 M potassium hydrogencarbonate (10.01 g, 100 mL) was added drop wise until pH of the suspension reached pH 4.80. The filtrate was concentrated and allow to cool to room temperature. The white crystalline salt was recrystallised from hot water. The crystals were dried with gentle heating producing a white crystalline powder (24.70 g, 94.6 %). ^{31}P-NMR (400 MHz, D_2O): δ -11.13, IR:1080 (s), 980 (s), 890 (s) cm^{-1}, UV (H_2O): 247 nm, MS: m/z 958.82 (M$^+$, 100 %).

3.1.5.7 Δ-$Na_8H[PW_9O_{34}]$

Δ-$Na_8H[PW_9O_{34}]$ was prepared in accordance to the literature.[10] To sodium tungstate dihydrate (12.0 g), dissolved in distilled water (14.8 mL) with stirring, was added to 85 % ortho-phosphoric acid (0.25 mL) followed by glacial acetic acid (2.2 ml). Gentle stirring produced a white precipitate which was isolated by filtration and washed for drying. The isomer was abteined depending on drying temperature.[10] Drying between $20 < T < 80$ °C obtained $Na_8H[A\text{-}PW_9O_{34}]$, whilst at $T > 80$ °C, $Na_8H[B\text{-}PW_9O_{34}]$ isomer appeared in the product. Complete isomerism was conducted at $T = 140$ °C for several hours. $Na_8H[A\text{-}PW_9O_{34}]$: ^{31}P-NMR (400 MHz, D_2O): δ -7.76, IR: 1056 (s), 937 (s), 884 (s) cm^{-1}. $Na_8H[B\text{-}PW_9O_{34}]$: ^{31}P-NMR (400 MHz, D_2O): δ -3.76, IR: 1063 (s), 887 (s) cm^{-1}.

3.1.5.8 $Li_5[PW_{11}Mn(H_2O)O_{39}]$

The synthesis was adapted from published methods.[11,12]$Li_7[PW_{11}O_{39}]$ (3.00 g, 1.10 mmol) was dissolved in distilled water (20 mL). $MnCl_2{\cdot}4H_2O$ (0.22 g, 1.10 mmol) was added to solution under stirring overnight. The resulting solution was filtered then concentrated under gentle heating to obtain an orange powder (2.80 g, 91.2 % %). IR: 1076 (s), 1050 (s), 951 (s), 881 (s) cm^{-1}, UV (H_2O): 253 nm.

3.1.5.9 $Li_5[PW_{11}Fe(H_2O)O_{39}]$

The synthesis was adapted from published methods.[11,12]$Li_7[PW_{11}O_{39}]$ (3.00 g, 1.10 mmol) was dissolved in distilled water (20 mL). $FeCl_2{\cdot}4H_2O$ (0.22 g, 1.10 mmol) was added to solution under stirring overnight. The resulting solution was filtered then concentrated under gentle heating to obtain a black powder (2.67 g, 88.1 %). IR: 1058 (s), 957 (s), 882 (s) cm^{-1}, UV (H_2O): 253 nm,

3.1.5.10 $Li_5[PW_{11}Co(H_2O)O_{39}]$

The synthesis was adapted from published methods.[11,12] $Li_7[PW_{11}O_{39}]$ (3.00 g, 1.10 mmol) was dissolved in distilled water (20 mL). $Co(NO_3)_2{\cdot}6H_2O$ (0.32 g, 1.10 mmol) was added to solution under stirring overnight. The resulting solution was filtered then concentrated under gentle heating to obtain a green powder (2.73 g, 89.0 %). ^{31}P-NMR (400 MHz, D_2O): δ -7.76, IR: 1056 (s), 937 (s), 884 (s) cm^{-1}. ^{31}P-NMR (400 MHz, D_2O): δ 462, IR: 1060 (s), 957 (s), 876 (s) cm^{-1}, UV (H_2O): 253 nm, MS: m/z 959 (M$^+$, 100 %).

3.1.5.11 $Na_5[PW_{11}Mn(H_2O)O_{39}]$

The synthesis was adapted from published methods.[11,12] $Na_7[PW_{11}O_{39}]$ (3.00 g, 1.06 mmol) was dissolved in distilled water (20 mL). $MnCl_2{\cdot}4H_2O$ (0.21, 1.06 mmol) was added to solution under stirring overnight. The resulting solution was filtered then concentrated under gentle heating to obtain an orange powder (2.67 g, 88.1 %). IR: 1076 (s), 1050 (s), 951 (s), 881 (s) cm^{-1}, UV (H_2O): 253 nm, MS: m/z 959 (M$^+$, 100 %).

3.1.5.12 $Na_5[PW_{11}Fe(H_2O)O_{39}]$

The synthesis was adapted from published methods.[11,12] $Na_7[PW_{11}O_{39}]$ (3.00 g, 1.06 mmol) was dissolved in distilled water (20 mL). $FeCl_2{\cdot}4H_2O$ (0.21, 1.06 mmol) was added to solution under stirring overnight. The resulting solution was filtered then concentrated under gentle heating to obtain a black powder (2.77 g, 91.4 %). IR: 1058 (s), 957 (s), 882 (s) cm^{-1}, UV (H_2O): 253 nm, MS: m/z 1368 (M$^+$, 100 %).

3.1.5.13 $Na_5[PW_{11}Co(H_2O)O_{39}]$

The synthesis was adapted from published methods.[11,12] $Na_7[PW_{11}O_{39}]$ (3.00 g, 1.06 mmol) was dissolved in distilled water (20 mL). $Co(NO_3)_2{\cdot}6H_2O$ (0.31, 1.06 mmol) was added to solution under stirring overnight. The resulting solution was filtered then concentrated under gentle heating to obtain a green powder (2.58 g, 85.0 %).^{31}P-NMR (400 MHz, D_2O): δ 462, IR: 1055 (s), 953 (s), 886 (s) cm^{-1}, UV (H_2O): 253 nm, MS: m/z 959 (M$^+$, 100 %).

3.1.5.14 $K_5[PW_{11}Mn(H_2O)O_{39}]$

The synthesis was adapted from published methods.[11,12] $K_7[PW_{11}O_{39}]$ (3.39 g, 1.15 mmol) was dissolved in distilled water (20 mL). $MnCl_2{\cdot}4H_2O$ (0.23 g, 1.15 mmol) was added to solution under stirring overnight. The resulting solution was filtered then concentrated under gentle heating to obtain an orange powder (3.27 g, 96.6 %). IR: 1076 (s), 1050 (s), 951 (s), 881 (s) cm^{-1}, UV (H_2O): 253 nm, MS: m/z 958.82 (M$^+$, 100 %).

3.1.5.15 $K_5[PW_{11}Fe(H_2O)O_{39}]$

The synthesis was adapted from published methods.[11,12] $K_7[PW_{11}O_{39}]$ (3.39 g, 1.15 mmol) was dissolved in distilled water (20 mL). $FeCl_2 \cdot 4H_2O$ (0.23 g, 1.15 mmol) was added to solution under stirring overnight. The resulting solution was filtered then concentrated under gentle heating to obtain a black powder (3.31 g, 97.6 %). IR: 1058 (s), 957 (s), 882 (s) cm^{-1}, UV (H_2O): 253 nm, MS: m/z 1368.21 (M^+, 100 %).

3.1.5.16 $K_5[PW_{11}Co(H_2O)O_{39}]$

The synthesis was adapted from published methods.[11,12] $K_7[PW_{11}O_{39}]$ (3.39 g, 1.15 mmol) was dissolved in distilled water (20 mL). $Co(NO_3)_2 \cdot 6H_2O$ (0.34 g, 1.15 mmol) was added to solution under stirring overnight. The resulting solution was filtered then concentrated under gentle heating to obtain a green powder (3.32 g, 97.8 %). ^{31}P-NMR (400 MHz, D_2O): δ 462, IR: 1078 (s), 957 (s), 881 (s) cm^{-1}, UV (H_2O): 253 nm, MS: m/z 958.82 (M^+, 100 %).

3.1.5.17 $K_5[PW_{11}Ni(H_2O)O_{39}]$

The synthesis was adapted from published methods.[11,12] $K_7[PW_{11}O_{39}]$ (3.39 g, 1.15 mmol) was dissolved in distilled water (20 mL). $NiCl_2 \cdot 6H_2O$ (0.27 g, 1.15 mmol) was added to solution under stirring overnight. The resulting solution was filtered then concentrated under gentle heating to obtain a black powder (3.15 g, 93.0 %). δ 462, IR: 1058 (s), 949 (s), 883 (s) cm^{-1}, UV (H_2O): 253 nm, MS: m/z 1369.34 (M^+, 100 %).

3.1.5.18 $K_5[PW_{11}Cu(H_2O)O_{39}]$

The synthesis was adapted from published methods.[11,12] $K_7[PW_{11}O_{39}]$ (3.39 g, 1.15 mmol) was dissolved in distilled water (20 mL). $Cu(NO_3)_2 \cdot 3H_2O$ (0.28 g, 1.15 mmol) was added to solution under stirring overnight. The resulting solution was filtered then concentrated under gentle heating to obtain a green powder (2.99 g, 88.1 %). δ 462, IR: 1099 (s), 1057 (s), 955 (s), 883 (s) cm^{-1}, UV (H_2O): 253 nm, MS: m/z 1371.89 (M^+, 100 %).

3.1.5.19 $K_5[PW_{11}Zn(H_2O)O_{39}]$

The synthesis was adapted from published methods.[11,12] $K_7[PW_{11}O_{39}]$ (3.39 g, 1.15 mmol) was dissolved in distilled water (20 mL). $Zn(NO_3)_2 \cdot 6H_2O$ (0.34 g, 1.15 mmol) was added to solution under stirring overnight. The resulting solution was filtered then concentrated under gentle heating to obtain a green powder (3.25 g, 95.7 %). ^{31}P-NMR (400 MHz, D_2O): -12.19 ppm. δ 462, IR: 1088 (s), 1057 (s), 955 (s), 889 (s) cm^{-1}, UV (H_2O): 253 nm, MS: m/z 1372.77 (M^+, 100 %).

Bibliography

[1] J. E. Toth and F. C. Anson, *J. Electroanal. Chem.*, 1988, **256**, 361–370.

[2] F. A. Couto, A. M. Cavaleiro, J. D. P. de Jesus and J. E. Simão, *Inorganica Chim. Acta*, 1998, **281**, 225–228.

[3] T. McCormac, B. Fabre and G. Bidan, *J. Electroanal. Chem.*, 1997, **425**, 49–54.

[4] D. McKay, Ph.D Thesis, University of Glasgow, 2008, 166–167.

[5] K. McAulay, Ph.D Thesis, University of Glasgow, 2017, 166–168.

[6] R. Kojima and K.-i. Aika, *Appl. Catal. A-Gen.*, 2001, **215**, 149–160.

[7] A. Daisley and J. S. Hargreaves, *J. Energy Chem.*, 2019, **39**, 170–175.

[8] J. Bartis, Y. Kunina, M. Blumenstein and L. C. Francesconi, *Inorg. Chem.*, 1996, **35**, 1497–1501.

[9] N. Haraguchi, Y. Okaue, T. Isobe and Y. Matsuda, *Inorg. Chem.*, 1994, **33**, 1015–1020.

[10] B. Moore and K. Foger, *Inorganica Chim. Acta*, 1991, **181**, 201–205.

[11] C. M. Tourné, G. F. Tourné, S. Malik and T. Weakley, *J. Inorg. Nucl. Chem.*, 1970, **32**, 3875–3890.

[12] F. Zonnevijlle, C. M. Tourne and G. F. Tourne, *Inorg. Chem.*, 1982, **21**, 2751–2757.

Chapter 4

Reducing Systematic Uncertainty in Computed Redox Potentials for Aqueous Transition-Metal-Substituted Polyoxotungstates

The following chapter is based on the publication: "Reducing Systematic Uncertainty in Computed Redox Potentials for Aqueous Transition-Metal-Substituted Polyoxotungstates."; J. A. Thompson, R. González-Cabaleiro, and L. Vilà-Nadal, *Inorg. Chem.*, 2023, **31**, 12260–12271.

4.1 Introduction

Polyoxometalates (POMs) are a diverse group of discrete metal-oxo clusters comprised of addenda and oxide atoms. Their self-assembly mechanism is initiated through the acidification of aqueous molybdate or tungstate oxoanions capable of forming several discrete clusters employing $\{MO_x\}$ as the principal building block. Partial hydrolysis of these clusters can generate a further class known as lacunary clusters, previously discussed in Section 1.2. This subclass of compounds represents the largest and most versatile class of lacunary compounds which has attracted significant interest in fields including but not limited to: (i) water oxidation; (ii) carbon dioxide reduction; (iii) and hydrogen evolution. Their structural and electronic diversity makes these molecules attractive for theoretical modelling to study the underlying properties of POM-based systems.

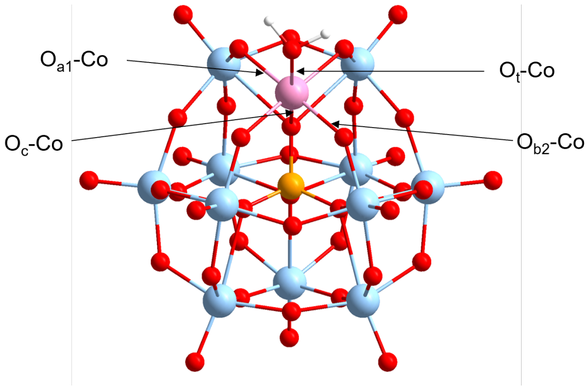

Figure 4.1: Schematic representation for the cobalt(II)-substituted Keggin $[PW_{11}Co(H_2O)O_{39}]^{q-}$ anion. Colours corresponding to W = cyan, O = red, P = orange, and Co = pink.

Early computational work by Poblet and co-workers began by rationalising the relative stability of rotational isomers of the plenary Keggin unit, $[XM_{12}O_{40}]^{q-}$. Their calculations modelled the Keggin as a fully anionic, gas-phase cluster, using employed local-density approximation (LDA) functional with Vosko–Wilk–Nusair parametrization, discussed previously in Section 2.3.4.1.[1] The authors reported the Keggin possess a simple electronic structure, comprising two bands: a fully delocalised oxo-band and an unoccupied d-metal orbital with some antibonding character with respect to the oxide orbitals. The authors reported that the higher energy of the lowest occupied molecular orbital (ca. 0.4 eV) in α-$[SiW_{12}O_{40}]^{4-}$ compared to the β-$[SiW_{12}O_{40}]^{4-}$ attributes to their enhanced stability with respect to reduction.[1] An inverse relation was shown for the reduced clusters: $[PW_{12}O_{40}]^{7-}$ and $[SiMo_{12}O_{40}]^{8-}$ wherein the β-isomer was shown to be 0.4 eV more stable with respect to reduction.[1] Incorporation of implicit solvation models has become routine in modelling of POM-based systems.[2–4]. An early example by Zhang and co-workers suggested implicit solvation did not significantly improve in reproducing experimental geometries. However, the selection of the exchange-correlation functional was crucial for obtaining accurate geometries. The authors reported that the closest description to the experimental geometries were obtained using Perdew–Burke–Ernzerhof (PBE) and Becke 1988 exchange and Perdew 86 (BP86) functionals.[2] However, generalised gradient approximation (GGA) functionals have been shown to overdelocalize electron density in reduced substituted clusters. For example, Lopez and co-workers demonstrated GGA-base approaches often delocalize density across over the belt-tungstens rather than the peripheral heteroatom.[4] On the other hand, employment of more expensive hybrid approaches, in this case, B3LYP (20 % Hartree–Fock (HF) exchange), provided the closest description to to experimental measurements.[4]

Computational models seeking to accurately reproduce redox potentials were initially performed using anionic systems and implicit solvation environments to model solution behaviour. These approximations often produce large uncertainties in absolute reduction potential attributed to the self-interaction error (SIE), as demonstrated in earlier work calculating redox waves for the monosubstituted Keggin, $[XMW_{11}O_{40}]^{q-}$.[3] That said, their model was able to correctly order reduction energies with respect to the experimental results.[3] Later, Rösch and co-workers explicitly located counterions onto the surface of POM to mitigate uncertainty associated with high anionic charge localised at the POM.[5] Their work included a systematic review on the influence of Hartree-Fock (HF) exchange on computed potentials.[5] The authors reported that increasing contributions to HF exchange (0 % PBE, 10 % TPSSh, 20 % B3LYP, 25 % PBE0) systematically increased computed potentials in their model.[5] Their model with the closest agreement with the literature was with the GGA-PBE functional, whilst hybrid approaches produced dispensaries ranging between 0.6–1.0 V.[5] An extension of this work to explicitly treat water obtained from molecular dynamic simulations was shown to improve their redox model.[6] However, its contribution was out-weighted by the selection of the functional.[6]

In this chapter, we will systematically explore the influence of the exchange-correlation functional for Mn(III/II), Fe(III/II), and Co(III/II), and Ru(III/II) redox couples present in $K_5[PW_{11}M(H_2O)^{-}O_{39}]$. We explore the current challenges in attaining precise predictions of redox potentials and provide an insight into the structural and electronic factors controlling it.

4.2 Computational Details & Theory

All computational results were obtained using the ARCHIE–WeSt high-performance computer based at the University of Strathclyde. DFT calculations were performed using the Amsterdam

Modelling Suite (AMS 2020.1) package.[7] In this work, several classes of exchange–correlation (x–c) functionals were employed, which include (i) generalized gradient approximation (GGA); (ii) hybrid; and (iii) range-separated hybrid functionals. GGA functionals considered were as follows: (i) PBE[8]; (ii) Perdew–Wang (PW91)[9]; and (iii) Becke 1988 exchange and Perdew 86 (BP86).[10,11] The hybrid x–c functionals considered were as follows: (i) Becke, 3-parameter, Lee–Yang–Parr (B3LYP*[12], B3LYP[13]); (ii) PBE0[14]; and (iii) Becke's half-and-half (BH&H).[15] Hybrid functionals were selected on their contributions of HF exchange (15 % B3LYP*, 20 % B3LYP, 25 % PBE0, and 50 % BH&H). The ωB97X method was selected as the range-separated hybrid functional.[16] We employed Slater basis sets comprising the following: (i) triple- polarization (TZP); (ii) triple- plus polarization (TZ2P); and (iii) quadruple- plus polarization (QZ4P).[17,18] Relativistic corrections were included by means of the zeroth order regular approximation formalism.[19] The effects of aqueous solvent were approximated by using the conductor-like screening model, as implemented by AMS.[20] For open shell molecules, unrestricted Kohn–Sham (UKS) theory was implemented, while restricted Kohn–Sham (RKS) theory was employed for closed shell systems. All harmonic vibrational frequencies were calculated using PBE coupled with the TZP basis set. The calculation of Gibbs free energies for hybrid-optimized systems were corrected by using the zero-point energies and entropic components obtained from GGA–vibrational frequencies-see Eqn. 6.1:

$$\Delta \mathrm{G} = \Delta \mathrm{H} + \Delta \mathrm{E}_{\mathrm{ZPE}} - \mathrm{T}\Delta \mathrm{S} \tag{4.1}$$

Herein, ΔH equates to the enthalpic component; $\Delta \mathrm{E}_{ZPE}$ is the difference in zero-point energy, and TΔS is the entropic component, under standard conditions, T = 298.15 K, P = 1.0 atm. The entropic and zero-point terms were computed using harmonic vibrational frequencies. Cramer and co-workers reported the free energy change for the standard hydrogen electrode (SHE) half-reaction ($1/2\mathrm{H}_2 \rightarrow \mathrm{H}^+ + \mathrm{e}^-$) equates to 4.24 eV.[21] This was used an external reference for all computed potentials.

To evaluate the discrepancy of the calculated versus crystallographic geometries, we employed mean absolute error (MAE), mean signed error (MSE), and standard deviation (STD) calculated using Eqn. 5.4-5.6:

$$\mathrm{MAE} = \frac{1}{\mathrm{N}} \sum_{\mathrm{i}} |d_{\mathrm{calc,\ j}} - d_{\mathrm{exp,\ j}}| \tag{4.2}$$

$$\mathrm{MSE} = \frac{1}{\mathrm{N}} \sum_{\mathrm{i}} (d_{\mathrm{calc,\ j}} - d_{\mathrm{exp,\ j}}) \tag{4.3}$$

$$\mathrm{STD} = \sqrt{\frac{1}{\mathrm{N}-1} \sum_{\mathrm{i}} (\mathrm{MSE} - (d_{\mathrm{calc,\ j}} - d_{\mathrm{exp,\ j}}))} \tag{4.4}$$

where d_{calc} and d_{exp} are the calculated and experimental bond distances, respectively.

4.3 Results and Discussion

4.3.1 Structural Benchmark

A structural benchmark was performed to assess the ability of the exchange–correlation (x–c) functional and basis set to describe $[\mathrm{PW}_{11}\mathrm{Co}(\mathrm{H}_2\mathrm{O})\mathrm{O}_{39}]^{q-}$. In this study, the accuracy of geometry optimisations for $[\mathrm{PW}_{11}\mathrm{Co}(\mathrm{H2O})\mathrm{O39}]^{q-}$ was assessed using mean absolute error (MAE), mean signed error (MSE), and standard deviation (STD) compared to crystallographic geometry.[22] Four types of oxygen atoms were examined: O_c and O_t corresponding to the heteroatom–oxygen and terminal–oxygen atoms, while O$_{a1}$ and O$_{b2}$ denote bridging (equatorial) oxygen groups bound to the newly incorporated transition-metal-see Figure 4.2.

Optimised geometries in [PW$_{11}$Co(H$_2$O)O$_{39}$]$^{q-}$ reproduced the crystallographic structure responsibly well. The equatorial bond parameters, O$_{a1}$ and O$_{b2}$, were generally reproduced within 0.05 Å. Conversely, the axial bond parameters proved more challenging, wherein some models produced discrepancies exceeding 0.15 Å, see Figure 4.2a. The electronic structure of [PW$_{11}$Co(H$_2$O)O$_{39}$]$^{5-}$ consists of two identifiable bands: (i) an oxo-band delocalised across the oxide atoms; (ii) and a d-orbital band. Co(II)-based orbitals are inserted between the occupied oxo and unoccupied addenda band possessing the electron configuration of $(\mathrm{d}_{xz})^2(\mathrm{d}_{yz})^2(\mathrm{d}_{xy})^1(\mathrm{d}_{z^2})^1(\mathrm{d}_{x^2-y^2})^1$. The energy levels of the anti-bonding orbitals, d^2_z and $\mathrm{d}^2_x{-}^2_y$, are significantly affected by HF exchange (see Figure SI-9.2). Hence, deviation from the actual value will create a more pronounced shift in computed geometries. Figure 4.2b reports uncertainty in geometry optimisations of [PW$_{11}$Co(H2O)O39]$^{q-}$ with respect to the selected model. Generally, DFT models tended to overestimate the size of inner coordination of Co(II). However, as the contribution of HF exchange increased, MSE negatively shifted leading to an underestimation of equilibrium geometries in PBE0 and BH&H systems. Figure 4.2c shows model uncertainty in geometry optimisations with respect to the chosen bond parameter. It is evident, the main source of uncertainty is the heteroatom–oxygen and terminal–oxygen bonds: O$_c$–Co and O$_t$–Co. Conversely, equatorial distances were generally well described and showed little variance across the tested models, reporting a range of 0.059 and 0.085 Å for O$_{a1}$–Co and O$_{b2}$–Co, respectively.

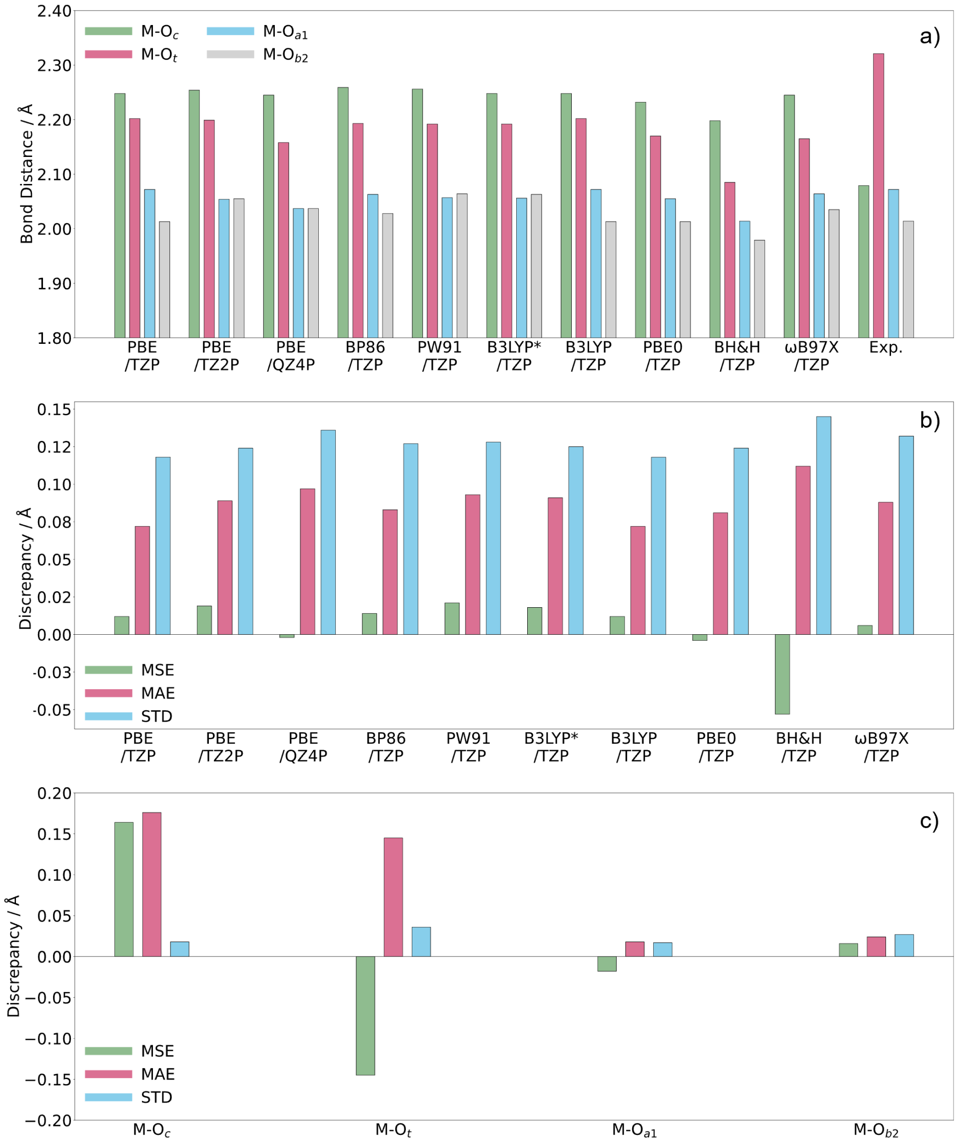

Figure 4.2: (a) Selected structural parameters for the cobalt(II)-substituted Keggin $[PW_{11}Co(H_2O)O_{39}]^{q-}$ anion referenced against the crystallographic structure taken from Cavaleiro and co-workers.[22] (b) MSE, MAE, and STD calculated for all applied functionals and basis sets. (c) MSE, MAE, and STD calculated for four types of metal–oxygen interactions. All bond distances are reported in Å.

4.3.2 Calculation of Redox Potentials

Cyclic voltammetric experiments have explored the redox behaviour for $[PW_{11}M(H_2O)O_{39}]^{q-}$ M = Mn(III/II)[23], Fe(III/II)[24], Co(III/II)[25,26], and Ru(III/II).[26–28] Figure 9.3 will be used to account for modifications to molecular geometries of $[PW_{11}M(H_2O)O_{39}]^{q-}$; M = Mn(II), Fe(II), Co(II), and Ru(II), under electrochemical processes.

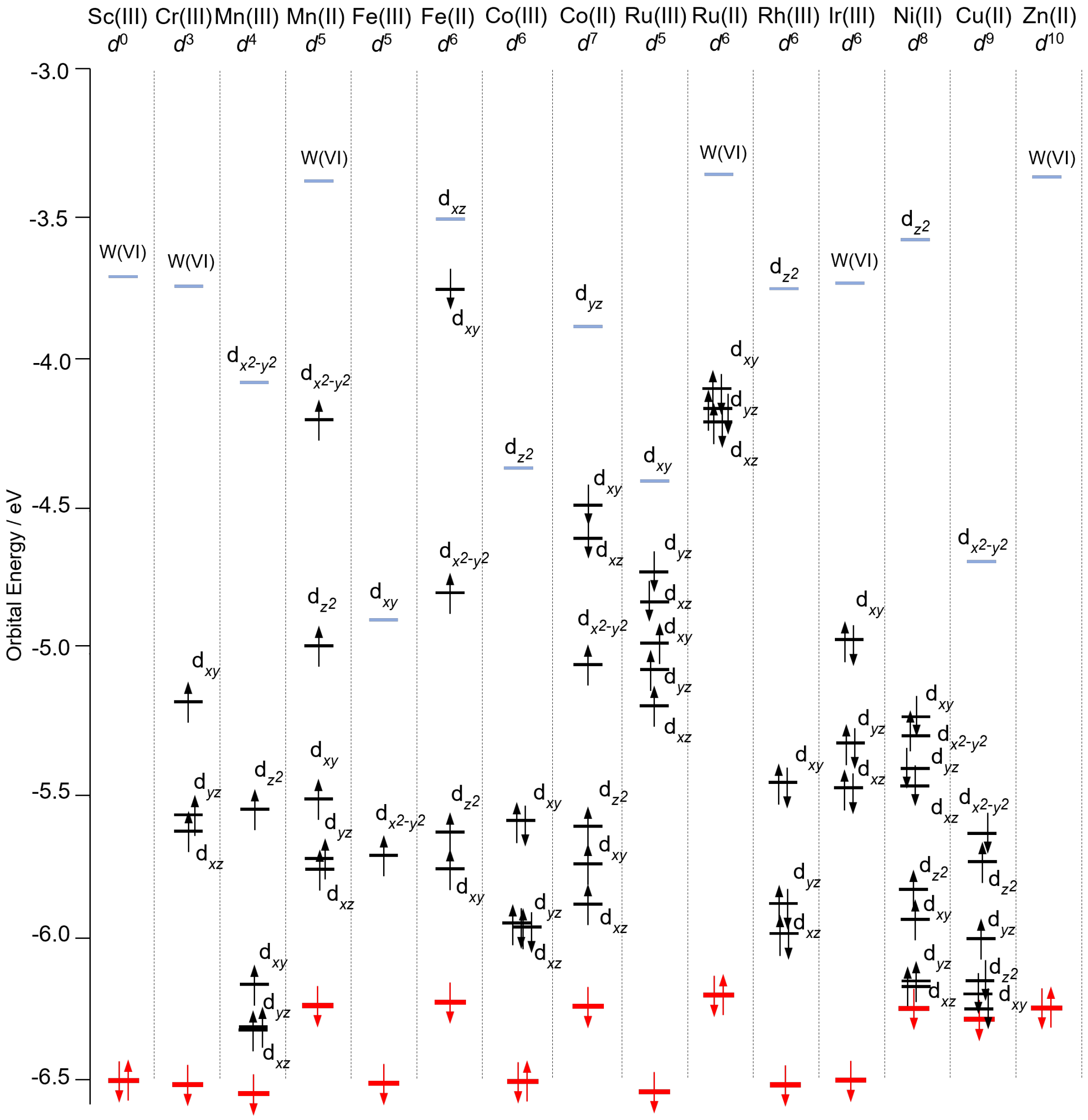

Figure 4.3: Schematic molecular orbital diagram for $[PW_{11}M(H_2O)O_{39}]^{q-}$ systems, optimized using the PBE/TZP level of theory. Herein, closed shell $[PW_{11}M(H_2O)O_{39}]^{q-}$ systems were computed with the RKS theory-distinguished by spin-paired orbitals. Open shell $[PW_{11}M(H_2O)O_{39}]^{q-}$ systems were computed with UKS theory and are distinguished by separate spin-up and spin-down orbitals. Colours correspond to red = O2(p), blue = W, and black = transition-metal. All orbital energies reported in eV.

One-electron reduction of $[PW_{11}Mn(H_2O)O_{39}]^{4-}$ induced expansion of O_{a1}–Mn and O_{b2}–Mn by 0.197 and 0.125 Å, respectively. Reduction of $[PW_{11}Mn(H_2O)O_{39}]^{4-}$ induces occupation of $d_{x^2-y^2}$ possessing strong $\sigma^*(O_{a1}\text{–M})$ and $\sigma^*(O_{b2}\text{–M})$ antibonding character. This interaction is formed by the overlap of oxide $2p_x$ or $2p_y$ orbitals with metallic $d_{x^2-y^2}$ orbitals. Geometry of $[PW_{11}Co(H_2O)O_{39}]^{4-}$ was shown to be sensitive to one-electron reduction leading to a reorganisation of the electronic state from singlet (S=0) to the triplet state (S=1). Conversely, $[PW_{11}M(H_2O)O_{39}]^{4-}$ (M = Fe(III) or Ru(III)) were not significantly affected by one-electron reduction due to he non-bonding character of the d_{xz}, d_{yz}, d_{xy} orbitals. Early computational models employed reduction energies (REs); defined as the energy difference between the one-electron reduced and oxidised forms, have employed charged systems coupled with implicit solvent models to reproduce experimental potentials. This assumption holds for parent Keggin and Wells-Dawson anions where additional or removal of an electron occurs at non-bonding orbitals, hence, the entropic and vibrational contributions to ΔG are negligible.[29] The antibonding character of $\sigma^*(O_c\text{–}M)$, $\sigma^*(O_{a1}\text{–}M)$, and $\sigma^*(O_{b2}\text{–}M)$ molecular orbitals makes computation of reduction energies (REs) unsuitable for modelling $[PW_{11}M(H_2O)O_{39}]^{q-}$; M = Mn(II) and Co(II) anions. Hence, all redox calculations will include entropic and vibrational contributions to account for modifications to molecular geometry under electrochemical processes.

4.3.3 Computation of Redox Potentials - Anionic Model

Redox potentials, $U^0{}_{Red}$ versus SHE, for Mn(III/II), Fe(III/II), Co(III/II), and Ru(III/II) couples present in $[XW_{11}M(H_2O)O_{39}]^{q-}$; X = As(V), Si(IV), Ge(IV), B(III), and Zn(II) are reported in Figure 4.4. The literature potentials for $[PW_{11}M(H_2O)O_{39}]^{q-}$ M = Fe(III/II)/Ru(III/II) were replicated within ca. 0.2 V. The closest agreement with literature potentials was achieved using $[AsW_{11}M(H_2O)O_{39}]^{q-}$ replicating within 0.16 V. Conversely, $[PW_{11}M(H_2O)O_{39}]^{q-}$ produced discrepancies of 0.8 and 1.0 V for M = Mn(III/II) and Co(III/II). Error increased as a function of anionic charge in $[XW_{11}M(H_2O)O_{39}]^{q-}$ which was attributed to increasing effect of the self-interaction error.

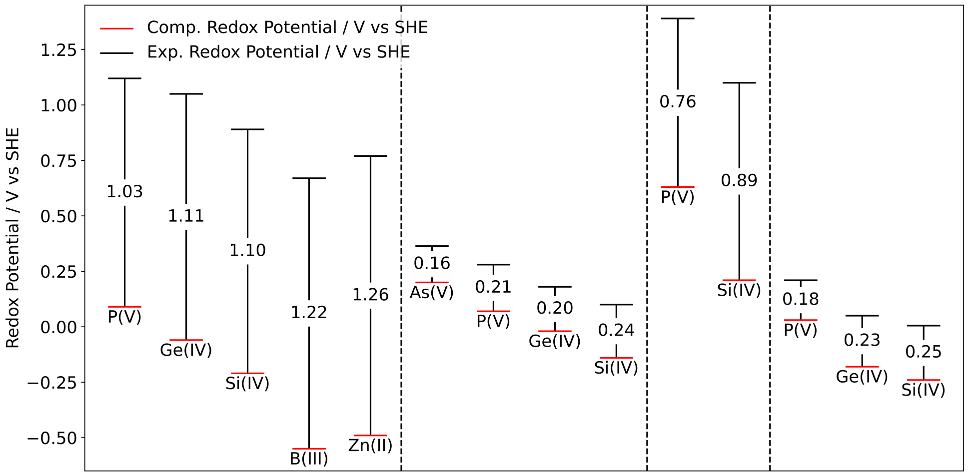

Figure 4.4: Redox potentials, $U^0{}_{Red}$ vs SHE, for Mn(III/II), Fe(III/II), Co(III/II), and Ru(III/II) couple present in $[XW_{11}M(H_2O)O_{39}]^{q-}$; X = As(V), Si(IV), Ge(IV), B(III), and Zn(II). All potentials were calculated using the PBE/TZP level of theory. Experimental potentials were obtained from Mn(III/II)[23], Fe(III/II)[24], Co(III/II)[25,26], and Ru(III/II).[26–28]

DFT calculations have been employed to systematically assess the accuracy of various exchange–correlation functional and basis set on the Mn(III/II), Fe(III/II), Co(III/II), and Ru(III/II) couples in $[PW_{11}M(H_2O)O_{39}]^{q-}$. see Figure 4.5 The effect of the basis set was restricted to the GGA-PBE functional. By increasing the size of the basis set (TZP → TZ2P → QZ4P) positive shifting of 400 mV was systematically induced across all tested redox couples. For example, $U^0{}_{red}$ in $[PW_{11}Co(H_2O)O_{39}]^{q-}$ increased from 0.76 to 1.11 V ($\Delta U^0{}_{Error}$ = 0.35 V) for TZP and QZ4P, respectively.

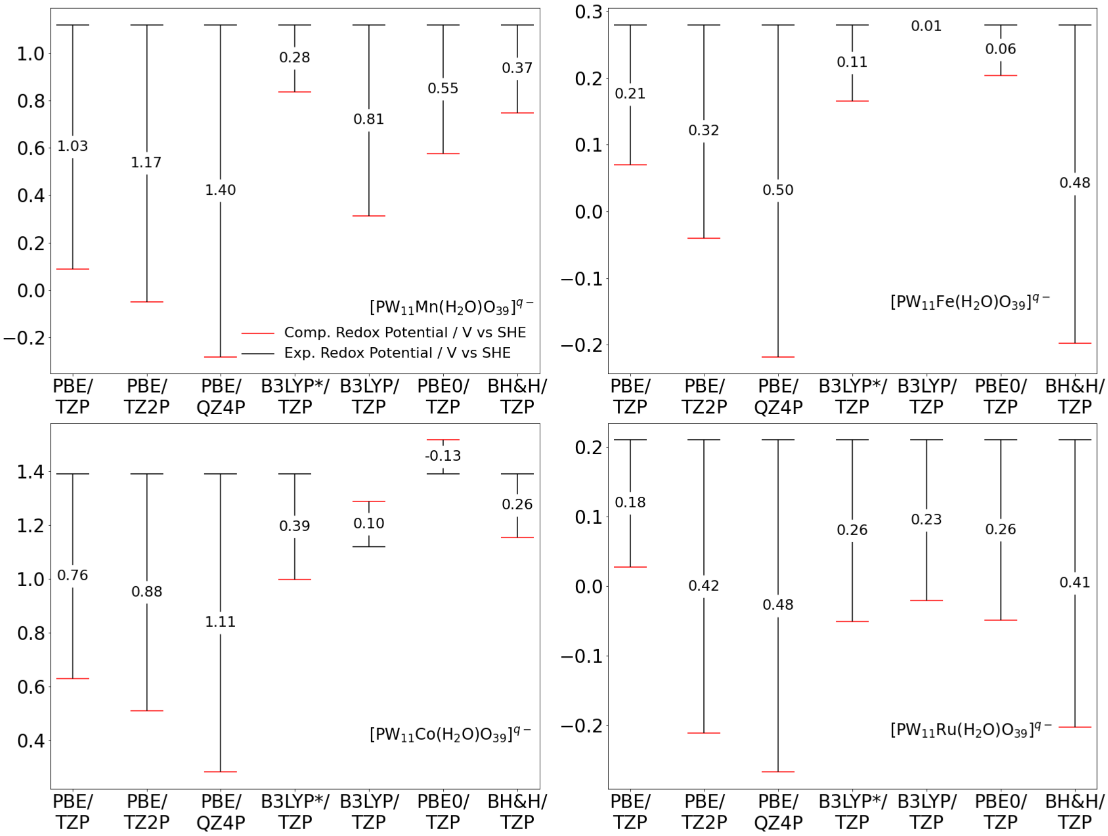

Figure 4.5: Redox potentials, $U^0{}_{Red}$ vs SHE, for Mn(III/II), Fe(III/II), Co(III/II), and Ru(III/II) redox couples in $[PW_{11}M(H_2O)O_{39}]^{q-}$. Experimental potentials were obtained from Mn(III/II)[23], Fe(III/II)[24], Co(III/II)[25,26], and Ru(III/II).[26–28]

We employed several x–c functionals including the hybrid class selected by their contributions to HF exchange (15 % B3LYP*, 20 % B3LYP, 25 % PBE0, and 50 % BH&H). Generally, hybrid functionals outperformed their respective GGA-based approaches. For example, $U^0{}_{Error}$ was minimised in $[PW_{11}Co(H_2O)O_{39}]^{q-}$ by incorporating 20 % HF exchange (B3LYP/TZP). $U^0{}_{Error}$ for $[PW_{11}Ru(H_2O)O_{39}]^{q-}$ was minimised to < 0.2 V using PBE/TZP (0 % HF exchange). The optimal x–c functional was not consistent across all the redox couples. This was evidenced for Fe(III/II), Co(III/II), and Ru(III/II) couples which were optimally reproduced using 20 % HF exchange producing $U^0{}_{Error}$ of 0.01, 0.10, and 0.23 V, whilst Mn(III/II) using 15 % HF exchange.

Thus far, $U^0{}_{Red}$ for $[PW_{11}M(H_2O)O_{39}]^{q-}$ has assumed a fully anionic system, without neutralizing their charge. However, chemical systems supporting large charges will likely exacerbate uncertainties attributed to the self-interaction errors. Previous work by Kremleva and co-workers reported that charge neutralisation using explicitly located alkali-metal counterions significantly reduced error in tri-Mn-substituted Keggin.[6]

4.3.4 Computation of Redox Potentials - Neutral Model

The metal-oxide framework of the POM contains several 4-fold (pocket A–F) and 3-fold pockets which are capable of electrostatically interacting with the counterion -see Figure 4.6. Herein, the integer value, such as in 4-fold pockets, represents the number of oxygen atoms that can interact with the counterion. In our calculations, we have assumed that counterion-oxygen interactions will preferentially occur at 4-fold pockets due to improved Coulomb interactions compared to 3-fold pockets.

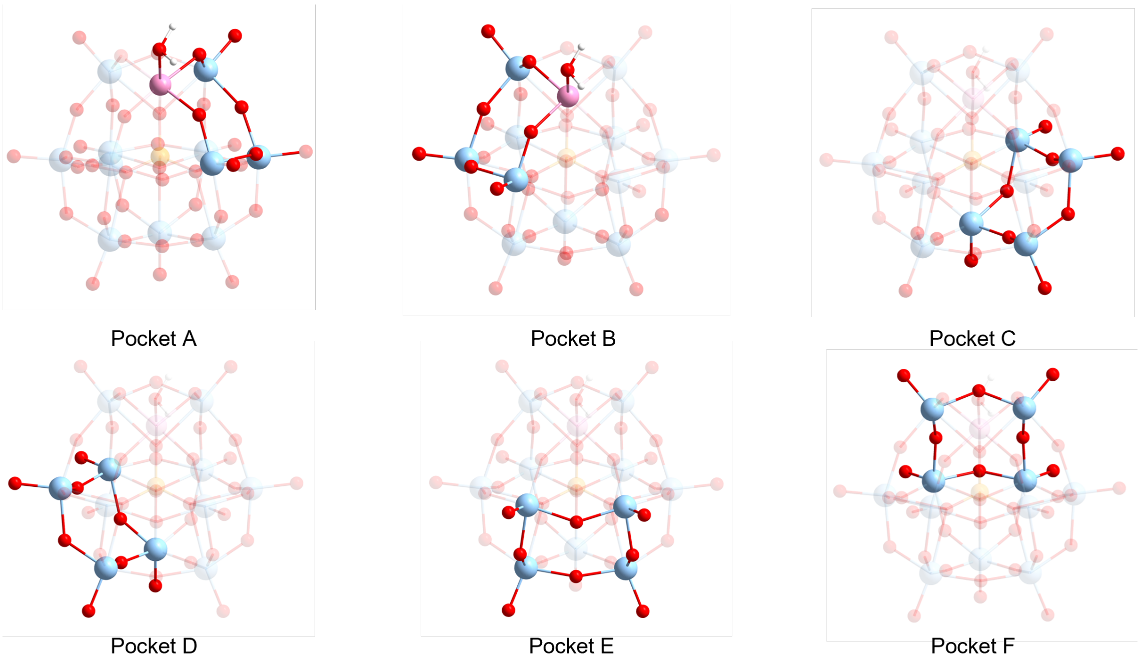
Pocket A Pocket B Pocket C

Pocket D Pocket E Pocket F

Figure 4.6: Schematic representations of 4-fold pockets (A–F) on the surface of $[PW_{11}Co(H_2O)O_{39}]^{5-}$ anions.

In this work, cation arrangements were identified based on their unoccupied pocket, for example, isomer-A features an absent cation–oxygen interaction at pocket A -see Figure 4.6 In solution, these isomers will routinely interchange. In order to establish the most probable conformation adopted in our system, we have determined the relative stability for all isomers -see Table 9.2. Relative stability was determined by comparing the electronic energy, ΔE_{Rel}, where the differences between isomers A-F were negligible, amounting to 1.11 kcal mol^{-1}. Cation arrangements at $[PW_{11}Co(H_2O)O_{39}]^{5-}$ demonstrated greater variance between isomers with ΔE_{Rel} amounting to 3.04 kcal mol^{-1}. The most stable isomer was A,D closely followed by A,C and A,F yielding a range of > 0.4 kcal mol^{-1}. Given the small electronic energy difference, it is reasonable to assume these will interchange in solution. However, to reduce computational cost, only A and A,D will be used for our redox calculations.

Table 4.1: Relative stability of cation arrangements on the surface of the Keggin $K_x[PW_{11}Co(H_2O)O_{39}]^{q-}$ (x = 4 or 5) salts.

Pocket	E_{Rel}
A	1.105
B	0.941
C	0.373
D	0.000
E	0.323
F	0.001
A,B	1.386
A,C	0.134
A,D	0.000
A,E	0.837
A,F	0.398
B,C	2.111
B,D	2.377
B,E	3.042
B,F	2.550
C,D	1.075
C,E	1.639
C,F	1.211
D,E	1.305
D, F	1.739
E,F	1.650

*All energies are reported in kcal mol^{-1}.

Calculated potentials, $U^0{}_{Red}$ versus SHE, for Mn(III/II), Fe(III/II), Co(III/II), and Ru(III/II) couples present in $K_x[XW_{11}M(H_2O)O_{39}]^{q-}$; X = As(V), Si(IV), Ge(IV), B(III), and Zn(II) are reported in Figure 4.7. To allow for comparison with the anionic model, shown in Figure 4.4, all potentials in Figure 4.7 were performed using PBE/TZP level of theory. Explicitly locating counterions positively shifted calculated potentials $K_x[XW_{11}M(H_2O)O_{39}]^{q-}$ by $>$ 500 mV. This is likely due to the electron-withdrawing effects of the counterions, which delocalize the excess negative charge within the system. The systemtic shift in potentials proved beneficial where M = Mn(III/II)/Co(III/II) but were to the detriment for M = Fe(III/II)/Ru(III/II) due to over-stabilisation of the ion-pairs, discussed later. Herein, $U^0{}_{Error}$ rarely exceed 0.50 V for $K_x[XW_{11}M(H_2O)O_{39}]^{q-}$ M = Mn(III/II)/Co(III/II), but exceeded 0.75 V for each test in the anionic model. Conversely, $U^0{}_{Error}$ rarely exceed 0.225 V for the anionic model but $U^0{}_{Error}$ exceeded 0.35 V in each test in the charge neutral model.

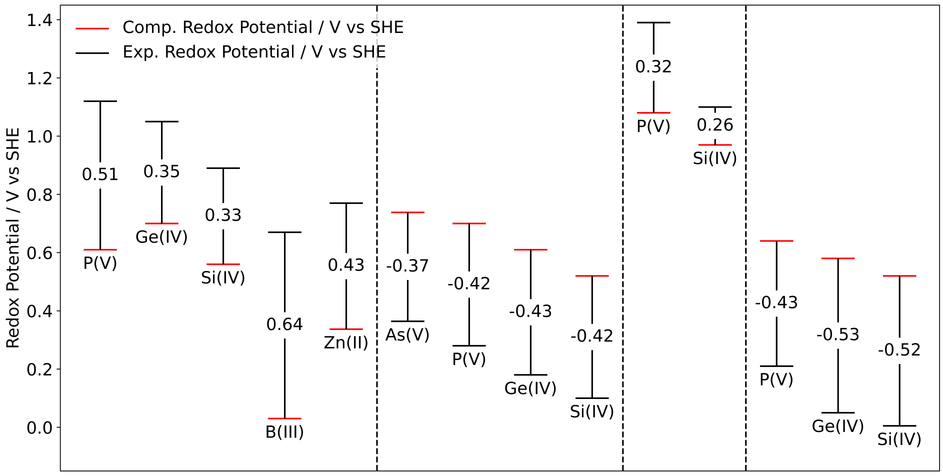

Figure 4.7: Calculated potentials, $U^0{}_{Red}$ vs SHE, for Mn(III/II), Fe(III/II), Co(III/II), and Ru(III/II) couple present in $K_x[XW_{11}M(H_2O)O_{39}]^{q-}$; X = P(V), Si(IV), Ge(IV), B(III), and Zn(II). All calculations were performed with the A and A,D cation arrangements. All potentials were calculated using the PBE/TZP level of theory. Experimental potentials were obtained from Mn(III/II) [23], Fe(III/II) [24], Co(III/II) [25,26], and Ru(III/II). [26–28]

Thus far, all models have been restricted to the lowest energy conformation: A and A,D isomers-see Table 9.2. Figure 4.8 explores the influence of cation rearrangements on computed potentials for $K_x[PW_{11}Co(H_2O)O_{39}]^{q-}$. The sensitivity of the model was determined at 0.18 V wherein the energetically favoured A + A,D couples understated literature potentials by 0.31 V, whilst D + B,E and F + B,E couples registered $U^0{}_{Error}$ of 0.13 V. This work highlights the significance of establishing cation arrangements at the POM to obtain consistent output from the model.

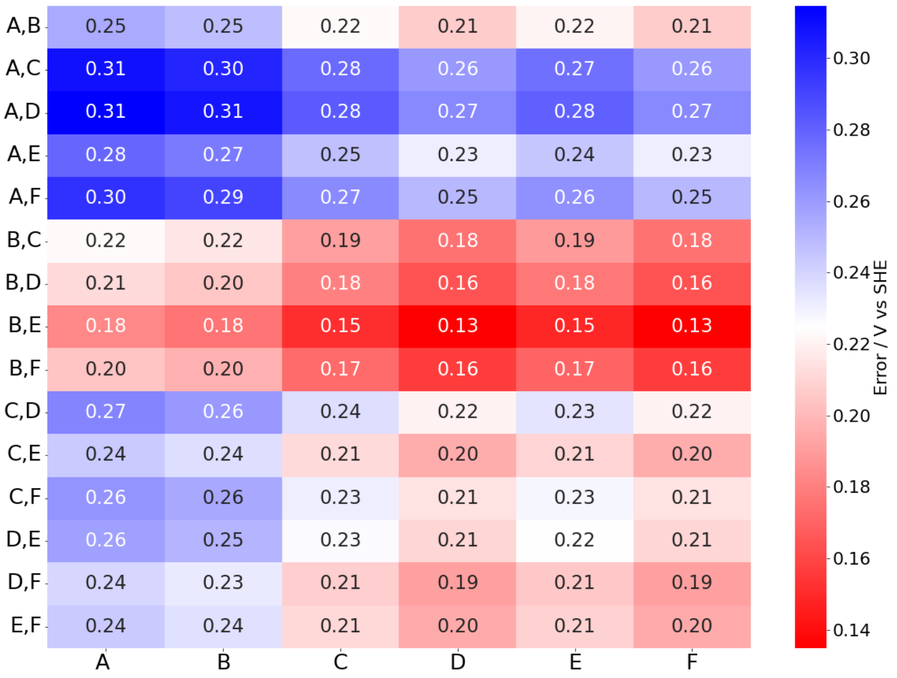

	A	B	C	D	E	F
A,B	0.25	0.25	0.22	0.21	0.22	0.21
A,C	0.31	0.30	0.28	0.26	0.27	0.26
A,D	0.31	0.31	0.28	0.27	0.28	0.27
A,E	0.28	0.27	0.25	0.23	0.24	0.23
A,F	0.30	0.29	0.27	0.25	0.26	0.25
B,C	0.22	0.22	0.19	0.18	0.19	0.18
B,D	0.21	0.20	0.18	0.16	0.18	0.16
B,E	0.18	0.18	0.15	0.13	0.15	0.13
B,F	0.20	0.20	0.17	0.16	0.17	0.16
C,D	0.27	0.26	0.24	0.22	0.23	0.22
C,E	0.24	0.24	0.21	0.20	0.21	0.20
C,F	0.26	0.26	0.23	0.21	0.23	0.21
D,E	0.26	0.25	0.23	0.21	0.22	0.21
D,F	0.24	0.23	0.21	0.19	0.21	0.19
E,F	0.24	0.24	0.21	0.20	0.21	0.20

Figure 4.8: Redox potentials for all cation rearrangements for $K_x[PW_{11}Co(H_2O)O_{39}]^{q-}$; x = 4 or 5, obtained using the PBE/TZP methodology. Gibbs free energies for all cation arrangements were computed using the zero-point energies and entropic components obtained from GGA–vibrational frequencies for A and A,D isomers. Experimental potentials were obtained from Mn(III/II)[23], Fe(III/II)[24], Co(III/II)[25,26], and Ru(III/II).[26–28]

We have investigated the influence of HF-exchange using several exchange-correlation functionals (15 % B3LYP*, 20 % B3LYP, 25 % PBE0, and 50 % BH&H) to compare with Figure 4.5 Analogous to the anionic model, hybrid methods generally outperformed their respective GGA-based approaches, see 4.9. However, optimal x–c functional was not consistent, analogous to findings of the anionic model. For example, $U^0{}_{Error}$ was minimised in $K_x[PW_{11}Co(H_2O)O_{39}]^{q-}$ by incorporating 15 % HF exchange (B3LYP*/TZP), whilst $U^0{}_{Error}$ for $K_x[PW_{11}Ru(H_2O)O_{39}]^{q-}$ was minimised to < -0.2 V using PBE/QZ4P (0 % HF exchange). Across all redox couples, $U^0{}_{Red}$ was positively shifted as HF exchange was increased which was attributed to the over-stabilization of the ion-pairs.

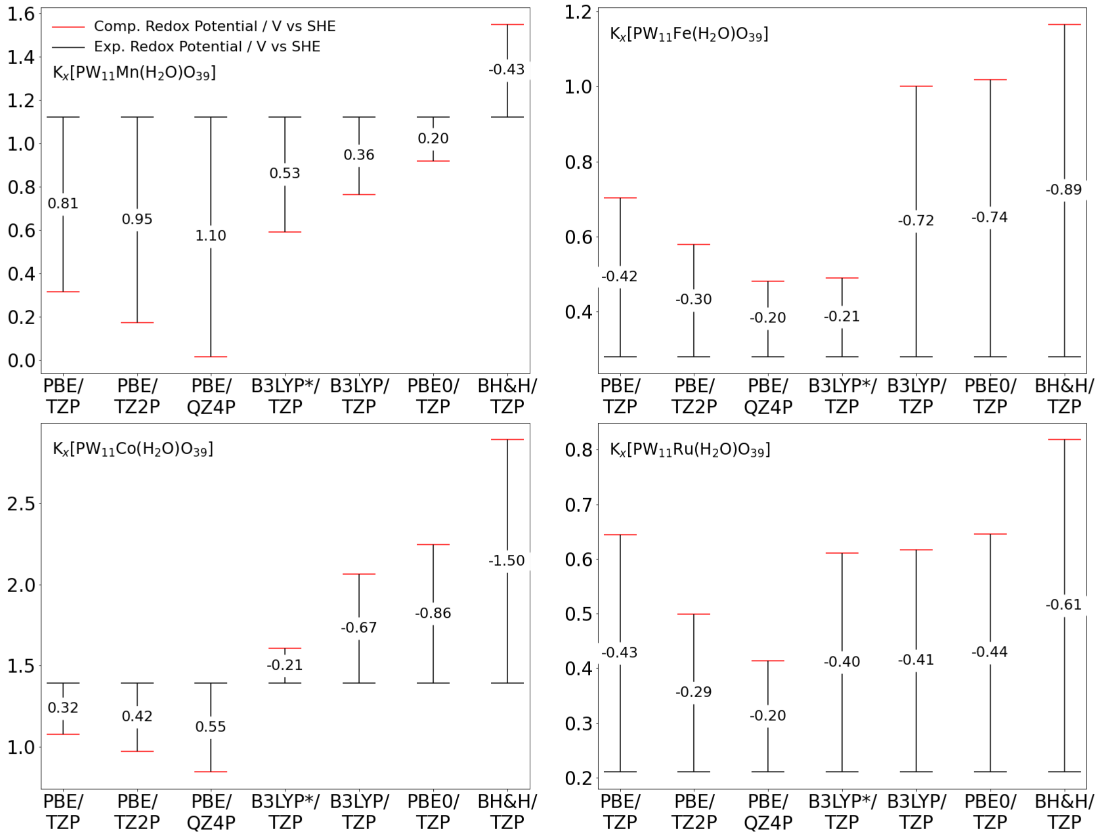

Figure 4.9: Redox potentials, $U^0{}_{Red}$ vs SHE, for Mn(III/II), Fe(III/II), Co(III/II), and Ru(III/II) redox couples in $K_x[PW_{11}M(H_2O)O_{39}]^{q-}$. All calculations were performed with the A and A,D cation arrangements. Experimental potentials were obtained from Mn(III/II)[23], Fe(III/II)[24], Co(III/II)[25,26], and Ru(III/II).[26–28]

By increasing the size of the basis set (TZP → TZ2P → QZ4P), calculated potentials were positively shifting of ca. 200-300 mV was systematically induced. For example, $U^0{}_{Error}$ in $K_x[PW_{11}Co(H_2O)O_{39}]^{q-}$ increased from 0.32 to 0.55 V for TZP and QZ4P, respectively. This positive shifting was beneficial to $K_x[PW_{11}M(H_2O)O_{39}]^{q-}$ M=Fe(III/II) or Ru(III/II) whose potentials were negatively shifted with respect to the literature.

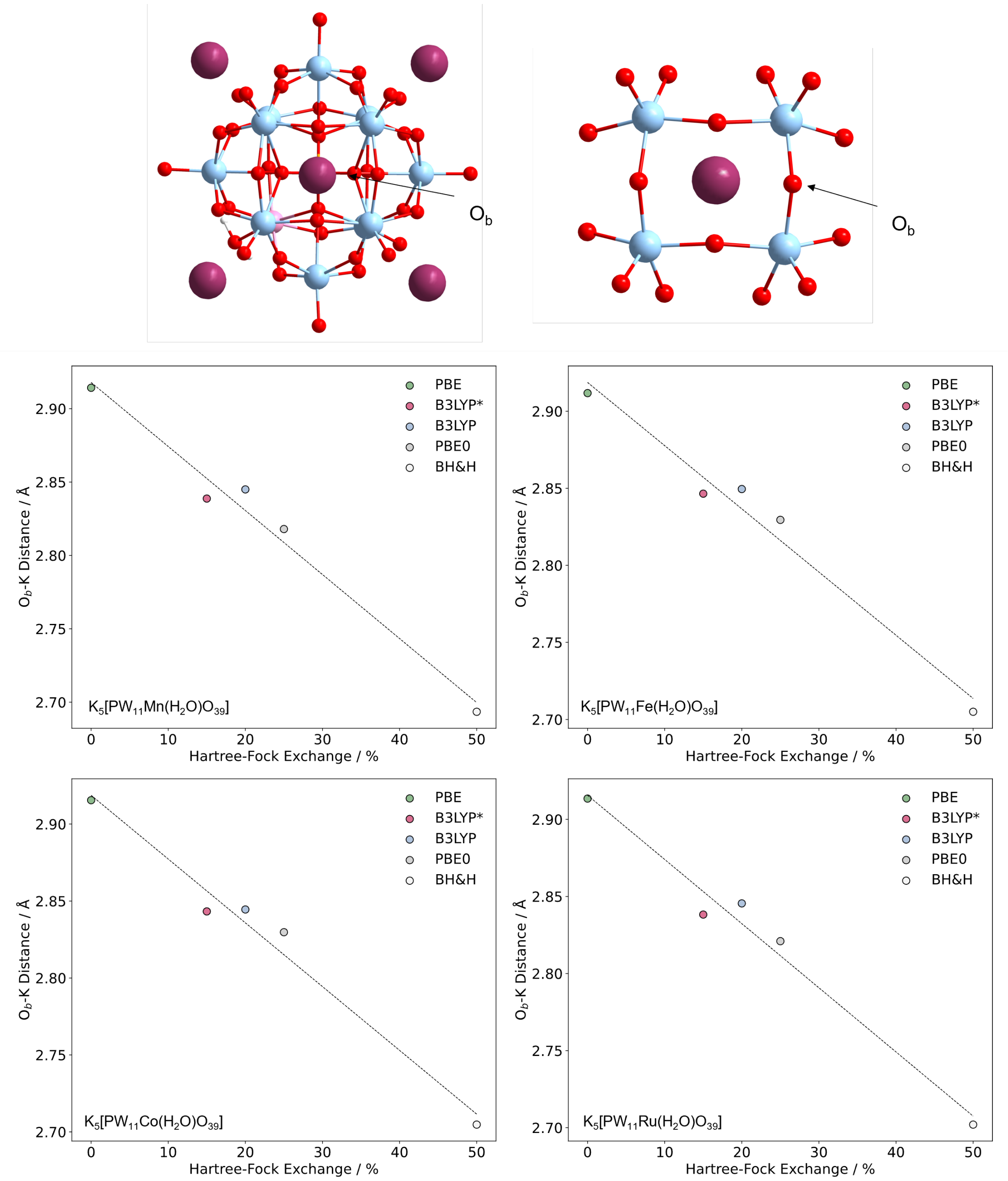

Figure 4.10: Average counterion–bridging oxygen distance (O_b–K) in $K_5[PW_{11}M(H_2O)O_{39}]$, where M = Mn(II), Fe(II), Co(II), and Ru(II) plotted as a function of HF exchange. All calculations were performed with the A and A,D cation arrangements.

Figure 4.9 shows that increasing contributions of HF exchange induced positive shifting in computed potentials. To rationalise this behaviour, average counterion–bridging oxygen (between pocket D) were against HF exchange, see Figure 4.10. Increasing the contribution of HF exchange brings the ion-pairs in closer proximity, over-stabilising the system inducing positive shifts in computed potential. To highlight this issue, $K_5[PW_{11}Co(H_2O)O_{39}]$ varied by 1.29 V by shifting from PBE to BH&H, reducing O_b–K distances by 0.2 Å. The average O_t–K and O_b–K distances for hydrated $[PW_{12}O_{40}][K(H_2O)_{16}]_3$ complexes reported by Kaledin and co-workers was 5.1 and 5.7 Å, respectively.[30] By contrast, our model generated O_t–K and O_b–K distances of ca. 4.1 and 2.8 Å for

$K_5[PW_{11}Co(H_2O)O_{39}]$. The current challenge in attaining accurate potentials is effectively controlling the proximity of the ion-pairing. Future work should focus on testing further O_t–K and O_b–K distances to obtain an optimal distance for precise redox modelling.

4.4 Conclusions

The objective of this chapter has been to highlight the challenges in computational redox modelling and provide a detailed analysis of the geometric and electronic factors controlling it. Throughout this chapter, DFT calculations have been performed to systematically study the influence of the basis set and HF-exchange using several exchange–correlation functionals (0 % PBE, 15 % B3LYP*, 20 % B3LYP, 25 % PBE0, and 50 % BH&H) in reproducing literature redox potentials for $[XW_{11}M(H_2O)O_{39}]^{q-}$ anions and their corresponding potassium salts.

Our work focused on explicitly locating K^+ counterions to reduce uncertainty attributed to the self-interaction error, which are exacerbated by chemical systems supporting large charges. Our work found that rendering the system charge neutral systematically induced positive shifting of computed potentials of ca. 500 mV. This proved beneficial where M = Mn(III/II)/Co(III/II) but were to the detriment for M = Fe(III/II)/Ru(III/II) due to excessive stabilisation of the ion-pairs. Unfortunately, there was no optimal x–c functional across the tested redox couples. However, methods exceeding 25 % HF exchange are generally recommended for $K_5[PW_{11}M(H_2O)O_{39}]$ systems due to their tendency to over exaggerate the proximity of the ion-pairing. Previous literature has highlighted a potential limitation of the model wherein O_t–K and O_b–K distances for hydrated $[PW_{12}O_{40}][K(H_2O)_{16}]_3$ complexes were calculated at 5.1 Å and 5.7 Å, respectively. By contrast, our charge-neutral model of $K_5[PW_{11}Co(H_2O)O_{39}]$ yielded O_t–K and O_b–K distances of approximately 4.1 Å and 2.8 Å, respectively. This highlights the current challenge in attaining accurate potentials is effectively controlling the proximity of the ion-pairing. Systematically exploring the effect of the optimal POM-cation distance will enhance our understanding of POM-cation pairing and enable agreement between theoretical and experimental results.

Bibliography

[1] X. López, J. M. Maestre, C. Bo and J.-M. Poblet, *J. Am. Chem. Soc.*, 2001, **123**, 9571–9576.

[2] F.-Q. Zhang, H.-S. Wu, X.-F. Qin, Y.-W. Li and H. Jiao, *J. Mol. Struct.*, 2005, **755**, 113–117.

[3] P. A. Aparicio, J. M. Poblet and X. López, *Eur. J. Inorg. Chem.*, 2013, **2013**, 1910–1916.

[4] P. A. Aparicio, X. Lopez and J. M. Poblet, *J. Mol. Eng. Mater.*, 2014, **02**, 1440004.

[5] A. Kremleva, P. A. Aparicio, A. Genest and N. Rösch, *Electrochim. Acta*, 2017, **231**, 659–669.

[6] A. Kremleva and N. Rösch, *J. Phys. Chem. C*, 2018, **122**, 18545–18553.

[7] G. te Velde, F. M. Bickelhaupt, E. J. Baerends, C. F. Guerra, S. J. A. van Gisbergen, J. G. Snijders and T. Ziegler, *J. Comput. Chem.*, 2001, **22**, 931–967.

[8] J. P. Perdew, K. Burke and M. Ernzerhof, *Phys. Rev. Lett.*, 1996, **77**, 3865–3868.

[9] Y. Wang, J. P. Perdew and K. Burke, *Derivation of a Generalized Gradient Approximation: The PW91 Density Functional*, Plenum Press, New York, 1998.

[10] A. D. Becke, *Phys. Rev. A*, 1988, **38**, 3098–3100.

[11] J. P. Perdew, *Phys. Rev. B*, 1986, **33**, 8822–8824.

[12] M. Reiher, O. Salomon and B. A. Hess, *Theor. Chem. Acc.*, 2001, **107**, 48–55.

[13] C. Lee, W. Yang and R. G. Parr, *Phys. Rev. B*, 1988, **37**, 785–789.

[14] *J. Chem. Phys.*, 1999, **110**, 5029–5036.

[15] A. D. Becke, *J. Chem. Phys.*, 1993, **98**, 1372–1377.

[16] J.-D. Chai and M. Head-Gordon, *J. Chem. Phys.*, 2008, **128**, year.

[17] R. Sure, J. G. Brandenburg and S. Grimme, *ChemistryOpen*, 2016, **5**, 94–109.

[18] E. V. Lenthe and E. J. Baerends, *J. Comput. Chem.*, 2003, **24**, 1142–1156.

[19] E. Van Lenthe, A. Ehlers and E.-J. Baerends, *J. Chem. Phys.*, 1999, **110**, 8943–8953.

[20] C. C. Pye and T. Ziegler, *Theor. Chem. Accounts Theor. Comput. Model.*, 1999, **101**, 396–408.

[21] D. G. Truhlar, C. J. Cramer, A. Lewis and J. A. Bumpus, *J. Chem. Educ.*, 2004, **81**, 596.

[22] F. M. Santos, P. Brandão, V. Félix, H. I. Nogueira and A. M. Cavaleiro, *Polyhedron*, 2015, **101**, 109–117.

[23] C. M. Tourné, G. F. Tourné, S. Malik and T. Weakley.

[24] J. E. Toth and F. C. Anson, *J. Electroanal. Chem.*, 1988, **256**, 361–370.

[25] J. Gamelas, A. Gaspar, D. Evtuguin and C. P. Neto, *Appl. Catal.*, 2005, **295**, 134–141.

[26] C. Rong and M. T. Pope, *J. Am. Chem. Soc.*, 1992, **114**, 2932–2938.

[27] M. Sadakane, D. Tsukuma, M. H. Dickman, B. Bassil, U. Kortz, M. Higashijima and W. Ueda, *Dalton Trans.*, 2006, 4271.

[28] S. Ogo, N. Shimizu, T. Ozeki, Y. Kobayashi, Y. Ide, T. Sano and M. Sadakane, *Dalton Trans.*, 2013, **42**, 2540–2545.

[29] C. Busche, L. Vilà-Nadal, J. Yan, H. N. Miras, D.-L. Long, V. P. Georgiev, A. Asenov, R. H. Pedersen, N. Gadegaard, M. M. Mirza, D. J. Paul, J. M. Poblet and L. Cronin, *Nature*, 2014, **515**, 545–549.

[30] A. L. Kaledin, Q. Yin, C. L. Hill, T. Lian and D. G. Musaev, *Dalton Trans.*, 2020, **49**, 11170–11178.

Chapter 5

Computation of ^{31}P NMR Chemical Shifts in Keggin-based Polyoxotungstates

The following chapter is based on the publication: "Computation of ^{31}P NMR Chemical Shifts in Keggin-based Polyoxotungstates"; J. A. Thompson and L. Vilà-Nadal, *Dalton. Trans.*, 2024, **53**, 564-571.

5.1 Introduction

Nuclear magnetic resonance (NMR) is routinely employed to provide information on the chemical environment of active nuclei, in solution and solid state. Abundant nuclei, such as, ^{1}H (99 %), ^{29}Si (92 %), and ^{31}P (100 %), often require low concentrations ($<$ 0.01 M) and short acquisition time.[1] For example, Maksimovskaya and co-workers studied the composition of hydrolysed Keggin solutions using ^{31}P NMR to provide information of the metal-oxo structure.[1] ^{31}P NMR resonance signals typically occur in the range of -350 to 350 ppm, relative to 85 % H_3PO_4 standard. Solubility is a prerequisite to solution-based ^{31}P NMR and can be controlled using counterions.[2] For decades, ^{31}P NMR has been an integral tool for identifying intermediates of self-assembly mechanisms in POMs[3], for example, the formation of intermediate species during the synthesis of $[P_8W_{48}O_{184}]^{40-}$ wheels.[3,4]

Early computational work modelling NMR chemical shifts in POMs performed optimisations with implicit solvation models, treating the clusters as charged anions, negating the influence of counterions, see Figure 6.2. Initial work modelling ^{99}Ru chemical shifts in $[PW_{11}Ru(DMSO)O_{39}]^{5-}$ were reported by Bagno and co-workers. Optimisations were performed without relativistic corrections and treating the clusters as charged anions.[5] Nevertheless, the authors noted the sensitivity of the system to the Ru–S distance, wherein shielding of the ^{99}Ru nucleus by 235 ppm was induced by shortening of d(Ru–S) by 0.045 Å.[5] In addition, shieldings produced from this model were often an order of magnitude lower than the experimental values.[5,6] Later, relativistic corrections were incorporated in DFT computations of ^{183}W chemical shifts in $[W_5O_{18}]^{6-}$, $[Ru(DMSO)PW_{11}O_{39}]^{5-}$, and $[PW_{11}O_{39}]^{7-}$.[7] The model correctly assigned the ordering of ^{183}W signals in$[W_5O_{18}]^{6-}$; wherein W6 was shielded relative to W1-W5.[7] Bagno and co-workers explored the effect of counterions using $[LiPW_{11}O_{39}]^{6-}$ as a reference. The authors reported that by incorporating Li^{+} positively potentials by approx. 53 ppm.[7] In 2006, Bagno and co-workers reported ^{183}W chemical shifts in tungsten-based POMs could be replicated (on average) within 35 ppm by using spin–orbit (SO) corrections coupled with implicit solvation.[8] Later, Kortz and co-workers performed DFT computations modelling ^{183}W NMR chemical shifts for mono-lacunary clusters, $[GeW_{10}X(H_2O)O_{36}]^{7-}$ (X^{+} = Li, Na, K) solvated by counterions with explicitly located water.[9] Their model successfully produced the ordering of three resonances in $[GeW_{10}X(H_2O)O_{36}]^{7-}$ and replciated the distance between W(B) and W(C) signals ($\Delta\delta = 26$ ppm vs 29 ppm).[9] Their calculations shown the influence of counterion was 19 ppm for $[GeW_{10}O_{36}]^{8-}$ systems.[9]. Vilà-Nadal and co-workers rationalised shifts in ^{183}W resonance signals at $[XW_{12}O_{40}]^{q-}$ to tungsten-bridging oxygen (O_b and O_c) bonding.[10] The authors revealed ^{183}W chemical shifts were linearly correlated with the tungsten- oxygen (O_b and O_c) bond distance, proposing that contraction of the WO_6 polyhedral increased the energy gap between the occupied and unoccupied orbitals involved in electronic transition, deshielding the nucleus.[10]

In 2014, Pascual-Borràs and co-workers introduced the prospect of applying linear scaling to computed chemical shifts to reduce mean absolute error (MAE). Herein, ^{17}O chemical shifts for $[W_6O_{19}]^{2-}$ were computed using implicit solvation with spin–orbit and relativistic corrections, an approach which averaged an MAE of 39 ppm.[11] By applying linear scaling corrections, the authors reduced MAE to 26 ppm across a sample size of 75 signals.[11] Later, Pascual-Borràs and co-workers using implicit solvation with spin–orbit and relativistic corrections, calculated ^{31}P chemical shifts in Keggin, $[PW_{12}O_{40}]^{3-}$, and Wells–Dawson, $[P_2W_{18}O_{62}]^{6-}$ anions.[12] Their work involved benchmarking several exchange-correlation functionals and reported an MAE of 2.6 ppm using their optimal approach of TZP/PBE//TZ2P/OPBE (NMR//optimization).[12] Linear scaling was applied to their model, reducing MAE to 0.5 ppm.[11,12] The authors rationalised observed trends in chemical shifts with respect to metal oxidation state, in which resonance signals became more positive as the metallic oxidation state increased (X = W(VI) > V(V) > Sn(IV) > Ru(II)) in $[P_2W_{17}M(H_2O)O_{61}]^{q-}$ anions.[12]

Computational models seeking to accurately reproduce chemical shifts have commonly been performed using anionic systems and implicit solvation models to replicate solution behaviour. However, these approximations often produce large uncertainties and currently rely on linear scaling to reduce obtain sufficiently accurate results. Furthermore, the role of counterions has not been thoroughly investigated, particularly for ^{31}P chemical shifts. This chapter seeks to address these concerns by employing density functional theory (DFT) calculations to reproduce experimental ^{31}P chemical shifts in Keggin and corresponding lacunary clusters, see Figure 5.2. The work will also present a systemic study into the infleunce of increasing contributions to HF exchange (0 % PBE, 10 % TPSSh, 20 % B3LYP, 25 % PBE0) through several exchange-correlation functionals and applied basis sets.

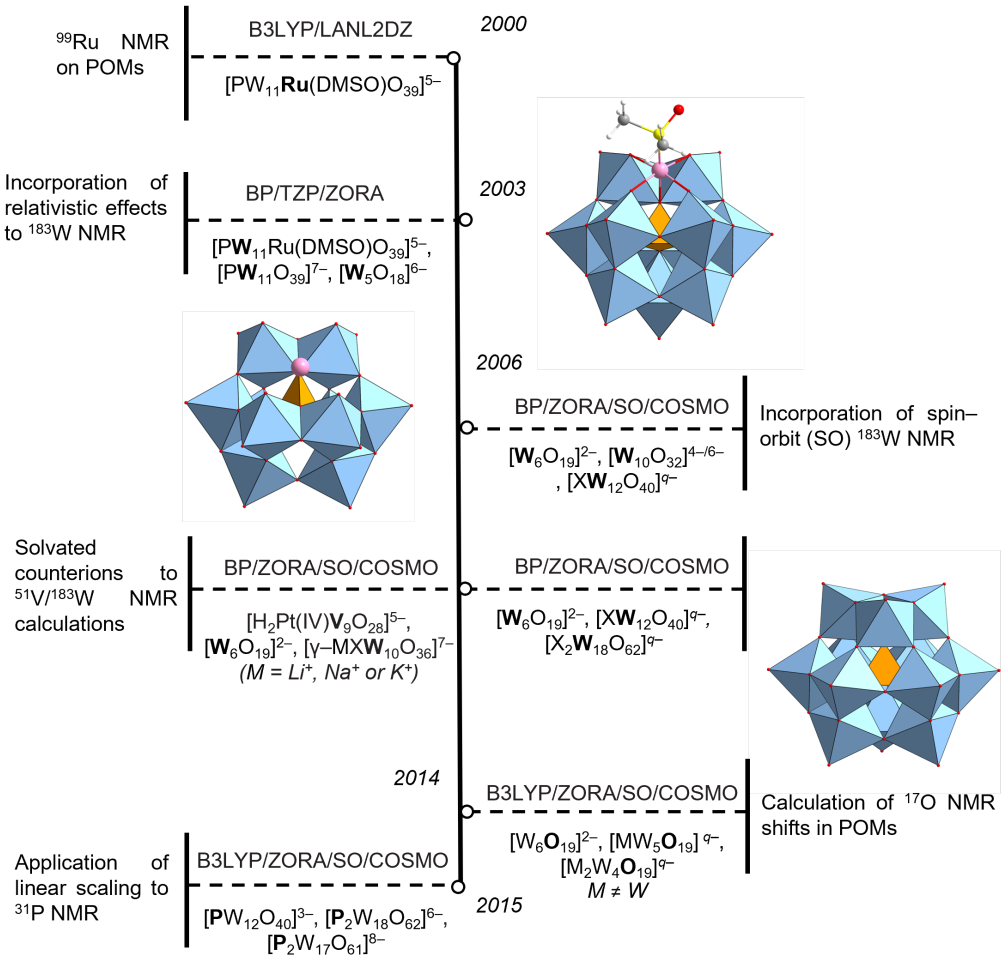

Figure 5.1: Timeline showing the progression in computed chemical shifts in polyoxometalates.[5–9,11,12]

5.2 Computational Details

All computational results were obtained using the ARCHIE-WeSt High-Performance Computer based at the University of Strathclyde. Density Functional Theory (DFT) calculations were performed using the Amsterdam Modelling Suite (AMS 2020.1) package.[13] In this work, two classes of exchange–correlation (x–c) functionals were employed, which include: (i) generalized gradient approximation (GGA); (ii) and hybrid methodologies. GGA functionals considered were Perdew–Burke–Ernzerhof (PBE).[14] The hybrid x–c functionals considered were: (i) Becke, 3-parameter, Lee–Yang–Parr (B3LYP*,[15] B3LYP[16]); (ii) Perdew–Burke–Ernzerhof (PBE0);[17] (iii) and Becke's half-and-half (BH&H).[18] Hybrid functionals were selected on their contributions of Hartree–Fock (HF) exchange (15 % B3LYP*, 20 % B3LYP, 25 % PBE0, and 50 % BH&H). We employed Slater basis sets comprising: (i) triple-ζ polarization (TZP); (ii) triple-ζ plus polarization (TZ2P); (iii) and quadruple-ζ plus polarization (QZ4P).[19,20] Relativistic corrections were included by means of the zeroth order regular approximation (ZORA) formalism.[21] The effects of aqueous solvent were approximated by using the conductor-like screening model (COSMO), as implemented by AMS.[22]

Structures were optimised using several x–c functionals of varying degrees of HF exchange (0 % PBE, 15 % B3LYP*, 20 % B3LYP, 25 % PBE0, 50 % BH&H). The effect of the basis set (TZ2P, QZ4P) was restricted to the GGA–PBE level of theory. Single-point calculations using PBE/TZP were employed to calculate ^{31}P NMR parameters (hyperfine couplings and isotropic shielding constants) with spin–orbit (SO) corrections. The notation for this procedure is expressed throughout the text as: Functional^{NMR}/Basis^{NMR}//Functional^{OPT}/Basis^{OPT}. The chemical shifts were referenced to 85 % H_3PO_4 using PH_3 as a secondary standard following the method suggested by van Wüllen[23]:

$$\delta(\mathrm{X_{calc}}) = \sigma(\mathrm{PH_{3calc}}) - \sigma(\mathrm{X_{calc}}) - 266.1 \tag{5.1}$$

where X is the phosphorus atom in the model system of interest and 266.1 is the difference in ppm between the absolute experimental chemical shielding of PH_3 (594.5 ppm) and 85 % H_3PO_4 (328.4 ppm) at 300 K.[24]

The chemical shift of a nucleus is dependent on the magnetic shielding tensor, σ. The shielding tensor can be rewritten in terms of the diamagnetic, paramagnetic, and spin–orbit contributions, see below:

$$\sigma = \sigma^{d} + \sigma^{p} + \sigma^{SO} \tag{5.2}$$

σ^d corresponds to the diamagnetic tensor which depends on the electron density at the ground state. σ^p equates to the paramagnetic tensor which depends on the excited states of the unperturbed system. Conventionally, σ^d is analogous across environments so changes in chemical shift is usually attributed to the paramagnetic part. The paramagnetic tensor can be expressed as:

$$\mathrm{u}_{ai} \propto -\frac{\langle \phi_g | \, H | \phi_s \rangle}{2\left({\epsilon_i}^0 - {\epsilon_a}^0\right)} \tag{5.3}$$

where ${\epsilon_i}^0$ and ${\epsilon_a}^0$ are the orbital energies of the occupied and unoccupied MOs involved in a given electronic transition, and the integral in the numerator is the first-order magnetic coupling between these orbitals.

Finally, to evaluate the discrepancy of the optimised and crystallographic geometries, we employed the mean absolute error (MAE) and mean signed error (MSE) obtained as:

$$\mathrm{MAE} = \frac{1}{\mathrm{N}} \sum_{\mathrm{i}} |\delta_{\mathrm{calc,\,j}} - \delta_{\mathrm{exp,\,j}}| \tag{5.4}$$

$$\mathrm{MSE} = \frac{1}{\mathrm{N}} \sum_{\mathrm{i}} (\delta_{\mathrm{calc,\,j}} - \delta_{\mathrm{exp,\,j}}) \tag{5.5}$$

$$\mathrm{STD} = \sqrt{\frac{1}{\mathrm{N}-1} \sum_{\mathrm{i}} (\mathrm{MSE} - (d_{\mathrm{calc,\,j}} - d_{\mathrm{exp,\,j}}))} \tag{5.6}$$

where δ_{calc} and δ_{exp} are the calculated and experimental chemical shifts, respectively.

5.3 Results and Discussion

5.3.1 Anionic Model

A structural benchmark was performed to assess the ability of the exchange–correlation (*x–c*) functionals and basis sets to replicate P-O distances for Keggin, $[PW_{12}O_{40}]^{3-}$ and lacunary: $[PW_{11}O_{39}]^{7-}$, $[A{-}PW_9O_{34}]^{9-}$ - see Figure 5.2. To assess the sensitivity of the DFT models on P-O distances, this was plotted as a function of computed chemical shifts, δ_{Calc} - see Figure 5.3. For Keggin, $[PW_{12}O_{40}]^{3-}$, all models reproduced experimental chemical shifts within 8 ppm - see Table 5.1 In this regard, optimisations using PBE0/TZP revealed the closest replication of the experimental, deviating by ca. 3 ppm. Optimisations using the PBE0/TZP level of theory demonstarted a closer agreement with experimental chemical shift with $Na_3[PW_{12}O_{40}]$ as opposed to $Li_3[PW_{12}O_{40}]$. Our DFT models were highly sensitive to P-O distance whereby increasing HF exchange from 15 % (B3LYP*) to 50 % (BH&H), decreased P-O by 0.026 Å resulting in a shift of ca. 8 ppm for $[PW_{12}O_{40}]^{3-}$. All DFT models for Keggin replicated the experimental P-O distances of 1.530 Å within 0.02 Å.[25]

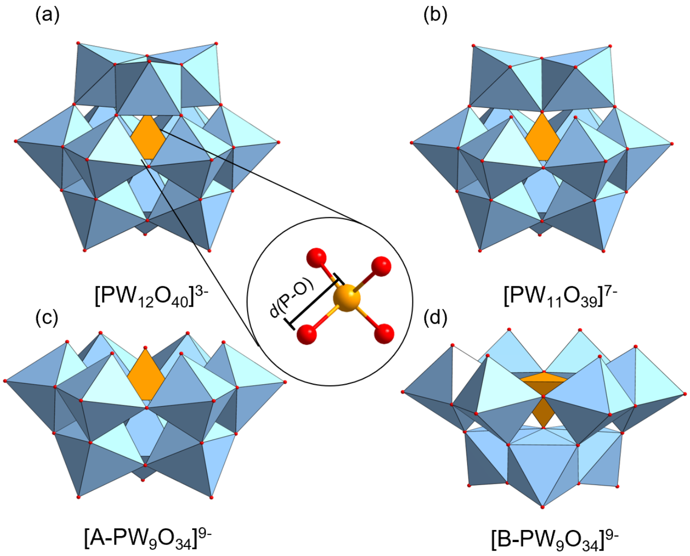

Figure 5.2: Polyhedral representations of the hydrolytic conversions of $[PW_{12}O_{40}]^{3-}$ to lacunary: $[PW_{11}O_{39}]^{7-}$, $[A{-}PW_9O_{34}]^{9-}$, and $[B{-}PW_9O_{34}]^{9-}$ clusters. Colours corresponding to W = cyan, O = red, and P = orange.

Equation 5.2 shows that the magnetic shielding tensor, σ, is comprised of the sum of three contributions: (i) diamagnetic; (ii) paramagnetic; (iii) and the spin–orbit (SO) terms. Vila-Nadal and co-workers reported that the diamagnetic tensor is predominately derived from core electrons which are not significantly influenced by the chemical environment.[10] Therefore, variations in chemical shift can largely be attributed the paramagnetic shielding tensor.[10] This term is dominated by the u_{ai} term, which is inversely proportional to the energy gap between the occupied and virtual MOs involved in electronic transition.

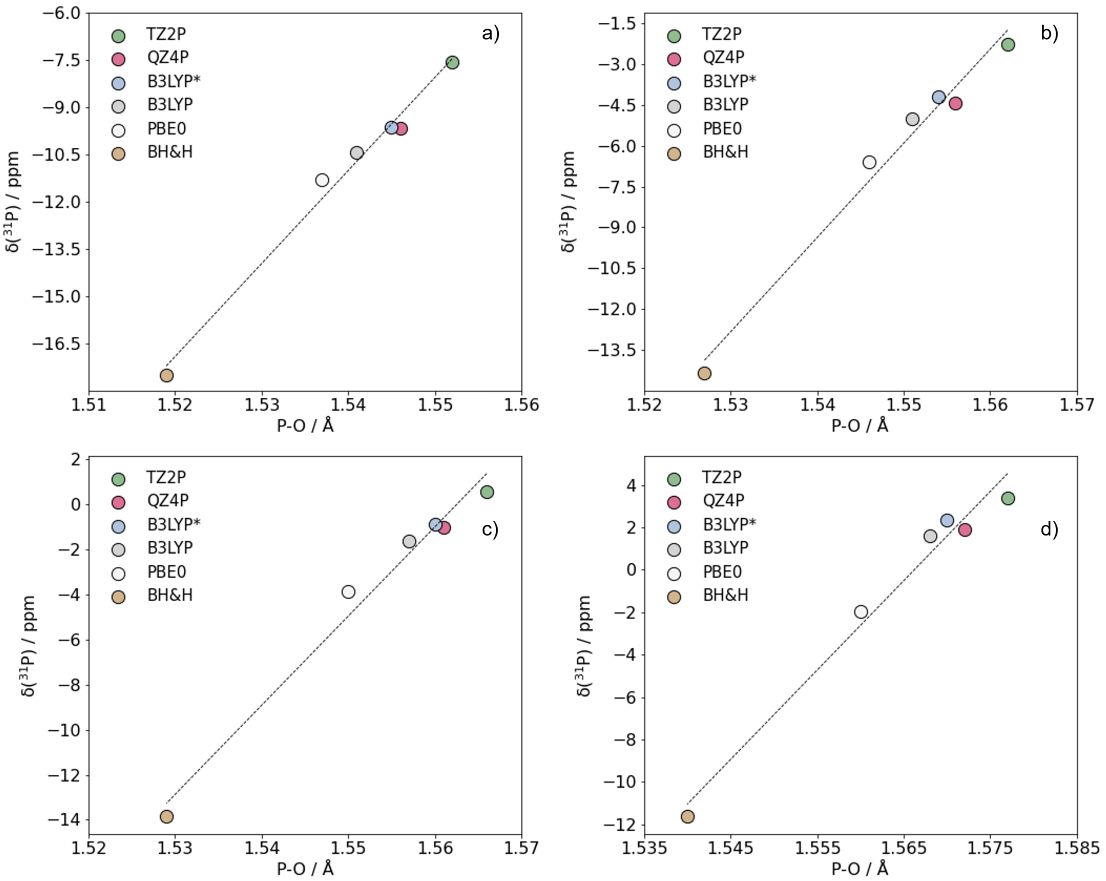

Figure 5.3: Computed chemical shift, δ_{Calc}, plotted as a function of P–O distance for the hydrolytic conversions of (a) $[PW_{12}O_{40}]^{3-}$ to lacunary: (b) $[PW_{11}O_{39}]^{7-}$, (c) $[A{-}PW_9O_{34}]^{9-}$, and (d) $[B{-}PW_9O_{34}]^{9-}$ clusters. Structures were optimised using several x–c functionals of varying degrees of HF exchange (0 % PBE, 15 % B3LYP*, 20 % B3LYP, 25 % PBE0, 50 % BH&H). The effect of the basis set (TZ2P, QZ4P) was restricted to the GGA–PBE level of theory -see Figure legend.

Chemical shifts computed using hybrid exchange-correlation functionals provided closer agreements to experimental than GGA-based approaches. Figure 5.3 shows all GGA-based approaches significantly underestimated P-O distances resulting in excessively shielded resonance signals. By contrast, increasing contributions of HF exchange progressively expanded the PO_4 tetrahedron, deshielding the resonance signals. With reference to Eqn. 5.2, as HF exchange is increased, the paramagnetic shielding tensor becomes progressively more negative as the energy gap between the occupied and virtual orbitals is increased. Thereby, the shielding tensor, σ, progressively becomes less positive, displacing δ_{Calc} to more positive regions.

5.3.2 Incorporation of alkali metal cations

Thus far, δ_{Calc} computations has assumed a fully anionic system, without neutralizing their charge. However, chemical systems supporting large charges have been shown to exacerbate large uncertainties. To investigate the effect of explicitly located counterions (X = Li^+, Na^+, K^+) we have localised cations on the surface of the POM, rendering our systems charge neutral. In this work, we have employed the same POM-cation orientations that were employed in Chapter 4.[26] The metal-oxide framework of the POM contains 4-fold (pocket A–F) and 3-fold pockets which are capable of electrostatically interacting with the alkali metal-cation -see Figure 4.6.[26] The integer refers to the number of counterion-oxygen interactions and our previous work has established such interactions preferentially occur at 4-fold pockets due to improved Coulombic attractive forces compared to 3-fold pockets.[26] Given the small electronic energy difference between cation arrangements, it is reasonable to assume these will interchange in solution. However, this will not be accredited for in this work.

Explicitly locating counterions (X = Li^+, Na^+) induced minimal deshielding of 0.5 − 1.5 ppm across all Keggin systems, see Table 5.1. The resonance signals in Keggin became progressively more shielded as ionic radii of the alkali-metal cation increased, though the effect was small. With reference to Eqn. 5.2, when cations are included in our systems, the paramagnetic shielding tensor becomes more negative as the energy gap between the occupied and virtual orbitals is increased. Consequently, the shielding tensor, σ, progressively becomes less positive, displacing δ_{Calc} to more positive regions. Generally, Beckes half-and-half (BH&H) produced signals that were furthest from the experimental data. In this work, hybrid functionals were selected on their contributions of Hartree–Fock (HF) exchange (15 % B3LYP*, 20 % B3LYP, 25 % PBE0, and 50 % BH&H). Table 5.1 shows as HF exchange is increased, resonance signals of Keggin were shifted upfield, for example, -10.27 (15 % B3LYP*) to -18.55 ppm (50 % BH&H) in Li3$[PW_{12}O_{40}]^{3-}$ salts and -10.80 (15 % B3LYP*) to -19.04 ppm (50 % BH&H) in $Na_3[PW_{12}O_{40}]$.

An assessment of the mono-lacunary systems were also not sensitive towards explicitly locating counterions (X = Li^+, Na^+, K^+) as resonance signals were shielded by ca. 2 ppm relative to their anionic counterparts. That said, our model reflects experimental observations where the mono-lacunary, $X_7[PW_{11}O_{39}]$ (X = Li^+, Na^+) is shifted downfield relative to the parent Keggin, $X_3[PW_{12}O_{40}]$. The experimental order of δ_{Exp} values is as follows: $X_7[PW_{11}O_{39}]$: Li^+ (upfield) > K^+ > Na^+ (downfield). Unfortunately, the current model was unable to replicate this trend, for example, PBE0/TZP showed the trend: K^+ (upfield) > Na^+ > Li^+ (downfield). We suggest that this is a result of the delicate POM-cation interactions, which are influenced by the orientation and proximity of the ion-pairing. Previous work by Poblet and co-workers studied POM-cation interactions of three different POMs, $[PW_{12}O_{40}]^{3-}$, $[SiW_{12}O_{40}]^{4-}$, and $[AlW_{12}O_{40}]^{5-}$, with three different monovalent cations Li^+, Na^+ and K^+ using molecular dyanmic simulations.[27] Later, Nyman and co-workers studied ion-pairing between Lindqvist and tetramethylammonium cations in $([(CH_3)_4N]^+, Cs)_8[M_6O_{19}]$ (M = Nb, Ta), combining experimental with theory.[28] The sensitivity of our model to ion-pair proximity was not explicitly accounted for. However, this highlights the current challenge in attaining reliable chemical shifts is effectively controlling the proximity of the ion-pairing. Future work systematically exploring the effect of the optimal POM-cation distance will enhance our understanding of POM-cation ion-pairing and potentially enable closer agreements between theoretical and experimental results. Across all test cases, the optimal method was not consistent for the lacunary clusters. However, PBE0/TZP (20 % exchange) generally well replicated the experimental shown by a mean absolute error (MAE) of 4.03 ppm, see Table 5.1. It is important to note that the lowest MAE value was reported for BH&H/TZP, however, this can be attributed to the fortuitous replication of $\delta(^{31}P)$ in $Na_8H[B{-}PW_9O_{34}]$.

Table 5.1: Computed δ_{Calc} signals for Keggin, $[PW_{12}O_{40}]^{3-}$ and their corresponding lacunary: $[PW_{11}O_{39}]^{7-}$, $[A{-}PW_9O_{34}]^{9-}$ with $[B{-}PW_9O_{34}]^{9-}$ clusters and their corresponding salts (X= Li^+, Na^+, K^+, TBA^+).[1,29]

System	PBE/TZ2P	PBE/QZ4P	B3LYP*/TZP	B3LYP/TZP	PBE0/TZP	BH&H/TZP	This Work	Lit.
$[PW_{12}O_{40}]^{3-}$ / H_2O	-7.56	-9.66	-9.63	-10.43	-11.30	-17.50		-14.60*
$Li_3[PW_{12}O_{40}]$	-7.90	-10.22	-10.27	-11.03	-12.84	-18.55	-15.41	
$Na_3[PW_{12}O_{40}]$	-8.28	-10.80	-10.65	-11.39	-13.04	-19.04	-15.36	
$[PW_{12}O_{40}]^{3-}$ / MeCN	-7.55	-9.62	-9.27	-9.97	-11.38	-17.50		
$TBA_3[PW_{12}O_{40}]$	-8.25	-11.40	-9.75	-10.68	-12.33	-19.65	-15.35	
$[PW_{11}O_{39}]^{7-}$ / H_2O	-2.29	-4.43	-4.21	-5.00	-6.59	-14.35		
$Li_7[PW_{11}O_{39}]$	-3.47	-5.38	-5.35	-6.16	-7.27	-14.92	-11.65	-11.20
$Na_7[PW_{11}O_{39}]$	-2.33	-4.65	-4.58	-5.37	-7.35	-14.28	-10.82	-10.65
$K_7[PW_{11}O_{39}]$	-3.40	-6.06	-6.05	-6.82	-8.55	-16.28	-11.13	-10.80
$[A\text{-}PW_9O_{34}]^{9-}$ / H_2O	0.55	-1.00	-0.86	-1.61	-3.87	-13.86		
$Na_8H[A\text{-}PW_9O_{34}]$	-0.99	-2.34	-2.39	-3.24	-5.10	-12.83	-7.76	-7.10
$[B\text{-}PW_9O_{34}]^{9-}$ / H_2O	3.41	1.89	2.33	1.60	-1.96	-11.64		
$Na_8H[B\text{-}PW_9O_{34}]$	11.05	9.23	9.17	8.15	6.28	-2.96	-3.76	-3.00
MAE	8.65	6.37	6.61	5.79	4.03	3.74		
MSE	8.65	6.37	6.61	5.79	4.03	-3.54		
STD	2.54	2.83	2.66	2.58	2.53	1.57		

5.3.3 Incorporation of alkylammonium cations

Aqueous solubility can be achieved using alkali metal cations (Li^+ and Na^+), modelled earlier. In a similar manner, solubility in organic solvent is generally accomplished using large alkylammonium cations. We have explored the influence of explicitly located alkylammonium cations and the effect of alkyl chain length in the following system: $[(n\text{–}C_xH_{2x+1})_4N]_3[PW_{12}O_{40}]$; where x= 1-4, see Table 5.2. The arrangement of akalyammonium cations around the surface of the POM is shown in Figure 9.14.

Table 5.2: Computed, δ_{Calc} for organic Keggin systems, $[(n\text{–}C_xH_{2x+1})_4N]_3[PW_{12}O_{40}]$, reported in ppm. $\Delta\delta_{Calc}$ represents the difference in δ_{Calc} relative to $[(n\text{–}C_4H_9)_4N]_3[PW_{12}O_{40}]$. All optimizations were performed using PBE0/TZP level of theory.

$[(n\text{–}C_xH_{2x+1})_4N]^+$	δ_{Calc}	$\Delta\delta_{Calc}$
$NH_4{}^+$	-13.00	0.67
$[(n\text{–}CH_3)_4N]^+$	-12.68	0.35
$[(n\text{–}C_2H_5)_4N]^+$	-12.70	0.37
$[(n\text{–}C_3H_7)_4N]^+$	-12.83	0.50
$[(n\text{–}C_4H_9)_4N]^+$	-12.33	0.00

*All energies are reported in kcal mol^{-1}.

All results were in close agreement with the experimental chemical shift (-15.35 ppm) using PBE0/ TZP level of theory. Our models for δ_{Calc} were insensitive to alkyl chain length in $[(n\text{–}C_xH_{2x+1})_4N]_3$-$[PW_{12}O_{40}]$. Optimisations using hybrid x–c functionals for $[(n\text{–}C_xH_{2x+1})_4N]_3[PW_{12}O_{40}]$ where x = 3 or 4 is CPU expensive. δ_{Calc} varied by 0.67 ppm from -12.33 ($[(n\text{–}C_4H_9)_4N]^+$) to -13.00 ($[NH_4]^+$). Given the small difference in $\Delta\delta_{Calc}$, it would be reasonable to employ $NH_4{}^+$ to model $[(n\text{–}C_4H_9)_4N]_3[PW_{12}O_{40}]$ in a bid to reduce computational cost.

5.3.4 Application of Linear Scaling

Previous work by Pascual-Borràs have accurately reproduced chemical shifts by means of linear scaling to reduce uncertainty from DFT outputs.[11,12] A linear regression model derived by plotting experimental chemical shifts as a function of computed isotropic shielding (σ), see Figure 5.4. In this work, δ_{Fitted} refers to chemical shifts that have been fine-tuned using this linear scaling model. The present model captured data using PBE/TZP//PBE0/TZP level of theory, taking the form: δ = bσ + a, in which the slope, b, is the scaling factor.

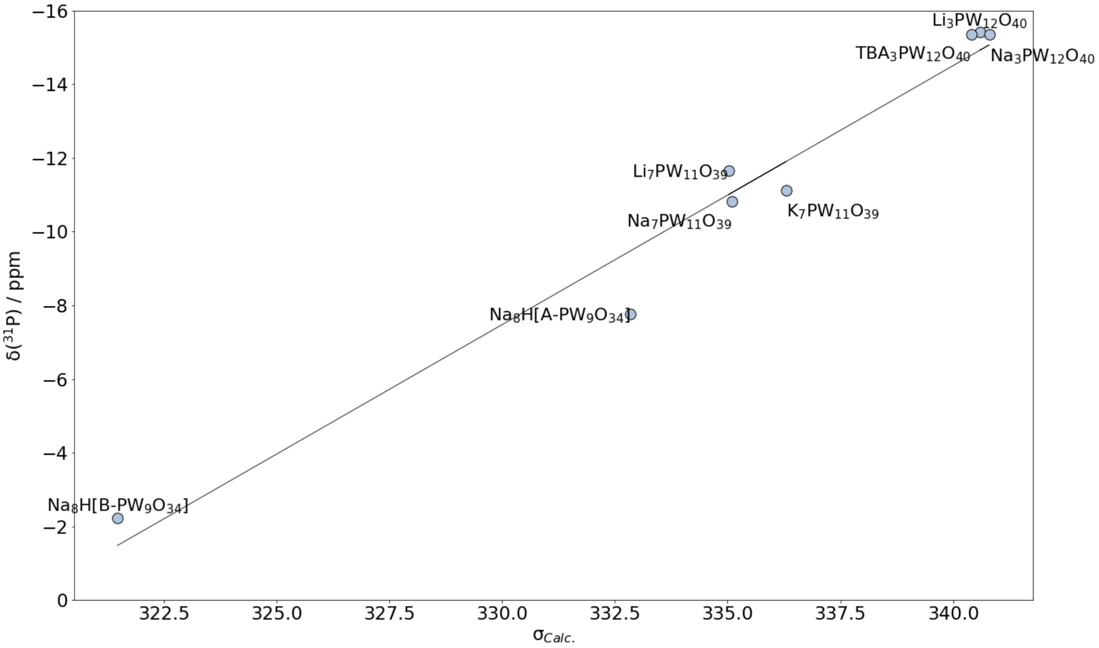

Figure 5.4: Computed isotropic shielding, σ_{Calc} using the PBE/TZP//PBE0/TZP methodology, plotted as a function of δ_{Exp}. The linear regression model was used to scale computed chemical shifts, analogous to previous work by Pascual-Borràs.[11,12] The equation used in this work was: -0.63σ + 199.19.

Figure 5.5 shows that δ_{Fitted} were in closer agreement with the experimental. Linear scaling reduced MAE and MSE to 0.86 and -0.02 ppm, respectively, for mono-lacunary systems. Additionally, δ_{Fitted} values replicated the experimental order of $X_7[PW_{11}O_{39}]$: Li^+ (upfield) $>$ K^+ $>$ Na^+ (downfield) see Table 9.4. Linear scaling proved crucial for obtaining reliable signals for $Na_8H[B{-}PW_9O_{34}]$ due to direct electrostatic interacting between the central tetrahedron and counterion - see Figure 9.13.

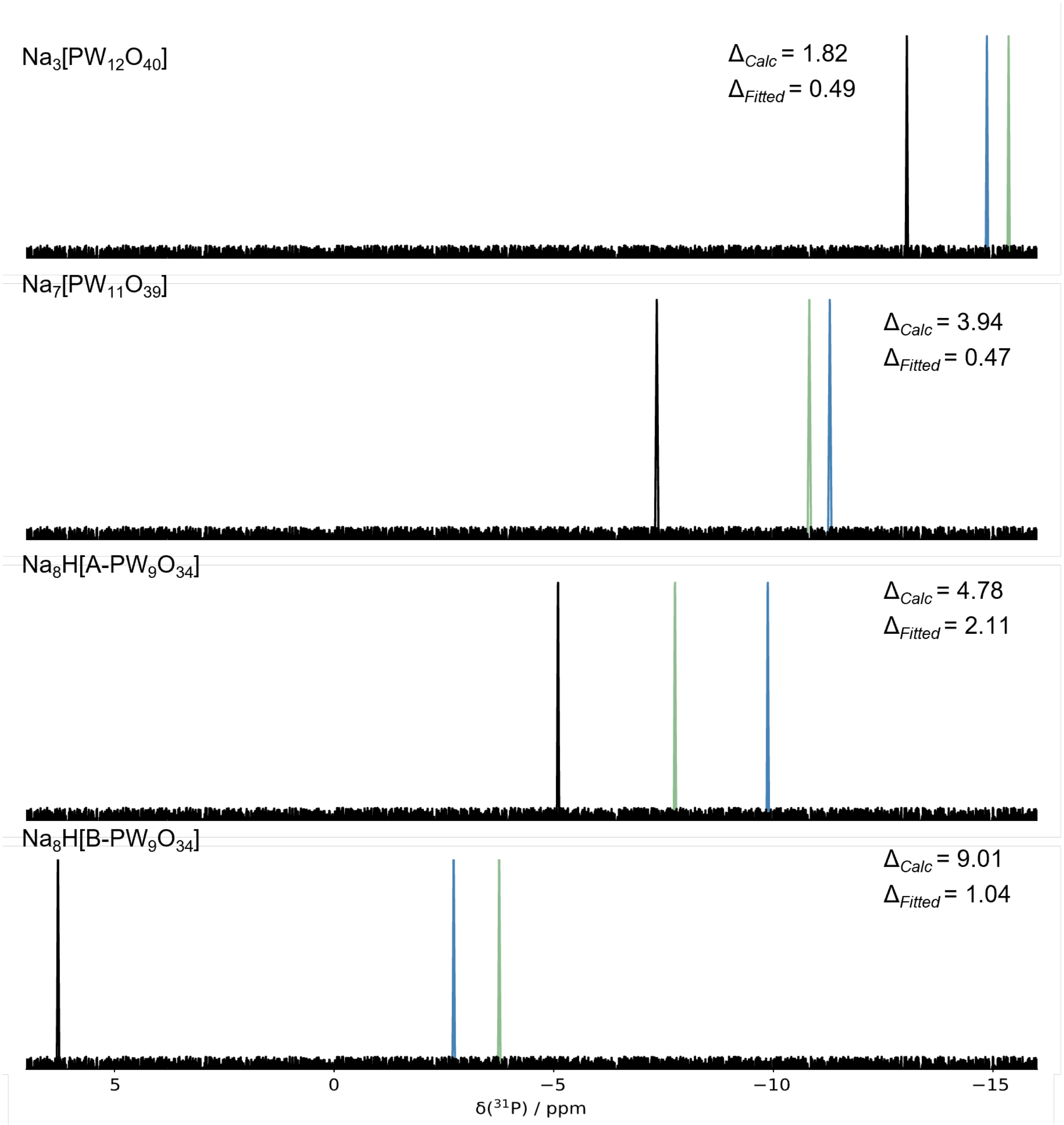

Figure 5.5: Computed (black), δ_{Exp}, fitted (blue), δ_{Fitted}, and experimental (green), δ_{Exp}, signals for Keggin, $Na_3[PW_{12}O_{40}]$ and their corresponding lacunary: $Na_7[PW_{11}O_{39}]$, $Na_8H[A-PW_9O_{34}]$, and $Na_8H[B-PW_9O_{34}]$ clusters.

5.3.5 Conclusions

Throughout this work, we have systematically studied the accuracy of exchange-correlation functionals and applied basis sets in reproducing chemical shifts in Keggin, $Na_3[PW_{12}O_{40}]$ and their lacunary clusters: $Na_7[PW_{11}O_{39}]$, $Na_8H[A-PW_9O_{34}]$, and $Na_8H[B-PW_9O_{34}]$. The objective of this chapter has been to highlight the challenges in modelling chemical shifts and provide an analysis of the geometric and electronic factors controlling it.

Early work using anionic systems and implicit solvation models were highly sensitive to P-O distance whereby increasing HF exchange from 15 % (B3LYP*) to 50 % (BH&H), caused P-O to vary by ca. 0.03 Å resulting in a shift of ca. 8 ppm for $[PW_{12}O_{40}]^{3-}$. Generally, hybrid exchange-correlation functionals were in closer agreement than GGA-based approaches that often underestimated P-O distances. As HF exchange was progressively increased, the central tetrahedron expanded, deshielding the resonance signals. Later, we explicitly located counterions (X = Li^+, Na^+, K^+) on the surface of the POM, rendering our systems charge neutral. For Keggin, δ_{Calc} was deshielded by 1.0–2.0 ppm, with respect to their anionic systems. Resonance signals were progressively shifted upfield as a function of HF exchange, for example, -10.27 (15 % B3LYP*) to -18.55 ppm (50 % BH&H) in $Li3[PW_{12}O_{40}]^{3-}$ salts and -10.80 (15 % B3LYP*) to -19.04 ppm (50 % BH&H) in $Na_3[PW_{12}O_{40}]$. However, obtaining reliable chemical shifts for $[B{-}PW_9O_{34}]^{9-}$ proved challenging due to direct electrostatic interactions between the located counterions and central tetrahedron. Optimal results were accomplished using the PBE/TZP//PBE0/TZP level of theory achieving a MAE and MSE of 4.0 ppm. Later, we employed linear scaling which proved crucial for the $[B{-}PW_9O_{34}]^{9-}$ system, replicating within 1.0 ppm of the experimental using this methodology.

Bibliography

[1] R. I. Maksimovskaya and G. M. Maksimov, *Coord. Chem. Rev.*, 2019, **385**, 81–99.

[2] A. Misra, K. Kozma, C. Streb and M. Nyman, *Angew. Chem., Int. Ed. Engl.*, 2020, **59**, 596–612.

[3] L. Vilà-Nadal and L. Cronin, *Nat. Rev. Mater*, 2017, **2**, 17054.

[4] R. Contant and A. Teze, *Inorg. Chem.*, 1985, **24**, 4610–4614.

[5] A. Bagno and M. Bonchio, *Eur. J. Inorg. Chem.*, 2002, **2002**, 1475–1483.

[6] A. Bagno, M. Bonchio, A. Sartorel and G. Scorrano, *Eur. J. Inorg. Chem.*, 2000, **2000**, 17–20.

[7] A. Bagno, M. Bonchio, A. Sartorel and G. Scorrano, *ChemPhysChem*, 2003, **4**, 517–519.

[8] A. Bagno, M. Bonchio and J. Autschbach, *Chem. - Eur. J.*, 2006, **12**, 8460–8471.

[9] N. Vankova, T. Heine and U. Kortz, *NMR chemical shifts of metal centres in polyoxometalates: relativistic DFT predictions*, 2009.

[10] L. Vilà-Nadal, J. P. Sarasa, A. Rodríguez-Fortea, J. Igual, L. P. Kazansky and J. M. Poblet, *Chem. Asian J.*, 2010, **5**, 97–104.

[11] M. Pascual-Borras, X. López, A. Rodriguez-Fortea, R. J. Errington and J. M. Poblet, *Chem. Sci.*, 2014, **5**, 2031–2042.

[12] M. Pascual-Borras, X. López and J. M. Poblet, *Phys. Chem. Chem. Phys.*, 2015, **17**, 8723–8731.

[13] G. t. Te Velde, F. M. Bickelhaupt, E. J. Baerends, C. Fonseca Guerra, S. J. van Gisbergen, J. G. Snijders and T. Ziegler, *J. Comput. Chem.*, 2001, **22**, 931–967.

[14] J. P. Perdew, K. Burke and M. Ernzerhof, *Phys. Rev. Lett.*, 1996, **77**, 3865.

[15] M. Reiher, O. Salomon and B. Artur Hess, *Theor. Chem. Acc.*, 2001, **107**, 48–55.

[16] C. Lee, W. Yang and R. G. Parr, *Phys. Rev. B*, 1988, **37**, 785.

[17] M. Ernzerhof and G. E. Scuseria, *J. Chem. Phys.*, 1999, **110**, 5029–5036.

[18] A. D. Becke, *J. Chem. Phys.*, 1993, **98**, 1372–1377.

[19] R. Sure, J. G. Brandenburg and S. Grimme, *ChemistryOpen*, 2016, **5**, 94–109.

[20] E. Van Lenthe and E. J. Baerends, *J. Comput. Chem.*, 2003, **24**, 1142–1156.

[21] E. Van Lenthe, A. Ehlers and E.-J. Baerends, *J. Chem. Phys.*, 1999, **110**, 8943–8953.

[22] C. C. Pye and T. Ziegler, *Theor. Chem. Acc.*, 1999, **101**, 396–408.

[23] C. van Wüllen, *Phys. Chem. Chem. Phys.*, 2000, **2**, 2137–2144.

[24] D. Chesnut, *J. Phys. Chem. A*, 2005, **109**, 11962–11966.

[25] G. M. Brown, M.-R. Noe-Spirlet, W. R. Busing and H. A. Levy, *Acta Crystallogr.*, 1977, 1038–1046.

[26] J. A. Thompson, R. González-Cabaleiro and L. Vilà-Nadal, *Inorg. Chem.*, 2023, **62**, 12260–12271.

[27] F. Leroy, P. Miró, J. M. Poblet, C. Bo and J. Bonet-Ávalos, *J. Phys. Chem. B*, 2008, **112**, 8591–8599.

[28] J. Sures, S. A. Serapian, K. Kozma, P. I. Molina, C. Bo and M. Nyman, *Phys. Chem. Chem. Phys.*, 2017, **19**, 8715–8725.

[29] M. Kozik, C. F. Hammer and L. C. W. Baker, *J. Am. Chem. Soc.*, 1986, **108**, 7627–7630.

Chapter 6

Controlling Ion-Pair Proximity in Aqueous Transition-Metal-Substituted Polyoxotungstates

This chapter describes the current limitations of redox modelling in polyoxometalates (POMs). Thereafter, we provide an extensive study of the accuracy of various exchange-correlation functions in reproducing experimentally obtained redox potentials in $X_5[PW_{11}M(H_2O)O_{39}]$ salts; where X= Li, Na or K, and M = Mn(III/II), Fe(III/II) or Co(III/II). Thereafter, we propose an alternate approach to redox modelling by explicitly specifying the heteroatom – counterion distance which was tested at discrete intervals.

6.1 Introduction

Electrochemical properties of POMs have been extensively studied using electrochemical techniques, i.e., cyclic voltammetry, in various solutions containing different electrolytes and electrodes. Early work investigating the reduction and oxidation processes of POMs were reported by Pope and co-workers measuring W(VII/VI) redox waves in $[XW_{12}O_{40}]^{q-}$; X = P(V), Ge(IV), Si(IV), B(III).[1] The authors showed an inverse relation (-0.18 V/Q) between the anion charge and W(VII/VI) potentials following the trend: P(V) > Ge(IV) > Si(IV) > B(III)[1] In 2010, Nadjo and co-workers combined experimental findings with Density Functional Theory (DFT) calculations that POM clusters supporting the same formal charge can exhibit different affinities for accepting electrons.[2]The authors reported that $[SiW12O40]^{4-}$ produces a potential of -230 mV (vs SCE), which is 40 mV more negative than the corresponding $[GeW12O40]^{4-}$ variant. Using DFT calculations, the authors attributed this observation to the larger ionic radii associated with the Ge(IV) heteroatom.[2] DFT calculations were employed to rationalise electron affinity of P(V)-based Keggin and Wells-Dawson clusters attributed to the lower lying LUMO orbitals in $[P_2W_{12}O_{62}]^{6-}$.[3]

Early computational work modelling redox potentials in POMs performed optimisations with implicit solvation often overlooking the influence of counterions. An early example computed the redox waves present in $[XW_{11}MO_{40}]^{q-}$ (M = W, Mo, V, Nb, and Ti) treating the cluster as fully ionic, modelling the solvent using a conductor–like screening model.[4] This model produced uncertainties, often exceeding 300 mV with respect to experimental potentials.[4] However, the mode correctly reproduced the inverse relation between the anion charge and W(VII/VI) potentials observed by Pope in $[XW_{12}O_{40}]^{q-}$; X = P(V), Si(IV).[4] A pioneering study by Rösch and co-workers reported potentials with explicitly located Li^+ cations disperesed across the surface of a tri-Mn-substituted Keggin, $Li_4[Mn(IV)_3(OH)_3(OH)_3(A-\alpha\text{-}SiW_9O_{34})]$.[5] The closest agreement with the experimental potential was calculated using GGA–PBE functional despite testing several exchange–correlation (*x-c*) functionals with the increase in contributions of Hartree-Fock (HF) exchange (0 % PBE, 10

% TPSSh, 20 % B3LYP, 25 % PBE0). The authors highlighted that computed potentials were positively shifted as HF exchange was increased.[5] Hybrid exchange–functionals generally overestimated potentials by 0.6–1.0 V.[5] Recently, Falbo and co-workers explicitly located Li^+ cations on the surface of a parent Keggin, $Na_3[SiW_{12}O_{40}]$ and noted that neutralizing the charged species reduced systematic uncertainty attributed to the self-interaction error.[6]

In our earlier work, we explored the accuracy of various exchange–correlation functionals in reproducing experimental potentials, $U^0{}_{Red}$, in anionic $[PW_{11}M(H_2O)O_{39}]^{q-}$ compounds where M = Mn(III/II), Fe(III/II), Co(III/II), and Ru(III/II).[7] The *x-c* functionals employed in this study were chosen to explore the influence of Hartree-Fock (HF) exchange (0 % PBE, 15 % B3LYP*, 20 % B3LYP, 25 % PBE0, and 50 % BH&H) for reproducing potentials. Our work involved explicitly located K^+ counterions which induced positive shifting of potentials by $>$ 500 mV which improved the accuracy of computed potentials where M = Mn(III/II)/Co(III/II), however, was to the detriment where M= Fe(III/II)/Ru(III/II) in $K_x[XW_{11}M(H_2O)O_{39}]^{q-x}$.[7] Such uncertainties in $U^0{}_{Red}$ were attributed to the over-stabilization of the ion-pairing between the counterion and POM cluster.[7] In this work, we have extended our work to systematically investigate the accuracy of various exchange–correlation functionals for Mn(III/II), Fe(III/II), and Co(III/II) couples present in $X_5[PW_{11}{}^{-}\ M(H_2O)O_{39}]$ where X = K(I) , Na(I) , Li(I). We explore the current challenges in attaining precise predictions of redox potentials and provide an insight into the geometric and electronic factors controlling it.

6.1.1 Computational Details

All computational results were obtained using the ARCHIE–WeSt high-performance computer based at the University of Strathclyde. DFT calculations were performed using the Amsterdam Modelling Suite (AMS 2020.1) package.[8] In this work, several classes of exchange–correlation (*x-c*) functionals were employed, which include (i) generalized gradient approximation (GGA); (ii) hybrid; and (iii) range-separated hybrid functionals. GGA functionals considered were as follows: (i) PBE[9]; (ii) Perdew–Wang (PW91)[10]; and (iii) Becke 1988 exchange and Perdew 86 (BP86).[11,12] The hybrid *x-c* functionals considered were as follows: (i) Becke, 3-parameter, Lee–Yang–Parr (B3LYP*[13], B3LYP[14]); (ii) PBE0[15]; and (iii) Becke's half-and-half (BH&H).[16] Hybrid functionals were selected on their contributions of HF exchange (15 % B3LYP*, 20 % B3LYP, 25 % PBE0, and 50 % BH&H). The ωB97X method was selected as the range-separated hybrid functional.[17] We employed Slater basis sets comprising the following: (i) triple-ζ polarization (TZP); (ii) triple-ζ plus polarization (TZ2P); and (iii) quadruple-ζ plus polarization (QZ4P).[18,19] Relativistic corrections were included by means of the zeroth order regular approximation formalism.[20] The effects of aqueous solvent were approximated by using the conductor-like screening model, as implemented by AMS.[21] For open shell molecules, unrestricted Kohn–Sham (UKS) theory was implemented, while restricted Kohn–Sham (RKS) theory was employed for closed shell systems. All harmonic vibrational frequencies were calculated using PBE coupled with the TZP basis set. The calculation of Gibbs free energies for hybrid-optimized systems were corrected by using the zero-point energies and entropic components obtained from GGA–vibrational frequencies-see Eqn. 6.1:

$$\Delta G = \Delta H + \Delta E_{ZPE} - T\Delta S \tag{6.1}$$

Herein, ΔH equates to the enthalpic component; ΔE_{ZPE} is the difference in zero-point energy, and TΔS is the entropic component, under standard conditions, T = 298.15 K, P = 1.0 atm. The entropic and zero-point terms were computed using harmonic vibrational frequencies. Cramer and co-workers reported the free energy change for the standard hydrogen electrode (SHE) half-reaction

($1/2H_2 \rightarrow H^+ + e^{-}$) equates to 4.24 eV.[22] This was used an external reference for all computed potentials.

6.2 Results and Discussion

6.2.1 Counterion Effect

Redox potentials, $U^0{}_{Red}$ vs SHE, for Mn(III/II), Fe(III/II), and Co(III/II) couples present in $X_5[PW_{11}M(H_2O)O_{39}]$ where X = K(I) , Na(I) , Li(I) are reported in Figure 6.1. Herein, we have explored the effect of Hartree-Fock (HF) exchange and the basis set on the accuracy of $U^0{}_{Red}$ for $X_5[PW_{11}M(H_2O)O_{39}]$. The employment of larger basis sets (TZ2P, QZ4P) positively shifted potentials for Mn(III/II) and Fe(III/II) couples providing closer reproductions of the literature, compared to triple-ζ + polarization (TZP) basis sets. By contrast, increasing basis set size produced poorer estimations of Co(III/II) couples, for example, $U^0{}_{Error}$ for $Li_5[PW_{11}Co(H_2O)O_{39}]$ increased from 0.43 to 0.66 V.

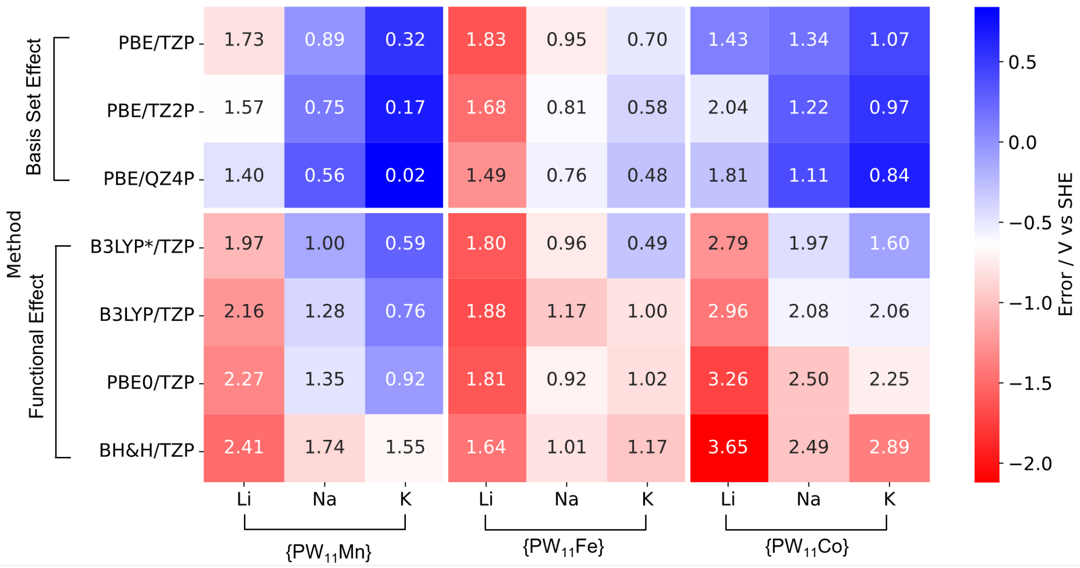

Method		{PW₁₁Mn}			{PW₁₁Fe}			{PW₁₁Co}		
		Li	Na	K	Li	Na	K	Li	Na	K
Basis Set Effect	PBE/TZP	1.73	0.89	0.32	1.83	0.95	0.70	1.43	1.34	1.07
	PBE/TZ2P	1.57	0.75	0.17	1.68	0.81	0.58	2.04	1.22	0.97
	PBE/QZ4P	1.40	0.56	0.02	1.49	0.76	0.48	1.81	1.11	0.84
Functional Effect	B3LYP*/TZP	1.97	1.00	0.59	1.80	0.96	0.49	2.79	1.97	1.60
	B3LYP/TZP	2.16	1.28	0.76	1.88	1.17	1.00	2.96	2.08	2.06
	PBE0/TZP	2.27	1.35	0.92	1.81	0.92	1.02	3.26	2.50	2.25
	BH&H/TZP	2.41	1.74	1.55	1.64	1.01	1.17	3.65	2.49	2.89

Figure 6.1: Redox potentials, $U^0{}_{Red}$ vs SHE, attributed to $X_5[PW_{11}M(H_2O)O_{39}]$ salts; where X= K(I), Na(I), Li(I) and M = Mn(III/II), Fe(III/II) or Co(III/II).

Hybrid exchange-correlation (x-c) functionals were selected to investigate the influence of Hartree-Fock (HF) exchange on $U^0{}_{Red}$ for $X_5[PW_{11}M(H_2O)O_{39}]$. $U^0{}_{Red}$ computed using GGA–PBE functional (0 % exchange) varied significantly with the choice of the counterion, for example, $\Delta U^0{}_{Error}$ varied from 0.51 to 1.63 V (K(I) → Li(I)). Thereafter, increasing contributions to HF exchange positively shifted potentials producing larger overestimations in $\Delta U^0{}_{Red}$ across all redox couples. Hybrid functionals containing 25 % HF exchange demonstrated small improvements to reducing $\Delta U^0{}_{Error}$, however exceeding this threshold did not provide any improvement. This general positive shifting in $\Delta U^0{}_{Red}$ was attributed to the over-stabilization of the ion-pairs, reported in earlier work.[7]

An important aspect of this investigation was to observe counterion trends to $\Delta U^0{}_{Red}$. Generally, $\Delta U^0{}_{Calc}$ is shown to positively shifted as the ionic radii of the counterion decreases (K(I) → Na(I) → Li(I)) in $X_5[PW_{11}M(H_2O)O_{39}]$, attributed to stronger electrostatic interactions between the

POM and positively charged counterions - see Figure 6.1. For example, $\Delta U^0{}_{Calc}$ computed using B3LYP*/TZP positively shifted by 1100 mV switching from K^+ to Li^+ in $X_5[PW_{11}Co(H_2O)O_{39}]$.

6.2.2 Influence of Ion-Pair Proximity

$U^0{}_{Calc}$ vs SHE, attributed to $X_5[PW_{11}M(H_2O)O_{39}]$ were positively shifted as HF exchange was increased. In our previous work, we rationalized this effect to the over-stabilization of the close contact ion-pairs. The significance of the ion-pair proximity is emphasised by the computed range (PBE 0 % → BH&H 50 %) in O_b–X distances for $X_5[PW_{11}Co(H_2O)O_{39}]$ calculated at 0.016, 0.325, 0.328 Å for Li, Na, and K salts, respectively. Herein, the computed range (PBE 0 % → BH&H 50 %) for the corresponding $\Delta U^0{}_{Calc}$ values were calculated at 2.219, 1.156, 1.816 V for Li, Na, and K salts, respectively. Kaledin and co-workers reported O_b–X for hydrated $[PW_{12}O_{40}][K(H_2O)_{16}]_3$ complexes at 6.0, 6.3, 5.7 Å for M = Li, Na, K, respectively.[23] By contrast, the PBE/TZP optimised model produced average O_b–X distances of 4.19, 4.96, and 5.47 Å in X5[PW11Co(H2O)O39] where X= Li, Na, K, respectively.[23]

Ion–pair proximity was assessed by explicitly locating heteroatom – counterion, d_{P-X}, geometries at discrete intervals, see Figure 6.2. For this work, we have explicitly employed PBE/TZP optimised geometries, followed by single point calculations for each distance interval permitting a more economical route of determining hybrid-based potentials. Expansion of the solvation shell (from the optimised state to 8 Å) negatively shifted computed potentials attributed to reduced electrostatic interactions in the ion – pairing. The significance of d_{P-X} was emphasised by the computed range (6 - 10 Å) in $U^0{}_{Calc}$ for $K_5[PW_{11}Co(H_2O)O_{39}]$ calculated at 0.52 V, employing PBE/TZP methodology. The effect of applied exchange–correlation functional and basis set was assessed. Herein, employment of larger basis sets (TZ2P, QZ4P) provided inferior approximations in reproducing experimental potentials, with respect to triple – ζ + polarization (TZP) basis sets. Employment of hybrid *x*-*c* functionals positively shifted of $U^0{}_{Calc}$ demonstrated by transitioning of $U^0{}_{Calc}$ from 0.90 to 2.16 V ($\Delta U^0{}_{Calc} = 1.26$ V, 6 Å) as HF exchange increased from 0 (PBE/TZP) to 50 % (BH&H/TZP).

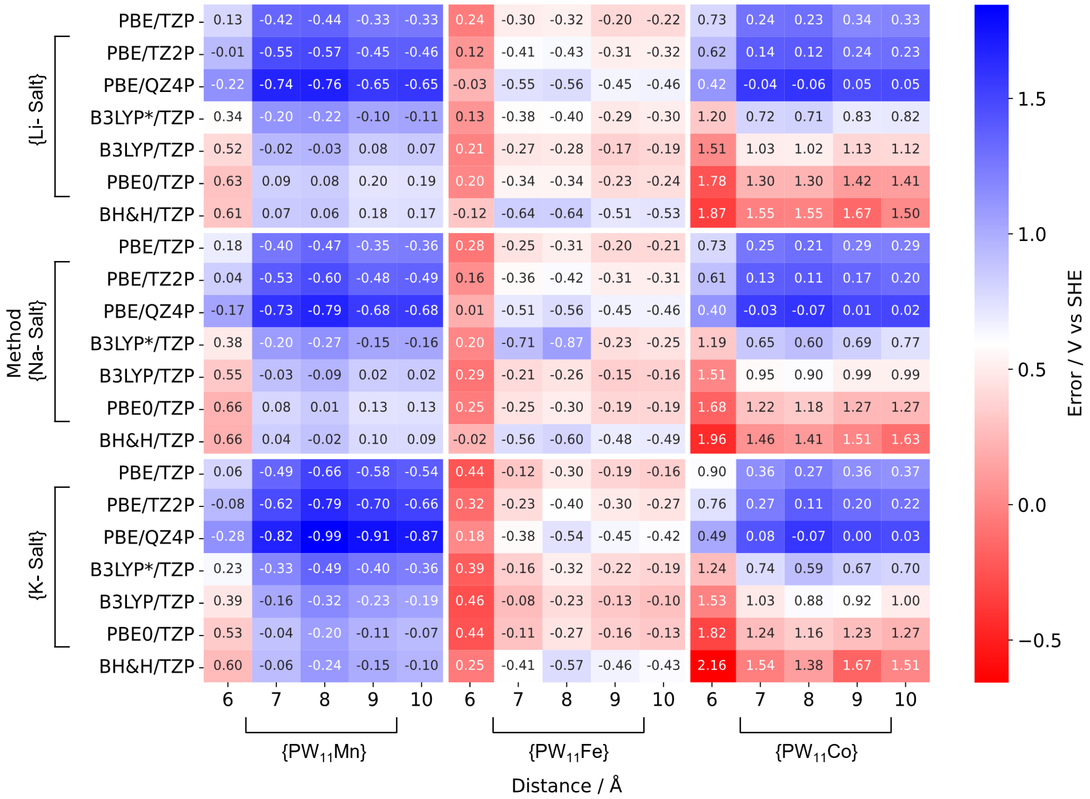

Method		{PW$_{11}$Mn}					{PW$_{11}$Fe}					{PW$_{11}$Co}				
		6	7	8	9	10	6	7	8	9	10	6	7	8	9	10
	PBE/TZP	0.13	-0.42	-0.44	-0.33	-0.33	0.24	-0.30	-0.32	-0.20	-0.22	0.73	0.24	0.23	0.34	0.33
{Li- Salt}	PBE/TZ2P	-0.01	-0.55	-0.57	-0.45	-0.46	0.12	-0.41	-0.43	-0.31	-0.32	0.62	0.14	0.12	0.24	0.23
	PBE/QZ4P	-0.22	-0.74	-0.76	-0.65	-0.65	-0.03	-0.55	-0.56	-0.45	-0.46	0.42	-0.04	-0.06	0.05	0.05
	B3LYP*/TZP	0.34	-0.20	-0.22	-0.10	-0.11	0.13	-0.38	-0.40	-0.29	-0.30	1.20	0.72	0.71	0.83	0.82
	B3LYP/TZP	0.52	-0.02	-0.03	0.08	0.07	0.21	-0.27	-0.28	-0.17	-0.19	1.51	1.03	1.02	1.13	1.12
	PBE0/TZP	0.63	0.09	0.08	0.20	0.19	0.20	-0.34	-0.34	-0.23	-0.24	1.78	1.30	1.30	1.42	1.41
	BH&H/TZP	0.61	0.07	0.06	0.18	0.17	-0.12	-0.64	-0.64	-0.51	-0.53	1.87	1.55	1.55	1.67	1.50
	PBE/TZP	0.18	-0.40	-0.47	-0.35	-0.36	0.28	-0.25	-0.31	-0.20	-0.21	0.73	0.25	0.21	0.29	0.29
{Na- Salt}	PBE/TZ2P	0.04	-0.53	-0.60	-0.48	-0.49	0.16	-0.36	-0.42	-0.31	-0.31	0.61	0.13	0.11	0.17	0.20
	PBE/QZ4P	-0.17	-0.73	-0.79	-0.68	-0.68	0.01	-0.51	-0.56	-0.45	-0.46	0.40	-0.03	-0.07	0.01	0.02
	B3LYP*/TZP	0.38	-0.20	-0.27	-0.15	-0.16	0.20	-0.71	-0.87	-0.23	-0.25	1.19	0.65	0.60	0.69	0.77
	B3LYP/TZP	0.55	-0.03	-0.09	0.02	0.02	0.29	-0.21	-0.26	-0.15	-0.16	1.51	0.95	0.90	0.99	0.99
	PBE0/TZP	0.66	0.08	0.01	0.13	0.13	0.25	-0.25	-0.30	-0.19	-0.19	1.68	1.22	1.18	1.27	1.27
	BH&H/TZP	0.66	0.04	-0.02	0.10	0.09	-0.02	-0.56	-0.60	-0.48	-0.49	1.96	1.46	1.41	1.51	1.63
	PBE/TZP	0.06	-0.49	-0.66	-0.58	-0.54	0.44	-0.12	-0.30	-0.19	-0.16	0.90	0.36	0.27	0.36	0.37
{K- Salt}	PBE/TZ2P	-0.08	-0.62	-0.79	-0.70	-0.66	0.32	-0.23	-0.40	-0.30	-0.27	0.76	0.27	0.11	0.20	0.22
	PBE/QZ4P	-0.28	-0.82	-0.99	-0.91	-0.87	0.18	-0.38	-0.54	-0.45	-0.42	0.49	0.08	-0.07	0.00	0.03
	B3LYP*/TZP	0.23	-0.33	-0.49	-0.40	-0.36	0.39	-0.16	-0.32	-0.22	-0.19	1.24	0.74	0.59	0.67	0.70
	B3LYP/TZP	0.39	-0.16	-0.32	-0.23	-0.19	0.46	-0.08	-0.23	-0.13	-0.10	1.53	1.03	0.88	0.92	1.00
	PBE0/TZP	0.53	-0.04	-0.20	-0.11	-0.07	0.44	-0.11	-0.27	-0.16	-0.13	1.82	1.24	1.16	1.23	1.27
	BH&H/TZP	0.60	-0.06	-0.24	-0.15	-0.10	0.25	-0.41	-0.57	-0.46	-0.43	2.16	1.54	1.38	1.67	1.51

Figure 6.2: Redox potentials, $U^0{}_{Red}$ vs SHE, attributed to $X_5[PW_{11}M(H_2O)O_{39}]$ salts; where X= Li, Na or K, and M = Mn(III/II), Fe(III/II) or Co(III/II).

$U^0{}_{Calc}$ extracted from explicitly located heteroatom – counterion pairs was employed to determine a polynomial relation, enabling the calculation of exact distances, d_{P-X}, by which redox error is minimized, see Figure 6.3. Herein, ion-pairing was restricted to 6- 10 Å, whereby any further constriction of d_{P-X} would lead to impracticable geometries. Figure 6.3 demonstrated that accuracy of $U^0{}_{Calc}$ for $X_5[PW_{11}Mn(H_2O)O_{39}]$ could not be improved past 0.30, 0.21, and 0.26 V where X= Li, Na and K, respectively. Polynomial relations for $X_5[PW_{11}Fe(H_2O)O_{39}]$ revealed ion-pair proximities upon which $U^0{}_{Error} \rightarrow 0$ V. Herein, instances where $U^0{}_{Error} \rightarrow 0$ V correspond to the optimal POM-cation distance to minimize error with respect to the experimental potentials. For potassium-based compounds, $K_5[PW_{11}Fe(H_2O)O_{39}]$, all investigated methods, with the exception of PBE/QZ4P could hypothetically achieve $U^0{}_{Error} \rightarrow 0$ V. All Co-based compounds, $X_5[PW_{11}Co(H_2O)O_{39}]$, computed using BH&H/TZP, intersected with $U^0{}_{Error} \rightarrow 0$ V on several occasions. For example, $Li_5[PW_{11}Co(H_2O)O_{39}]$ demonstrated $U^0{}_{Error} \rightarrow 0$ V with d_{P-X} at 7.137, 7.532, and 9.934 Å. No intersection points for PBE/QZ4P were present.

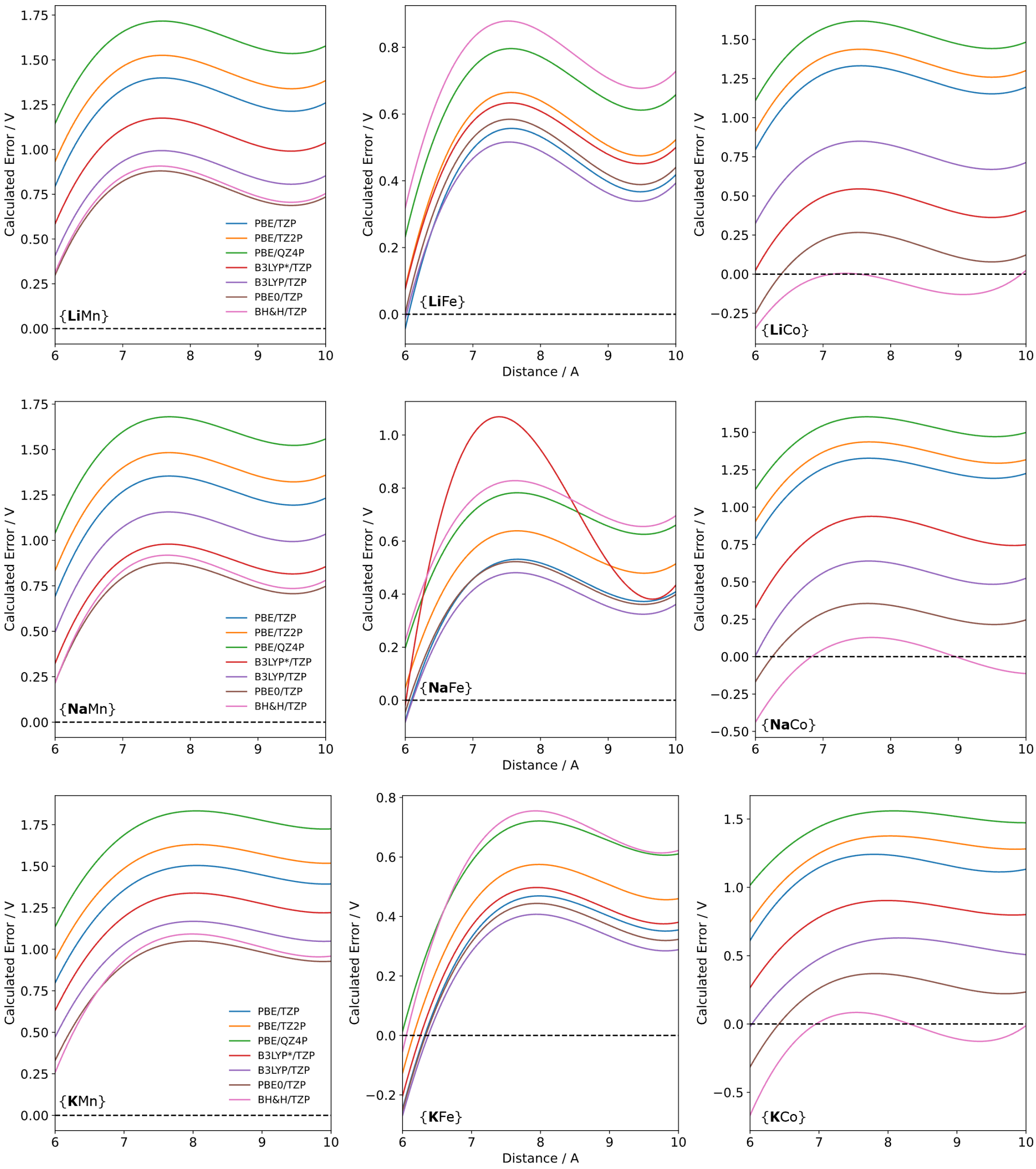

Figure 6.3: Third-order polynomial ($f(x)=ax^3+bx^2+cx+d$) relations calculated using $U^0{}_{Calc}$ obtained from explicitly located ion-pair proximities (6 - 10 Å) intervals.

$U^0{}_{Calc}$ was determined from the intersection points to validate the polynomial ($f(x)=ax^3+bx^2+cx+d$) relations, see Table 6.1. By employing the polynomial relations, $U^0{}_{Error}$ rarely exceed 50 mV. The strongest case was shown for $Li_5[PW_{11}Fe(H_2O)O_{39}]$ which replicated $U^0{}_{Calc}$ within 4 mV. Replication of experimental potentials, $U^0{}_{Exp}$, from GGA functionals outperformed the computationally expensive hybrid methodologies. For example, closest reproduction of $U^0{}_{Exp}$ in $K_5[PW_{11}Fe(H_2O)O_{39}]$ was accomplished using PBE/TZ2P ($U^0{}_{Error}$ = 23 mV) whereas the BH&H functional exceeded $U^0{}_{Error}$ = 250 mV.

Table 6.1: U^0_{Calc} calculated using third-order polynomial ($f(x)=ax^3+bx^2+cx+d$) relation. All potentials were recorded in V vs SHE.

System	Method	d_{P-X}	U^0_{Calc}	U^0_{Error}
$Li_5[PW_{11}Fe(H_2O)O_{39}]$	PBE/TZP	6.049	0.204	-0.004
	B3LYP/TZP	6.016	0.242	-0.042
$Li_5[PW_{11}Co(H_2O)O_{39}]$	PBE0/TZP	6.382	1.543	-0.015
		7.137	1.364	0.140
	BH&H/TZP	7.532	1.336	0.192
		9.934	1.502	0.026
$Na_5[PW_{11}Fe(H_2O)O_{39}]$	PBE/TZP	6.092	0.214	-0.010
	B3LYP*/TZP	6.011	0.194	0.010
	B3LYP /TZP	6.106	0.213	-0.009
	PBE0/TZP	6.056	0.209	-0.005
$Na_5[PW_{11}Co(H_2O)O_{39}]$	PBE0/TZP	6.250	1.627	-0.112
	BH&H/TZP	6.830	1.504	0.011
		8.957	1.566	-0.052
$K_5[PW_{11}Fe(H_2O)O_{39}]$	PBE/TZP	6.321	0.230	-0.036
	PBE/TZ2P	6.156	0.217	-0.023
	B3LYP*/TZP	6.260	-0.063	0.257
	B3LYP/TZP	6.372	-0.048	0.242
	PBE0/TZP	6.334	-0.048	0.242
	BH&H/TZP	6.054	-0.074	0.268
$K_5[PW_{11}Co(H_2O)O_{39}]$	PBE0/TZP	6.026	1.380	0.127
		6.418	1.441	0.066
	BH&H/TZP	6.955	1.428	0.079
		8.313	1.269	0.238

6.3 Conclusions

The purpose of this study has been to systematically study the accuracy of various exchange–correlation (*x*-*c*) functionals in reproducing experimental redox properties in $X_5[PW_{11}M(H_2O)O_{39}]$ salts; where X= Li, Na or K, and M = Mn(III/II), Fe(III/II) or Co(III/II). The *x*-*c* functionals employed in this study were selected on their respective contributions to Hartree-Fock (HF) exchange (0 % PBE, 15 % B3LYP*, 20 % B3LYP, 25 % PBE0, and 50 % BH&H). Herein, increasing contributions to HF-exchange coincided with positive shifting of computed potentials, U^0_{Calc}, attributed to the overstabilisation of the ion-pairing. In some instances, strong sensitivity towards Hartree-Fock (HF) exchange was observed, for example, $Li_5[PW_{11}Co(H_2O)O_{39}]$ salts ranged by $>$ 1000 mV shifting from 0 to 50 % exchange. The effect of the applied basis set, restricted to the GGA-PBE functional was explored. By increasing the size of the basis set (TZP → TZ2P → QZ4P) negative shifting by 200 mV was induced in the calculated potentials.

The current challenge in attaining accurate potentials is effectively controlling the proximity of the ion-pairing. Herein, we explicitly specified the heteroatom – counterion, d_{P-X}, geometries at discrete intervals (6 - 10 Å). Our proposed method permits an economical route for attaining accurate potentials, as opposed to necessitating CPU-expensive optimisations with hybrid *x-c* functionals. Expansion of the solvation shell (from the optimised state to 8 Å) reduced closed-contact electrostatic interactions in the ion-pairing, resulting in a systematic (negative) shifting of computed potentials. The significance of ion-pair proximity was demonstrated by the range in $U^0{}_{Calc}$ for $K_5[PW_{11}Co(H_2O)O_{39}]$ determined at 0.52 V, computed using PBE/TZP.

Polynomial relations were determined using potentials obtained from explicitly located heteroatom – counterion pairs, enabling the minimization of $U^0{}_{Error}$. For example, potassium-based compounds, $K_5[PW_{11}Fe(H_2O)O_{39}]$, with the exception of PBE/QZ4P methods could hypothetically achieve $U^0{}_{Error} \rightarrow 0$ V. In practise, accuracy of up to 89 % was achieved using the PBE/TZ2P method, reporting discrepancies of 23 mV. Application of hybrid methodologies, such as B3LYP*/ TZP in $K_5[PW_{11}Fe(H_2O)O_{39}]$ produced large discrepancies of $\sim$ 260 mV, highlighting current limitations of hybrid third-order polynomial relations. Future work must explore polynomial relations for more reliable modelling with respect to experimental work.

Bibliography

[1] M. T. Pope and G. M. Varga Jr, *Inorganic Chemistry*, 1966, **5**, 1249–1254.

[2] I.-M. Mbomekallé, X. López, J. M. Poblet, F. Sécheresse, B. Keita and L. Nadjo, *Inorganic chemistry*, 2010, **49**, 7001–7006.

[3] X. López, J. A. Fernández and J. M. Poblet, *Dalton Transactions*, 2006, 1162–1167.

[4] P. A. Aparicio, J. M. Poblet and X. López, *Eur. J. Inorg. Chem.*, 2013, **2013**, 1910–1916.

[5] A. Kremleva, P. A. Aparicio, A. Genest and N. Rösch, *Electrochim. Acta*, 2017, **231**, 659–669.

[6] E. Falbo and T. J. Penfold, *J. Phys. Chem. C*, 2020, **124**, 15045–15056.

[7] J. A. Thompson, R. González-Cabaleiro and L. Vilà-Nadal, *Inorg. Chem.*, 2023, **62**, 12260–12271.

[8] G. te Velde, F. M. Bickelhaupt, E. J. Baerends, C. F. Guerra, S. J. A. van Gisbergen, J. G. Snijders and T. Ziegler, *J. Comput. Chem.*, 2001, **22**, 931–967.

[9] J. P. Perdew, K. Burke and M. Ernzerhof, *Phys. Rev. Lett.*, 1996, **77**, 3865–3868.

[10] Y. Wang, J. P. Perdew and K. Burke, *Derivation of a Generalized Gradient Approximation: The PW91 Density Functional*, Plenum Press, New York, 1998.

[11] A. D. Becke, *Phys. Rev. A*, 1988, **38**, 3098–3100.

[12] J. P. Perdew, *Phys. Rev. B*, 1986, **33**, 8822–8824.

[13] M. Reiher, O. Salomon and B. A. Hess, *Theor. Chem. Acc.*, 2001, **107**, 48–55.

[14] C. Lee, W. Yang and R. G. Parr, *Phys. Rev. B*, 1988, **37**, 785–789.

[15] *J. Chem. Phys.*, 1999, **110**, 5029–5036.

[16] A. D. Becke, *J. Chem. Phys.*, 1993, **98**, 1372–1377.

[17] J.-D. Chai and M. Head-Gordon, *J. Chem. Phys.*, 2008, **128**, year.

[18] R. Sure, J. G. Brandenburg and S. Grimme, *ChemistryOpen*, 2016, **5**, 94–109.

[19] E. V. Lenthe and E. J. Baerends, *J. Comput. Chem.*, 2003, **24**, 1142–1156.

[20] E. Van Lenthe, A. Ehlers and E.-J. Baerends, *J. Chem. Phys.*, 1999, **110**, 8943–8953.

[21] C. C. Pye and T. Ziegler, *Theor. Chem. Accounts Theor. Comput. Model.*, 1999, **101**, 396–408.

[22] D. G. Truhlar, C. J. Cramer, A. Lewis and J. A. Bumpus, *J. Chem. Educ.*, 2004, **81**, 596.

[23] A. L. Kaledin, Q. Yin, C. L. Hill, T. Lian and D. G. Musaev, *Dalton Trans.*, 2020, **49**, 11170–11178.

Chapter 7

High Temperature Ammonia Synthesis using Mono-Substituted Polyoxotungstates

This chapter outlines the growing importance of producing ammonia. Section 7.1 outlines the current challenges faced by heterogeneous catalysis of ammonia, referencing mechanistic studies using DFT calculations. We present the first study of heterogeneous ammonia synthesis using POMs and compare against current leaders in the field.

7.1 Introduction

Nitrogen is an essential element necessary to sustain oceanic and terrestrial life on Earth. This element is abundant in the Earth's atmosphere as a diatomic gas. The molecular bond is inert due to the high bond enthalpy (940.95 kJ mol^{-1}) and zero dipole moment. Hence, most multicellular organisms will use fixed resources i.e ammonia (NH_3) and nitrate ($NO_3{}^{-}$) for sources of nitrogen.[1,2] The availability of fixed nitrogen resources has an acute agricultural and ecological significance because they are often the limiting nutrients in most biological ecosystems.[1,2] Throughout the nineteenth century, Sir William Crookes had been exploiting sewage waste of London for agricultural purposes. However, it became apparent that simple recycling of sewage waste was not sustainable for ensuring the supply of wheat.[3] In 1898, his Presidential Address to the British Association called for the Advancement of Science to provide an economical route for fixing nitrogen for use as fertiliser.[3] In 1908, Fritz Haber and Carl Bosch introduced an artificial procedure for ammonia synthesis using high pressure hydrogen and nitrogen at elevated temperatures (650–750 K) and pressures (150-300 atm), shown by Equation 7.1.[4–6] Haber-Bosch processes obtain hydrogen from fossil fuel sources such as natural gas, oil and coal which raises doubts regarding its sustainability. The Haber-Bosch process consumes fossil fuels such as natural gas and coal contributing to global anthropogenic carbon dioxide emissions estimated around 1-2 %.[4–6]

$$3\,H_2(g) + N_2(g) \longrightarrow 2\,NH_3(g) \tag{7.1}$$

The aforementioned reaction is exothermic under standard conditions ($\Delta H^\circ = -92$ kJ mol^{-1}). Theoretically, the ammonia equilibrium concentration can be increased by employing high pressures coupled with low temperatures, according to Le Chatelier's principle.[6] However, under standard conditions, the formation rate is extremely slow and unsuitable for industry. Hence, the Haber–Bosch process is run using extreme temperatures (650–750 K) and pressures (150-300 atm).[4–6] Further energy costs are introduced with the production of hydrogen which is sourced from steam-methane reforming (SMR) and water-gas shift (WGS) processes.[4–6]

The active catalyst is derived from iron oxides, $Fe_{1-x}O$, Fe_2O_3, and Fe_3O_4, known as wüstite, hematite, and magnetite, respectively.[7–10] The activity of single crystal iron catalysts is dependent on orientation of the faces. Somorjai *et al.* reported the Fe(111) and Fe(211) crystal faces are the most active due to the presence of C_7 sites.[7–10] Incorporated into the formulation are electronic and structural promoters to improve activity. The nature of electronic (potassium) promoters has been shown to enhance reaction kinetics by facilitating dissociative chemisorption of nitrogen.[10–12] The electronic promoter facilitates the pronounced charge transfers from the metal d-band to π^* orbitals of the adsorbed N_2 molecule, enabling stronger back donation and weakening the N-N bond.[10] The structural promotor, typically in the form of alumina, stabilises the active Fe(111) planes and is involved in restructuring the less active surfaces, such as: Fe(110).[8] The proposed mechanism involves the reaction of alumina with iron to form the spinel structure: $FeAl_2O_4$, which serves as a template for surfaces with the (111) and (211) planes.[8]

Ammonia synthesis, at Fe(111) surfaces, proceeds via a Langmuir–Hinshelwood mechanism in which dissociative chemisorption of nitrogen is the rate determining step, see Equation 7.2 - 7.7.[13,14]

$$\mathrm{N_2\,(g) + 2\,^* \rightarrow 2\,N^*} \tag{7.2}$$

$$\mathrm{H_2\,(g) + 2\,^* \rightarrow 2\,H^*} \tag{7.3}$$

$$\mathrm{N^* + H^* \rightarrow NH^* + {}^*} \tag{7.4}$$

$$\mathrm{NH^* + H^* \rightarrow NH_2{}^* + {}^*} \tag{7.5}$$

$$\mathrm{NH_2{}^* + H^* \rightarrow NH_3{}^* + {}^*} \tag{7.6}$$

$$\mathrm{NH_3{}^* \rightarrow NH_3\,(g) + {}^*} \tag{7.7}$$

* corresponds to a vacant surface site. In this mechanism, significant energy inputs are required for dinitrogen dissociation, hence the high pressure/temperature system employed in current industrial processes.

The Haber-Bosch process is credited with the sustenance of approximately 30 % of the global population.[4–6] However, this process is highly energy intensive, requiring elevated temperatures (650–750 K) and pressures (150-300 atm) to achieve acceptable turnover. By contrast, the bacterial enzyme, nitrogenase reduces dinitrogen to ammonia under ambient conditions (< 40 °C, atmospheric pressure) utilising protons, electrons, and the hydrolysis of adenosine triphosphate (ATP) - see Figure 7.1.[2,15,16] Since its discovery, significant interest in understanding how nitrogenase activates one of the most inert molecular bonds to provide the foundations for achieving the highly desirable, and so far unmet, goal of developing sustainable and efficient synthetic strategies for producing ammonia.

Consequently, development of new chemical systems seeking to mimic the FeMo-co site in nitrogenase have been reported. Peters *et al.*, 2014 demonstrated successful binding and reduction of dinitrogen with $[(CPR_3)Fe–N_2]$ ($R = {}^i$Pr) generating 4.6 ± 0.8 equivalents NH_3/Fe using excess potassium graphite (KC_8) in Et_2O at -78 °C under 1 atm N_2.[17] The presence of carbon in the inner coordination sphere was used to mimic the interstitial carbon located at the center of the iron-molybdenum cofactor (FeMo-co).[17,18] A further study by Kuriyama *et al.*, 2016 utilising a $[Co(N_2)(^{R}PNP)]$ ($R={}^t$Bu, ^{t}BuPNP= 2,5-bis(di-tert-butylphosphinomethyl)pyrrolide complex demonstrated nitrogen reduction producing 4.2 ± 0.1 NH_3 equivalents.[19] The electron rich P- based ligand was used to stabilise Co under various oxidation states through π-back bonding

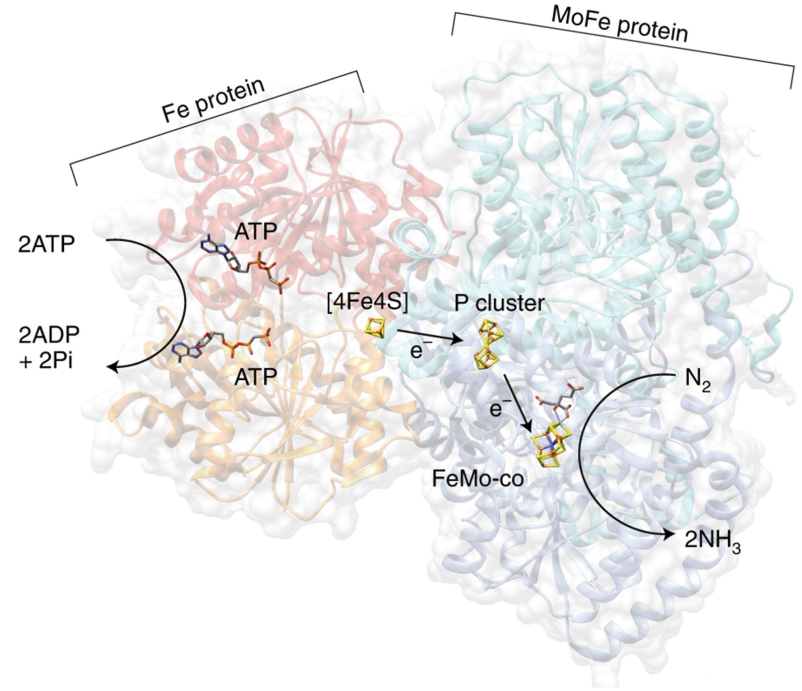

Figure 7.1: Crystal structure of the nitrogenase enzyme comprising of the Fe and MoFe proteins for electron transfer. The flow of electrons is initiated by the association of the reductase domain (Fe protein) to the intermediate P cluster then the catalytic domain (MoFe protein) enabling catalysis. Figure taken from Foster *et al.*, 2018.[1]

to the empty d-orbitals of Co. The ammonia yield increased to 15.9 ± 0.2 with the use of 200 and 184 equivalents of KC_8 and$[H(OEt_2)_2]BArF_4$.[19] The quantity and cost of the aforementioned reducing agent and proton sources required to achieve acceptable yields continues to be a significant drawback.

Studies seeking to mimic the nitrogenase FeMo-co structure have took to incorporating sulphur and carbon atoms into the inner coordination sphere of ammonia catalysts. Mercado *et al.*, 2015 synthesised the first Fe complex containing FeMo-co analogue ligands (sulphur and carbon) and demonstrated N_2 binding.[20] The group observed upon reduction, an Fe- S bond dissociated for a weakened Fe-N_2 bond to form. Whilst the catalyst displayed a promising activity profile over time, a significant amount catalytically inactive complexes were produced diminishing its industrial viability. The flexibility of the Fe–C interaction has been thought to greatly influence the binding of dinitrogen to a single Fe site. A two-coordinate $[(CAAC)_2Fe]$ complex [CAAC = cyclic(alkyl)(amino)carbene] was shown to bind and catalytically fixate dinitrogen through a flexible three-coordinate $[(CAAC)_2Fe(N_2)]$ system, at T < 80 °C.[21] Unfortunately, the activity of the catalyst is highly temperature dependent, and proved ineffective at room temperature producing only 0.4 ± 0.2 NH_3 equivalents.[21]

In a similar manner, the incorporation of hydrides into the inner coordination sphere to mimic the bridging hydrides of FeMo-co have been reported. A notable study by Arnet *et al.*, 2015 investigated the nitrogen binding efficiency of a diiron sulfide complex with a hydride incorporated into the inner coordination sphere.[22] The reactions with nitrogenase substrates demonstrated that the hydride can behave as a base or nucleophile and reduction of the iron atoms allows binding to N_2. Attempts to mimic the morphology of FeMo-co have led to the development of $[Mo_3S_4Ti]$

clusters capable of fixating nitrogen.[23] The catalyst demonstrated greater catalytic activity in the presence of HCl with respect to H_2O producing 0.12 and 0.29 equivalents of NH_3 respectively.[23] Unfortunately, this reaction obligates the employment of excess amounts of oxidation agents (KC_8) which diminishes the commercial viability of this process. Further attempts by Zhang *et al.*, 2020 demonstrated using first-principles calculations that a Fe_2/MoS_2 cluster exhibited high catalytic activity for electrochemical nitrogen reduction reaction (NRR) with an impressive overpotential of 0.21 V.[24] Rather worryingly, no yield was reported so it is unclear how the activity compares to other examples in the literature.[24]

Metal nitrides have emerged as a promising class of heterogeneous ammonia catalysts, where activity comparable, or even exceeding, conventional classes of catalyst.[25] Before the development of the Haber-Bosch catalyst, uranium nitride was considered for Haber-Bosch. Uranium could be promoted to yield an ammonia synthesis yield between 1.0 - 2.5 % at 550 °C and 100 pressures.[26] However, its cost was expensive which impeded its application to industry. Early studies by Mittasch drew attention to molybdenum metal as under ammonia synthesis conditions, detectable level of nitride were discovered during catalysis, later identified as the active form of the catalyst. Molybdenum nitride was reported to generate an ammonia synthesis yield of 1.5 % under 550 °C and 100 pressures.[26] Favourable combinations with iron, cobalt, nickel, and promoting with alkali metals were shown to improve the activity of the material. Promoted molybdenum was shown to yield ammonia at 4.0 % under 550 °C and 100 atmospheres pressure.[26]

Later, the development of ternary molybdenum nitrides have been shown to exceed the activity shown by binary nitrides.[27] Considerable interest in Co_3Mo_3N-related catalysts and when suitably promoted, can exceed the activity of conventional iron based Haber–Bosch catalysts. The high activity of Co_3Mo_3N was attributed to the intermediate nitrogen binding energy obtained from combining two metals. Density Functional Theory (DFT) calculations were employed to determine the turnover frequency (TOF) as a function of nitrogen binding energy, (E_N), demonstrating the averaged binding energy of the two metals approaches the optimum in terms of turnover frequency (TOF).[28] The high activity of Fe and Ru, the building blocks of the two current industrial processes, are shown. Early work by Mittasch recognised the high activity of osmium outlining an interesting group trend within the d-block elements.[26] Theoretical calculations have proven insightful for the study of elementary mechanistic steps of ammonia synthesis. Hargreaves *et al.* proposed that cobalt-molybdenum nitride proceeds through a Eley–Rideal/Mars–van Krevelen (associative) mechanism.[29] The energy barrier of the rate-determining step (RDS) a 90 kJ mol$^{˘1}$ was smaller smaller for the E-R/MvK mechanism because the hydrogen reacts directly with surface activated nitrogen.[29] The competing Langmuir–Hinshelwood (dissociative) mechanism proceeds by homolysis of the diatomic nitrogen before being hydrogenated.[29]

Thermal decomposition of tetrabutylammonium (TBA) salts $(TBA)_4H_3[PW_{11}O_{39}]$ and $(TBA)_4$-$H_x[PW_{11}M(H_2O)O_{39}]\cdot nH_2O$, x = 3-(oxidation number of M), M = Mn(II), Co(II), Ni(II), Cu(II) or Fe(III), n = 0–3 were investigated by thermogravimetric analysis.[30] The minimum temperature to onset of decomposition for $(TBA)_x[PW_{11}M(H_2O)O_{39}]$; M = Mn(II), Fe(III), Co(II), Ni(II), Cu(II), varied ca. 45 °C across the metal-substituted compounds. Initial decomposition of $(TBA)_7[PW_{11}O_{39}]$ started at a higher temperature relative to the former compounds.[30] Decomposition of the parent compound began at ca. 310 °C before becoming destroyed at 600 °C.[30] Later, Ilhan and co-workers employed TGA–DTA–MS and TGT techniques to study the thermal decomposition mechanism of ammonium phosphotungstate hydrate ($(NH_4)_3(PW_{12}O_{40})\cdot{}_xH_2O$ (APhT) in inert gas.[31] The authors reported a thermal stability of 640 K for anhydrous APhT after which conversion to cubic structure phosphotungstate bronze ($(PO_2)_2(WO_3)_{24}$, PhTB) which is stable up to 1250 K.[31] Further decomposition liberates a mixture comprising of light black coloured WO_3 and $(PO)_2(WO_3)_{16}$ mixture.[31]

The development of new chemical systems capable of producing ammonia using lower energy inputs and sustainably sourced hydrogen would have significant economic and environmental benefits. The production of ammonia at ambient temperatures would allow for a more favourable equilibrium position. Furthermore, any modification that allows for ammonia synthesis at lower pressures and temperatures would significantly reduce overall production costs. Future batch processes for ammonia production must also be scalable to meet a growing global demand. To date, no work has investigated the efficacy of mono-transition-metal-substituted polyoxotungstates as ammonia synthesis catalysts despite their broad catalytic scope.[32–34] In this study, we seek to explore the efficacy of mono-substituted clusters as heterogeneous ammonia catalysts and establish a relationship between metal composition and activity.

7.2 Results & Discussion

7.2.1 Pre-Reaction

FT-IR spectra of the mono-substituted salts, $K_5[PW_{11}M(H_2O)O_{39}]$ where M = Mn, Fe Co, Ni, Cu, Zn displayed vibrational bands in the range of 800 - 1200 cm^{-1}. The position of $\upsilon(W\text{-}O_t)$ bands (tungsten-terminal oxygen) were observed between 955 - 960 cm^{-1}. The P–O stretching vibrations attributed to the central tetrahedron in Keggin anion, $[PW_{12}O_{40}]^{3-}$ give rise to one band observed at ca. 1080 cm^{-1}. This vibrational band is split into two for the substituted complexes attributed to the asymmetric stretching of the P–O bonds. This vibrational splitting was localised between 1060-1070 cm^{-1} across all compounds.

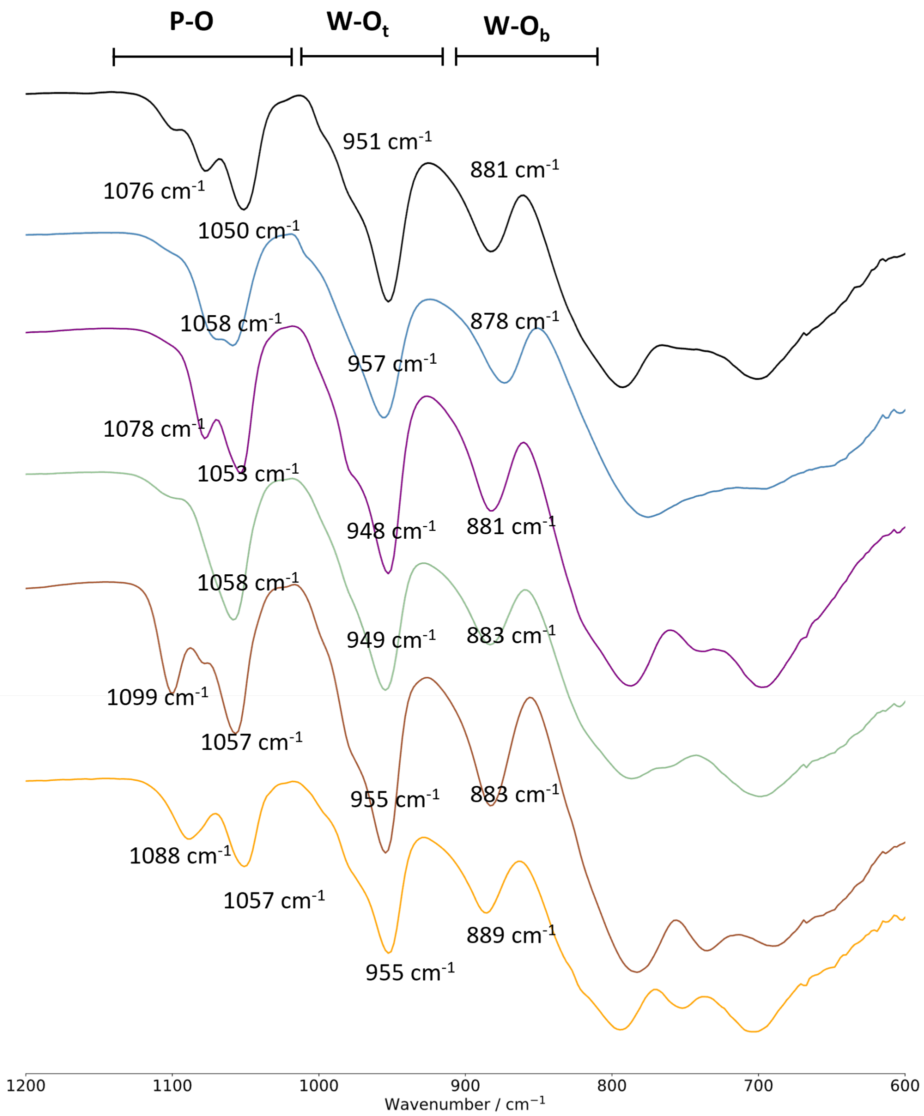

Figure 7.2: FT-IR Spectra for pre-reacted $K_5[PW_{11}M(H_2O)O_{39}]$. Colours corresponding to Mn (black), Fe (blue), Co (purple), Ni (green), Cu (brown), and Zn (yellow).

UV-Vis spectra for the investigated complexes presented characteristic UV bands at 260 nm which was attributed to the O → W charge transfer transition. However, $d \rightarrow d$ charge bands have previously been reported by Santos and co workers using compounds with 1-alkyl-3-methylimidazolium cations.[35] ^{31}P NMR was used to confirm the incorporation of the transition-metal. NMR spectroscopy was unsuitable for some candidates because of the paramagnetic nature of transition metal centres resulting in very short T_1 and T_2 relaxation times. This limitation restricted NMR analysis to $K_5[PW_{11}M(H_2O)O_{39}]$ where M= Co(II) and Zn(II) compounds. The formation of the diamagnetic $K_5[PW_{11}Zn(H_2O)O_{39}]$ compound was confirmed by the presence of a singlet at -12.19 ppm, deshielded by $\sim$ 3.0 ppm relative to parent Keggin compound. ^{31}P singlet for $K_5[PW_{11}Co(H_2O)O_{39}]$ compound was detected at 462.34 ppm, significantly deshielded relative to the parent Keggin compounds, attributed to the paramagnetic shift.[36]

7.2.2 Ammonia Synthesis Rate

The procedure used to determined the ammonia synthesis rates, see Chapter 3, began by testing a blank reactor which generated an average yield of ca. 0.5 μmol h^{-1} g^{-1}. Table 7.1 reports synthesis rates which were calculated by interpolating linear reductions in conductivity, corresponding to the consumption of protons by NH_3, with respect to time. Herein, steady state ammonia synthesis rates, under 400 °C and ambient pressure, were calculated as shown in Appendix D.

The activity for ammonia production of the corresponding clusters was investigated at 400 °C for 8 hrs under under N_2/H_2 (1:3). The vent gas was bubbled through a solution of 0.00108 M H_2SO_4 and the conductivity was measured. Reactions performed at steady state will present a linear decrease in conductivity as a function of time. We seek to establish relationship between metal composition and activity. Analysis of the mono-substituted potassium salts, $K_5[PW_{11}M(H_2O)O_{39}$ suggest the incorporated transition metal had a significant impact on synthesis rate ranging from 20.7 $\{PW_{11}Mn\}$ to 7.8 μmol h^{-1} g^{-1} $\{PW_{11}Cu\}$. All precursor compounds produced comparatively poor ammonia synthesis yields, not exceeding 6 μmol h^{-1} g^{-1}. Ammonia synthesis rates generated from the aforementioned compounds are insignificant when compared against Co_3Mo_3N reported by Aika and Kojima (652 μmol h^{-1} g^{-1}) using similar conditions.[27]

Table 7.1: Ammonia synthesis rates for tested potassium salts at 400 °C under 3:1 H_2/N_2, conducted under supervision of Dr. Angela Daisley.

System	Load / g	Rate / μmol h^{-1} g^{-1}
Blank	N/A	0.53
$K_5[PW_{11}Mn(H_2O)O_{39}]$	0.309	20.09
$K_5[PW_{11}Fe(H_2O)O_{39}]$	0.301	11.90
$K_5[PW_{11}Co(H_2O)O_{39}]$	0.309	18.88
$K_5[PW_{11}Ni(H_2O)O_{39}]$	0.303	12.66
$K_5[PW_{11}Cu(H_2O)O_{39}]$	0.303	7.72
$K_5[PW_{11}Zn(H_2O)O_{39}]$	0.305	9.38
Co_3Mo_3N	0.4	652

Note: Co_3Mo_3N treated at 673 K under 0.1 MPa with a flow rate of 60 ml min^{-1} of 3:1 N_2: H_2 ratio, as reported by Aika and Kojima.[27]

7.2.3 Post-Reaction

FT-IR spectra for tested mono-substituted salts, $K_5[PW_{11}M(H_2O)O_{39}]$ where M = Mn, Fe revealed two bands within 1060-1070 cm^{-1} due to the asymmetric stretching of the P–O bonds. By contrast, the splitting υ_{as}(P–O) vibrations was not observed for the remaining catalysts. Previous work by Gamelas and co-workers demonstrated that disappearance of the υ_{as}(P–O) splitting occurred within the range of 280–310°C range, the specific temperature of which varied with the salt considered.[30] FT-IR spectra of $K_5[PW_{11}Co(H_2O)O_{39}]$ revealed a singular υ(P–O) vibration within 1075–1078 cm^{-1} coinciding with frequencies of the parent compound.[30] In this study, breakdown of υ(P–O) vibrations for $K_5[PW_{11}M(H_2O)O_{39}]$ where M = Ni, Cu, and Zn suggests poorer thermal stability of the compounds strongly correlating with the temperatures (ca. 450°C) of decomposition reported by Gamelas and co-workers.[30]

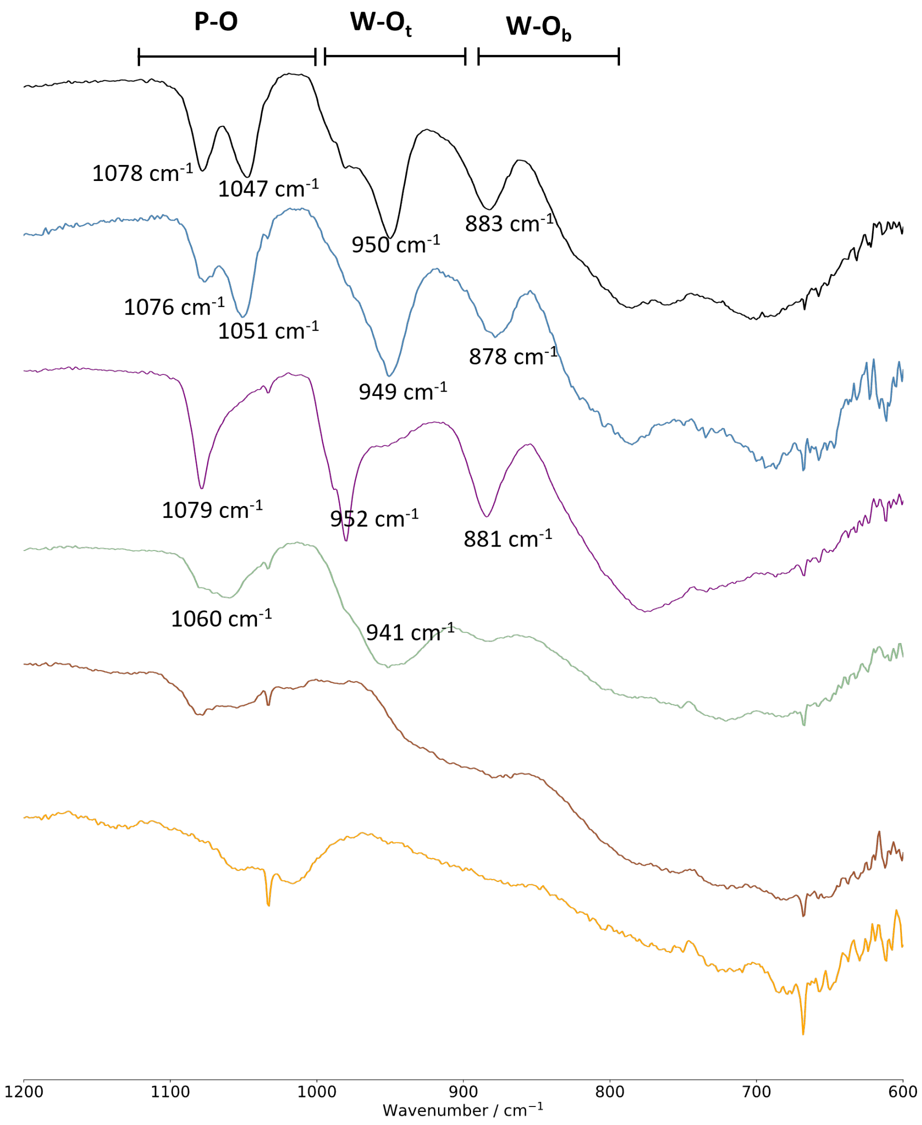

Figure 7.3: FT-IR Spectra for post reacted $K_5[PW_{11}M(H_2O)O_{39}]$. Colors corresponding to Mn (black), Fe (blue), Co (purple), Ni (green), Cu (brown), and Zn (yellow).

Powder X-ray diffraction (XRD) experiments were performed for phase identification of the crystalline material. Note, XRD patterns for $K_5[PW_{11}M(H_2O)O_{39}]$; M= Ni, Cu were performed by Mr Mohamed Hosny Elsayed Mostafa Mahmoud. XRD patterns recorded post reaction for the mono-substituted salts, $K_5[PW_{11}M$- (H_2O) $O_{39}]$, where M = Mn, Fe, and Co, have noticeably presented the characteristic peaks corresponding to Figure 7.4. XRD patterns for $K_5[PW_{11}M(H_2O)O_{39}]$, where M = Ni, Cu, and Zn have shown the crystal structure has decomposed under ammonia synthesis conditions. The decomposition product has a distinct dark blue colour, which alongside XRD patterns confirmed the presence of phosphotungstate bronze, $(PO_2)_2(WO_3)_{24}$ crystals. These findings correlated with previous work by Yusufoglu and co-workers who confirmed the presence of dark blue of phosphotungstate bronze $(PO_2)_2(WO_3)_{24}$ crystals with XRD patterns following thermal decomposition (> 640 K) of ammonium phosphotungstate hydrate.[31] Evidently, mono-substituted salts, $K_5[PW_{11}M$- (H_2O) $O_{39}]$ as ammonia synthesis are unsuitable due to a lack of thermal stability. Future work should focus on expansion to more thermally stable POM clusters, for example, Wells-Dawson which may represent a feasible step in identifying more efficacious ammonia synthesis POM catalysts.

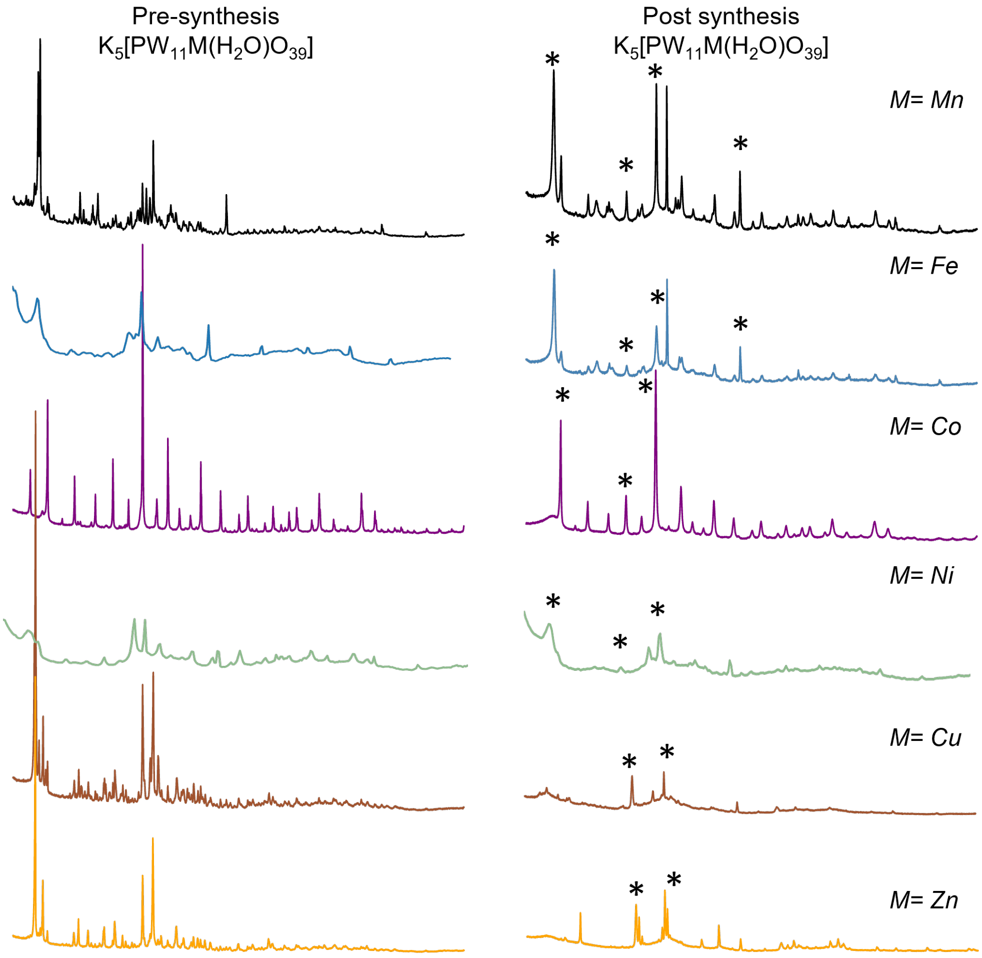

Figure 7.4: XRD patterns for pre- and post reaction samples. * corresponds to phosphotungstate bronze, $(PO_2)_2(WO_3)_{24}$ crystals reported previously by Roy and co-workers.[37] Colors corresponding to Mn (black), Fe (blue), Co (purple), Ni (green), Cu (brown), and Zn (yellow). Note that XRD patterns for $K_5[PW_{11}M(H_2O)O_{39}]$; M= Ni, Cu were performed by Mr Mohamed Hosny Elsayed Mostafa Mahmoud.

7.3 Conclusions

The purpose of this study has been to systematically study the efficacy of mono-substituted salts, $K_5[PW_{11}M(H_2O)O_{39}]$ at 400 °C under 3:1 H_2/N_2. The significance of the metal composition in $K_5[PW_{11}M(H_2O)O_{39}]$ was demonstrated by the range in ammonia synthesis rates of 12.37 μmol h^{-1} g^{-1}. In this study, the most active catalyst was $K_5[PW_{11}Mn(H_2O)O_{39}]$ reporting a rate of 20.09 μmol h^{-1} g^{-1}, whilst $K_5[PW_{11}Zn(H_2O)O_{39}]$ only produced 7.72 μmol h^{-1} g^{-1}. The comparatively poor thermal stability of $K_5[PW_{11}M(H_2O)O_{39}]$; where M = Ni, Cu, and Zn raises doubts over its suitability, confirmed by the breakdown of μ(P-O) shown using IR. XRD patterns suggest the crystal structure had decomposed into phosphotungstate bronze $(PO_2)_2(WO_3)_{24}$ crystals which show little to no activity.

FT-IR spectra on the post-reaction catalysts revealed the disappearance of the two bands attributed to the asymmetric stretching of the P–O bond upon heating. The breakdown of υ(P–O) vibrations for $K_5[PW_{11}M(H_2O)O_{39}]$; M = Ni, Cu, and Zn comparatively poorer thermal stability correlating with the temperatures (°C) of decomposition in previous work. FT-IR Spectra of the $K_5[PW_{11}Co(H_2O)O_{39}]$ compound revealed a singular υ(P–O) vibration within 1075–1078 cm^{-1} coincide with frequencies of the parent compound, suggesting liberation of the peripheral heteroatom. XRD patterns for $K_5[PW_{11}M(H_2O)O_{39}]$, where M = Ni, Cu, and Zn have shown the crystal structure has decomposed during ammonia synthesis conditions. XRD patterns confirm the decomposition products are comprised of phosphotungstate bronze $(PO_2)_2(WO_3)_{24}$ crystals.

No previous work has studied the efficacy of mono-transition-metal-substituted polyoxotungstates as heterogeneous ammonia catalysts despite their broad catalytic scope. However, the activity of mono-substituted salts, $K_5[PW_{11}M(H_2O)O_{39}]$ falls short of the current leaders in ammonia synthesis. Future work should continue to explore the relationship between metal composition and activity. The recyclability of the Keggin unit during catalysis is a hindrance for its application to ammonia synthesis. Therefore, future work should focus on clusters which demonstrated comparatively greater thermal stability, such as Wells-Dawson compounds.

Bibliography

[1] S. L. Foster, S. I. P. Bakovic, R. D. Duda, S. Maheshwari, R. D. Milton, S. D. Minteer, M. J. Janik, J. N. Renner and L. F. Greenlee, *Nat. Catal.*, 2018, **1**, 490–500.

[2] B. M. Hoffman, D. Lukoyanov, Z.-Y. Yang, D. R. Dean and L. C. Seefeldt, *Chem. Rev.*, 2014, **114**, 4041–4062.

[3] A. Bashford, *Soil and Food: Agriculture and the Fertility of the Earth*, Columbia University Press, 2014.

[4] J. Humphreys, R. Lan and S. Tao, *Adv. Energy Sustainability Res.*, 2021, **2**, 1–23.

[5] D. R. MacFarlane, P. V. Cherepanov, J. Choi, B. H. Suryanto, R. Y. Hodgetts, J. M. Bakker, F. M. F. Vallana and A. N. Simonov, *Joule*, 2020, **4**, 1186–1205.

[6] V. Kyriakou, I. Garagounis, A. Vourros, E. Vasileiou and M. Stoukides, *Joule*, 2020, **4**, 142–158.

[7] N. Spencer, R. Schoonmaker and G. Somorjai, *J. Catal.*, 1982, **74**, 129–135.

[8] D. Strongin, S. Bare and G. Somorjai, *J. Catal.*, 1987, **103**, 289–301.

[9] G. A. Somorjai and N. Materer, *Top. Catal.*, 1994, **1**, 215–231.

[10] G. P. Connor and P. L. Holland, *Catal. Today*, 2017, **286**, 21–40.

[11] K.-i. Aika, H. Hori and A. Ozaki, *J. Catal.*, 1972, **27**, 424–431.

[12] D. Strongin and G. Somorjai, *J. Catal.*, 1988, **109**, 51–60.

[13] P. Stoltze and J. Nørskov, *J. Catal.*, 1988, **110**, 1–10.

[14] C. D. Zeinalipour-Yazdi, J. S. J. Hargreaves, S. Laassiri and C. R. A. Catlow, *Royal Soc. Open Sci.*, 2021, **8**, 210952.

[15] H. L. Rutledge and F. A. Tezcan, *Chem. Rev.*, 2020, **120**, 5158–5193.

[16] R. D. Milton, R. Cai, S. Abdellaoui, D. Leech, A. L. De Lacey, M. Pita and S. D. Minteer, *Angew. Chem. Int. Ed.*, 2017, **56**, 2680–2683.

[17] S. E. Creutz and J. C. Peters, *J. Am. Chem. Soc.*, 2014, **136**, 1105–1115.

[18] Y. Lee, N. P. Mankad and J. C. Peters, *Nature Chem.*, 2010, **2**, 558.

[19] S. Kuriyama, K. Arashiba, H. Tanaka, Y. Matsuo, K. Nakajima, K. Yoshizawa and Y. Nishibayashi, *Angew. Chem.*, 2016, **128**, 14503–14507.

[20] I. Čorić, B. Q. Mercado, E. Bill, D. J. Vinyard and P. L. Holland, *Nature*, 2015, **526**, 96–99.

[21] G. Ung and J. C. Peters, *Angew. Chem. International Edition*, 2015, **54**, 532–535.

[22] N. A. Arnet, T. R. Dugan, F. S. Menges, B. Q. Mercado, W. W. Brennessel, E. Bill, M. A. Johnson and P. L. Holland, *J. Am. Chem. Soc.*, 2015, **137**, 13220–13223.

[23] Y. Ohki, K. Uchida, M. Tada, R. E. Cramer, T. Ogura and T. Ohta, *Nature Comms.*, 2018, **9**, 1–6.

[24] H. Zhang, C. Cui and Z. Luo, *The Journal of Physical Chemistry C*, 2020, **124**, 6260–6266.

[25] J. S. J. Hargreaves, *Coord. Chem. Rev.*, 2013, **257**, 2015–2031.

[26] A. Mittasch and A. C. Frankenburg, W, 1950, **2**, 81–104.

[27] R. Kojima and K.-i. Aika, *Appl. Catal. A-Gen.*, 2001, **215**, 149–160.

[28] C. J. Jacobsen, S. Dahl, B. S. Clausen, S. Bahn, A. Logadottir and J. K. Nørskov, *J. Am. Chem. Soc.*, 2001, **123**, 8404–8405.

[29] C. D. Zeinalipour-Yazdi, J. S. J. Hargreaves and C. R. A. Catlow, *J. Phys. Chem. C.*, 2018, **122**, 6078–6082.

[30] J. A. Gamelas, F. A. Couto, M. C. N. Trovão, A. M. Cavaleiro, J. A. Cavaleiro and J. D. P. de Jesus, *Thermochim. Acta*, 1999, **326**, 165–173.

[31] S. Ilhan, A. Kalpakli, C. Kahruman and I. Yusufoglu, *Thermochim. Acta*, 2012, **546**, 1–7.

[32] S. H. Szczepankiewicz, C. M. Ippolito, B. P. Santora, T. J. Van de Ven, G. A. Ippolito, L. Fronckowiak, F. Wiatrowski, T. Power and M. Kozik, *Inorg. Chem.*, 1998, **37**, 4344–4352.

[33] Y. Cui, L. Shi, Y. Yang, W. You, L. Zhang, Z. Zhu, M. Liu and L. Sun, *Dalton Trans.*, 2014, **43**, 17406–17415.

[34] H. G. T. Ly, G. Absillis and T. N. Parac-Vogt, *New. J. Chem.*, 2016, **40**, 976–984.

[35] F. M. Santos, P. Brandão, V. Félix, H. I. Nogueira and A. M. Cavaleiro, *Polyhedron*, 2015, **101**, 109–117.

[36] W. B. Swanson, D. Tabaczynski, D. Lis, E. Zurek and M. Kozik, *Polyhedron*, 2021, **204**, 115174.

[37] S. C. Roy, W. Assenmacher, T. Linden, L. Esser, W. Mader and R. Glaum, *Z. Naturforsch. B*, 2016, **71**, 543–552.

Chapter 8

Summary and Outlook

8.1 Conclusion

In this thesis, the molecular and electronic behaviour of Keggin-based polyoxometalates in different physical environments have been investigated by means of Density Functional Theory (DFT) and validated our models with experimental testing.

To summarise, we have achieved the following:

- Developed an accurate computational method to calculate experimental redox potentials for mono-substituted polyoxotungstates, $X_5[XW_{11}M(H_2O)O_{39}]$; where Mn(III/II), Fe(III/II), Co(III/II) and X = Li, Na and K.

- Expanded on previous methodology for calculating ^{31}P δ_{Exp} by expanding to Keggin, $[PW_{12}O_{40}]^{3-}$ and corresponding lacunary clusters: $[PW_{11}O_{39}]^{7-}$, $[\text{A-}PW_9O_{34}]^{9-}$ and $[\text{B-}PW_9O_{34}]^{9-}$.

- We investigated the potential of mono-substituted polyoxotungstates, $K_5[XW_{11}M(H_2O)O_{39}]$; where M = Mn(II), Fe(II), Co(II), Ni(II), Cu(II), Zn(II) as ammonia synthesis catalysts under 400°C under 3:1 H_2/N_2.

We have demonstrated the one-electron redox processes can significantly distort molecular geometries of $[PW_{11}M(H_2O)O_{39}]^{q-}$ (see Chapter 3). In particular, one-electron oxidation significantly distorted the inner coordination sphere of M present within $[PW_{11}M(H_2O)O_{39}]^{q-}$; where M= Mn or Co. This behaviour was attributed to their electronic nature, whereby the frontier molecular orbitals contained significant σ^* antibonding character. This is no longer true for $[PW_{11}M(H_2O)O_{39}]^{q-}$; where M= Fe or Ru because due to FMOs having predominantly non-bonding character. From this example, we have emphasised the importance of accounting for enthalpic, entropic, and zero-point contributions in redox modelling. Thereafter, we presented a systematic review of several exchange-correlation functionals and basis sets in reproducing observed redox potentials, $U^0{}_{red}$ vs SHE. The structural benchmark confirmed that both GGA and hybrid functionals produce comparable geometries, both of which were in close agreement with the literature. However, these classes of functionals return very different results with respect to the electronic structure. In Chapter 3, we have demonstarted that hybrid x–c functionals generally outperformed GGA methodologies by reducing $U^0{}_{Error}$ across the M(III/II) redox couples. A prominent example was shown with $U^0{}_{Error}$ in $[PW_{11}Mn(H_2O)O_{39}]^{q-}$ which decreased by ca. 73 % from 1.03 to 0.28 V by incorporating B3LYP*/TZP (15 %) as opposed to PBE/TZP (0 %). However, the optimal functional was not consistent across all redox couples. In addition, we have shown discrepancies between computed and observed potential increased as a function of molecular charge of the system. This was attributed to the increasing contribution of the self-interaction error. To address this, POM clusters were charge neutralised by alkali-metal (potassium) counterions such that the self-interaction error (SIE) is reduced. However, uncertainties can arise from the highly charged nature of POMs that generate a strong electrostatic attraction with the surrounding counterions leading to an over-stabilization of the close contact ion-pairs. We have rationalised this behaviour of the ion-pair systems to the selection of the exchange-correlation functional in which $U^0{}_{Calc}$ was positively shifted as the contribution to Hartree-Fock exchange was increased. The significance of ion-pair proximity was shown by the range in O_b–K of ca. 0.2 Å in $K_5[PW_{11}Co(H_2O)O_{39}]$ (0 % PBE to 50 % BH&H) which reflected in the range of 1.29 V for $U^0{}_{Calc}$.

We expanded on this work by investigating the effect of the alkali-metal counterion for reproducing observed potentials in $X_5[PW_{11}M(H_2O)O_{39}]$ (Chapter 5). We observed large uncertainties arose for Li-based systems attributed to the strong electrostatic attraction with the POM cluster leading to extreme over-stabilization effects in the close contact ion-pairs. The significance of ion-pairing was evidenced by $U^0{}_{Error}$ of 0.51 to 1.63 V for K^+ and Li^+ counterions, respectively. Furthermore, increasing contributions to HF exchange positively shifted computed potentials which further contributed to the detriment of Li-based systems. Therefore, optimisation-based approaches are generally unsuitable for redox modelling due to unpredictable over-stabilization effects and significant computational expense. To address this issue, we have presented a new proposal which uses PBE/TZP optimised geometries, followed by single point calculations for each distance interval permitting an economical route of obtaining hybrid-based potentials. The proximity was assessed by explicitly locating heteroatom – counterion, d_{PX} geometries at discrete intervals. We observed expansion of the solvation shell beyond 8 Å negatively shifted potentials which were attributed to reduced attractive electrostatic forces. Analogous to our previous work, strong dependencies on pairing was shown, for example, $U^0{}_{Calc}$ in $K_5[PW_{11}Co(H_2O)O_{39}]$ ranged by 0.52 V, across 6 - 10 Å intervals employing PBE/TZP. Within this approach, all iterations of $U^0{}_{Calc}$ were collected, enabling the exact calculation for d_{P-X} at which $U^0{}_{Error}$ is minimized. By employing the polynomial relations, we could report $U^0{}_{Error}$ as low as 4 mV observed for for $Li_5[PW_{11}Fe(H_2O)O_{39}]$. In this approach, GGA functionals outperformed the more expensive hybrid methodologies. An example given is $K_5[PW_{11}Fe(H_2O)O_{39}]$ which revealed $U^0{}_{Error}$ of 23 and 250 mV using PBE/TZ2P and BH&H/TZP, respectively.

In addition to redox modelling, we have explored electronic and structural properties of POM by simulating their ^{31}P NMR spectra (Chapter 4). In this work, we compared the accuracy of anionic and charge neutralised systems in reproducing observed ^{31}P chemical shifts, δ_{Exp}. We observed that all spectra were in close agreement with the observed suggesting, therefore, such simulations are an effective tool for investigating structural changes of POMs. We observed for the anionic systems that hybrid x–c functionals proved superior in reproducing $\delta_{Exp}(^{31}P)$ with respect PBE/TZP optimised systems couple with either triple-ζ plus polarization (TZ2P) or quadruple-ζ plus polarization (QZ4P) basis sets. This was attributed to the expansion of the central tetrahedron which increased as a function of exact exchange. Generally, incorporation of explicitly located counterions had minimal impact on ^{31}P NMR spectra, often deshielding signals by $<$ 2 ppm. However, notable exceptions were observed for $Na_8H[B{-}PW_9O_{34}]$ which remain challenging to model due to direct electrostatic interaction between the central tetrahedron and alkali metal cations. However, we have shown reasonable accuracy can be achieved with correctional fitting.

Finally, pioneering work exploring the capability of POMs as heterogeneous ammonia catalysis was explored. In this work, we have compared the efficacy of several (first-row) metal-substituted Keggin clusters in which we reported the transition metal had a significant impact on synthesis rate ranging from 20.7 $\{PW_{11}Mn\}$ to 7.8 μmol h^{-1} g^{-1} $\{PW_{11}Cu\}$. Powder X-ray diffraction revealed peaks corresponding to phosphotungstate bronze $(PO_2)_2(WO_3)_{24}$ crystals suggesting decomposition of the catalyst during synthesis. Furthermore, FT-IR spectroscopy further suggested breakdown of the $K_5[PW_{11}M(H_2O)O_{39}]$ (M = Ni, Cu, Zn) cluster due to removal of υ(P–O) vibration. The limited thermal stability will likely inhibit their application for industrial use.

8.2 Future Outlook

DFT approaches remain the most feasible approach to quantitatively reproduce redox potentials and equilibrium geometries of POMs, however, it is not without its limits. The composition of POMs, i.e transition metals present a significant challenge to most exchange-correlation functionals. To achieve highly accurate analysis of POM redox potentials will require significant benchmarking to document the strengths and limitations of each *x-c* functional, for any specific case. Such work would provide adequate information for the training of machine learning algorithms, capable of theorising redox waves for new POM complexes.

Our current work for POM-catalysed ammonia synthesis is so far, limited to Keggin-based compounds, however, expansion to more thermally stable POM clusters, for example, Wells-Dawson clusters represent a feasible step in identifying more efficacious ammonia synthesis POM catalysts due to their inherently improved thermal stability. Further efforts into identifying key intermediate species, such as, nitrogen binding interactions with POM clusters is currently unknown. Identification of these reactive intermediates would allow for the computational study of mechanisms which can be used to explore structure-activity relationships.

Chapter 9

Appendices

9.1 Appendix A

This section provides further information in relation to Chapter 4: "Reducing Systematic Uncertainty in Computed Redox Potentials for Aqueous Transition- Metal-Substituted Polyoxotungstates".

9.1.1 Molecular Orbital Diagrams

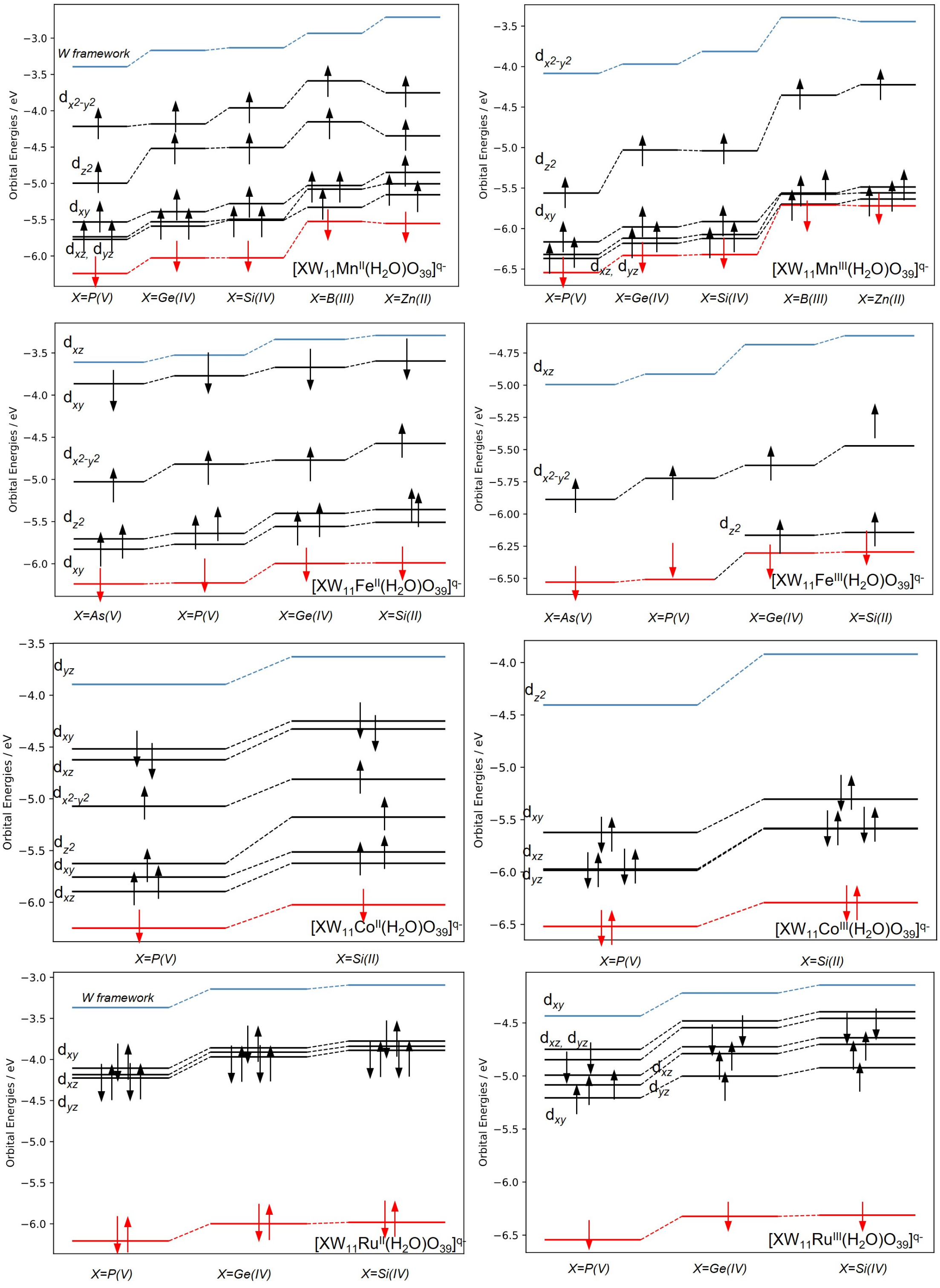

Figure 9.1: Schematic molecular orbital diagram for Mn(III/II), Fe(III/II), Co(III/II), and Ru(III/II) couples present in $[XW_{11}M(H_2O)O_{39}]^{q-}$; X= As(V), Si(IV), Ge(IV), B(III), Zn(II) calculated at the PBE/TZP level of theory. All energies were reported in eV.

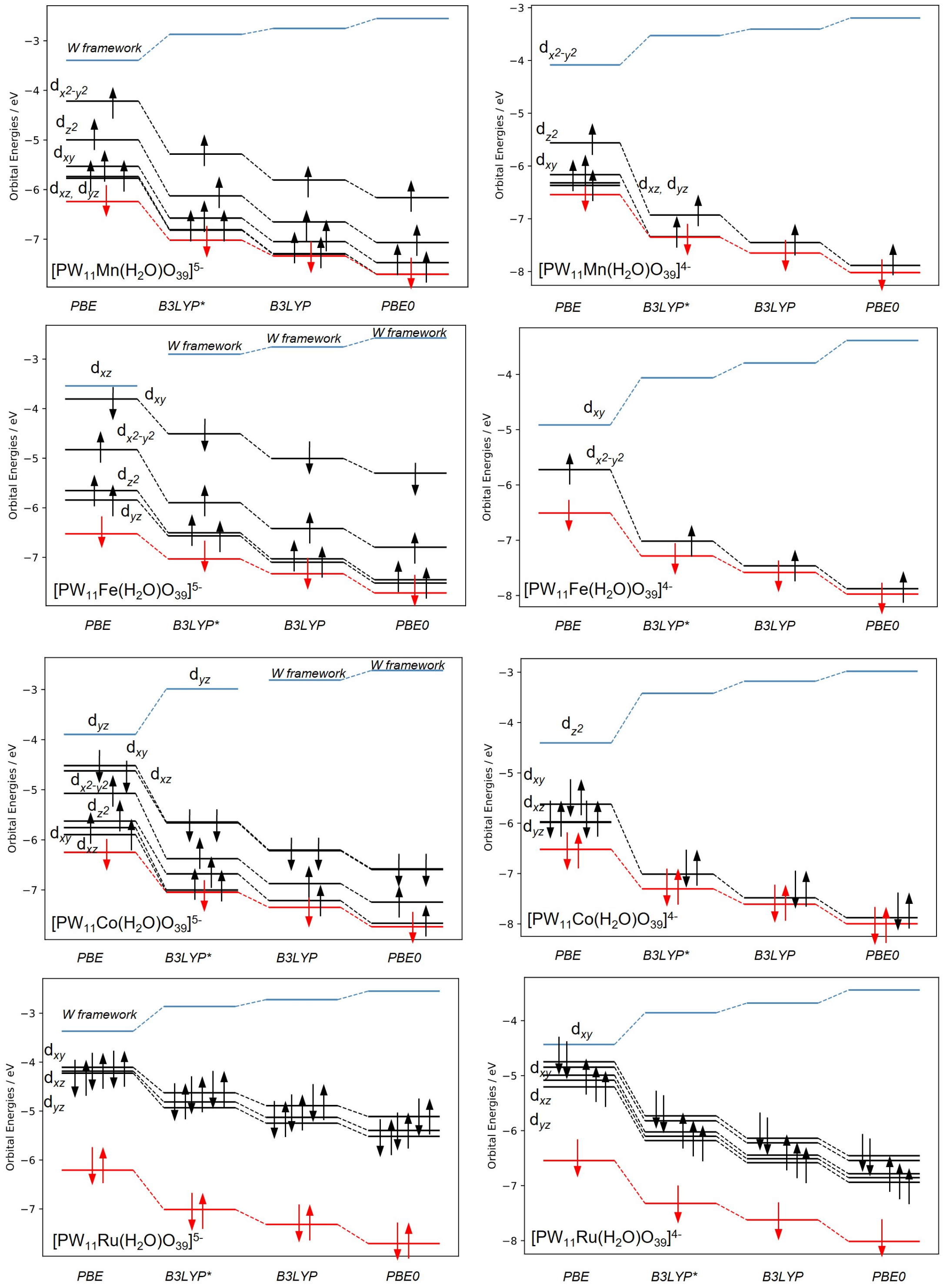

Figure 9.2: Schematic molecular orbital diagram for Mn(III/II), Fe(III/II), Co(III/II), and Ru(III/II) couples present in $[PW_{11}M(H_2O)O_{39}]^{q-}$ performed using GGA-PBE and hybrid functionals selected on their respective contributions of Hartree-Fock (HF) exchange (15 % B3LYP*, 20 % B3LYP, 25 % PBE0, and 50 % BHH).

9.1.2 Molecular Geometries

Table 9.1: Optimized geometries of $[PW_{11}M(H_2O)O_{39}]^{q-}$ performed using PBE / TZP. Bond lengths and angles reported in Å and °, respectively.

$[PW_{11}M(H_2O)O_{39}]^{q-}$	O_c-P	O_c-M	O_t-M	O_{a1}-M	O_{b2}-M	O_{a1}-W	O_{b2}-W	O_{a1}-M-O_{b2}
$[PW_{11}Mn(H_2O)O_{39}]^{4-}$	1.555	2.302	2.338	1.940	1.923	1.880	1.868	173.2
$[PW_{11}Mn(H_2O)O_{39}]^{5-}$	1.558	2.377	2.303	2.137	2.048	1.829	1.833	168.0
$[PW_{11}Fe(H_2O)O_{39}]^{4-}$	1.565	2.236	2.179	2.021	1.963	1.859	1.864	171.3
$[PW_{11}Fe(H_2O)O_{39}]^{5-}$	1.562	2.275	2.226	2.047	2.013	1.840	1.833	170.8
$[PW_{11}Co(H_2O)O_{39}]^{4-}$	1.586	1.964	1.976	1.910	1.917	1.877	1.844	177.1
$[PW_{11}Co(H_2O)O_{39}]^{5-}$	1.561	2.248	2.202	2.072	2.013	1.831	1.824	173.5
$[PW_{11}Ru(H_2O)O_{39}]^{4-}$	1.579	2.129	2.151	2.029	2.028	1.881	1.859	178.3
$[PW_{11}Ru(H_2O)O_{39}]^{5-}$	1.576	2.149	2.166	2.066	2.031	1.849	1.831	177.4

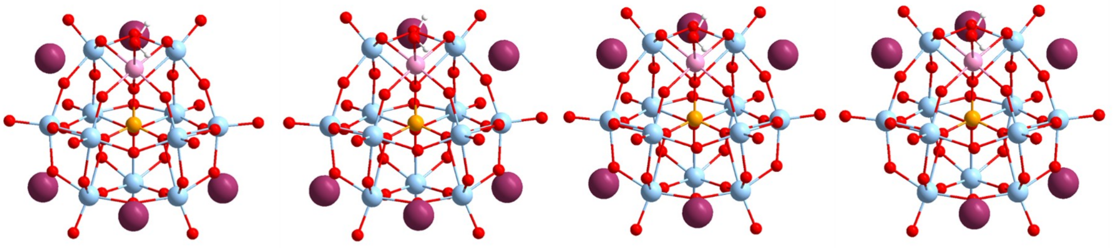

Isomer- A Isomer- B Isomer- C Isomer- D

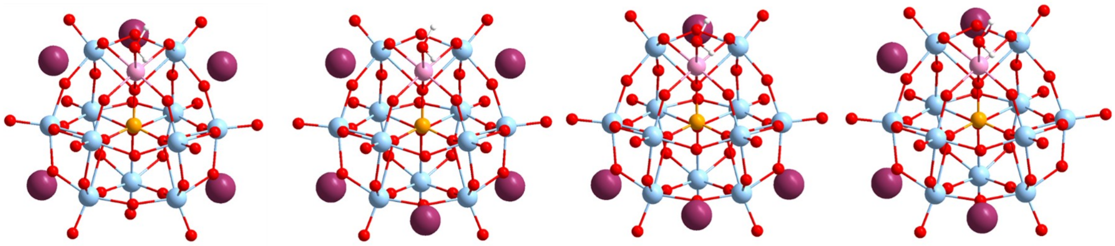

Isomer- E Isomer- F Isomer-A, B Isomer-A, C

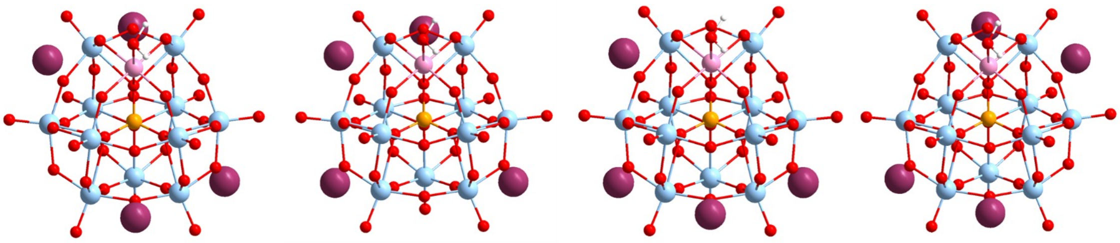

Isomer-A, D Isomer-A, E Isomer-A, F Isomer-B, C

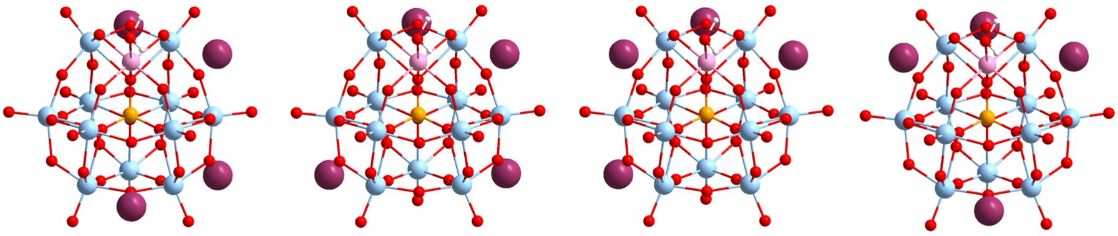

Isomer-B, D Isomer-B, E Isomer-B, F Isomer-C,D

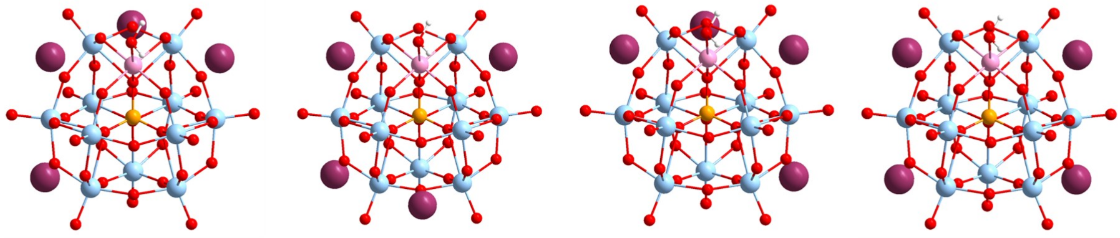

Isomer-C, E Isomer-C, F Isomer-D, E Isomer-E, F

Figure 9.3: All cation arrangements for $K_x[PW_{11}M(H_2O)O_{39}]$; x = 4 or 5. The isomers were labelled based on vacancies. For example, isomer-D corresponds to the isomer without a cation-oxygen interaction at pocket D

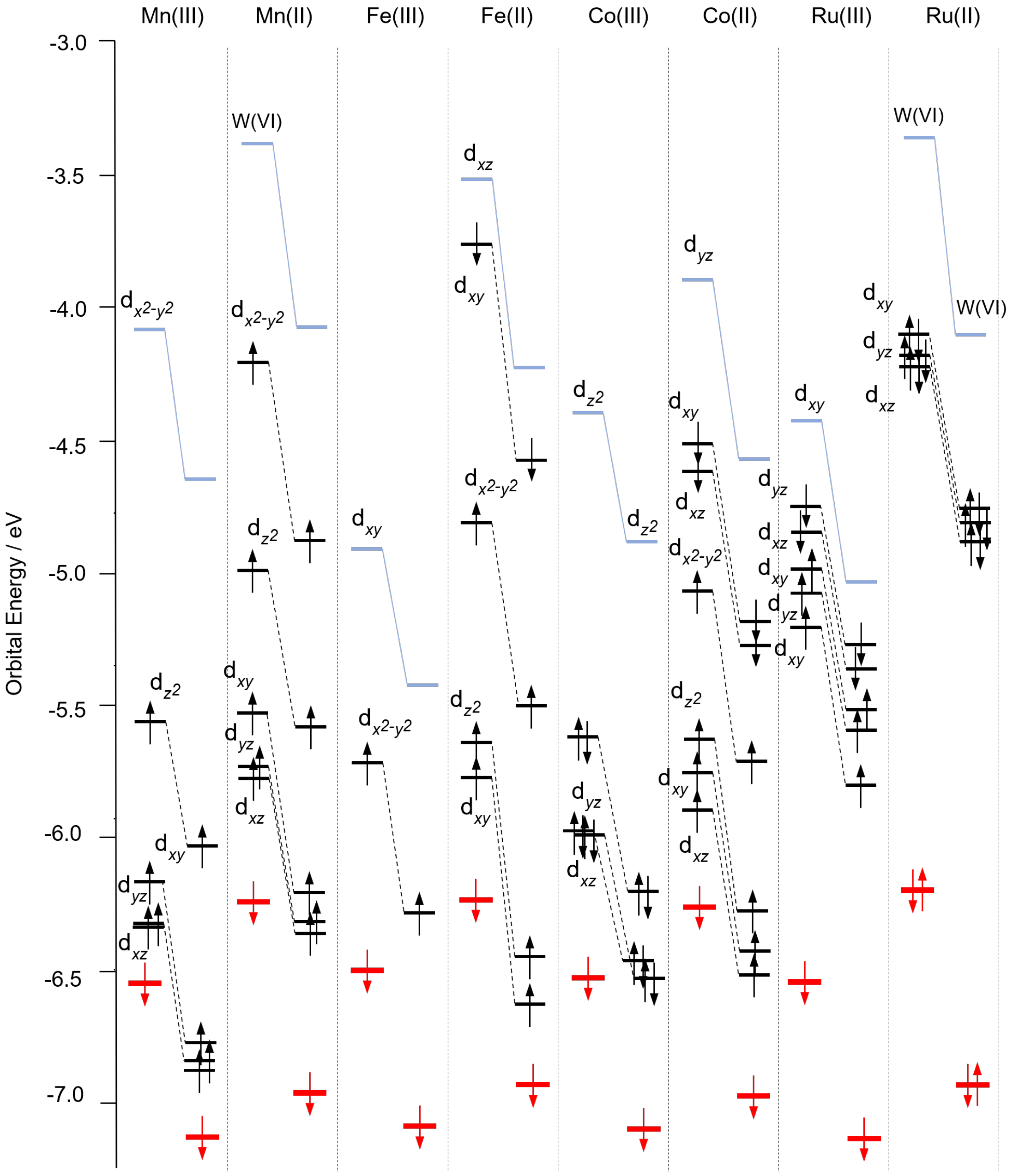

Figure 9.4: Schematic molecular orbital diagram for [PW$_{11}$M(H$_2$O)O$_{39}$]$^{q-}$ (left) and corresponding K$_x$[PW$_{11}$M(H$_2$O)O$_{39}$]$^{q-x}$; x= 4 or 5 (right) optimized using PBE/TZP level of theory. Colours correspond to red = O2(p), blue = W, and black = transition-metal. All orbital energies reported in eV.

Table 9.2: Optimized geometric parameters of the A and A,D isomers in $K_x[PW_{11}M(H_2O)O_{39}]^{q-x}$; x= 4 or 5 performed using PBE /TZP. Bond lengths and angles reported in Å and °, respectively.

$K_x[PW_{11}M(H_2O)O_{39}]$	O_c-P	O_c-M	O_t-M	O_{a1}-M	O_{b2}-M	O_{a1}-W	O_{b2}-W	O_{a1}-M-O_{b2}
$K_4[PW_{11}Mn(H_2O)O_{39}]$	1.557	2.414	2.258	2.167	2.039	1.831	1.825	166.8
$K_5[PW_{11}Mn(H_2O)O_{39}]$	1.554	2.316	2.292	1.949	1.920	1.891	1.860	172.7
$K_4[PW_{11}Fe(H_2O)O_{39}]$	1.564	2.256	2.150	2.027	1.955	1.868	1.858	170.6
$K_5[PW_{11}Fe(H_2O)O_{39}]$	1.562	2.302	2.162	2.099	1.996	1.837	1.824	169.4
$K_4[PW_{11}Co(H_2O)O_{39}]$	1.585	1.967	1.966	1.919	1.913	1.880	1.843	177.1
$K_5[PW_{11}Co(H_2O)O_{39}]$	1.560	2.251	2.151	2.067	2.066	1.839	1.829	173.4
$K_4[PW_{11}Ru(H_2O)O_{39}]$	1.578	2.131	2.140	2.036	2.018	1.891	1.851	177.0
$K_5[PW_{11}Ru(H_2O)O_{39}]$	1.574	2.253	2.150	2.077	2.019	1.856	1.825	177.0

9.2 Appendix B

This section provides further information in relation to Chapter 6: "Computation of ^{31}P NMR Chemical Shifts in Keggin-based Polyoxotungstates".

9.2.1 Nuclear Magnetic Resonance (NMR)

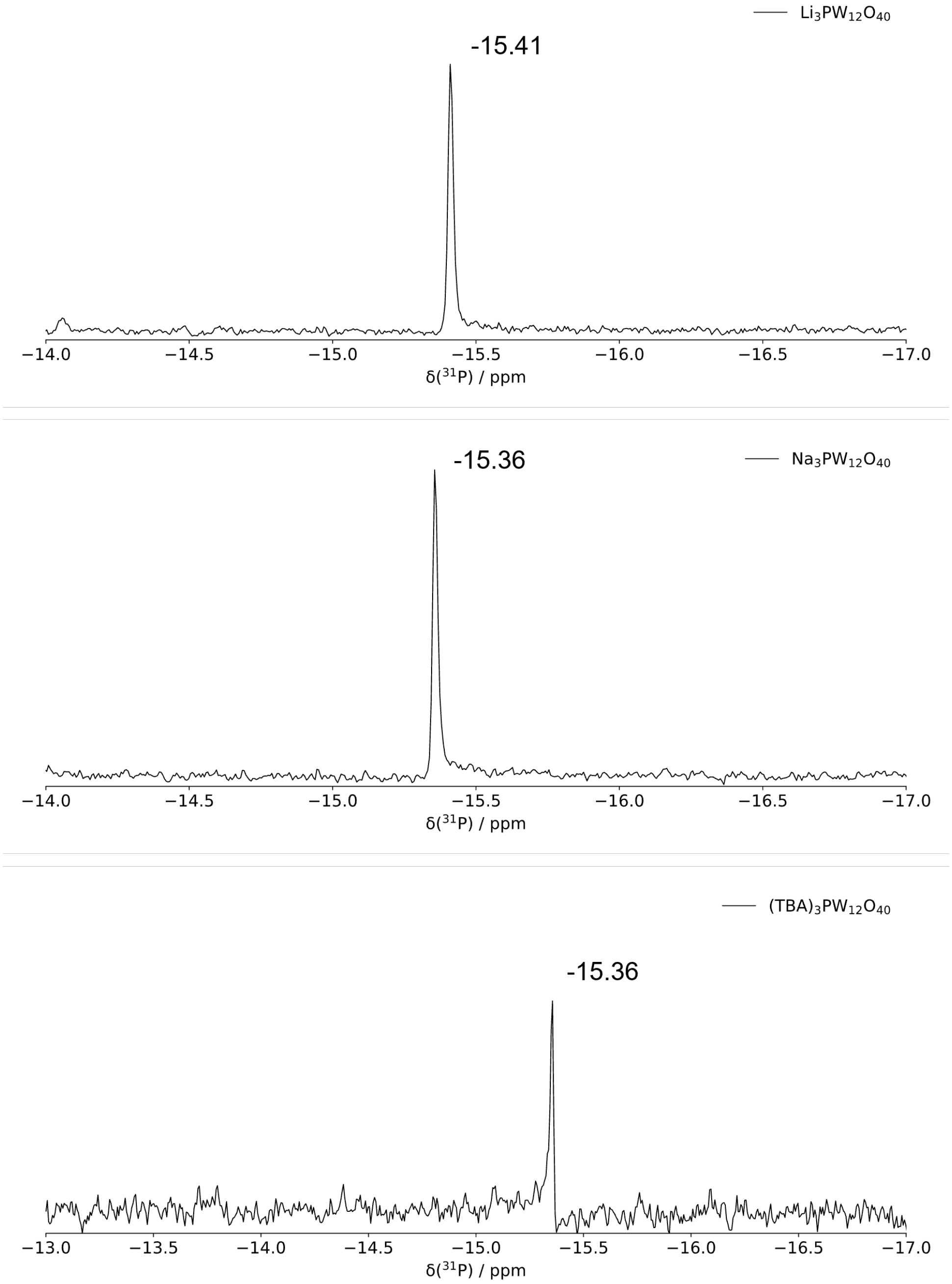

Figure 9.5: ^{31}P spectra of 50 mg Keggin, $X_3[PW_{12}O_{40}]$ ($X = Li^+$, Na^+, TBA^+) samples, recorded in D_2O. $TBA_3[PW_{12}O_{40}]$ salts (50 mg) were recorded in CD_3CN.

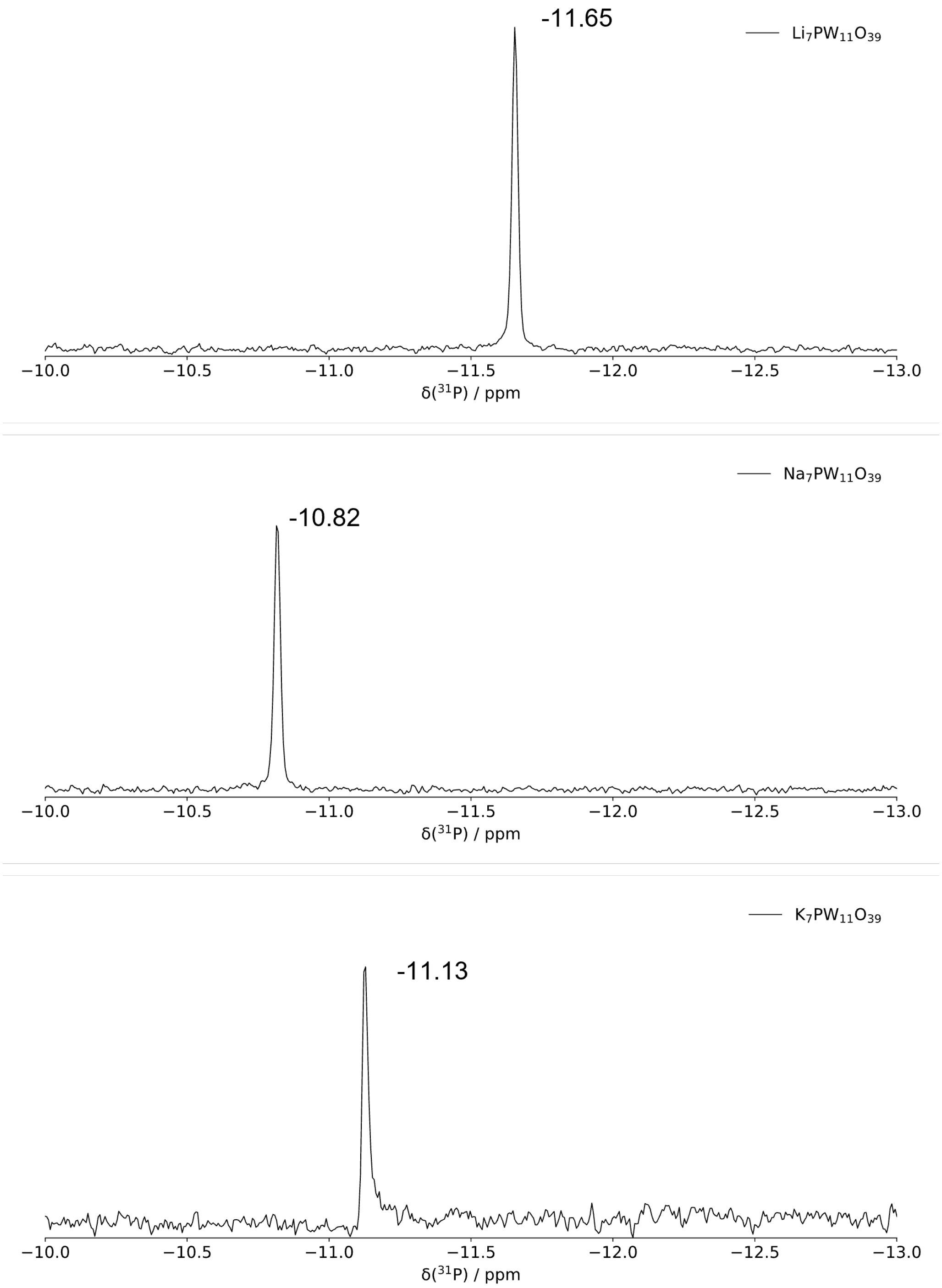

Figure 9.6: ^{31}P spectra of 50 mg mono-lacunary Keggin, $X_7[PW_{11}O_{39}]$ ($X = Li^+$, Na^+, K^+) samples, recorded in D_2O.

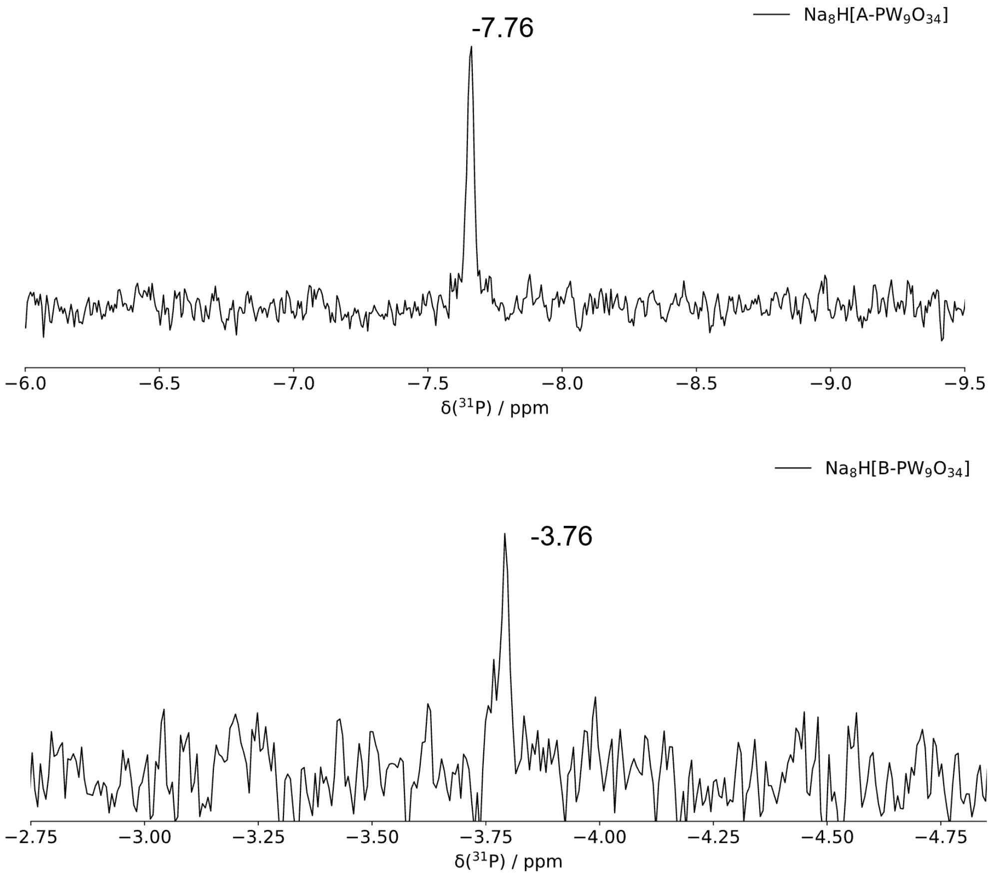

Figure 9.7: ^{31}P spectra of 50 mg tri-lacunary Keggin, $Na_8H[PW_9O_{34}]$ samples, recorded in D_2O.

9.2.2 Fourier-Transform Infrared (FT-IR)

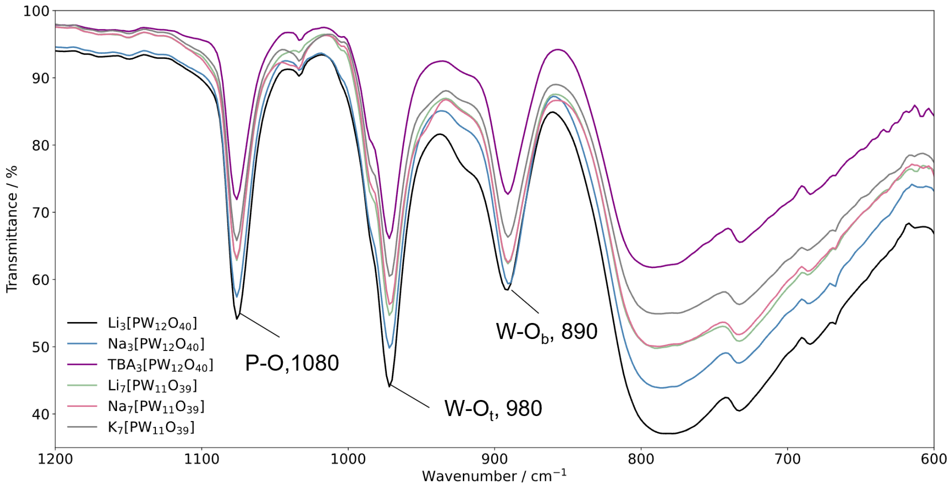

Figure 9.8: FT-IR spectra of Keggin, $X_3[PW_{12}O_{40}]$ ($X = Li^+, Na^+, TBA^+$) and mono-lacunary Keggin, $X_7[PW_{11}O_{39}]$ ($X = Li^+, Na^+, K^+$) samples.

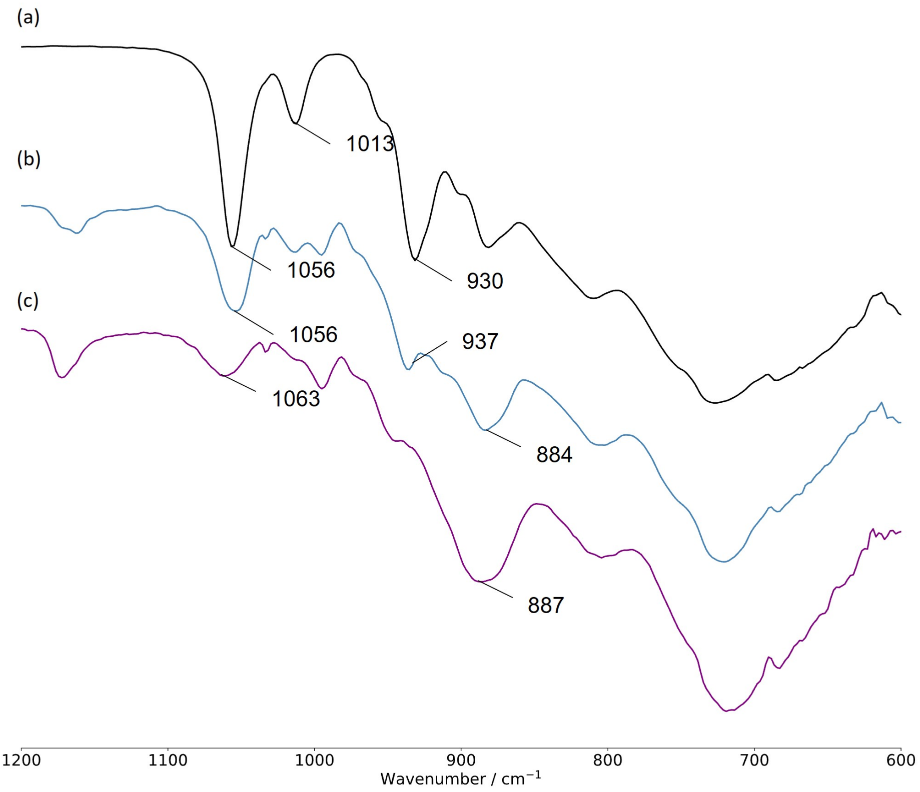

Figure 9.9: FT-IR spectra of tri-lacunary Keggin samples, $Na_8H[\Delta\text{-}PW_9O_{36}]$, freshly prepared and allowed to air-dry at room temperature, given by (a). However, if $Na_8H[\Delta\text{-}PW_9O_{36}]$ is dried at 140 °C for 1-2 h, then the spectrum shown by (b) is given. Prolonged heating ($>$ 15 h) at 140 °C produced spectra (c).

9.2.3 Ultraviolet-Visible (UV-Vis)

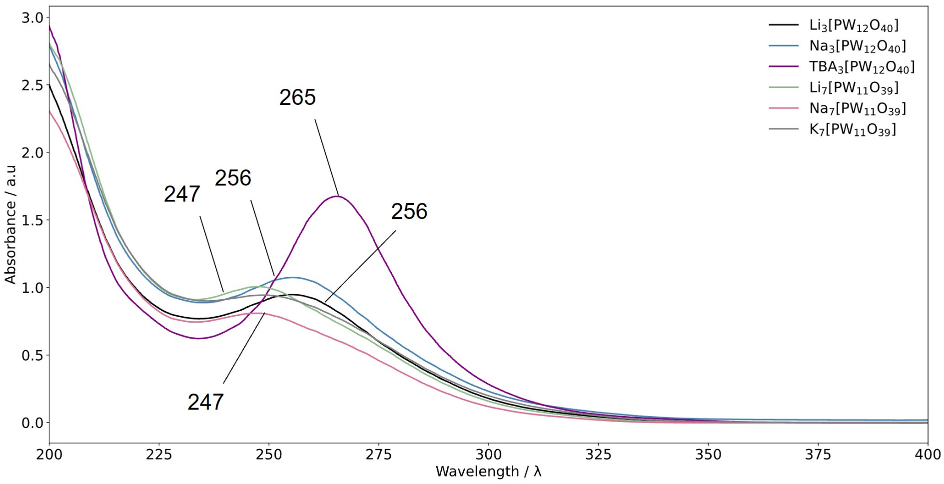

Figure 9.10: UV-Vis spectra for 30 μM solutions of Keggin, $X_3[PW_{12}O_{40}]$ (X = Li^+, Na^+) and mono-lacunary Keggin, $X_7[PW_{11}O_{39}]$ (X = Li^+, Na^+, K^+) samples, recorded in aqueous solution. 30 μM solutions solutions of $TBA_3[PW_{12}O_{40}]$ were recorded in acetonitrile.

9.2.4 Electrospray Ionisation Mass-Spectrometry (ESI-MS)

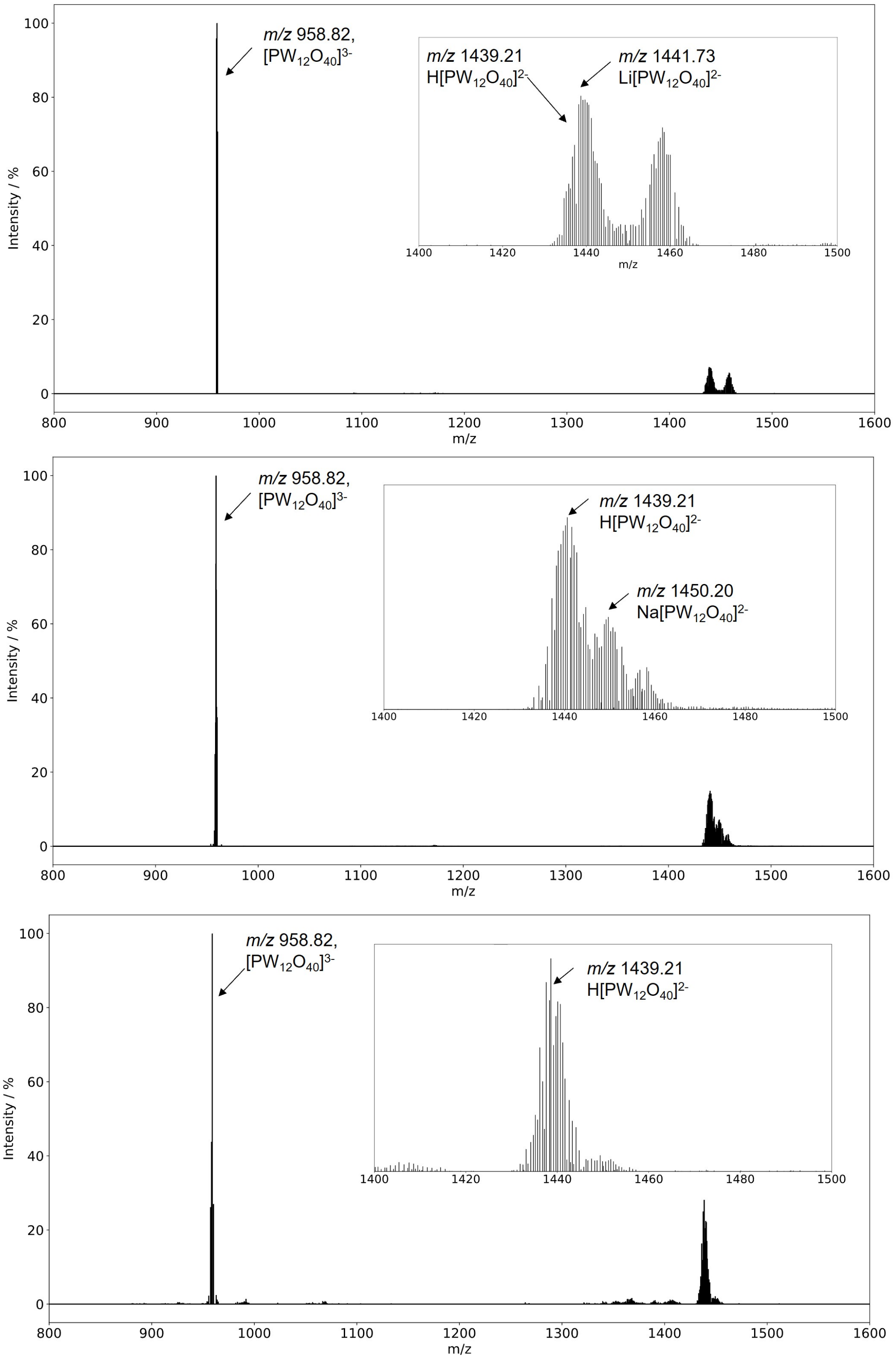

Figure 9.11: ESI-MS spectra for 1000 ppm solutions of Keggin, $X_3[PW_{12}O_{40}]$ ($X = Li^+$, Na^+) clusters recorded in aqueous solution (top, middle) and $TBA_3[PW_{12}O_{40}]$ recorded acetonitrile (bottom).

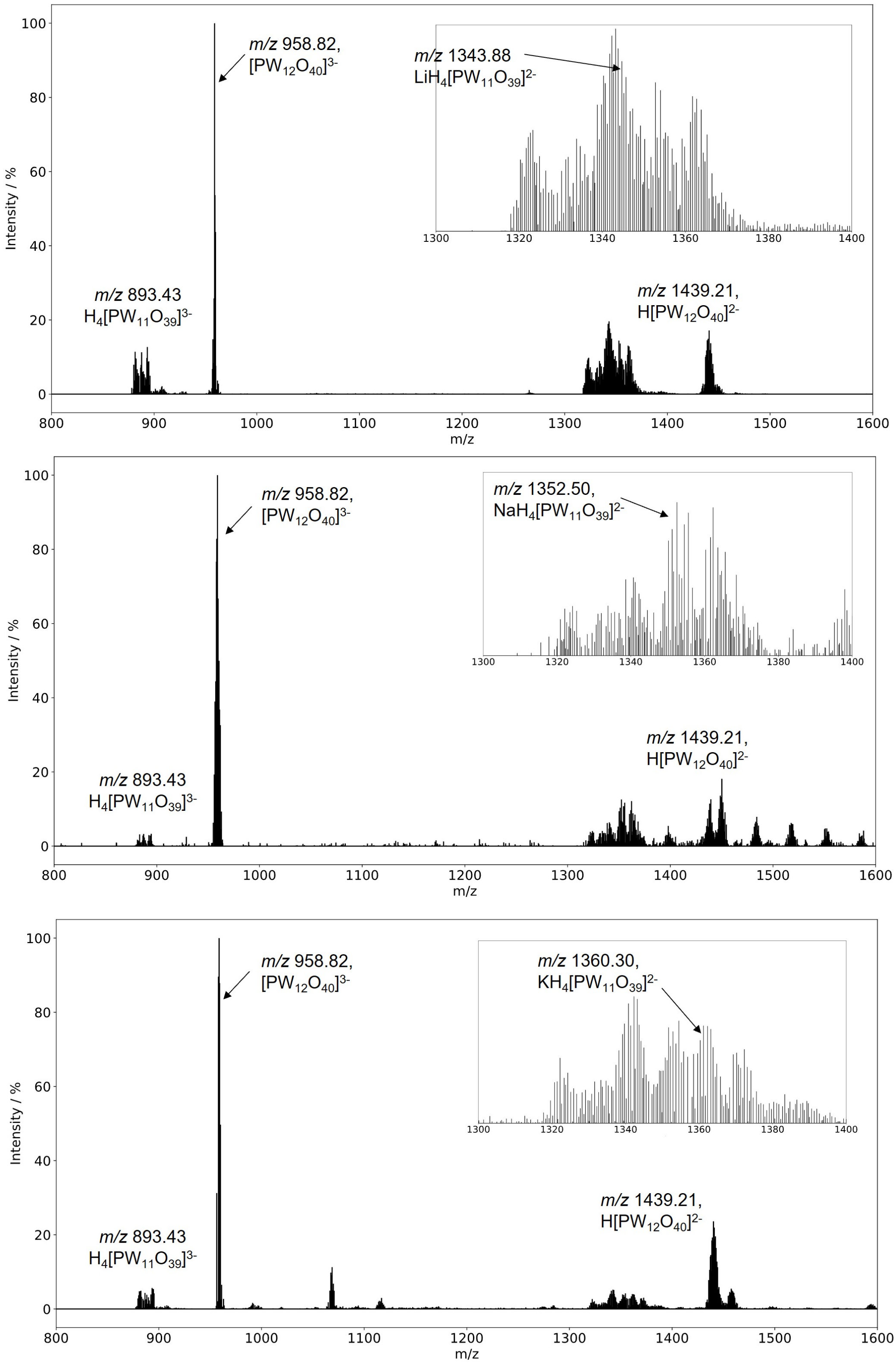

Figure 9.12: ESI-MS spectra for 1000 ppm solutions of mono-lacunary Keggin, $X_7[PW_{11}O_{39}]$ (X = Li^+, Na^+, K^+) samples, recorded in aqueous solution.

Table 9.3: Summary of observed fragments from the ionisation of Keggin, $X_3[PW_{12}O_{40}]$ ($X = Li^+, Na^+$) and mono-lacunary Keggin, $X_7[PW_{11}O_{39}]$ ($X = Li^+, Na^+, K^+$) clusters.

Anion	Observed m/z	Predicted m/z
$[PW_{12}O_{40}]^{3-}$	958.82	959.0
$H[PW_{12}O_{40}]^{2-}$	1439.21	1439.02
$Li[PW_{12}O_{40}]^{2-}$	1441.73	1441.98
$Na[PW_{12}O_{40}]^{2-}$	1450.20	1450.01
$H_4[PW_{11}O_{39}]^{3-}$	839.43	839.74
$H_5[PW_{11}O_{39}]^{2-}$	1341.27	1341.12
$LiH_4[PW_{11}O_{39}]^{2-}$	1343.88	1344.08
$NaH_4[PW_{11}O_{39}]^{2-}$	1352.50	1352.11
$KH_4[PW_{11}O_{39}]^{2-}$	1360.30	1360.16

9.2.5 Density Functional Theory (DFT)

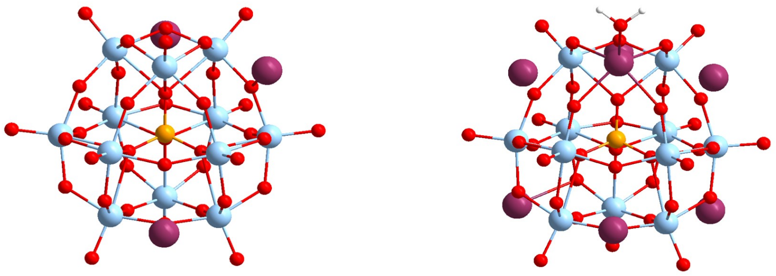

$X_3[PW_{12}O_{40}]$

$X_7[PW_{11}O_{39}]$; X= Li, Na, K

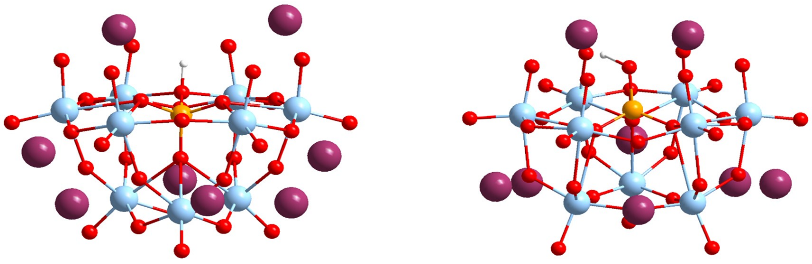

$Na_8H[A\text{-}PW_9O_{34}]$

$Na_8H[B\text{-}PW_9O_{34}]$

Figure 9.13: Geometries for Keggin, $X_3[PW_{12}O_{40}]$ ($X = Li^+, Na^+$), mono-lacunary, $X_7[PW_{11}O_{39}]$ ($X = Li^+, Na^+, K^+$) and tri-lacunary Keggin, $Na_8H[PW_9O_{34}]$ samples, optimised at PBE0/TZP level of theory.

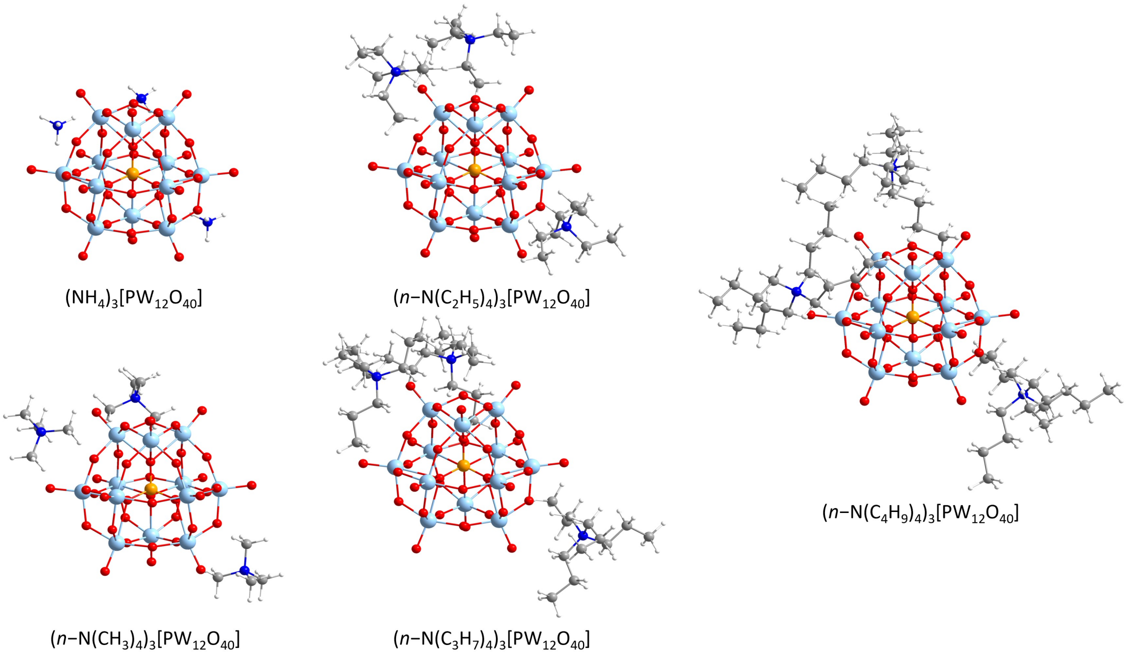

$(NH_4)_3[PW_{12}O_{40}]$

$(n\text{-}N(C_2H_5)_4)_3[PW_{12}O_{40}]$

$(n\text{-}N(C_4H_9)_4)_3[PW_{12}O_{40}]$

$(n\text{-}N(CH_3)_4)_3[PW_{12}O_{40}]$

$(n\text{-}N(C_3H_7)_4)_3[PW_{12}O_{40}]$

Figure 9.14: Geometries for Keggin, $[(n\text{-}C_xH_{2x+1})_4N]_3[PW_{12}O_{40}]$; where x = 0-4, optimised at PBE0/TZP level of theory.

Table 9.4: Computed, δ_{Calc}, fitted, δ_{Fitted}, and experimental, δ_{Exp} signals for Keggin, $X_3[PW_{12}O_{40}]$ (X = Li^+, Na^+, TBA^+), mono-lacunary Keggin, $X_7[PW_{11}O_{39}]$ (X = Li^+, Na^+, K^+) and tri-lacunary Keggin, $Na_8H[PW_9O_{34}]$ clusters.

System	δ_{Calc}	δ_{Fitted}
$Li_3[PW_{12}O_{40}]$	-12.84	-14.73
$Na_3[PW_{12}O_{40}]$	-13.04	-14.87
$TBA_3[PW_{12}O_{40}]$	-12.33	-14.62
$Li_7[PW_{11}O_{39}]$	-7.27	-11.24
$Na_7[PW_{11}O_{39}]$	-7.35	-11.29
$K_7[PW_{11}O_{39}]$	-8.55	-12.04
$Na_8H[A-PW_9O_{34}]$	-5.10	-9.87
$Na_8H[B-PW_9O_{34}]$	6.28	-2.72

Table 9.5: Computed energies (PBE/TZP) for the highest occupied (HOMO), lowest unoccupied molecular orbitals (LUMO) and the corresponding energy gap for Keggin, $X_3[PW_{12}O_{40}]$ (X = Li^+, Na^+, TBA^+), mono-lacunary Keggin, $X_7[PW_{11}O_{39}]$ (X = Li^+, Na^+, K^+) and tri-lacunary Keggin, $Na_8H[PW_9O_{34}]$ clusters. All energies are reported in eV.

System	HOMO	LUMO	Gap
$Li_3[PW_{12}O_{40}]$	-7.909	-5.466	2.443
$Na_3[PW_{12}O_{40}]$	-7.608	-5.117	2.491
$TBA_3[PW_{12}O_{40}]$	-7.877	-3.993	3.884
$Li_7[PW_{11}O_{39}]$	-7.591	-4.766	2.825
$Na_7[PW_{11}O_{39}]$	-7.097	-4.181	2.916
$K_7[PW_{11}O_{39}]$	-6.749	-3.828	2.921
$Na_8H[A-PW_9O_{34}]$	-6.549	-3.305	3.244
$Na_8H[B-PW_9O_{34}]$	-6.702	-3.586	3.116

9.3 Appendix C

This section provides further information in relation to Chapter 6: "Controlling Ion-Pair Proximity in Aqueous Transition-Metal-Substituted Polyoxotungstates".

9.3.1 Cyclic Voltammetry (CV)

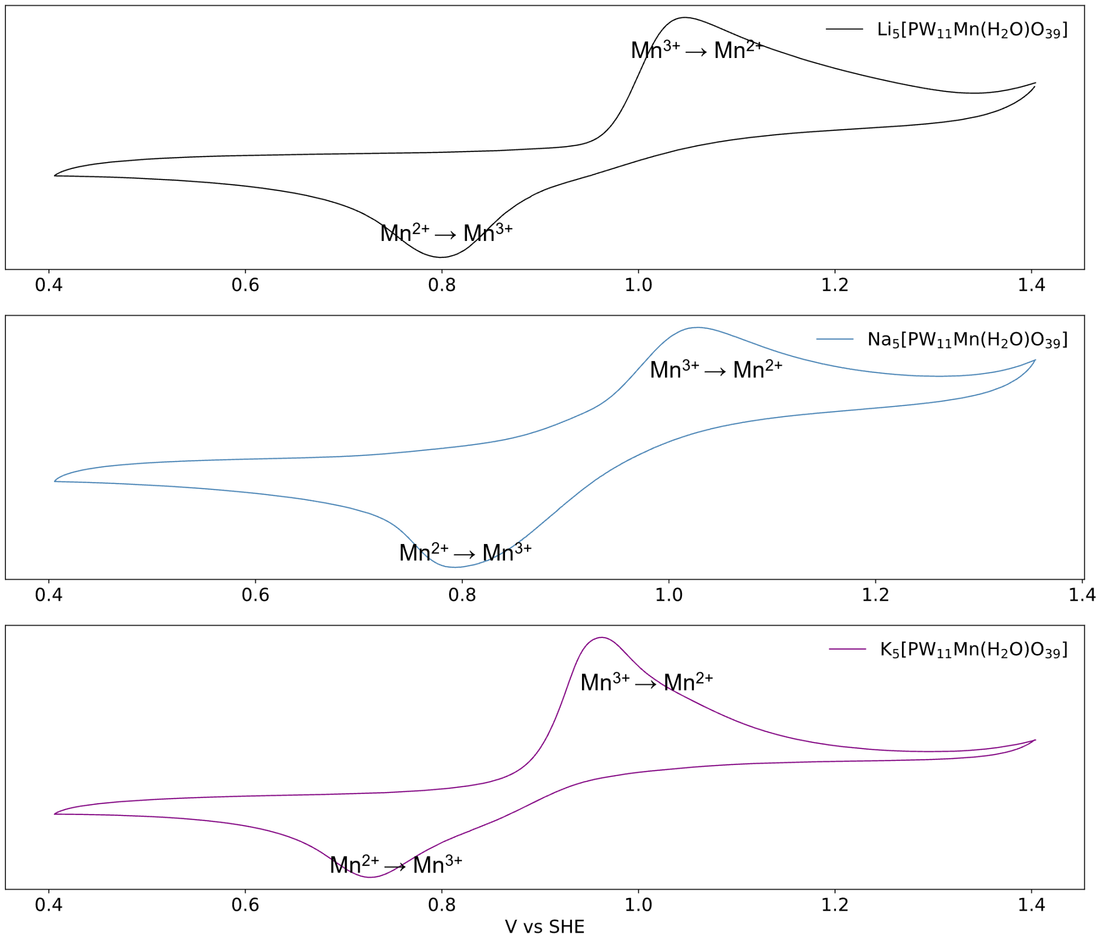

Figure 9.15: Cyclic voltammogram at the glassy carbon electrode for the manganese(II)-substituted Keggin, $X_5[PW_{11}Mn(H_2O)O_{39}]$; X = Li, Na, and K salts. All scans were recorded using 10 mM heteropolyanion (HPA) and an appropriate 0.2 M acetate (pH 4.80) solution, scan rate 10 mV s^{-1}. All potentials are recorded against the standard hydrogen electrode (SHE).

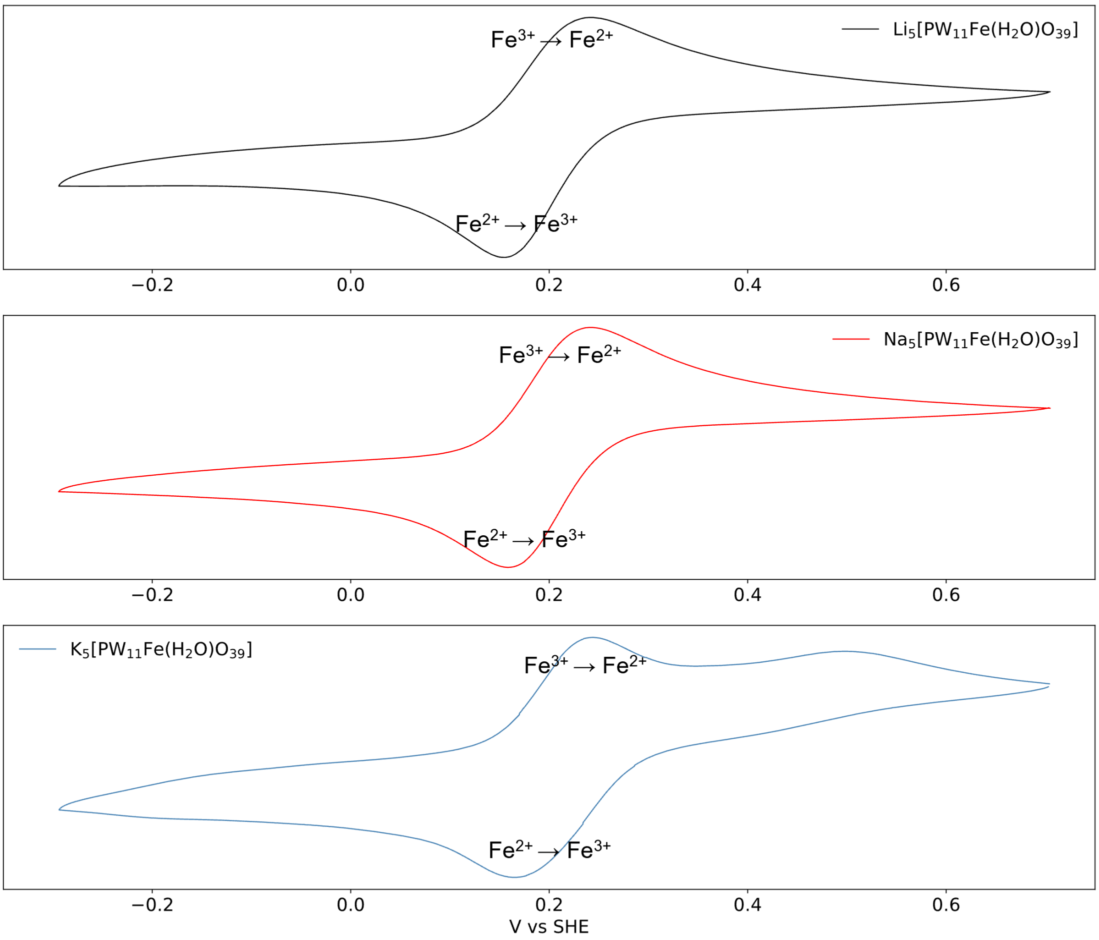

Figure 9.16: Cyclic voltammogram at the glassy carbon electrode for the iron(II)-substituted Keggin, $X_5[PW_{11}Fe(H_2O)O_{39}]$; X = Li, Na, and K salts. All scans were recorded using 10 mM heteropolyanion (HPA) and an appropriate 0.2 M acetate (pH 4.80) solution, scan rate 10 mV s^{-1}. All potentials are recorded against the standard hydrogen electrode (SHE).

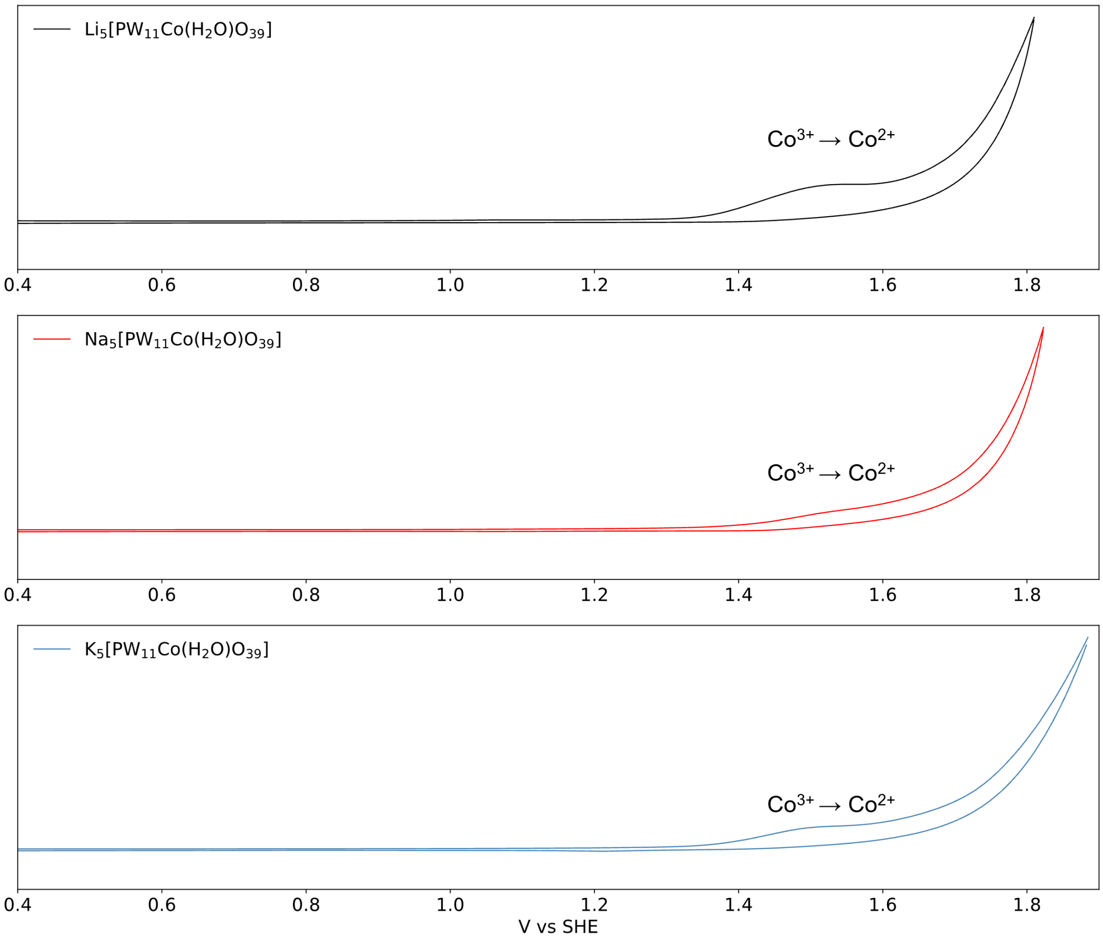

Figure 9.17: Cyclic voltammogram at the glassy carbon electrode for the cobalt(II)-substituted Keggin, $X_5[PW_{11}Co(H_2O)O_{39}]$; X = Li, Na, and K salts. All scans were recorded using 10 mM heteropolyanion (HPA) and an appropriate 0.2 M acetate (pH 4.80) solution, scan rate 10 mV s^{-1}. All potentials are recorded against the standard hydrogen electrode (SHE).

9.3.2 Nuclear Magnetic Resonance (NMR)

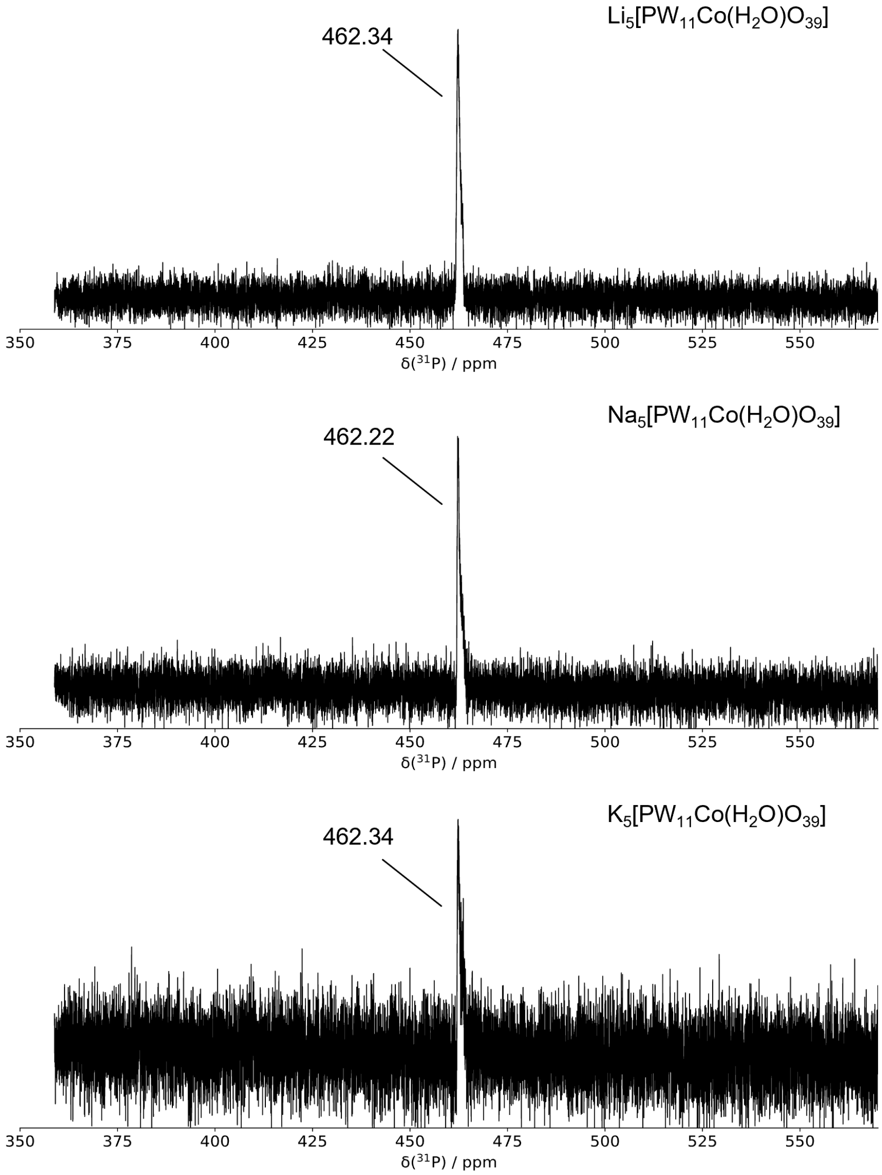

Figure 9.18: ^{31}P spectra of 50 mg cobalt(II)-substituted Keggin, $X_5[PW_{11}Co(H_2O)O_{39}]$; X = Li, Na, and K salts, recorded in D_2O.

9.3.3 Fourier-Transform Infrared (FT-IR)

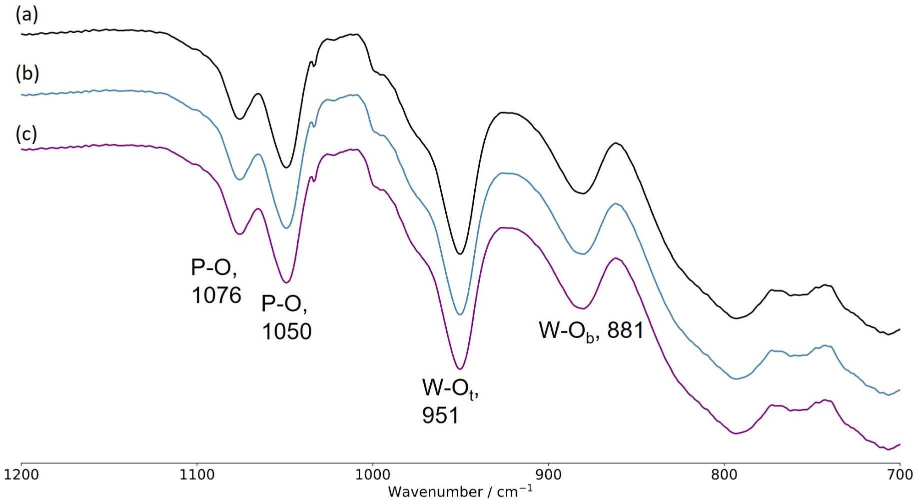

Figure 9.19: FT-IR spectrum for manganese(II)-substituted Keggin, $X_5[PW_{11}Mn(H_2O)O_{39}]$ salts. (a) X = Li, (b) X = Na, (c) and K salts.

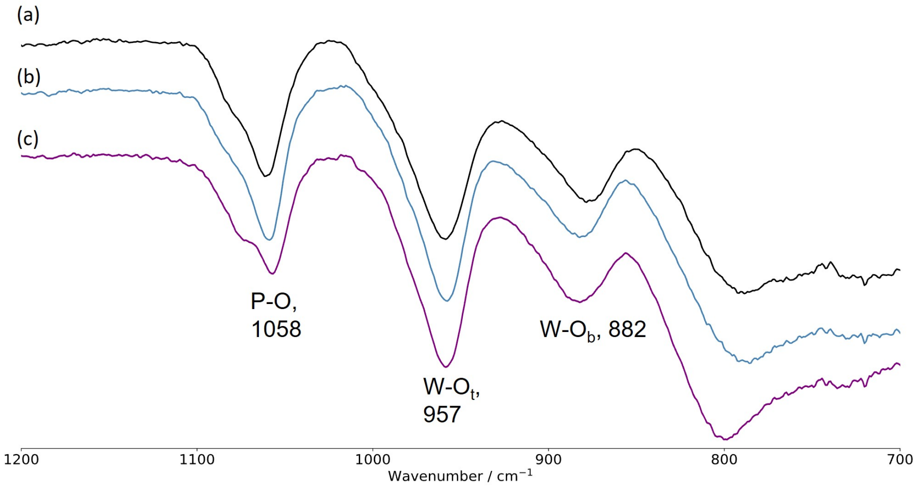

Figure 9.20: FT-IR spectrum for iron(II)-substituted Keggin, $X_5[PW_{11}Fe(H_2O)O_{39}]$ salts. (a) X = Li, (b) X = Na, (c) and K salts.

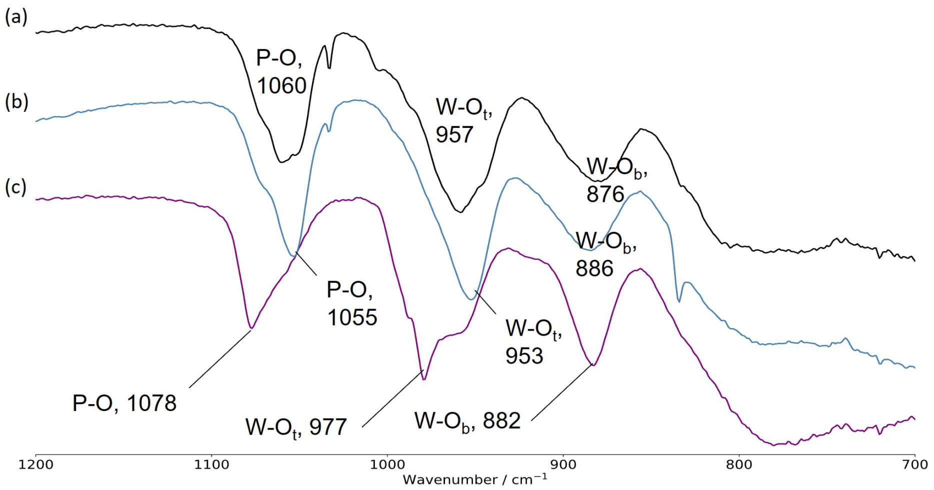

Figure 9.21: FT-IR spectrum for cobalt(II)-substituted Keggin, $X_5[PW_{11}Co(H_2O)O_{39}]$ salts. (a) X = Li, (b) X = Na, (c) and K salts.

9.3.4 Ultraviolet-Visible (UV-Vis)

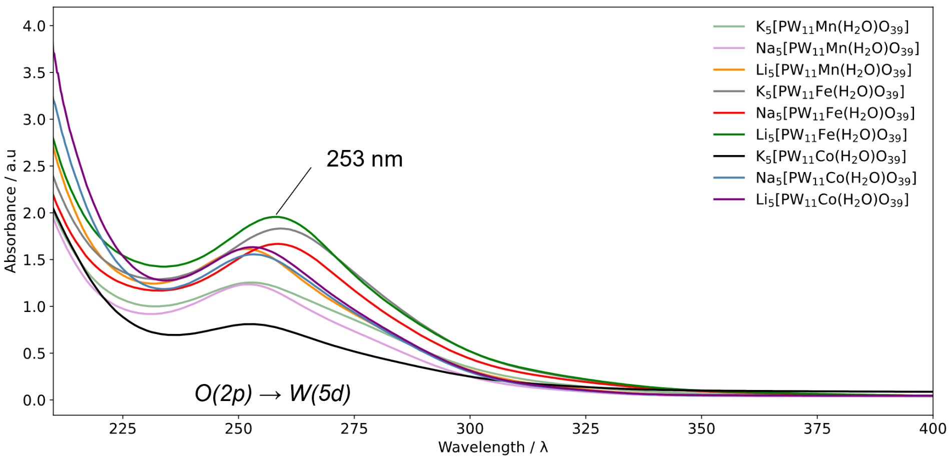

Figure 9.22: UV-Vis spectra for 30 M solutions of the mono-substituted Keggin, $X_5[PW_{11}M(H_2O)O_{39}]$; X = Li, Na, and K, M = Mn(III/II), Fe(III/II), and Co(III/II), salts recorded in aqueous solution.

9.3.5 Electrospray Ionisation Mass-Spectrometry (ESI-MS)

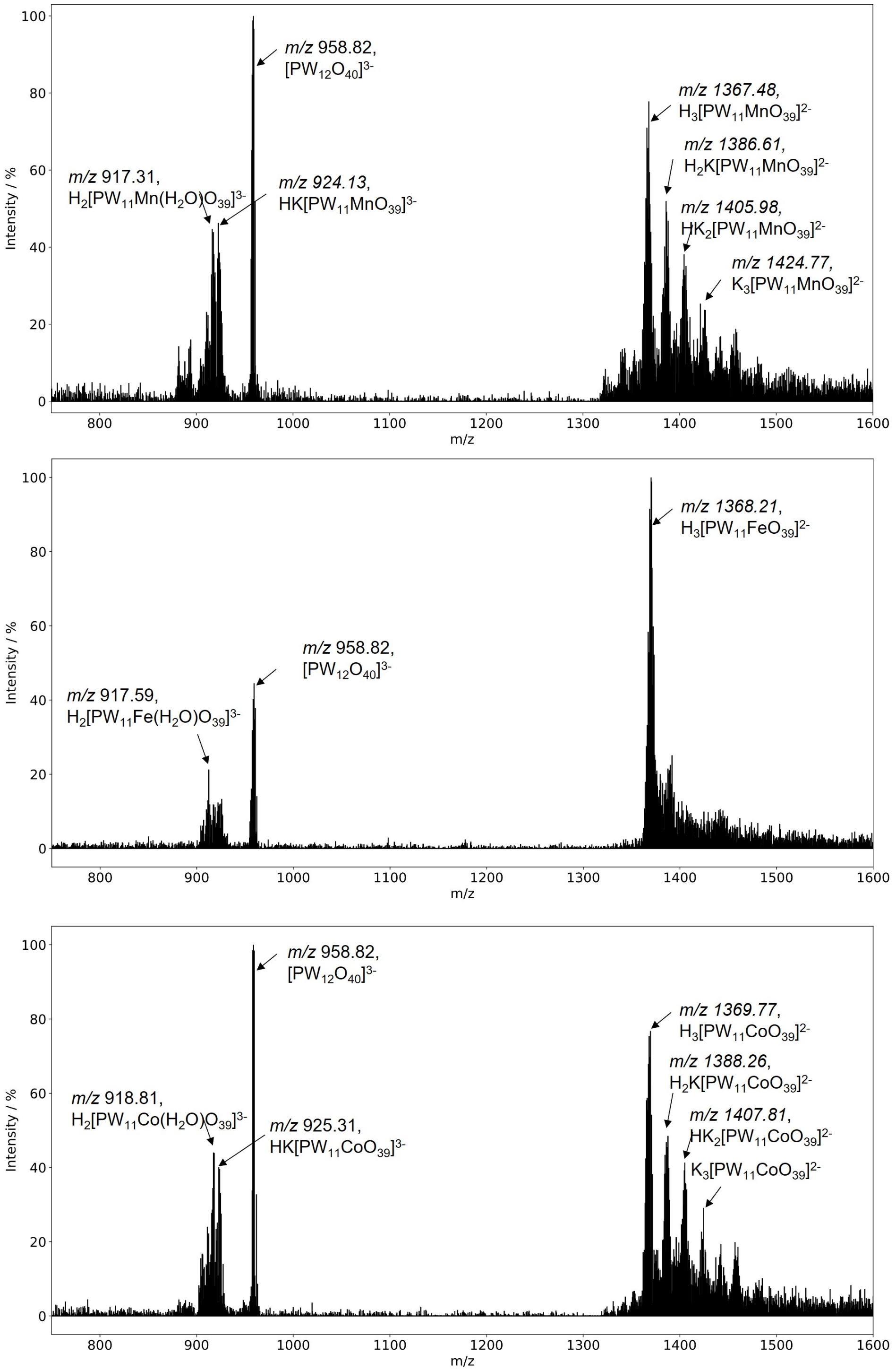

Figure 9.23: ESI-MS spectra for 1000 ppm solutions of mono-substituted Keggin, $K_5[PW_{11}M(H_2O)O_{39}]$; M = Mn(III/II), Fe(III/II), and Co(III/II), recorded in aqueous solution.

9.3.6 Structural Benchmark

An assessment of the structural parameters in $K_5[PW_{11}Co(H_2O)O_{39}]$ was performed to assess the accuracy of applied exchange-correlation (x-c) functionals and basis sets and its ability to precisely describe the system of interest. To assess the influence of Hartree-Fock (HF) exchange and basis set on the optimised geometry of $K_5[PW_{11}Co(H_2O)O_{39}]$, MSE and MAE were used to examine performance against the crystallographic structure, reported by Cavaleiro and co-workers.[1] Herein, four oxygen environments were examined: Oc and Ot which correspond to the heteroatom-oxygen and terminal-oxygen atoms, while O_{a1} and O_{b2} denote bridging (equatorial) oxygens bound to the incorporated transition-metal.

In our previous work, we shown equilibrium geometries in $[PW_{11}Co(H_2O)O_{39}]^{5-}$ were generally well described across all examine applied exchange-correlation (x-c) functionals and basis sets, rarely exceeding discrepancies of 0.18 Å. To explore the influence of explicitly located counterions, we have incorporated calculations for $[PW_{11}Co(H_2O)O_{39}]^{5-}$ computed with B3LYP/TZP - see Figure 9.24a and 9.24b. Figure 9.24a depicts selected structural parameters employed to assess the accuracy of applied functionals and basis sets. Herein, explicitly locating counterions on the POM surface did not significantly distort the inner coordination sphere of the newly incorporated transition-metal. Figure 9.24b reports that increasing contributions of Hartree-Fock (HF) exchange become increasingly overestimated with respect to crystallographic geometries (MSE $>$ 0). All entries for $K_5[PW_{11}Co(H_2O)O_{39}]$ deviated more from experimental values relative to the charged $[PW_{11}Co(H_2O)O_{39}]^{5-}$, systems. Reproduction of heteroatom-oxygen and terminal-oxygen bonds: O_c-Co and O_t-Co was the primary source of computed error. However, equatorial distances, O_{a1}-Co and O_{b2}-Co, accurately described (MAE $>$ 0.01 Å) and were not systematically over- or underestimated with respect to experimental measurements.

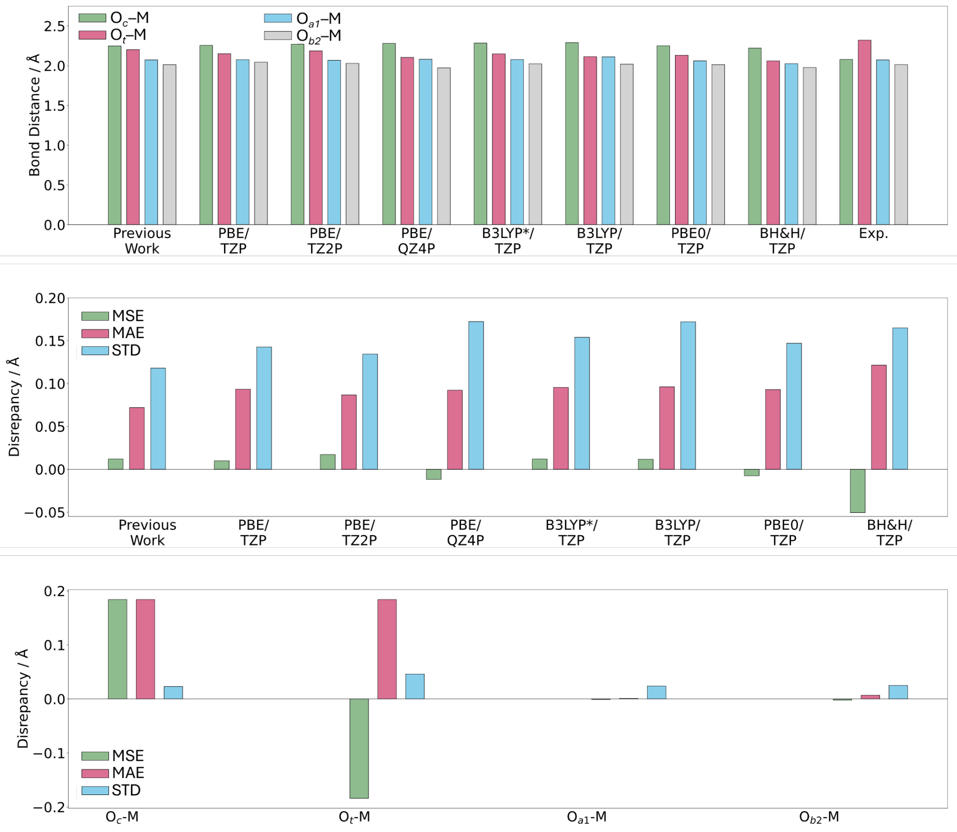

Figure 9.24: Selected structural parameters for $K_5[PW_{11}Co(H_2O)O_{39}]$ referenced against the crystallographic structure taken from Cavaleiro and co-workers[1]. (b) MSE, MAE, and STD calculated for all examine applied exchange-correlation (x-c) functionals and basis sets. (c) MSE, MAE, and STD calculated for four types of metal–oxygen interactions. All bond distances are reported in Å.

9.3.7 Electronic Structure

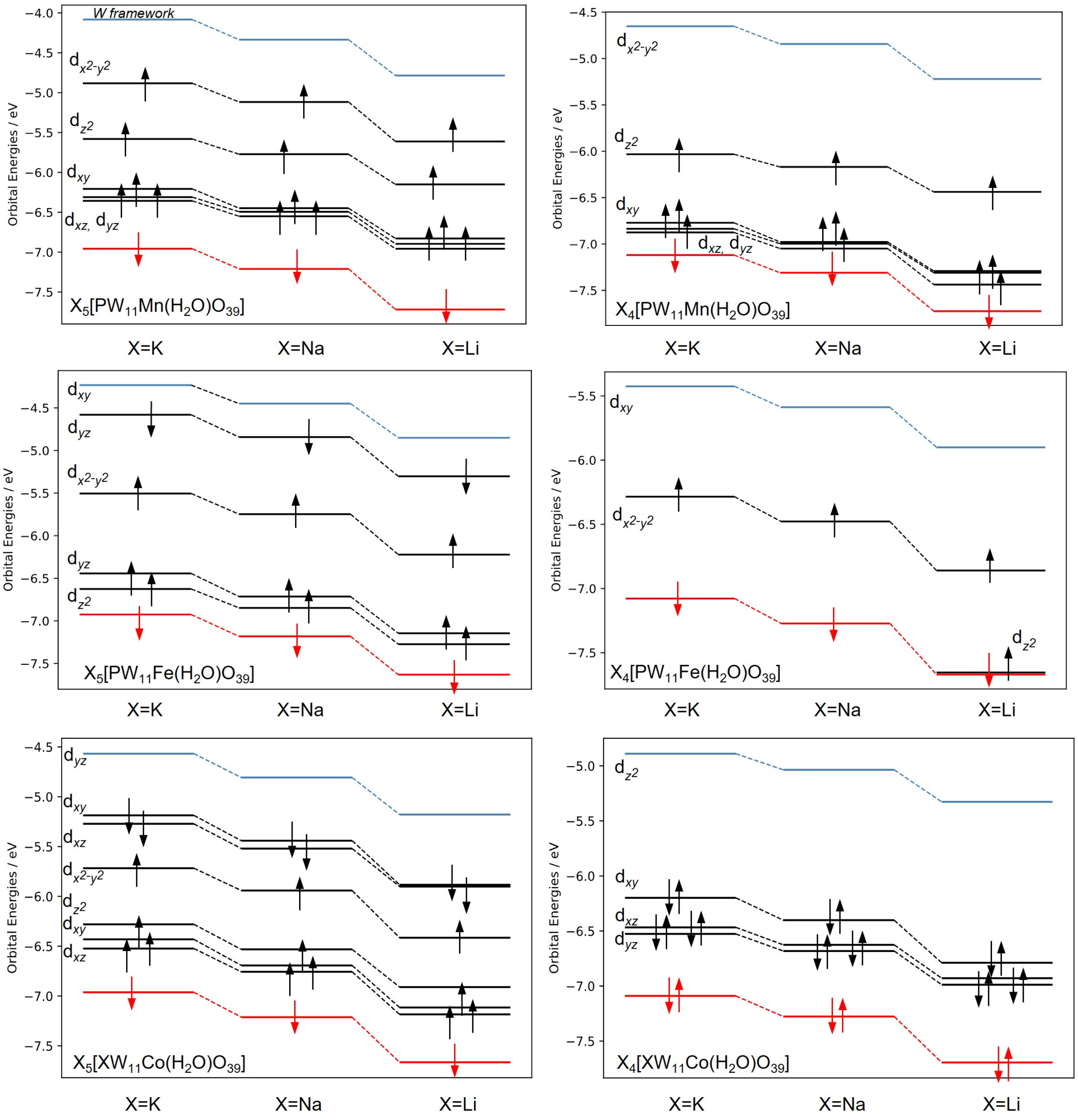

Figure 9.25: Schematic molecular orbital diagram for $X_5[PW_{11}M(H_2O)O_{39}]$ (left) and corresponding $X_4[PW_{11}M(H_2O)O_{39}]$; X = Li, Na, and K, M = Mn(III/II), Fe(III/II), and Co(III/II) compounds. All complexes were optimized using PBE/TZP level of theory. Colours correspond to red = O2(p), blue = W, and black = transition-metal. All orbital energies reported in eV.

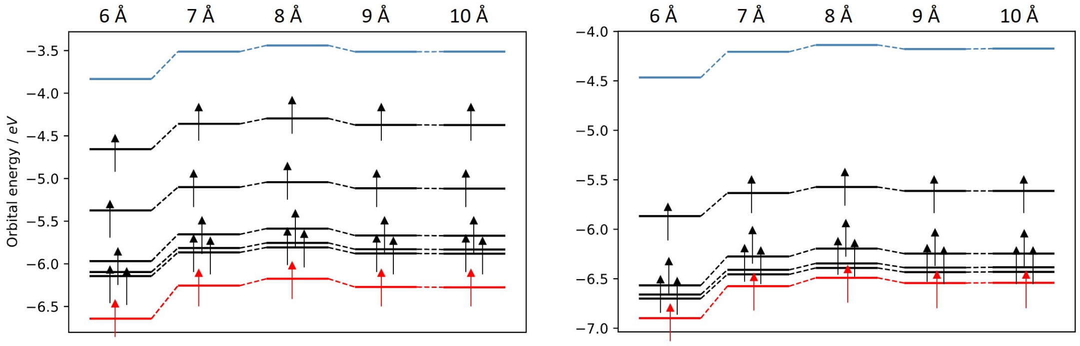

$K_5[PW_{11}Mn(H_2O)O_{39}]$ $K_4[PW_{11}Mn(H_2O)O_{39}]$

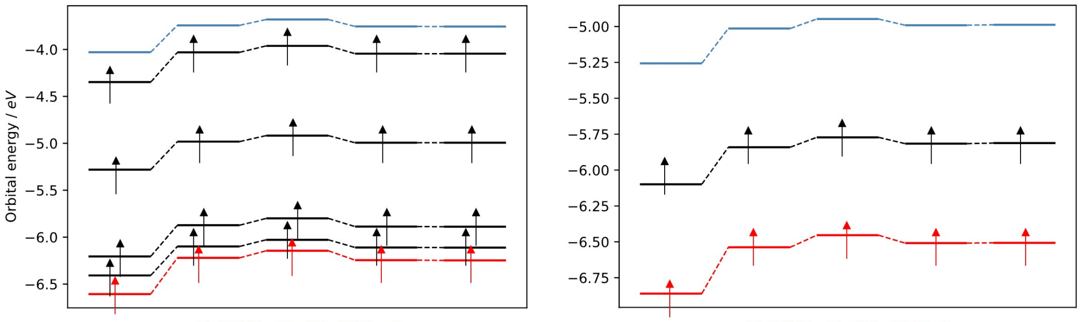

$K_5[PW_{11}Fe(H_2O)O_{39}]$ $K_4[PW_{11}Fe(H_2O)O_{39}]$

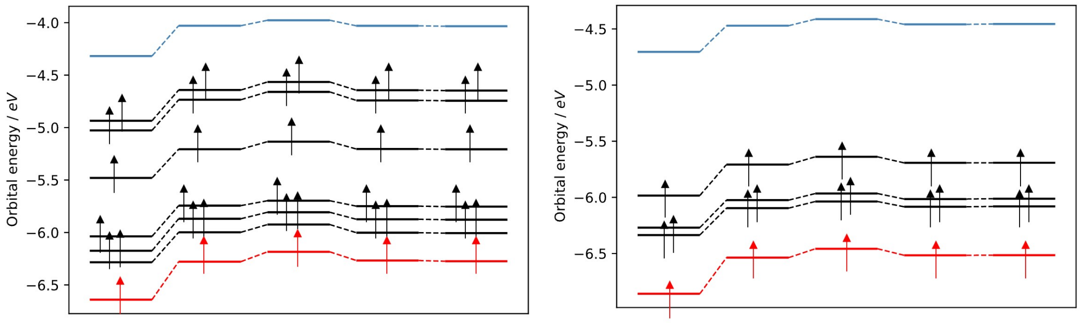

$K_5[PW_{11}Co(H_2O)O_{39}]$ $K_4[PW_{11}Co(H_2O)O_{39}]$

Figure 9.26: Schematic molecular orbital diagram for $K_5[PW_{11}M(H_2O)O_{39}]$ (left) and corresponding $K_4[PW_{11}M(H_2O)O_{39}]$; M = Mn(III/II), Fe(III/II), and Co(III/II) compounds at fixed intervals (6 (left)- 10 Å (right)) for d_{P-X}. All complexes were optimized using PBE/TZP level of theory. Colours correspond to red = O2(p), blue = W, and black = transition-metal. All orbital energies reported in eV.

9.4 Appendix D

This section provides further information in relation to Chapter 6: "High Temperature Ammonia Synthesis using Mono-Substituted Polyoxotungstates".

9.4.1 Calculation of Ammonia Synthesis Rate from Conductivity Measurement

Mean conductivity measurements across six different H_2SO_4 (0.00108 mol L^{-1}) and $(NH_4)_2SO_4$ solutions are reported in Table 9.6.[2–4]

Table 9.6: Conductivity of H_2SO_4 (0.00108 mol L^{-1}) and $(NH_4)_2SO_4$ solutions recorded in µS cm^{-1}.

H_2SO_4	$(NH_4)_2SO_4$
836	320
828	319
830	320
844	321
836	315
832	325
834*	320*

* Mean conductivity of H_2SO_4 (0.00108 mol L^{-1}) and $(NH_4)_2SO_4$.

The following equations demonstrated how ammonia synthesis rates were calculated with respect to conductivity.[2–4] For each experiment 200 mL of 0.00108 mol L^{-1} of H_2SO_4 was used, shown below[2–4]:

$$n\mathrm{H_2SO_4} = \text{concentration} \times \text{volume} \tag{9.1}$$

$$n\mathrm{H_2SO_4} = 0.00108\,\mathrm{mol\,L^{-1}} \times 0.2\,\mathrm{L} \tag{9.2}$$

$$n\mathrm{H_2SO_4} = 2.16 \times 10^{-4}\, mol \tag{9.3}$$

Determine mole ratio for equivalent H^+ in NH_3:

$$2\,\mathrm{NH_3} + \mathrm{H_2SO_4} \rightarrow \mathrm{(NH_4)_2SO_4} \tag{9.4}$$

$$2.16 \times 10^{-4} \times 2 = 4.32 \times 10^{-4}\; n\; NH_3 \tag{9.5}$$

Hence, 4.32 × 10^{-4} moles ammonia is required to completely react with H_2SO_4.[2–4] Therefore, the change in conductivity for the above reaction is as follows[2–4]:

$$\Delta\mathrm{S} = \mathrm{S}_{T0} - \mathrm{S}_{Tx} \tag{9.6}$$

$$\Delta\mathrm{S} = 834 - 320 \tag{9.7}$$

$$\Delta\mathrm{S} = 514\,\mu\mathrm{S\,cm^{-1}} \tag{9.8}$$

Then, calculate the number of moles required for the change in conductivity:

$$n\mathrm{H_2SO_4}\,\text{consumed} = \frac{4.32 \times 10^{-4}}{514\,\mu\mathrm{S\,cm^{-1}}} \tag{9.9}$$

$$n\mathrm{H_2SO_4}\,\text{consumed} = 8.41 \times 10^{-7}\,\mathrm{mol} / \mu\mathrm{S\,cm^{-1}} \tag{9.10}$$

9.4.2 Conductivity Time Profiles

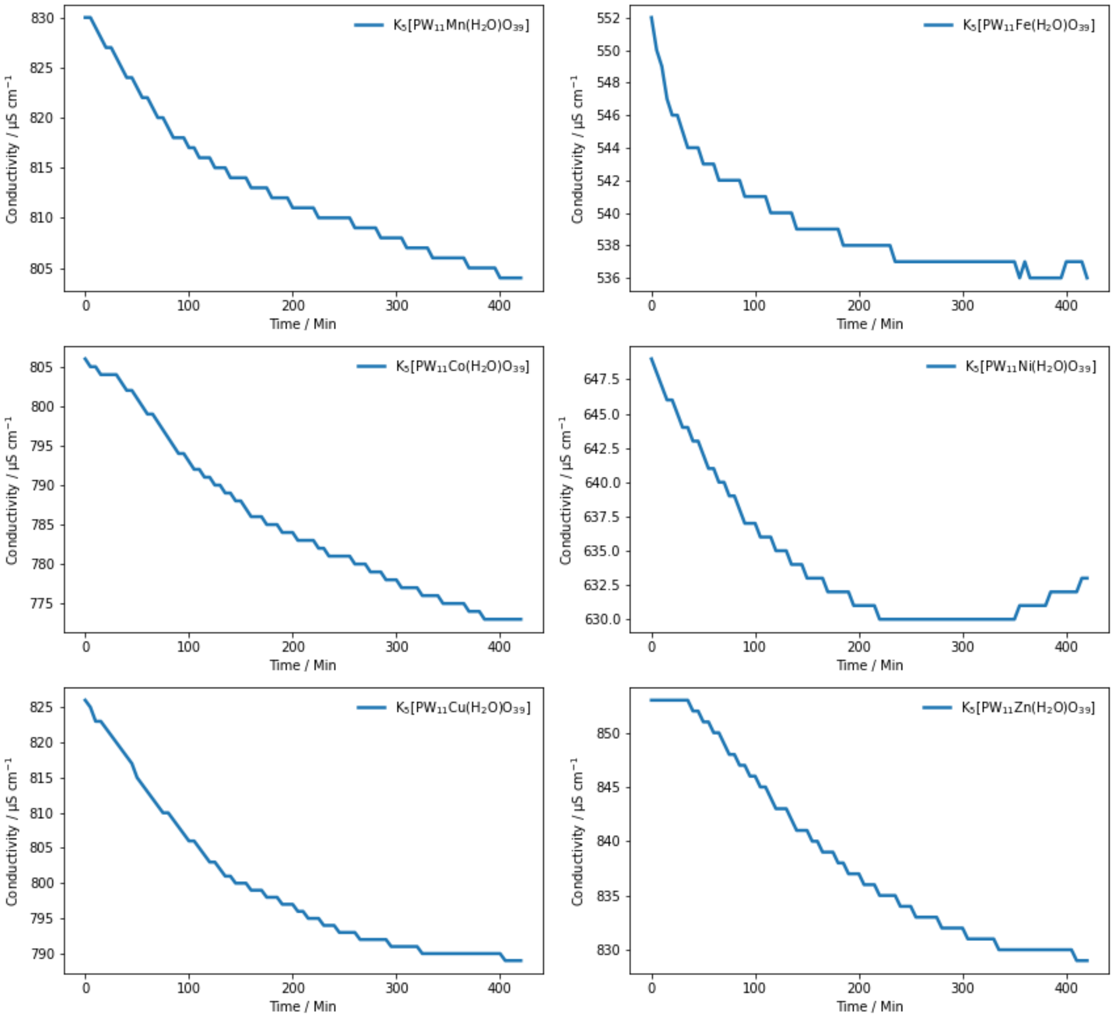

Figure 9.27: Reaction conductivity profiles for Keggin-based potassium salts, $K_5[PW_{11}M(H_2O)O_{39}]$. This procedure has been employed in several previous publications.[4–6]

9.4.3 Nuclear Magnetic Resonance (NMR)

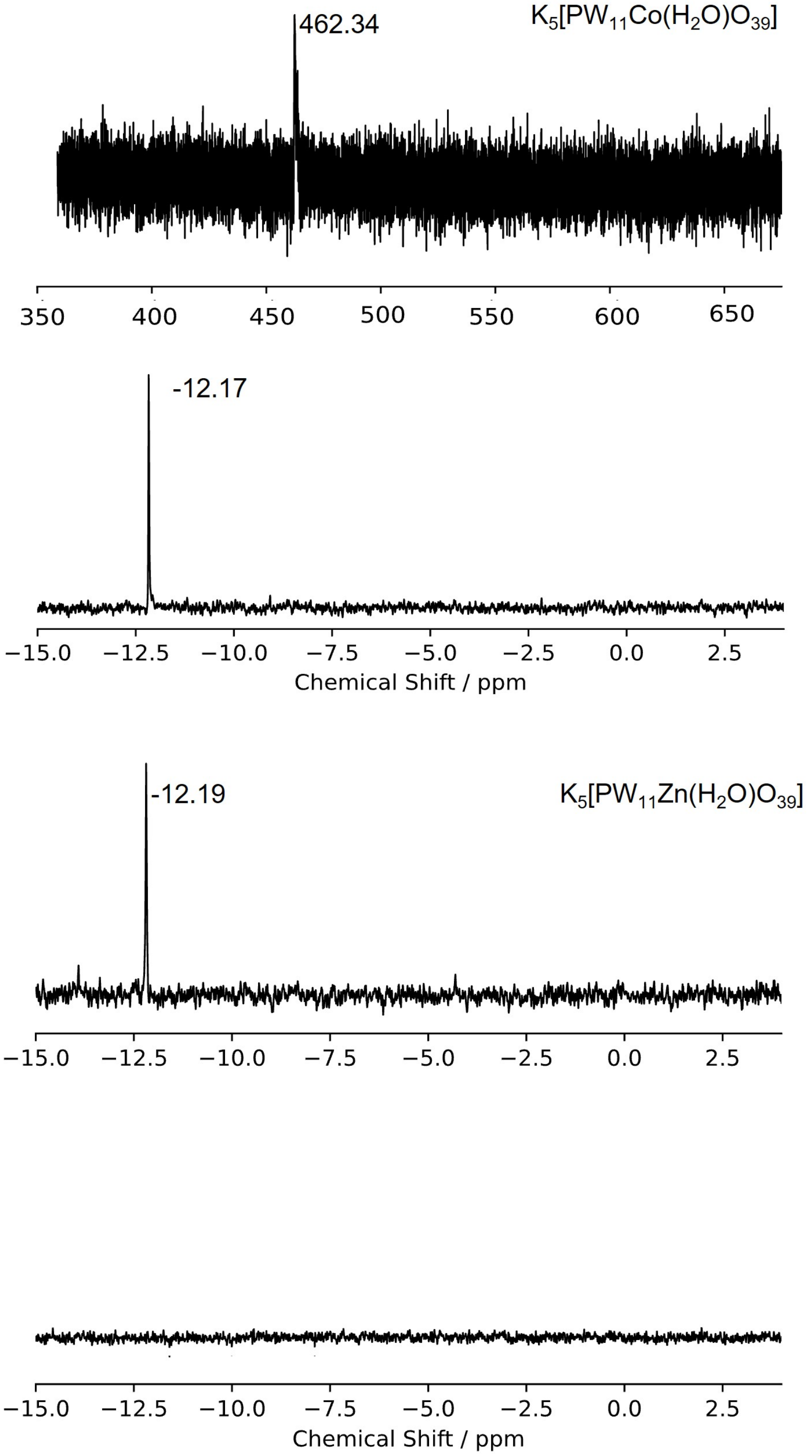

Figure 9.28: ^{31}P spectra of 50 mg mono-substituted Keggin, $k_5[PW_{11}Co(H_2O)O_{39}]$; M = Co(II) or Zn(II) recorded pre-reaction (top) and post-reaction (bottom), recorded in D_2O.

9.4.4 Ultraviolet-Visible (UV-Vis)

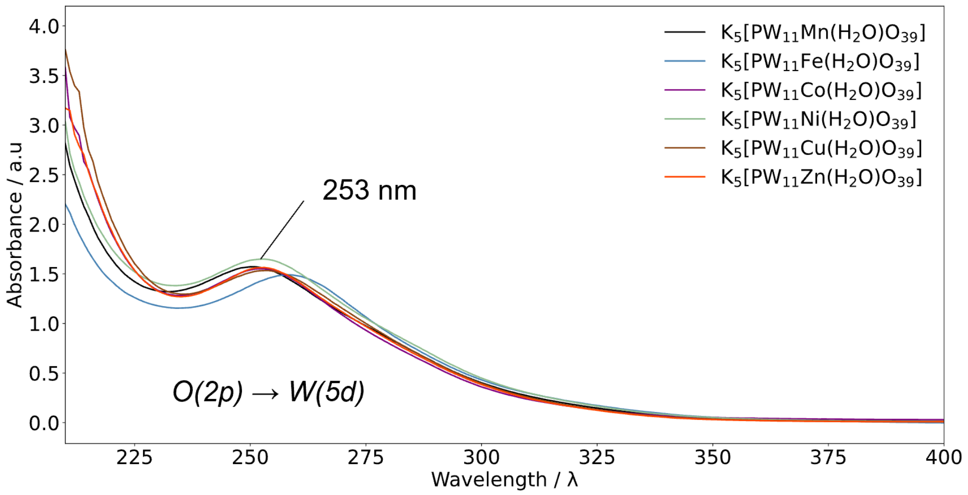

Figure 9.29: UV-Vis spectra for 30 μM solutions of the mono-substituted Keggin, $K_5[PW_{11}M(H_2O)O_{39}]$; M = Ni(II), Cu(II), and Zn(II) salts recorded in aqueous solution.

9.4.5 Electrospray Ionisation Mass-Spectrometry (ESI-MS)

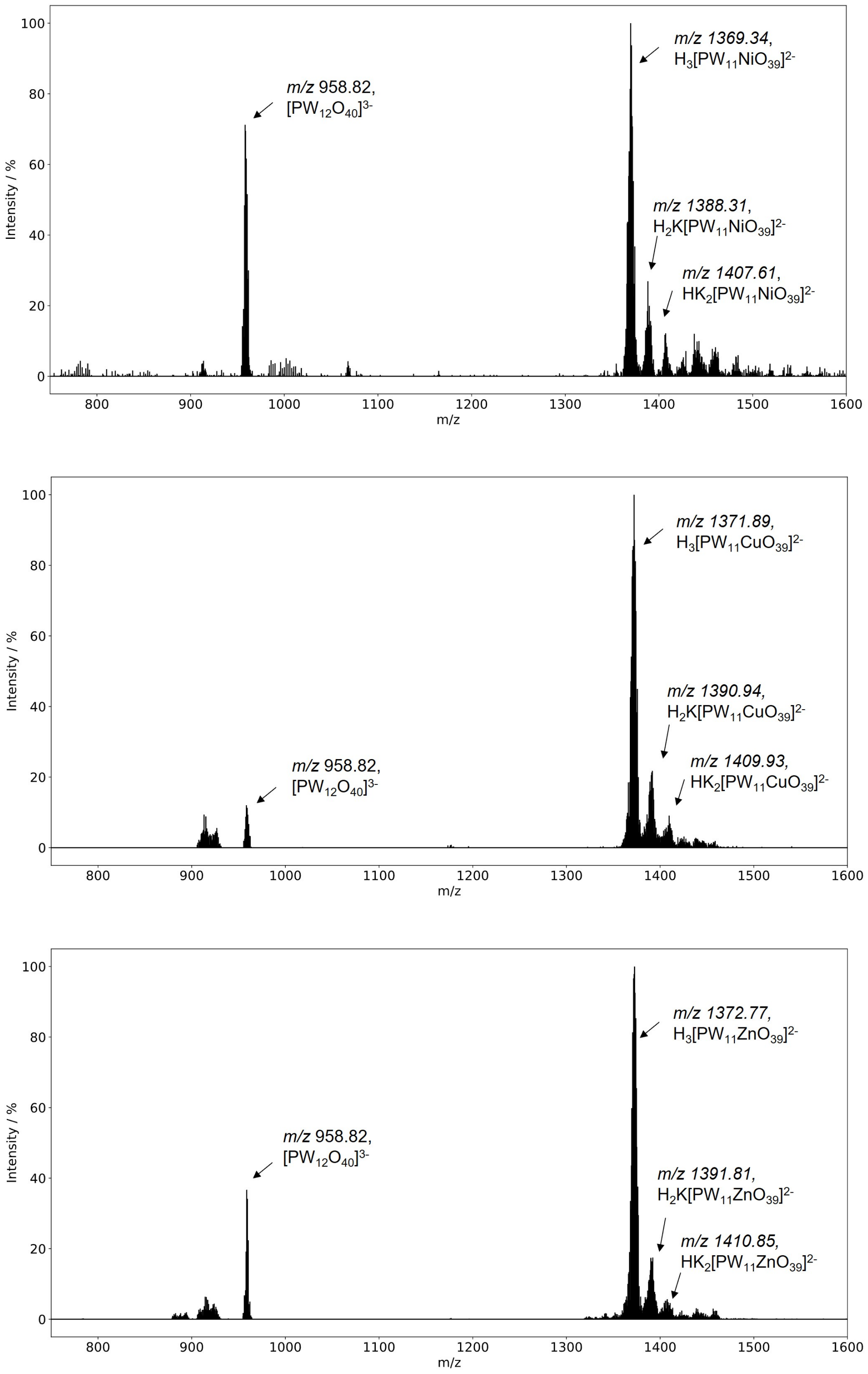

Figure 9.30: ESI-MS spectra for 1000 ppm solutions of mono-substituted Keggin, $K_5[PW_{11}M(H_2O)O_{39}]$; M = Ni(II), Cu(II), and Zn(II) salts recorded in aqueous solution.

Bibliography

[1] M. Balula, J. Gamelas, H. Carapuça, A. Cavaleiro and W. Schlindwein, *Eur. J. Inorg. Chem.*, 2004, **2004**, 619–628.

[2] K. McAulay, Ph.D Thesis, University of Glasgow, 2017, 166–168.

[3] D. McKay, Ph.D Thesis, University of Glasgow, 2008, 166–167.

[4] A. Daisley and J. S. Hargreaves, *J. Energy Chem.*, 2019, **39**, 170–175.

[5] A. Daisley, J. Hargreaves, R. Hermann, Y. Poya and Y. Wang, *Catal. Today*, 2020, **357**, 534–540.

[6] A. Daisley, M. Higham, C. R. A. Catlow and J. S. Hargreaves, *Faraday Discuss.*, 2023, **243**, 97–125.